Solvency Effects on Biopolymer Interactions in Pectin Gels

Alessandro Gulotta

School of Food Science and Nutrition

University of Leeds

Submitted in accordance with the requirements for the degree of

Doctor of Philosophy

December 2018

The candidate confirms that the work submitted is his own and that appropriate credit has been given where reference has been made to the work of others.

To my Family

Acknowledgements

First of all, I would like to express my gratitude to both of my supervisors, Prof. Brent Murray and Dr. Johan Mattsson, for their support, guidance and patience throughout my Ph.D. studies. They have been a source of inspiration for the entire period I have spent at the University of Leeds. I cannot be grateful enough for all of this.

Thanks to all the members of Centre of Doctoral Training in Soft Matter and Functional Interfaces program (SOFI CDT). I learnt so many things during these years, in both science and in life. I am proud to be in the first cohort of the SOFI CDT program.

Thanks to Mondelez International and Dr. Evelien Beuling. She has always been enthusiastic about my work and she delivered me strong motivation.

A big thanks to Dr. Daniel Baker for his help during these years. His support helped me to understand and learn many new things. Besides the physics and Matlab *etc.*, Dan is a good friend and he has been always there for me.

I would like to express my gratitude to Prof. Luca Cipelletti at Montpellier University for allowing me to use his amazing equipment. I learnt so much from him in such a limited time.

Thanks to Dr. Michael Ries, for his guidance on NMR experiments and data interpretation. They have been very precious.

Another special thanks to Dr. Arwen Tyler for inviting me to Diamond and ISIS in Didcot. It was amazing.

Thanks to all my beloved friends: Michael H., Elena S., Massimo C., Mattia V., Alessia M., Erica M., Adriano M. and Riccardo P. I cannot imagine my life without these guys. Thanks.

Thanks to Mum and Dad. Nothing would have been possible without you. Thanks for the 24/7 support and love. Thanks to nana and grandpa. There isnt a moment during the day I stop thinking of you.

Lastly, a special thank you to Gül. Thanks for all your support and love you give me every second of our days.

Abstract

Low methoxyl pectin (LMP) is a biopolymer widely used in the food and pharmaceutical industries for its gelling properties mediated via divalent ions. Gel formation of LMP strongly depends on both the chemical characteristics of the polymer and the environmental conditions of gel preparation. Unlike high methoxyl pectin, LMP does not require co-solutes to induce gelation, *i.e.*, sugars, allowing the possibility of reducing the calorie content of foods requiring a gel texture. In addition, there is increased interest in LMP as fat substitute in confectionery products. Although some work has been done on highly fractionated LMP with Ca^{2+}, virtually no detailed work seems to have been reported on commercial LMP + Ca^{2+} + high sugar concentrations, despite the fact that work on fractionated LMP suggests that the presence of sucrose, for example, can have a significant effect on LMP gelation. This thesis couples rheology and dynamic light scattering (DLS) to investigate the process of gelation of LMP samples in presence of a range of different sugars (at 60 *wt.* %) including fructose, D-psicose, sorbitol and invert sugar (1:1 M fructose and glucose). In addition, to compare with the results of previous studies [1] [2], LMP gelation in the presence of 40 *wt.* % sorbitol was also investigated. Selected systems were also studied via complementary static scattering techniques including a novel rheospeckle set-up that allows simultaneous rheology and DLS analysis. Rheological characterization of both the sol and gel states of LMP prepared in water (*i.e.*, without added sugars) show agreement with studies performed in the past. However, small angle light scattering revealed the presence of abnormally large structures (compared to conventional pectin molecule dimensions) that may coexist with smaller ones detected via static light scattering. These large pectin molecular structures may explain some unexpected results obtained for LMP gels prepared in high concentrations of sugars. Thus, although some sugars tend to speed up gelation, at certain calcium concentrations the mixture of larger and smaller structures appears to get trapped in a non-equilibrium gel state, that can only be resolved be re-heating (gel melting) and re-cooling. In other words, the normal thermoreversibility of LMP gels is disrupted. After the thermal cycling such gels

increase in strength. However, other sugars seem to disrupt gelation completely so that this effect is not seen. The effects of the different sugars are probably related to different specific sugar-sugar interactions that depend on their exact stereochemistry.

Abbreviations

LMP	Low methoxyl pectin
$[Ca^{2+}]$	Calcium concentration
$SHMP$	Sodium hexametaphosphate
T	Temperature
t	time
$\bar{\tau}$	Shear stress
$\dot{\gamma}$	Shear rate
η	Viscosity
C^*	Overlap concentration
M_w	Molecular weight
G	Shear modulus
G'	Storage modulus
G''	Loss modulus
γ	Strain rate
LVE	Linear viscoelastic range
ω	Angular frequency
λ	Wavelength
q	Scattering vector
$I(q)$	Scattered intensity
n	Refractive index
$\Re_{ex}$	Excess Rayleigh ratio
R_g	Radius of gyration
g_{2-1}	Time intensity autocorrelation function
${g_1}^2$	σ-renormalized time intensity autocorrelation function
$\tilde{t}$	Lag-time
MSD	Mean square displacement
KWW	Kohlrausch-Williams-Watts function
$< \tau >$	Averaged time scale of relaxation
Γ	Decay rate
β	Stretch exponent in Kohlrausch-Williams-Watts function
D	Diffusion coefficient
Λ	q-dependent power-law exponent
R_h	Hydrodynamic radius
Y	Scattered intensity ratio
df	Fractal dimension
OZ	Ornstein-Zernike function
ξ	Correlation length
Ξ	Static correlation length

List of Publications

Chapters 3 and 4:
Gulotta A., Mattsson J., Cipelletti L., Murray B.S. Dynamics of gel formation in aqueous solutions of low methoxyl pectin and the effects of added fructose. *Ready for submission.*

Chapter 5:
Gulotta A., Mattsson J., Cipelletti L., Murray B.S. (2018/2019). Static properties of low methoxyl pectin in sol and gel state. A multiscale approach. *In preparation.*

Chapter 6:
Gulotta A., Mattsson J., Murray B.S. (2018). A rheological and DSL study of low methoxyl pectin gel formation in presence of co-solutes. *In preparation.*

Contents

List of Figures

Chapter 1

Introduction to Pectins and Techniques Used

1.1 Pectin - an overview

1.1.1 Chemical Properties

Pectins are a heterogeneous mixture of structural polysaccharides, located in the primary cell walls of the middle lamella of most land plants [1] [2].Pectins are usually extracted from fruits by acid treatment (*e.g.* hydrochloric acid, nitric) at high temperatures. Parameters for this initial process can be tuned to avoid degradation reactions that could damage the final product. Once filtered, pectin is collected via alcohol precipitation (*e.g.* isopropanol or ethanol). The precipitate is then washed with alcohol, dried and milled to obtain a pectin powder [2]. The washing process with alcohol is a key factor to obtain two well-defined classes of pectins, called high-methoxyl (*HMP*) and low-methoxyl (*LMP*) pectins . In order to properly define these two classes, it is necessary to identify their chemical features first.

Despite their heterogeneity, the main constituent of pectins (*i.e.*, $\approx 60\%$ of the pectin by weight) is D-galacturonic acid (*GalA*), linked together via glycosidic bonds to form a polymer. The chemical structure of pectin is shown in Fig.1.1 and it can be divided into three blocks. The first one, homogalacturonan (*HG*),

is a linear and stiff polymer of ≈ 100 *GalA*, connected via by α-(1,4) glycosidic linkages. At this level, some of the C-6 carboxyl groups can be methyl-esterified.

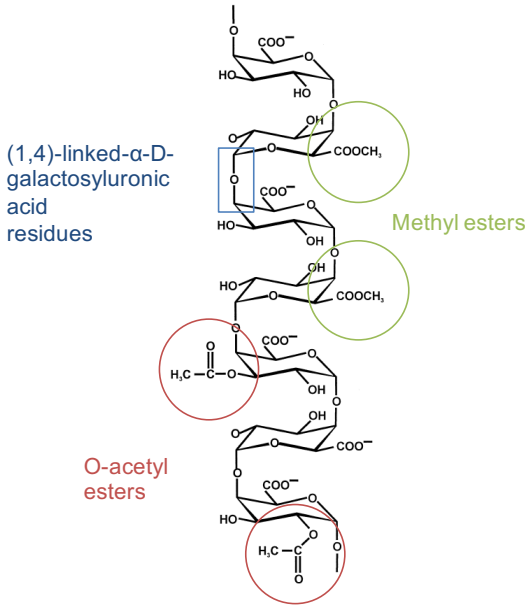

Figure 1.1: Chemical structure of pectin, adapted from [3]

The second block is called rhamnogalacturonan I (*RG I*), a branched heteropolymer that contains a backbone of repeating [→4)-α-D-galactosyluronic acid-(1→2)-α-L-rhamnogalacturonan acid-(1→]. This polysaccharide shows an O-acetylation at C-2 and/or C-3 on the GalA residues and a substitution at C-4 of the *RG I* residues with neutral and acidic oligosaccharides side chains. The exact nature of the side chains depends on the type of plant and its environmental conditions but are mainly linear and branched residues of α-L-arabinofuranosyl and/or β-D-galactopyranosyl. Moreover, other components such as glycosyl residues, ferulic and coumaric acids may be present [3].

Finally, the third block is called rhamnogalacturonan II (*RG II*). Here, the backbone is the homogalacturonan (≈ nine *GalA* residues) which may be methyl-esterified at C-6. On the backbone, four hetero-oligomeric substitutions are present. Thanks to their side chains, they can carry sugar residues such as apiose, fucose, aceric acid, xylose [4][5].

Even if both intra- and inter-molecular interactions and positions of these regions are still under scientific debate, pectin structure is often described as having two different regions: (i) smooth – rich in *HG* and (ii) hairy – rich in *RG II* and I [6]. The structural complexity of pectin is mainly due to the hairy regions, which may influence characteristics, such as molecular weight, aggregation in solution. Normally, the extraction process also affects this part of the molecule, *e.g.* via chemical and/or enzymatic modification [7] [4] [2].

As mentioned above, the *HG* chains are partially esterified with methyl groups. The degree of esterification (*DE*), defined as the molar ratio of methyl-esterified *GalA* to the total *GalA* present in pectin, determines two classes of pectins known as high methoxyl pectin (*HMP*) and low methoxyl pectin (*LMP*). In particular, *DE* for *HMP* is $\geq 50\%$, whereas *LMP* has a $DE < 50\%$. Recalling the extraction process, the product obtained after washing with alcohol is *HMP*. Prolonged alcohol washes allow a de-esterification process to obtain *LMP*. Alternatively, *LMP* can be produced by controlled acid or alkali de-esterification. The process can be finely-tuned to alter either the overall *DM* and/or the distibution of free carboxyl groups on the *HG* chain. Lastly, pectin de-esterification reactions via ammonia, give amidated carboxylic groups. These intrinsic characteristics will be recalled later on, since they are important regarding *LMP* gelation [2].

The gel formation for these two classes of pectins is completely different. *HMP* gels spontaneously form on cooling down hot mixtures of *HMP* in the presence of high concentration of low molecular co-solutes (*e.g.*, sucrose) at low pH (< 3). Hydrogen bonding and hydrophobic interactions are the main driving forces for gel formation. *HMP* gelation has been extensively studied elsewhere (*e.g.*, see [1][8][9]) but will not discussed in detail in this work. On the other hand, *LMP* requires the presence of divalent ions, such as Ca^{2+} to form a gel.

1.1.2 Low methoxyl pectin: sol and gel characterization

In this section, key aspects of *LMP* are discussed. General definitions of a gel and, more specifically, gel formation of *LMP* is followed by a description of key variables that influence the phenomena. Extensive reviews of the topic can be found in references Taylor *et al.* [1], Da Silva *et al.* [2] and Fraeye *et al.* [10].

Definition of a gel state

A gel is a network of material at relatively low weight fraction within a high weight fraction of solvent (liquid) that exhibits mechanical properties of a solid material, *i.e.*, a material that does not flow. Both components, together with the dispersing medium, extend to fill the whole system [11] [12]. In a polymer context, gels can be divided into two classes, depending on the nature of the cross-links (*i.e.*, links between polymer chains): chemical and physical gels [13].

Chemical gels are characterized by strong chemical bonds between the network elements, which are not reversible. The formation of these materials are due to chemical processes such as condensation, vulcanization, and polymerization [13]. These aspects will not be discussed further in this work, since the research is concerned with physical gels.

Physical gels can be classified as: (i) strong – permanent bonds at set experimental conditions, such as glassy and/or microcrystalline nodes; (ii) weak – temporary association between polymer chains, *e.g.*, hydrogen bonding, electrostatic interactions [13]. The solid-like behaviour is dependent on the observational time scale.

The time scale of observation during the measurements of the gel properties depends on the analytical technique used to characterize them. Analytical techniques to characterize gels are discussed later in this work.

Furthermore, the gel formation is not an instantaneous process and it is time-dependent, *i.e.*, gel curing (or ageing), occurs. Considering a number of polymer molecules dispersed in an aqueous medium, the addition of a cross-linking agent generates several events that are interconnected. A generalized cartoon of gelation is shown in Fig.1.2.

The first stage of gelation is shown in Fig. 1.2(a). (i) Here, polymer molecules (green lines) dispersed in an aqueous media, *i.e.*, the sol state, have a conformation and organization that depends on a number of characteristics, such their intrinsic chemical characteristics (linear or branched structures), the concentration, entanglements, solvent conditions (repulsion or attraction between chains).

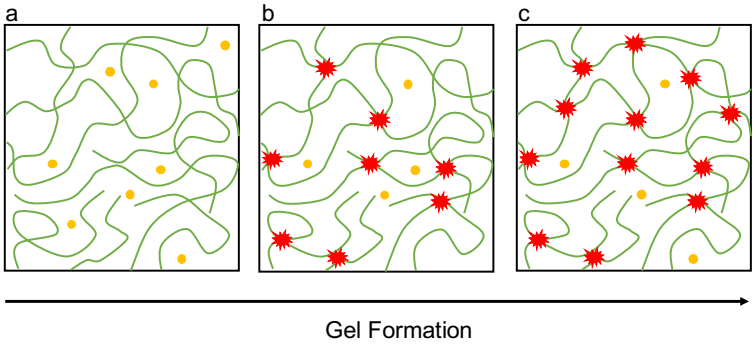

Figure 1.2: Illustration of the gelation. (a) Polymer chains (green lines) dispersed in an aqueous medium; yellow dots represent the cross-linker agents. (b) Progressive cross-linking between polymer chains and formation of a pre-gel state. (c) Formation of a macroscopic network (gel).

In Fig.1.2(b), the cross-linker agent (yellow dots) stabilizes chain-chain junctions (red symbols in the figure). As the gelation process continues, the number of the junctions increases. During this event, the material passes from a sol to a gel state, *i.e.*, self-supporting structure. There are many theories behind gelation including the percolation theory [13].

(ii) In the gel state (Fig.1.2(c)), the material continues to age (gel-curing). In this situation, the the cross-linking agent diffuses through the mesh of the gel, which is mostly occupied by water, to form additional cross-links. The gel, even if the polymer chains have a largely disordered structure and a high volume fraction of liquid solvent, behaves like a solid in terms of its mechanical properties [13][14]. These changes are usually determined via rheological characterization.

Gel formation in low-methoxyl pectins

As mentioned earlier, LMP leads to gel structures on adding divalent ions, such as calcium (Ca^{2+}), zinc (Zn^{2+}), iron (Fe^{2+}) [15] [16]. The divalent ions act as a cross-

linking agent between dissociated carboxyl groups of the *LMP* chain (Fig.1.3(a)). The so-called junction zones occur when at least 6-14 consecutive dissociated carboxyl groups between different *LMP* chains are linked via such ions (Fig.1.3(a)) [17] [18].

The model associated with this type of junction zone is the so-called egg-box model, originally developed for alginate gels [19]. Similarly to alginates, two-fold symmetrical antiparallel galacturonans helices are packed with Ca^{2+} ions between them [1] [10] [18]. Subtle differences in pectins, including Ca^{2+} coordination induced by oxygen atoms, stereospecificity and related molecular Ca^{2+}-pectin chain association, have been extensively studied [1][18][20] [21] in the past. Widely accepted at the present time, Braccini and Pérez [18] propose an adapted the egg-box model for pectins. Besides electrostatic interactions, egg-boxes are also stabilized by van der Waals and hydrogen bonds [18]. The life-time of the junction zone also depends on the strength of the electrostatic interactions [1], which in turn depends on the presence of other screening ions in the system.

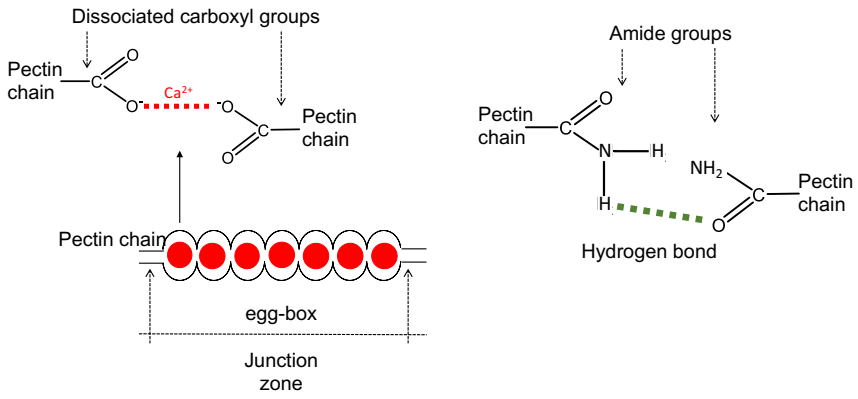

Figure 1.3: (a) Upper figure shows the interaction between Ca^{2+} and dissociated carboxyl groups of two different *LMP* chains. Bottom figure shows the egg-box model proposed by [18]. (b) Hydrogen bonding between amide groups of two different *LMP* chains.

As reported by different authors [22] [23] [24] [25], Ca^{2+} ions may also interact with single dissociated carboxyl groups, forming mono-complexes that are not formally participating in the junction zone stabilization. In this condition, the excess +1 charge promotes the reduction of the electrostatic repulsion between

LMP chains, enhancing their close proximity and, promoting cross-link formation with neighbouring chains.

Due to the acid nature of the carboxyl groups, the Ca^{2+} ion affinity varies with pH due to the varying charge on the pectin molecule. The optimal affinity condition usually occurs in pH ranges between 5 and 7.5. By decreasing the pH, the charge on *LMP* decreases, the ionic strength increases and the *LMP*-cation affinity decreases [2]. However, this effect may be compensated by the presence of amide groups. Here, hydrogen bonds between amide groups (non-charged) of different polymer chains, contribute to the gel structure (Fig.1.3(b)).

Several studies performed in amidated *LMP* highlighted the synergy between the two types of interactions, that lead to relatively strong gels, compared to the junction zones based solely on just on type of cross-linking mechanism. [17] [26] [27]. Moreover, amidated *LMP* gels show more thermal reversibility and appear more optically-transparent [2].

Additional interactions during gel formation in *LMP* are (i) H- bonds between undissociated carboxyl groups and (ii) hydrophobic interactions between methoxylated regions [17] (in fact, these two mechanisms are the main interactions responsible for *HMP* gel formation).

Even though *LMP* gelation is mainly induced by divalent cation interactions and H- bonding between amide groups (when present), a number of other different factors also affect the final gel state, both intrinsic and extrinsic, discussed in the following section.

Intrinsic factors

Intrinsic factors are related to chemical and spatial configuration characteristics of the biopolymer. Firstly, the chemical process used for the modification of *DM* decrease in pectins to obtain *LMP* is rather invasive, causing partial depolymerisation of the pectin. The level of depolymerisation affects the pectin chain length and the molecular weight (M_w), giving both wanted and unwanted characteristics during *LMP* gel formation. Broadly speaking, there are three situations: (i) lower M_w might increase the pectin gel strength; (ii) gel strength of *LMP* with a limited depolymerisation can be compensated by adding an excess of divalent

ions; (iii) accentuated depolymerisation makes gel formation not possible. Therefore, *DM* reduction for *LMP* production represents a crucial factor determining the properties of the final product.

To control the depolymerisation, recent studies on enzymatic demethylation highlighted the possibility of a better control of this procedure [7] [10]. The advantage of the enzymatic process increases on the selectivity of demethylation, controlling the overall distribution of non-methoxylated *GalA* along the chain [28] [29]. As reported in literature, a blockwise distribution of non-methoxylated *GalA* enhances the calcium binding during gel formation, compared to pectins with a random distribution of carboxyl groups.

As reported in section 1.1, *LMP* also carries side chains (*RG I* and *II* regions) that carry neutral sugars. The number and density of the side chains have both advantages and disadvantages in terms of gelation. A limited density may induce syneresis (*i.e.*, solvent separation from the gel structure). On the other hand, an excessive number of side chains may cause steric hindrance that disrupt the *LMP*-ion interactions and junction zone stabilization [10] [2].

Amidated carboxylic groups ($\approx$ 15-18%) added during pectin de-esterification via ammonia, enhance the gel formation of *LMP* for the reasons explained above. In this situation, the amount of divalent ions to form a gel can be lowered.

Lastly, the presence of acetyl groups in some pectins may interfere with the *LMP*-ion interactions and frustrate gelation. However, a high degree of acetylation is known only in certain pectin sources, *e.g.* sugar-beet [10] [2].

Extrinsic factors

The amount of divalent ions used to stabilize *LMP* junction zones is usually described with a stoichiometric ratio $R = 2[Ca^{2+}]/[COO^{-}]$, which relates the divalent ion concentration to the concentration of non-methoxylated *GalA* of *LMP*. Fig.1.4 shows a three-domain phase diagram, *i.e.*, R vs. *LMP* concentration ($[LMP]$), often used to describe this phenomena. The first curve, called the gelation threshold, divides the plane in two parts: (i) *sol* state below the gelation threshold and (ii) *gel* state above the gelation threshold.

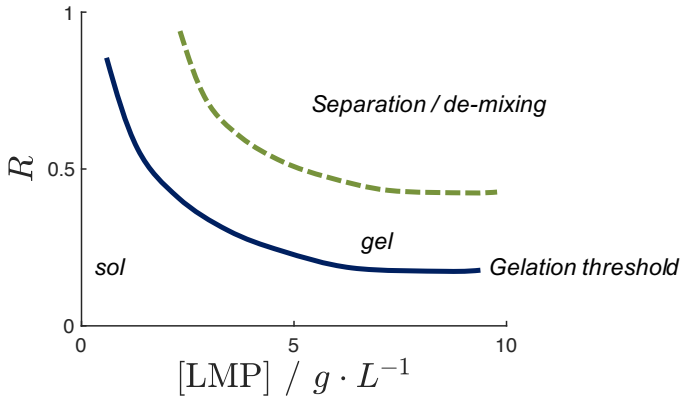

Figure 1.4: R vs. $[LMP]$ phase diagram to identify gel formation and separation.

Assuming R values between 0 and 1 and $[LMP]$ between 0 and 10 g L^{-1}, cross-link stabilization is achieved by keeping R constant and increasing the pectin concentration or vice versa. It is assumed that up to $R = 0.5$, all the calcium ions are used to stabilize the junction zones. Above this value, calcium ions can contribute to the stiffness of the gel due to non-specific electrostatic screening [10][1].

The third domain, observed in the upper part of the plane, denotes the limit where phase separation/syneresis may occur. High values of R ($\approx$1) at low $[LMP]$, may result in LMP precipitation effects. On the other hand, high $[LMP]$ leads to syneresis [10], *i.e.*, phase separation. In the presence of amide groups in LMP, the third domain is shifted towards higher R values, for the reasons described earlier.

Repulsion between pectin chains may be controlled by the presence of additional ions. As reported in literature [2] [30] [31], LMP in $[NaCl] = 0.1$ M at neutral pH, where the carboxyl groups are fully charged, behaves rheologically as a random coil polymer. Thus, 0.1 M $NaCl$ is considered as a good solvent for pectins. In poorer solvents (lower salt concentrations), LMP aggregation may occur.

Reduced repulsion induced by the solvent conditions enhances the flexibility of the LMP chains and allows easier coordination of the Ca^{2+} in the junction

zones. Thus, LMP in good solvents require less Ca^{2+} to form gels [32] [33]. On the other hand, in poorer solvent conditions, LMP may give more rapid sol to gel transitions, but with lower overall gel strength, compared to samples in presence of $NaCl$ [2]. As noted earlier, however, this may be compensated by mono-complexes between single Ca^{2+} ions and LMP chains [25] (see section 1.1.2).

Depending on $[LMP]$ and $[Ca^{2+}]$, gel formation kinetics may proceed rapidly, increasing the probability of heterogeneous gelation throughout the sample. To avoid these effects, phosphates (*e.g.* sodium hexametaphosphate $SHMP$) are usually included in LMP solutions for their tendency to chelate calcium ions and therefore slow down the junction zone formation. [34][35][36].

Conventionally, LMP is dispersed in aqueous media at relatively high temperatures (T >70°C), to give a homogeneous solution. Once the cross-linking agent is added, the solution is cooled down. The T decrease lowers the thermal energy of molecules, enabling the junction zone stabilization [2]. Being a physical gel, subsequently temperature increasing normally allows reversal of the gel state into the sol state, *i.e.*, disassembling of junction zones . In principal, this procedure can be repeated, within T ranges that do not cause excessive depolymerization of the pectin. The last extrinsic variable to consider is the presence of co-solutes. This in fact is the main aim of this thesis, discussed in detail in the following section.

1.1.3 Presence of co-solutes as an extrinsic factor

As previously discussed, LMP does not require co-solutes to induce gelation. Commonly, most of the commercialized LMP-based products are prepared in the presence of a variety of ingredients, such as sugars, proteins, other polysaccharides. Being a complex system, both the dynamics of gel formation and the final properties of the gel are affected by interactions with these other components [2].

Gel formation of LMP in the presence of sugars is related to two main factors.

(a). The first one refers to the sugar's ability to bind water in the system. The effect promotes a reduction of the free water in the system, in turn reducing hy-

dration of the pectin chains and so facilitating junction zone formation mediated by the divalent ions. As reported in the literature, the ability of a sugar to bind water depends of the number of hydroxyl groups (-OH) and its stereochemistry. A classic example is the comparison between D-glucose and D-fructose. These sugars have identical number of carbons, oxygens and hydrogens (*i.e.*, $C_6H_{12}O_6$) but they behave differently in aqueous solution. The reason is the position of the -OH groups, as axial or equatorial (Fig.1.5). In solution, glucose can form two conformations, known as α-D-glucopyranose ($\approx$ 36%) and β-D-glucopyranose ($\approx$ 64%) (Fig.1.5(a)). On the other hand, fructose in solution assumes three conformations: β-D-fructopyranose ($\approx$ 67%), β-D-fructofuranose ($\approx$ 27%), and α-D-fructofuranose ($\approx$ 6%) [37]. Fig.1.5(b) shows the most predominant form of fructose in solution, *i.e.*, β-D-fructopyranose

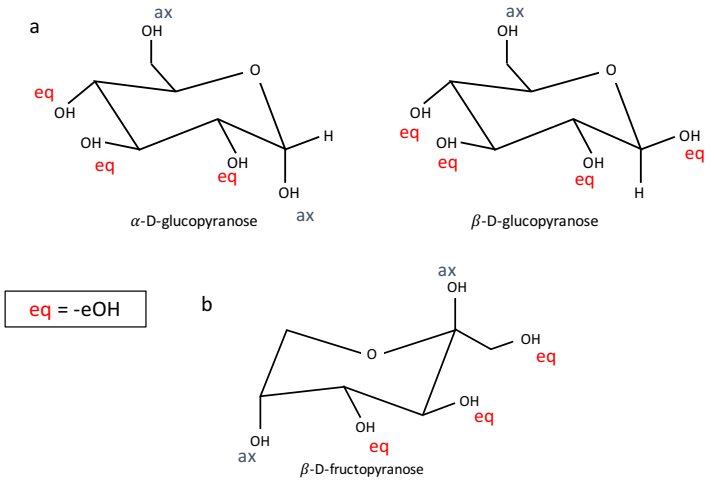

Figure 1.5: (a) Glucose structures in aqueous solution: α-D-glucopyranose ($\approx$ 36%) and β-D-glucopyranose ($\approx$ 64%). (b) Major form of fructose in solution: β-D-fructopyranose.

According to [38], the distance between the equatorial hydroxyl group (-eOH) and the carbon in the sugar ring is $\approx$ 4.86 Å. This distance matches the space between molecules in a water lattice, *i.e.*, 4.9 Å. Hence, it is assumed that sugars with a high number of -eOH fit well into the water structure, partially explaining their very high solubility in water.

As shown in Fig.1.5, β-D-fructopyranose has fewer -eOH, reducing its ability to bind water. The sugar-water structure effect vanishes when linear chain carbohydrates are used, *e.g.*, sorbitol, glycerol.

These considerations are valid up to $\approx$ 35-40 *wt.* % of sugar in solution [39]. Above these concentrations, sugar-sugar and water-water interactions may dominate, commonly called clustering effects [40] [41] [42] [43] [44]. In these conditions, the sugar solutions changes their physicochemical characteristics. This aspect is still under debate and still being actively investigated by many researchers.

LMP gel development and curing in presence of sugars, such as glucose, fructose, sucrose (up to $\approx$ 40 *wt.* %) has been investigated by some authors via rheological experiments [17][45][46][47]. Generally, both formation kinetics and final strength of the gels follow the order: sucrose (strongest) > glucose > fructose > plain (no sugars added). This effect is consistent with the fact in the reduction of free water in the system. On the other hand, nobody appears to have investigated the interactions between *LMP* and sugars. Such work requires more sophisticated techniques, combined with molecular simulations.

At high concentrations of sugars, the clustering effects may change the behaviour of the pectin molecules. In a clustered environment, it is unclear where pectin sits; one can suppose additional clusters, occupied by the pectin. Due to the pectin hydration characteristics, *i.e.* 0.25-0.35 g H_2O for each 1 g of pectin [48], the polymer is expected to be surrounded by a layer of water.

For the high concentration of sugars in solution, $\geq$ 60 *wt.* % , these materials are considered as a good glass-formers. A glass is in an amorphous solid-like material, whose molecules show very long time scales of relaxation, > 100 s. These materials are widely studied via broadband dielectric spectroscopy (BDS) [49]. In the last decade, *BDS* was used to understand the dynamics of hydration of proteins dispersed in high concentrations of co-solutes. As reported by several authors[41][49] [50][51] distinct relaxation time-scales between sugar and protein, suggests distinct hydration effects, confirming, somehow, a net separation of the components. This technique may help the understanding of both sugar and *LMP* hydration.

Another technique used to study water-sugar interactions is ^{1}H NMR, via diffusivity and relaxometry tests. ^{1}NMR has been extensively used to understand

concentrated sugar systems [52] [43] [39], but LMP is not directly detectable at the concentration normally used for gelation. The high M_w of LMP makes its signal poorly distinguished of the noise-baseline. On the other hand, relaxometry experiments, in particular spin-spin (T_2) relaxations, can be used to probe the water mobility in such complex systems. Knowing the T_2 of bulk water (2 s at 25°C), the relaxation time decrease is believed to be due to water binding. However, T_2 is highly dependent on proton exchange dynamics [53].

(b). The second effect is related to the ability of certain sugars to form complexes with divalent ions, making them less available for junction zone stabilization. According to references [46][47][26], rheological characterization of LMP gels showed decreased mechanical strength, with slower dynamics of formation. This behaviour was attributed to the sugar-ion complex formation.

The mechanism of complex formation between divalent ions and sugars has also been investigated via NMR [54] [55] and chromatography techniques [56]. In particular, it has been found that ring-sugars with the particular conformation axial-equatorial-axial are more likely to form complexes with di- and trivalent ions [54]. On the contrary, with open-chain sugars (*e.g.*, sorbitol, xylitol), the ion complexation occurs cis-cis-triol configuration [57].

The effect of the polysaccharide-ion complex formation is reduced when amidated LMP is used. In this case, lowering the pH of the solution promotes gel formation via H-bonding between amide groups. Thus gel formation is relatively unaffected by the type of sugar.

Background on experimental techniques

1.2 Rheology

Rheology is the science of deformation and flow. The word itself derives from the Greek words *"-rhèō"* and *"-logia"*, *i.e.* study of flow.The study of flow extends to deformation due to the ability of soft-solid materials to flow when exposed to stress.

Characterization of rheological properties are provided by a variety of techniques and one of the common ones is the rheometer. Initially, the measurement

system is assumed to be a double parallel plate where the upper one is connected to the driving system and the bottom one is stationary.

1.2.1 Viscous systems

Fluids are divided into two defined classes: (a) Newtonian, *e.g.* solutions of small molecules, such as sugars, and low concentrations of polymers; (b) non-Newtonian *e.g.* more concentrated solutions of high M_w polymers or suspended solids. In this section both behaviours are explained. Rotation velocity from the motor and characteristics of the measuring system (*i.e.* size, area of plates, cones) allow the extrapolation of rheological parameters.
Fig.1.6(a) shows the easiest set-up, a parallel-plate geometry (explained later). As sketched in the figure, the tested sample resides between two plates with area A, with spacing h and perfect assumed adhesion between the sample and the plate. Typically, one of the plates (bottom) is stationary and the upper moves tangentially at velocity v on application force F to create shear and flow.

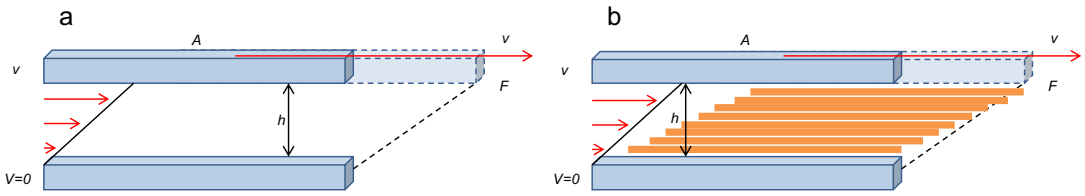

Figure 1.6: (a) Parallel-plate configuration with a tangential movement of the upper plate; (b) sheared fluid represented as a sliding of n-stacked layers.

Before moving to the definition of rheological parameters, it is important to understand what happens to a fluid when a shear is applied. Formally, the application of stress determines the liquid elements flow over or past each other [58] creating a friction that depends on the fluid characteristics. A sheared fluid can be imagined as a number of sliding stacked layers where, the velocity of a single layer increases linearly with respect to the previous one (Fig.1.6(b)). The velocity gradient in the direction of the flow is called shear rate $\dot{\gamma}$ and the force

per unit area is the shear stress $\bar{\tau}$ (or σ) [58]. Therefore:

$$\bar{\tau} = \frac{F}{A} \qquad [Pa] \tag{1.1}$$

$$\dot{\gamma} = \frac{v}{h} \qquad [s^{-1}] \tag{1.2}$$

Additionally, one has to define an intrinsic parameter describing the fluid characteristics, called viscosity (η). The viscosity derives from the aforementioned friction between fluid elements that occurs during shearing, *i.e.* the resistance of the fluid that opposes the shear applied. Viscosity is defined as:

$$\eta = \frac{\bar{\tau}}{\dot{\gamma}} \qquad [Pa \cdot s] \tag{1.3}$$

In Newtonian fluids, viscosity is independent on both degree and time of shear applied (Fig.1.7(a)), *i.e.*, direct proportionality between $\dot{\gamma}$ and $\bar{\tau}$ by starting from the origin (Eq.1.4) [45]. η is the proportionality constant and it is independent of $\dot{\gamma}$.

$$\bar{\tau} = \eta \cdot \dot{\gamma} \qquad [Pa] \tag{1.4}$$

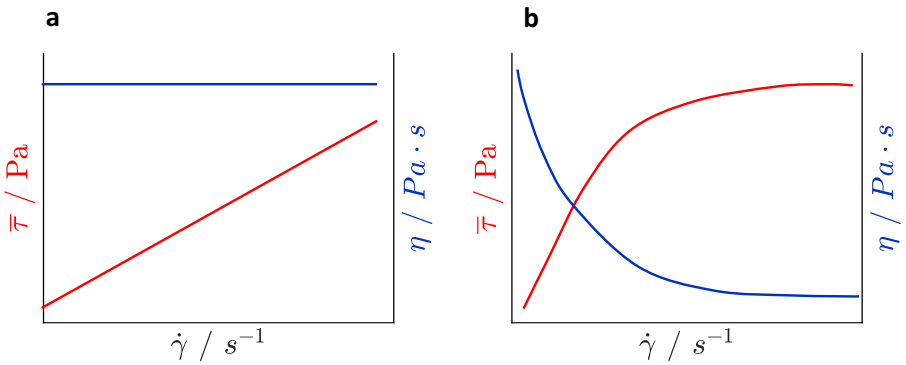

Figure 1.7: (a) Viscosity and flow response vs. shear rate for a Newtonian fluid and for a (b) non-Newtonian fluid (in this case, shear-thinning behaviour).

Deviations from ideal Newtonian behaviour occur when the fluid increases in complexity; as mentioned earlier, this is the case of non-Newtonian fluids.

Here, $\dot{\gamma}$ and $\bar{\tau}$ are not linearly dependent and the plot does not start from the origin. This is a result of structural changes of the fluid. Mainly, there are two situations: shear thinning (pseudo-plastic) and shear thickening. In shear thinning behaviour, $\bar{\tau}$ vs. $\dot{\gamma}$ plot starts from the origin and gradually increases at higher $\dot{\gamma}$ (Fig.1.7(b)). Contrarily, viscosity shows a gradual decay as a function of $\dot{\gamma}$.

Shear thinning behaviour is typical of complex fluids such as polymer solutions, glues, shampoos. In the context of polymers, shear thinning behaviour provides useful information on the conformation of the chains, aggregation, overlapping. A typical η vs. $\dot{\gamma}$ plot for a polymer is sketched in Fig.1.8(a). As shown, viscosity assumes three regimes: (i) at low $\dot{\gamma}$, η shows a plateau, indicating the rest condition where polymer chains adopt their equilibrium three dimensional conformation (Fig.1.8(b)). In this situation, η is termed the zero-shear viscosity η_0. (ii) At intermediate $\dot{\gamma}$, the shear rate causes the re-orientation of the chains and their partial aligment (Fig.1.8(c)); as a consequence of this, η decreases as a function of the $\dot{\gamma}$. (iii) In the final region, the very high $\dot{\gamma}$ cause a strong aligment of the polymer chains and interactions between them disappear (Fig.1.8(d)) and the viscosity becomes constant (η_∞) arising solely due to the friction of aligned chains gliding off each other [58].

Shear thinning behaviour in these solutions depends on polymer concentration $[C]$. Generally, low concentrations (dilute regime) show Newtonian behaviour due to lack of short range interactions between chains, *i.e.* $\eta \propto [C]$. As $[C]$ increases, η_0 (defined as $\eta_0 = \lim_{\dot{\gamma}\to 0} \eta(\dot{\gamma})$) increases and the shear thinning behaviour starts to be observed. The double logarithm plot η_0 vs. $[C]$ shown Fig.1.9 identifies the chain-chain interactions behaviour as a function of their concentration. The critical polymer concentration C^* denotes the border between the dilute and semi-dilute regime, *i.e.*, where short range interactions between polymer chains occur. At intermediate $[C]$, the chain-chain interactions become stronger up to the critical overlap concentration (C^{**}). Here, the steeper change in η_0, corresponds to chain entanglements.

Staudinger in the 1920s, formalized the procedure to determine the intrinsic viscosity $[\eta]$ and M_w via viscosity measurements of dilute polymer solutions (di-

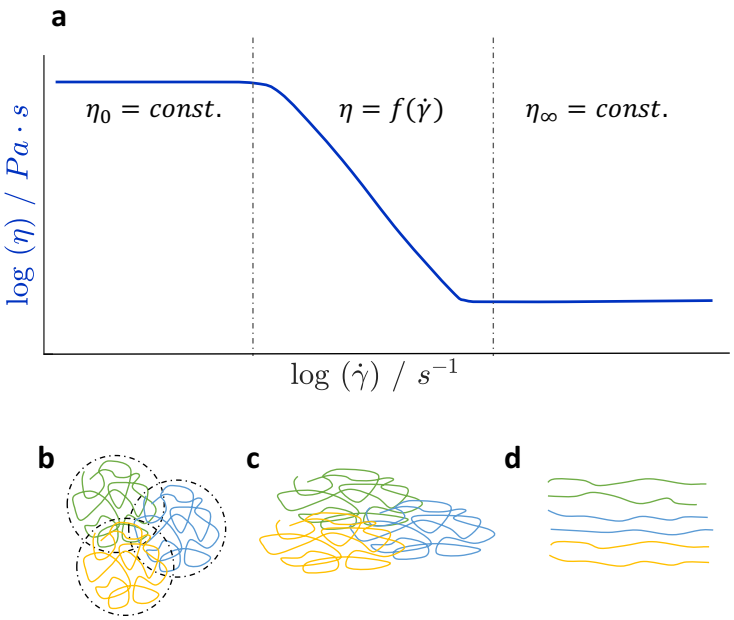

Figure 1.8: (a) Double-logarithm plot of viscosity η vs. shear rate $\dot{\gamma}$, divided in three regimes. (b), (c) and (d) show typical polymer behaviours at correspondent shear-regimes.

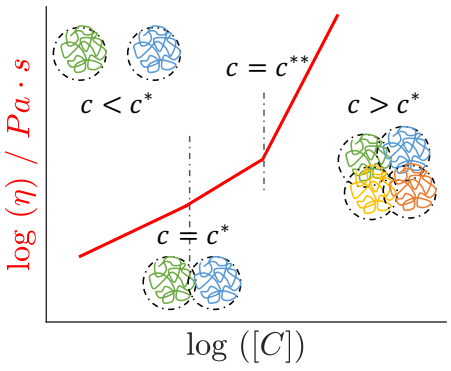

Figure 1.9: Double-logarithm of η_0 vs. polymer concentration $[C]$ and relative polymer coils conformation, at $C \lessgtr C^*$

luted regime). The original procedure established $[\eta]$ from (i) inherent viscosity η_{inh} and (ii) reduced viscosity η_{red} in the limit of $C = 0$.

$$\eta_{inh} = \ln\left(\frac{\eta_0}{\eta_s} \cdot \frac{1}{C}\right) \tag{1.5}$$

where the η_0 refers to the polymer solution and η_s is the viscosity of the solvent. The ratio in the first term of the equation is known as relative viscosity.

$$\eta_{red} = \left(\frac{(\eta_0 - \eta_s)}{\eta_s} \cdot \frac{1}{C}\right) \tag{1.6}$$

The first term of Eq.1.6 represents the specific viscosity η_{sp}, a parameter widely used in polymer rheology. Here, the plot of both η_{inh} and η_{red} vs. polymer concentration allow the extrapolations of $[\eta]$ as:

$$[\eta] = \lim_{c \to 0} \eta_{red} \quad [cm^3 g^{-1}] \tag{1.7}$$

Graphically, $[\eta]$ represents the intercept of the linear fit of the above vs. C. The molecular weight determination from the intrinsic viscosity corresponds to a relation commonly known as Mark-Houwink:

$$[\eta] = K \cdot {M_w}^a \tag{1.8}$$

where the prefactor K and the exponent a depend on the polymer-solvent interactions and their values for numerous systems are tabulated in literature. However, variability of parameters such as chemical structure, molar mass distribution, solvent conditions, strength of various physical-chemical interactions may compromise the final M_w result. The calculation of the parameters K and a can be obtained via supplementary techniques [59].

Another behaviour that occurs in non-Newtonian fluids is shear thickening. For these materials η increases as function of $\dot{\gamma}$, *i.e.* the shear stress induces a structuring process. This is typical of fluids such as ceramic suspensions, starch dispersions, natural rubber. The effect is due to rearrangements of fluid components to form a more complex structure.

As discussed above, η values in non-Newtonian fluids are $\dot{\gamma}$-dependent. The η notation in these case takes the name of apparent viscosity η_{app}. Certain materials

do not exhibit flow at low $\dot{\gamma}$, they need to reach a certain shear stress to flow. This critical shear stress, called the yield point, representing the border between no-flow and flow occurs when the external forces overcome internal structure forces, such as intermolecular forces, physical-chemical bonds, hydrogen bonds. Below the yield point the material behaves as a solid elastic material and external stresses are immediately recovered when the shear stress is removed (explained in following section, *i.e.* elastic materials). This characteristic is present in products such as toothpastes, gels, emulsion paints.

Another example of a non-Newtonian fluid is one that shows time-dependent flow behaviour. One can track temporal η_{app} by presetting constant $\dot{\gamma}$ intervals. This allows the identification of structural changes over time such as hardening or softening. A basic scenario for η_{app} vs. time at constant $\dot{\gamma}$ is shown in Fig.1.9: (b) η_{app} decrease (*e.g.* paints, ketchup); (c) η_{app} decrease (*e.g.* gels). For comparative reasons, Newtonian fluid is included as well ((a) curve).

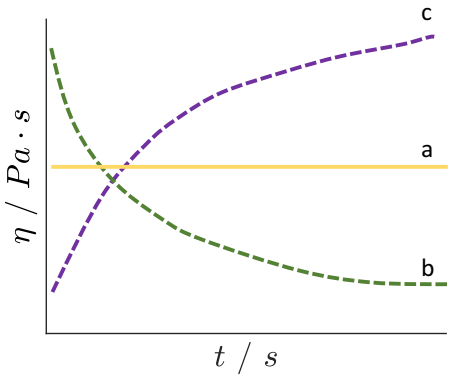

Figure 1.10: (a) no shear stress/viscosity change over time; (b) decreasing of shear stress/viscosity over time; (c) increasing of shear stress/viscosity over time.

1.2.2 Elastic systems

As described previously, one can model samples as residing between two plates (Fig.1.11) (surface area A) separated by a distance h where one of them is stationary. When a shear force F is applied, the sample undergoes homogeneous

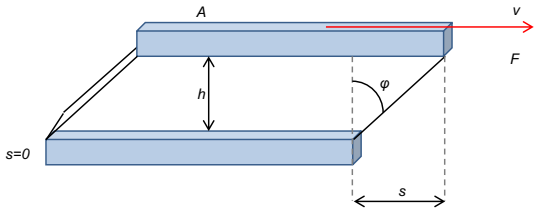

Figure 1.11: Two plate system used to describe a deformation for an elastic material.

deformation and the resultant deflection s gives the deflection angle φ. Shear deformation (or strain) is defined as:

$$\gamma = \frac{s}{h} = \tan\varphi \qquad [1] \tag{1.9}$$

Although strain is dimensionless, it is a common rule to express it as a percentage, *e.g.* γ= 0.1 or 10% means that in a 1 mm gap (h), the sample deflects by 0.1 mm (s). In a perfectly elastic material, shear stress/deformation is a material constant when the test is performed in the reversible-elastic, *i.e.* non-destructive range. This ratio is defined as the shear modulus (G) and is a measure of the rigidity of the tested material [59].

$$G = \frac{\bar{\tau}}{\gamma} \qquad [Pa] \tag{1.10}$$

where $\bar{\tau}$ is the shear stress applied. Ideal elastic behaviour can be compared to a spring and its elongation when a force is applied. The spring elongates (deflects) with a length proportional to the load applied. Once the force is removed, the spring returns to the initial state (zero deflection). This behaviour is directly comparable to elastic solids described by Hooke′s law, where $\bar{\tau}$ is directly proportional to γ with a constant of proportionality G. An ideal elastic solid (or Hookean solid) shows independence on shear load and time during deformation [59].

1.2.3 Viscoelastic systems

Viscoelastic systems represent the third class of materials, where their intrinsic characteristics lie somewhere between that of viscous and elastic systems. De-

pending on whether the viscous or elastic component is dominant, one finds either viscoelastic liquids or solids.
Maxwell formalized empirically the viscoelastic liquid (VEL) behaviour (Maxwell model) with the aid of a dashpot (viscous component) and a spring (elastic component) linked in series. When a force is applied to one of the extremities of the system two events occur: (i) the spring elongates immediately up to a constant deflection value, which is proportional to the force applied; (ii) when the spring is entirely elongated, the dashpot starts to move. The movement (distance of the piston) of the dashpot depends on both force and application time. Force removal results in an immediate spring recovery, but, on the other hand, the dashpot remains stationary. Therefore, this irreversible deformation depends on force and time applied.

As well as VEL, viscoelastic solids (VES) can be formalized with the dashpot and spring. The model was developed by Meyers, Kelvin and Voigt and it is generally called the Kelvin/Voigt model. For VES, the two components are firmly linked in parallel. When a force is applied to the system, the spring does not elongate immediately and is slowed down by the dashpot, hence, the two elements move together. The total system elongation depends on both force and time of stretching. Once the force is removed, the spring aims to recoil immediately but, again, it is slowed down by the dashpot. In recovery conditions, the spring represents the driving force of the dashpot to return to its initial position.

For viscoelastic materials, there are a variety of tests to assess their mechanical properties. In the simplest case, the aforementioned load and recovery time/behaviour of both VEL and VES can be assessed with stress relaxation tests.

In this case, a certain step strain is applied to the material and kept constant during the experiment. After the application of the the step strain, the deformation of the material tends to returns to its stress-free state due to internal relaxations that compensate the internal stresses [59]. This process delay is a characteristic relaxation time, which is the key factor of the experiment. Fig.1.12 shows γ vs. t representation of ideally elastic/viscous and VES/VEL. Conventionally, results are plotted as a double-logarithm of shear modulus G vs. time

(t). This facilitates the mathematical description of the curve as an exponential function $\bar{\tau}(t) = \gamma_0 \cdot G \cdot exp(-t/\dot{\lambda})$, where $\dot{\lambda} = \eta/G$ is the relaxation time in seconds. G and η represent the spiral spring (elastic) and the dashpot in the Maxwell model (viscous), respectively. Complex systems may be described as multiple exponential decays which, in turn, can be represented with the generalized Maxwell model, *i.e.* a number of serial spring-dashpot systems connected in parallel, indicating a number of relaxation processes within a material.

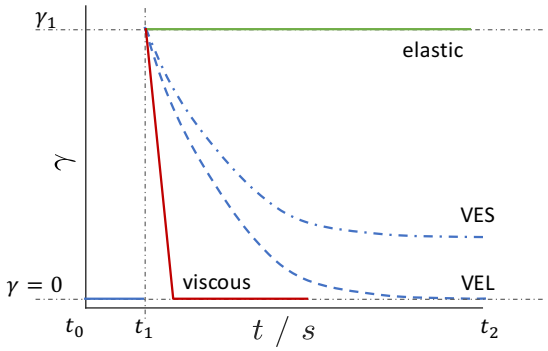

Figure 1.12: Stress relaxation test, γ vs. t. Red trace represents a viscous fluid; green-trace is characteristic of elastic materials; VES and VEL traces represent the response of viscoelastic solid and fluid, respectively.

Nowadays, the rheology of viscoelastic materials are most frequently rheologically characterized with oscillatory tests. Once again, the sample sits between two plates with defined gaps, area (Fig.1.13). Instead of unidirectional shear, the upper plate moves back and forth due to an applied shear force $\pm F$. The oscillation causes a characteristic deflection path $\pm s$ with a deflection angle $\pm\varphi$.

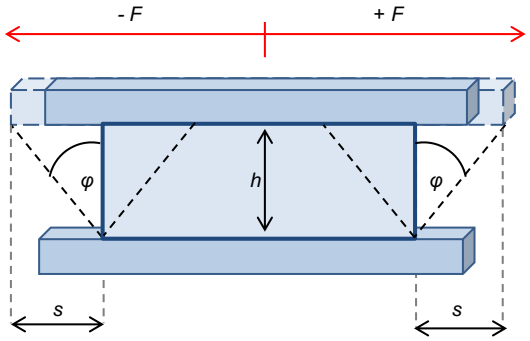

Figure 1.13: Two plates system used to describe behaviour for viscoelastic material oscillatory test.

Oscillatory movement is represented as sinusoidal wave with a characteristic frequency and an amplitude. Assuming the parallel-plate configuration (Fig.1.13) where the upper plate is connected to a driving wheel through a cardan joint, the rotation of the wheel causes the characteristic back and forth movement of the upper plate, applying an oscillatory stress to the material. The force F is measured at the bottom plate. Due to the time-dependency, the notation of rheological parameters changes to $\tau(t)$, $\gamma(t)$, $\dot{\gamma}(t)$.

As shown in Fig.1.14(a), the position of the wheel at either 0° and 180° corresponds to the stationary position of the plate, whereas the position at 90° and 270° to the maximal shift on the right and left, respectively. The imposition of $\gamma(t)$ and/or $\dot{\gamma}(t)$ occurs at the upper (preset) plate and measurement of $\tau(t)$ at the bottom one (response).

Oscillation curves in Fig.1.14, show the sinusoidal response in terms of $\tau(t)$ of both $\gamma(t)$ and $\dot{\gamma}(t)$ for an ideally elastic (b) and viscous material (c). As shown in Fig.1.14(b), $\tau(t)$ and $\gamma(t)$ are in phase with a characteristic shift angle $\delta = 0°$. However, $\delta = 90°$ for $\dot{\gamma}(t)$, *i.e.* when $\gamma(t)$ is at 0° or 180°, $\dot{\gamma}(t) =$ maximum, and vice-versa. This explains Hooke's law, for ideal elastic behaviour. For ideally

viscous behaviour (Fig.1.14(c)), the same concept applies. In this case, $\tau(t)$ and $\dot{\gamma}(t)$ are in phase and $\gamma(t)$ has a $\delta = 90°$.

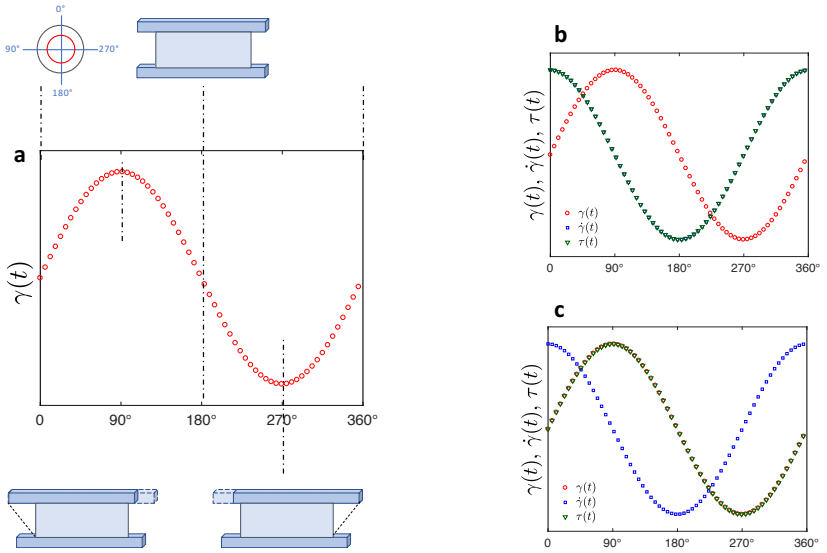

Figure 1.14: (a) Sine wave for oscillatory tests and position of the plate. Sinusoidal responses of $\tau(t)$, $\gamma(t)$ and $\dot{\gamma}(t)$ for ideally (b) elastic and (c) viscous material.

In a viscoelastic material, the phase shift δ shown in Fig.1.15 is between 0° and 90°, (*i.e.*, in between the ideal Hookean solid and ideal Newtonian fluid) and gives an estimation of the viscous versus elastic contributions.

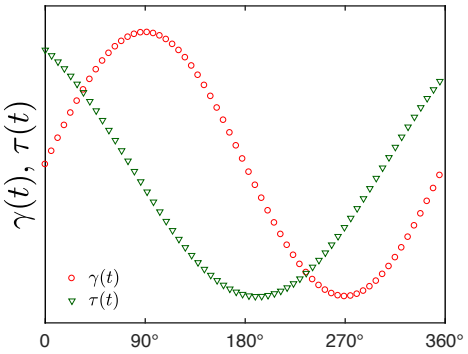

Figure 1.15: Phase shift between shear stress and shear strain that is occurring in viscoelastic materials.

In mathematical notation, when the shear stress is the pre-set:

$$\tau(t) = \tau_A \cdot \sin(\omega t + \varphi) \tag{1.11}$$

where τ_A is the amplitude of the wave, ω is the frequency and t is the time. As noted previously, the phase shift (or loss angle) is crucial to understand which behaviour is dominant. The parameters can also be expressed as complex numbers:

$$\tau^* = \tau_{(0)} \cdot e^{i(\omega t + \varphi)} \tag{1.12}$$

$$\gamma^* = \gamma_{(0)} \cdot e^{i\omega t} \tag{1.13}$$

Thus, the complex modulus G^* can be defined as:

$$G^* = \frac{\tau^*}{\gamma^*} = \frac{\tau_{(0)}}{\gamma_{(0)}} \cdot e^{i\varphi} = G' + iG'' \tag{1.14}$$

According to Euler′s formula, $e^{i\varphi} = cos(\varphi) + isin(\varphi)$ therefore G' and G'' can be defined as:

$$G' = \frac{\tau_{(0)} \cdot cos(\varphi)}{\gamma_0} \tag{1.15}$$

$$G'' = \frac{\tau_{(0)} \cdot sin(\varphi)}{\gamma_0} \tag{1.16}$$

The complex modulus G^* describes the viscoelastic properties of a material, with both elastic and viscous contributions. G' is the elastic modulus associated with deformation energy stored by the sample during shear. Once removed, all the stored energy is used to recover (partially or entirely) the initial structure. In other words, G' gives information on the elastic behaviour of the tested material. G'', the so called loss modulus, measures the deformation energy dissipated during shear due to friction forces and dissipated as heat. When the shear stress is removed, the structure of the material appears irreversibly changed – the loss modulus represents the viscous component of the tested material.

The parameters, *i.e.* $G^{'}$,$G^{''}$,η^* are usually extrapolated from different types of oscillatory tests, set by the measuring system, the rheometer. These oscillatory tests include strain, frequency, time and temperature dependence.

Amplitude Sweep

In this measurement, a known amplitude sinusoidal wave (stress or strain) is applied, whilst the frequency is kept constant. An amplitude sweep tests the linear viscoelastic range LVE, *i.e.* range where reversible changes occur. Fig.1.16 shows a typical response of a gel-like sample in $G^{'}$ and $G^{''}$ notation. As shown, in the low strain regime, $G^{'} > G^{''}$, indicates a dominant elastic contribution, rather a viscous one. LVE identifies the regions where the linear-elastic and linear-viscous behaviour, *i.e.*, Hooke's and Newton's laws, respectively, are valid. The linearity persists up to a maximum strain γ_L. The intrinsic characteristics of the material may show some peculiarities in terms of moduli and LVE response, due to: (i) non-homogeneous structures of the material, *i.e.* creep or flow-*like* response at low γ; (ii) frequency dependence, *e.g.*,a pre-set of high frequencies may lead to a higher $G^{'}$ response due to internal rigidity of internal structures in fast motion; (iii) in the high γ regime, $G^{''}$ may increase before decaying, forming a peak.

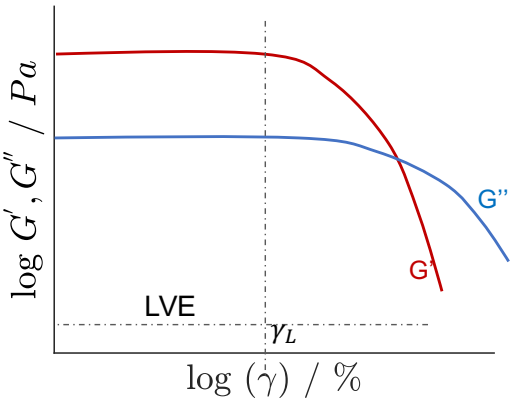

Figure 1.16: Response of $G^{'}$ and $G^{''}$ versus stress (strain) during an amplitude sweep test.

Frequency Sweep

This measurement assesses the frequency response of a material at constant γ. Since frequency f is measured in Hz $= s^{-1}$ (ω = rad s^{-1}), its value probes the time-dependence of the deformation of the tested material. A self-explanatory example is provided by the frequency dependence of a silicone polymer polydimethylsiloxane *PDMS*. If dropped on a hard surface, *PDMS* bounces as a rubber ball, whereas at rest conditions it starts to flow. In terms of moduli and frequency, the bouncing process occurs in very short time-scales, corresponding to high frequencies, with $G^{'} > G^{''}$. The opposite behaviour occurs at rest, with $G^{''} > G^{'}$ at long time-scales and low frequencies. Therefore, the observation time of the experiments is important. Fig.1.17 shows a generalized $G^{'}/G^{''}$ vs. frequency plot.

Moduli/frequency responses depend on the sample components. For example, in terms of polymers, the response may differ depending on the presence or absence of cross-linking (chemical) and the molar mass distribution. The literature provides a large variety of these examples and modelling methods to characterize the polymer [11][59]. Due to their cross-links (junction zones), the moduli response for gels is similar to cross-linked polymers. However, this similarity has to be taken with caution due to the nature of the cross-links. The three-

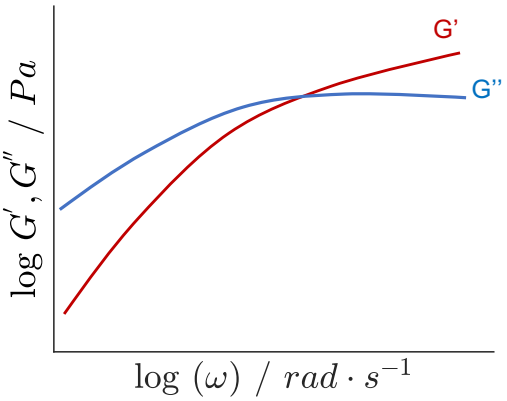

Figure 1.17: $G^{'}$ and $G^{''}$ signals versus frequency during a frequency sweep test.

dimensional structure of many gels is built up from numerous relatively weak physical cross-links (hydrogen bonding, electrostatic interactions). This gives experimental issues such as very low magnitude moduli, at rest and time-evolution due to breakage-reformation of cross-links. However, the frequency dependency of $G^{'}/G^{''}$ vs. for gels can be sub-categorized, into weak (frequency dependent) or strong (frequency independent) [45].

Time Sweep

Time dependent oscillatory analysis with both γ and frequency constant under isothermal conditions may be useful to characterize strengthening or softening of a material. For example, tracking of gel-curing, *i.e.*, an increase in strength due to cross-link development and/or tracking gel-point (where $G^{'}$ becomes higher than $G^{''}$). Another example, similar to the one explained above, is the study of thixotropic materials, *i.e.*, where contiguous γ and f steps are used to track loss and recovery of the structure [45][59].

1.2.4 Measurement devices

Rheometer

Commonly, rheometers can be divided into two categories: (i) controlled shear rate where the operator pre-sets velocity v and shear rate $\dot{\gamma}$ and tracks torque M ($M = N \cdot m$) hence shear stress τ; (ii) controlled shear stress where M and τ are pre-set and resulting v and $\dot{\gamma}$ are measured. Controlled shear stress rheometers are nowadays widely used and an important feature of any rheometer is the bearing that carries the surfaces that apply a stress (or strain) to the system. Compensation must be made for internal friction and internal effects that effect the apparent torque of the sample. Modern rheometers are equipped with Peltier elements which ensure high cooling/heating rates.

The elements carrying the surfaces in direct contact with the sample are the 'geometries'. The choice of a suitable geometry depends on the sample and its viscosity. Within the variety of geometries available, Fig.1.18 shows the most common ones.

(a) Concentric cylinders are ideal for low viscosity fluids, where the sample resides between the bob and the cup, in a double-gap set-up. Generally, a narrower gap ensures η measurements are achievable at high $\dot{\gamma}$.

(b) Cone-plate. This is ideal for viscous solutions but it has some limitations. Two factors characterize this geometry: the radius (or diameter) and the cone angle. In terms of size, the diameter ranges from few mm up to decades of mm. The cone angle varies between 1 and 4°. Due to the its cone shape, the strain across the gap is constant. However, for viscous materials with big particulates, this geometry is not suitable. On the other hand less sample is required and air bubbles can be squeezed out during setting the gap.

(c) Parallel-plate. Here two plates with the same radius but variable gap are used. This geometry is particularly useful for oscillatory measurements of soft-solid materials. If used in rotational mode, common side effects may occur, especially due to the gap h pre-set, *e.g.* turbulent flow, shear inhomogeneities. In all the cases, the gap should be appropriate to the tested material and it can be set automatically via normal force control, *i.e.*, a controlled force is imposed by the upper plate during the experiment, ensuring contact between the sample

and both plates. The advantages of this set-up are the possibility to test samples with larger particles; the gap can be set to reduce stresses on the sample and therefore, the time to reach an equilibrium condition can be short. In addition there is the possibility to use the automatic normal force adjustment to set the gap, particularly useful in situations of high shear rates or temperature changes (thermal expansion or contraction). Regarding disadvantages, the shear is non constant across the gap, *i.e.* minimum $\dot{\gamma}$ values at the centre and maximum $\dot{\gamma}$ at the edge. This effect is translated into edge failures, flow inhomogeneities; in temperature-dependence tests, larger gaps may also lead to temperature gradients [59].

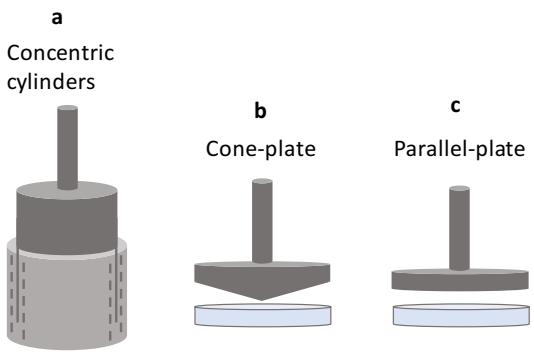

Figure 1.18: Rheometer geometries: (a) concentric cylinders; (b) cone-plate; (c) parallel-plate.

Capillary viscometry

In the absence of a suitable geometry for low viscosity measurements, *i.e.* large diameter cone-plates, concentric cylinders alternative methods may be used. Capillary viscometers are widely used due to their simple experimental set-up and fast result outputs via simple calculations. Generally, three types of capillary viscometers are used: Ostwald, Ubbelohde and Cannon-Fenske. By way of example, Ubbelohde is sketched in Fig.1.19. Measurements are performed as follows: the device sits in the vertical position in a thermostated environment, *e.g.* water bath; fluid sample is poured in (C) and sucked via a vacuum up to position (D), whilst the venting tube (B) is closed; when the fluid fills the space D and the

temperature is equilibrated, (A) and (B) are opened. At this point, the fluid starts to flow due to gravity with a pressure equal to the hydrostatic pressure which, in turn, is proportional to the shear rate and shear stress [59]. The flow time between point M_1 and M_2 depends on the viscosity of the fluid and the characteristics of the capillary (bold lines in figure), *i.e.* length L and diameter d. Dynamic (or shear) viscosity η is calculated as:

$$\eta = k\rho \tag{1.17}$$

where k is a constant provided from the manufacturer, expressed in $mm^2\ s^{-1}$; ρ is the density of the fluid (mg mm^{-3}) and t is the measured time in seconds between the point M_1 and M_2.

Recalling what has been explained in section 1.2.1 on polymer M_w determination, the η value obtained with capillary viscometers corresponds to the zero-shear viscosity η_0. Hence, the calculation formalism on $[\eta]$ and M_w determination is the same.

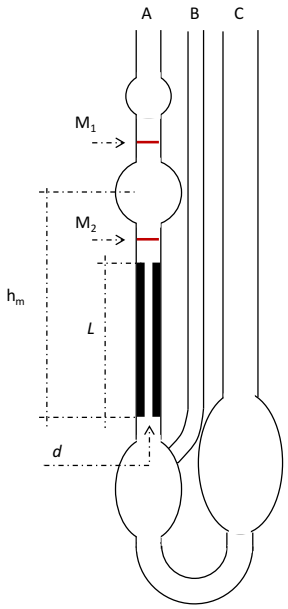

Figure 1.19: Ubbelohde capillary viscometer.

1.3 Scattering Techniques

Scattering techniques such as X-ray, light and neutron scattering, are key techniques to study structural and dynamical properties of different materials, *e.g.*, colloids, polymers, *etc.* To introduce scattering with a basic example, one can imagine a sample composed of solid particles dispersed in aqueous solution. When the sample is irradiated, a radiation-matter (sample) interaction generates scattering, caused by refractive index variations due to the scattering material (particles) in the medium (water). In static scattering (SLS): angular dependence of scattered intensity gives information on structure in terms of shape and interaction of objects in diluted and concentrated systems, respectively. In dynamic scattering (DLS) the time-dependence of fluctuations in the scattered radiation yields information on the dynamics of the probed matter, *e.g.*, Brownian motion of the scatterers. The choice of scattering mode and radiation wavelength, allows investigation at different length scales. Scattering theory is rather complex and this section provides a simplified summary. A full description of the theory and mathematical notation is provided by Berne and Pecora [60]. This section thus aims to provide the background for the static and dynamic light scattering measurements used. Finally, a few remarks on special aspects of X-ray scattering will be made.

1.3.1 Static Light Scattering

Fig.1.20 shows a sketch of a classic light scattering (LS) set-up. A light source (*e.g.* laser) with wavelength λ interacts with the electronic cloud of a number of particles N (for simplicity, scattered objects will be called particles), suspended in a volume V_s of a solution with refractive index n. This light-matter interaction creates an oscillation of the electric field (dipole moment α) , that causes an emission of light. At this point, the light emitted either passes through the sample or is scattered. The latter is collected in a detector, positioned at a distance$R$ from the sample and angle θ from the incident direction.

As mentioned in the introduction, the angular dependence of a SLS experiments allows the identification of structure/interactions of the probed material.

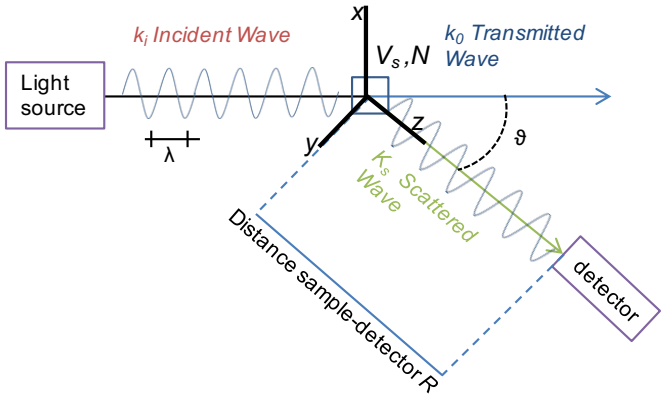

Figure 1.20: Static light scattering experiment. Schematic diagram of spatial disposition of components and factors that are involved during the analysis

To understand this aspect, a brief theoretical explanation of radiation-matter-position relationship is provided. Considering a incident radiation source as an electromagnetic plane wave:

$$E_1(\mathbf{r}, t) \equiv E_0 \cdot exp[i(\mathbf{k}_i \cdot \mathbf{r} - \omega t] \tag{1.18}$$

Where E_0 is the amplitude of the wave, $[i(\mathbf{k}_i \cdot \mathbf{r} - \omega t]$ represent the phase ϕ (number of oscillations) that varies with time ωt (where ω is the frequency measured in rad s^{-1}). More specifically, the phase includes the terms $\mathbf{k}_i$ and $\mathbf{r}$, which are known as propagation vector and position, respectively. A complete oscillation of the wave corresponds to a phase change of 2π, with a separation between the phases equal to a wavelength λ. Therefore:

$$|\mathbf{k}_i| = k = \frac{2\pi}{\lambda} \tag{1.19}$$

In *SLS*, the evaluation of the electric field after a scattering event is based on a number of assumptions such as: (i) most photons pass through the sample and few of them are scattered, with negligible multiple scattering, *i.e.* weak scattering; (ii) scattering particles are smaller than the wavelength and therefore reflections/attenuations of the light can be neglected, *i.e.* Rayleigh-Gans-Debye (*RGD*) approximation; (iii) elastic scattering, *i.e.*, the aforementioned frequency

ω after scattering does not change, therefore the magnitude of scattered wave-vector is equal to the incident one, *i.e.* $\mathbf{k}_i = \mathbf{k}_s$; (iv) the electromagnetic wave passing through a medium can be described in terms of the local dielectric constant, *i.e.* Maxwell equation [61]. These assumptions, together with the scattering volume V and the distance between the particle and detector R give the fundamental physical description of light scattering. Moreover, mathematical manipulation of the latter, allow the identification of the dipole moment, the event that generates emission of light (scattering) [60]. Often, for simplicity, most of the variables discussed above are enclosed as a single amplitude term, which here is called b.

In terms of propagated and scattered vector, the scattering centres in a medium are represented as follow Fig.1.21:

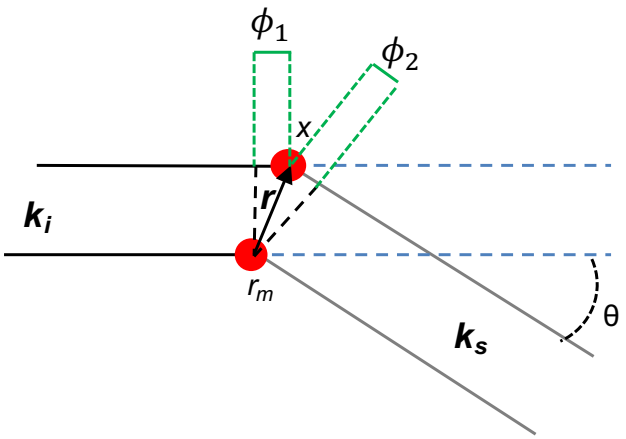

Figure 1.21: Incident and scattered wave-vector of two scattering centres with relative phase change.

The waves scattered by the centres (red dots in the figure) have different phases ϕ. The phase of the incident wave at position r_m equals to $\phi_1 = \mathbf{k}_i \cdot \mathbf{r}_m$. A phase change from scattering centre to detector at a position $\mathbf{x}$ is $\phi_2 = \mathbf{k}_s \cdot (\mathbf{x} - \mathbf{r}_m)$. The total phase change from source to detector corresponds to total phase change ϕ_t:

$$\phi_t = \phi_1 + \phi_2 = \mathbf{k}_i \cdot \mathbf{r}_m + \mathbf{k}_s \cdot (\mathbf{x} - \mathbf{r}_m) = \mathbf{k}_s \cdot \mathbf{x} + (\mathbf{k}_i - \mathbf{k}_s) \cdot \mathbf{r}_m$$

where the term $\mathbf{k}_s \cdot \mathbf{x}$ = constant because it derives from the detector position; the difference $(\mathbf{k}_i - \mathbf{k}_s)$ is denoted as scattering wave vector $\mathbf{q}$. Graphically:

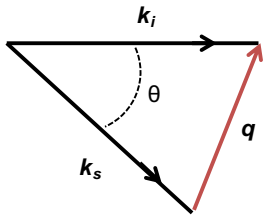

Figure 1.22: Graphical representation of the scattering vector q.

Since $\mathbf{k}_i = \mathbf{k}_s = k = \frac{2\pi}{\lambda}$:

$$q = \frac{4\pi}{\lambda} sin\frac{\theta}{2} \tag{1.20}$$

The scattering vector q, is the experimental quantity that probes interference effects at different length scales, with the reciprocal of q given a rough approximation of length scale. The scattering vector, multiplied by Planck's constant and divided by 2π gives the momentum transferred to the system by the photons [62][63].

Therefore, the total scattered wave amplitude, containing each wave amplitude from each scattering centre can be written as:

$$\psi = \sum_{i=1}^{N} b_i \cdot exp[i\mathbf{q} \cdot r_i] \tag{1.21}$$

Where b_i is the amplitude of the i-th center and the exponential factor is the phase factor. In practice, detectors in a LS set-up measure intensity $I(q)$, a quantity proportional to the square of the scattered amplitude. The measured $I(q)$ is averaged over the acquisition period t. The brackets $\langle ... \rangle$ represent this averaging. For ergodic materials, the time average equals the ensemble average. Hence, $I(q)$ becomes:

$$I(q) \quad = \left\langle \sum_{i=1}^{N} \sum_{j=1}^{N} b_i b_j \cdot exp[i\mathbf{q} \cdot r_i - r_j] \right\rangle \tag{1.22}$$

Experimentally, the scattered intensity carries contributions from the investigated object, solvent and machine set-up. The absolute scattered intensity, *i.e.* scattering from the particle (scattered object) is determined with the excess Rayleigh ratio $\Re_{ex}(q)$

$$\Re_{ex}(q) = \frac{I(q) - I_s(q)}{I_{ref}(q)} \cdot \left(\frac{n}{n_s}\right)^2 \cdot \Re_{ref} \tag{1.23}$$

Where $I(q)$ is the scattering intensity of the sample (at given q), $I_s(q)$ is the contribution of the solvent, $I_{ref}(q)$ is the intensity of the reference sample. Most commonly, the reference sample is toluene, since its Rayleigh ratio $\Re_{ref}$ is well documented in the literature and takes into account the experimental set-up. n_s and n_{ref} are the refractive index of solvent and toluene, respectively.

For quantitative SLS analysis and non-spherical particles of finite size, $\Re_{ex}(q)$ can be written as:

$$\Re_{ex}(q) = K \cdot C \cdot M_w \cdot P(q) \cdot S(q) \tag{1.24}$$

Where:

$$K = 4\pi^4 n^2 \frac{\left(\frac{dn}{dc}\right)^2}{N_A \lambda^4} \tag{1.25}$$

and C is the particle concentration, M_w is the molecular weight and dn/dc is refractive index increment. The other two terms are called the form factor $P(q)$ and structure factor $S(q)$. The former accounts for the internal particle interference (size and shape of a particle) while the second accounts for inter-particle interference [62]. Experimentally, the quantification of these two parameters requires distinct experiments and it is strongly dependent on the sample concentration.

For sufficiently dilute systems, particles are spatially separated and therefore, uncorrelated, *i.e.* the average of $I(q)$ depends on the summation of the scattering from single particles. In this situation, therefore, one can get information on the shape/dimension of a particle. For small q and isotropic particles, the form factor

given by the Guinier expression is :

$$P(q) = 1 - \frac{R_g^2 q^2}{3} + ... \tag{1.26}$$

where R_g is the mean-square radius of gyration. The Guinier expression derives from the mathematical expansion of either $P(q)$ for a sphere and/or a random-coil polymer molecule [61]. The above expression allows the calculation of R_g for any scattered object and holds for $qR_g < 1$. Often, Eq.1.26 is generally found as the Guinier approximation $P_{(q)} = exp(\frac{-q^2 \cdot {R_g}^2}{3})$, which allows easier extrapolation of experimental data to obtain R_g

In the condition where $qR_g << 1$, the structure factor S is related to the osmotic compressibility of the fluid [62]. In this condition, S is directly related to the second virial coefficient A_2. Therefore, A_2 and Eq.1.26 can simplify Eq.1.24 to:

$$\frac{Kc}{\Re_{ex}(q)} = \frac{1}{M_w}\left(1 + \frac{q^2 R_g^2}{3}\right) + 2A_2 C \tag{1.27}$$

In these limits, Eq.1.27 allows the determination of M_w, R_g and A_2, via a graphical method called Zimm plot [62].

For $qR_g > 1$, the form factor must be calculated using the full formula for $P_{(q)}$, which depends on the basis of the shape of the scattered object. Form factor models for a wide variety of shapes can be found in the literature [61] [63].

Beyond the RGD regime (*i.e.* $qR_g >> 1$), none of these approximations are valid and Lorenz-Mie theory should be used. A good descripiton for data modelling is provided by Otto Glatter, chapter 8 of reference [61].

As briefly explained earlier in the text, the structure factor $S(q)$ accounts for inter-particle interactions, *i.e.* attraction or repulsion, something that is likely to occur when the sample concentration is increased [62]. Considering:

$$\Re_\theta = KCM_w S_Q \rightarrow \frac{Kc}{\Re_{ex}(q)_\theta} = \frac{1}{M_w S(q)} \tag{1.28}$$

For small and monodisperse particles, at sufficiently low q, $\Re_{ex}(q)$ relates to the osmotic compressibility through the following expression:

$$\frac{KC}{\Re_{ex}(q)_\theta} = \frac{1}{RT}\left(\frac{\partial \Pi}{\partial C}\right)_{T,P} \tag{1.29}$$

Where R is the universal gas constant, T is the absolute temperature and Π is the osmotic pressure. Expanded as a function of concentration, Π:

$$\frac{\Pi}{RT} = \frac{1}{M_w}c + 2A_2C^2 + ... \tag{1.30}$$

Combining Eq.1.28 and Eq.1.30, one can obtain the structure factor S_Q:

$$S(q) = \frac{1}{1 + 2A_2M_wC + ...} \tag{1.31}$$

1.3.2 Dynamic Light Scattering

Dynamic light scattering (DLS) takes account of temporal fluctuations in the intensity of scattered radiation due to the motion of scattered entities. Appropriate data analysis yields important characteristics of the tested material, such as relaxation times, diffusion, size. Temporal fluctuations of the scattered light are collected (at the detector) as a speckle pattern, as shown Fig.1.23. The grain-like white spots represent the scattered intensities collected and, temporal fluctuations of these are caused by the movement of the particles. For example, for small particles that undergo to Brownian motion, the speckles will fluctuate quickly and the grains will be in different positions. On the other hand, arrested fluctuations of the speckle pattern are typical of jammed materials.

Figure 1.23: Typical speckle pattern.

As part of the LS set-up, an autocorrelator compares the integrated intensities and compares them at a t and time $t + \tilde{t}$. This temporal space is formally called

lag time $\tilde{t}$. The final output of the intensities at different $\tilde{t}$ (at specific q) is given as a time-intensity auto-correlation function g_2:

$$g_2(q,\tilde{t}) = \frac{\langle I(q,0)I(q,\tilde{t})\rangle}{\langle I(q)\rangle^2} \tag{1.32}$$

Where the brackets denote the average of the ensemble fluctuations. Fig.1.24 sketches g_2 vs. $\tilde{t}$ plots that identify the nature of the scatterers. (i) Red line shows a steep-like decay from 1 to 0 at low $\tilde{t}$. In this situation, small and monodisperse particles fluctuate fast through the media as a random walk (Brownian motion); in terms of g_2, there is no correlation between the intensities at time t and $t + \tilde{t}$. (ii) Larger diameter particles lead to g_2 decay at longer $\tilde{t}$ (blue line). However, this situation may also occur for small particles dispersed in a higher viscosity medium. (iii) Lastly, for dynamically arrested materials, such as gels or glasses, g_2 does not decay to g_2 =0, leading a plateau at higher lag times (purple line in the figure).

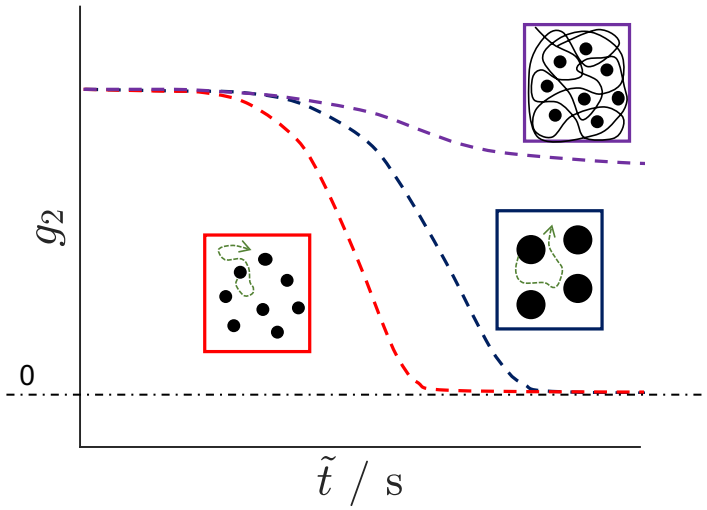

Figure 1.24: DLS results at fixed q for: (i) red trace: small particles, (ii) blue trace: large particles; (iii) purple trace: dynamically arrested materials.

Mathematical conversions are usually needed to obtain the diffusivity and

therefore, hydrodynamic radius, *e.g.*, via the Stokes-Einstein relation. The field auto-correlation function $g_1\ (q,\tilde{t})$ is obtained from $g_2\ (q,\tilde{t})$ via the Siegert relation:

$$g_2(q,\tilde{t}) = 1 + \sigma\big[g_1(q,\tilde{t})\big]^2 \tag{1.33}$$

where σ is the spatial coherence factor, a parameter related to the number of speckles detected at the surface area of the detector. As mentioned, g_1 correlates the electric field at different times and relative lag times. The electric field of an ensemble of particles N corresponds to:

$$E(q,\tilde{t}) = \sum_{j=1}^{N} a_j(q,\tilde{t}) e^{-iq\mathbf{R}_j(\tilde{t})} \tag{1.34}$$

Where a is the amplitude of the scattered field and R_j is the position of the particle j.

For a Gaussian distribution of particle displacements $\Delta R_{(\tilde{t})}$ given by:

$$g_1(q,\tilde{t}) = e^{-\frac{q^2}{6}\left\langle \Delta R^2(\tilde{t})\right\rangle} \tag{1.35}$$

Where $\left\langle \Delta R^2(\tilde{t})\right\rangle$ is the time dependent mean square displacement (MSD). For monodisperse particles that undergo to Brownian motion, $\left\langle \Delta R^2(\tilde{t})\right\rangle = 6D\tau$ where D is the translational diffusion coefficient. The $g_1(q,\tilde{t})$ vs. $\tilde{t}$ plots can be described with (i) cumulant analysis (not discussed here) or (ii) exponential function $g_1(q,\tilde{t}) = e^{-\Gamma\tau}$ where, $\Gamma = 1/\tau = D\cdot q^2$ and τ is the characteristic time of decay. Knowledge of D allows the estimation of hydrodynamic radius R_h via the Stokes-Einstein:

$$R_h = \frac{k_B T}{6\pi\eta D} \tag{1.36}$$

Where k_B is the Boltzmann constant, T is the absolute temperature and η is the viscosity of the medium.

τ is termed the relaxation time. In practice, $g_1(q,\tilde{t})$ broadens before decaying to 0, due to polydispersibility in the size and nature of the scattering particles. This gives a distribution of relaxation times and can be described by the stretched

exponential function of Kohlrausch-Williams-Watts (KWW) type:

$$g_1(q,\tilde{t}) = e^{-(\Gamma\tilde{t})^{\beta}} \tag{1.37}$$

where β ($0 < \beta \leq 1$) is the stretching parameter and is a measure of the width of the τ distribution [64]. Due to the influence of β on the overall relaxation time, the averaged relaxation time $< \tau >$ is [65]:

$$< \tau >= \frac{\tau}{\beta}\tilde{\Gamma}(\beta^{-1}) \tag{1.38}$$

where $\tilde{\Gamma}$ is the Euler gamma function.

As previously mentioned, in ergodic media (*i.e.*, small scattering objects dispersed in Newtonian fluids), particles freely diffuse through the sample volume and, over time, all possible spatial configurations are sampled. Therefore, time and ensemble averages are equivalent. In the case of materials with arrested dynamics, scatterers are localized around averaged positions (sub-regions) and their Brownian motion is limited; in other words, time and ensemble average are different. Therefore, $g_2(q,\tilde{t})$ needs to be tracked at different sample positions, *e.g.*, by rotating the scattering volume and so, an ensemble average can be constructed using Eq.1.32 [66]. Pusey and van Megen (1989) [67] developed a model for non-ergodic media that allows a correct data acquisition for samples with arrested dynamics. The final output of the model is:

$$g_1(q) = \frac{Y-1}{Y} + \frac{1}{Y}(g_2(q,\tilde{t}) - \sigma^2)^2 \tag{1.39}$$

where:

$$Y = \frac{\langle I(q)\rangle_E}{\langle I(q)\rangle_T} \tag{1.40}$$

and (i) $\langle I(q)\rangle_E$ is the scattered intensity of the ensemble average, *i.e.* rotation of the sample; (ii) $\langle I(q)\rangle_T$ is the scattered intensity of the time average, *i.e.* sample at fixed position. Usually, in non-ergodic media $\langle I(q)\rangle_T > \langle I(q)\rangle_E$. After its introduction, the model was (i) tested and used to extrapolate diffusion coefficient values for tracer particles trapped in gels and (ii) compared to other models [66] [68] [69]. [70].

Typically, $g_2(q,\tilde{t})$ for non-ergodic systems (Fig.1.24) appears firstly as a smooth decay at low $\tilde{t}$ due to the thermal diffusion of scatterers [71], followed by a plateau whose height depends on the degree of dynamical arrest. As mentioned in *SLS*, $L \approx q^{-1}$ represents the length scale L at which interference effects being observed. For non-ergodic media, dynamics at different L may appear different. For example, probing dynamics at low q (and high L) may show high plateaus, corresponding a high degree of dynamical arrest. Vice-versa for dynamics at high q and small L. These intrinsic features allow the determination of an elastic modulus, which links *DLS* with rheological studies [72]. In conclusion, for *DLS* experiments on non-ergodic material, the q-dependence becomes crucial.

Recent *DLS* studies on polymeric gels show an ultra-slow decay of $g_2(q,\tilde{t})$ that occurs at $\tilde{t} >> 100s$, *i.e.*, beyond the time-scale of the occurrence of the plateau discussed above [71]. However, due to set-up configurations, most modern *LS* instruments are equipped with photon-detectors and correlators where $\tilde{t}_{Max} \approx 100s$, which makes the secondary decay non-detectable. In terms of *LS* set-ups, such secondary decay detection can be achieved with CCD camera detectors. This is explained in more detail in the following section.

LS set-up II: Small Angle Light Scattering

In this section, a brief overview of small angle light scattering (*SALS*) is provided. Following Ferri (1997) [73] and Cipelletti and Weitz (1999) [74], the *SALS* set-up shown in Fig.1.25(a) works as follows: radiation from a laser passes through a beam splitter and is conveyed to the scattering cell (sample). Between the two, part of the radiation is collected in a photodiode (PDii) that quantifies the incident radiation. Scattered and transmitted radiation are collimated via lens (L) where: (i) transmitted radiation hits a beam stopper and, through a mirror configuration, the radiation is measured by a photodiode (PDt); (ii) the CCD camera objective lens magnifies and captures the focal plane and this allows the picture acquisition. In this configuration, scattering with same q magnitude is mapped to pixels lying on a ring centered with respect to the optical axis Fig.1.25(b) [74]. The characteristic radius of the ring, together with the distances of both lens and beam stop, allow the extrapolation of q. Full details on both q

and intensity I calculations are provided in [73].

The power of $SALS$ derives from its ability to probe much larger length scales, typically q between 200 cm^{-1} and 14000 cm^{-1} that, in turn, corresponds to 0.06 $< \theta <$ 5°.

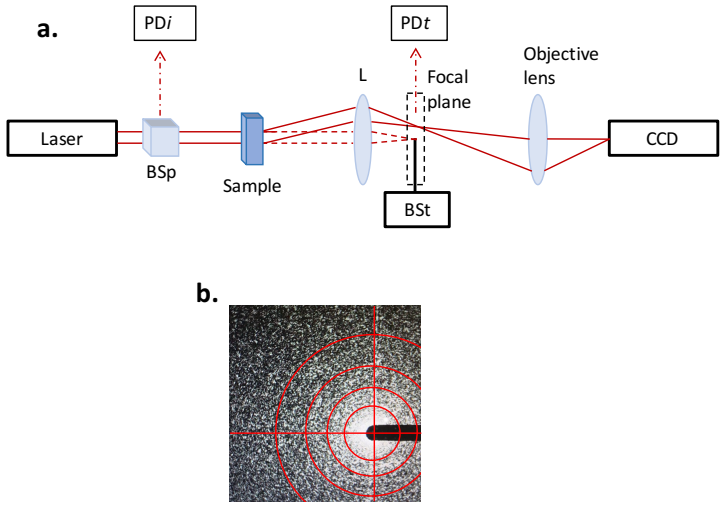

Figure 1.25: (a) Small angle light scattering set-up; (b) circle-mapping pixels in speckle pattern of a $SALS$ experiment.

An example of $I(q)$ vs. q for a polymer solution is sketched in Fig.1.26. As shown, at high q, the solid line shows a power-law regime, which indicates a fractal morphology where, the exponent indicates the fractal dimension df (*i.e.* self-similar structures across different length scales). Specifically, variations of the intermediate scattering function df describe: (i) $df = 2$ Gaussian conformation in θ solvent; (ii) $df \leq 2$ extended chain in good solvent; (iii) $df > 2$ semi-collapsed chain in poor solvent conditions; (iv) $df > 2$ has been previously ascribed branched polymers [75].

At intermediate q, $I(q)$ starts to bend down, leading to a plateau at low q. In this situation, the roll-off point corresponds to $\xi = 1/q$, *i.e.*, a characteristic length-scale. A different scenario shown in the figure is represented by the dashed line: this extends the power-law behaviour at low q, indicating the existence of structures bigger than the size of the scattering object and/or aggregation effects. In other words, the plateau formation indicates the crossover between the

organization of the gel structure to the internal re-arrangements of the polymer chains [75][76].

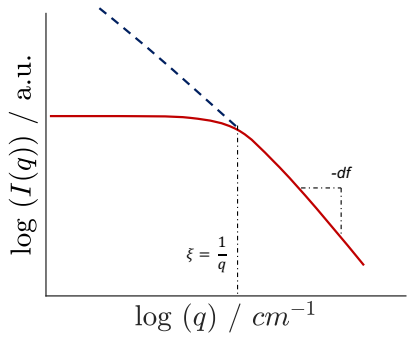

Figure 1.26: Sketch of the intensity $I(q)$ vs. q plot typical of a polymer solution.

LS set-ups III: rheo-speckle

The rheo-speckle is a custom-built up instrument that couples rheology and a LS to perform simultaneous analysis. Generally speaking, a CCD-based LS set-up (explained section 1.2.1) is placed underneath a rheometer. Compared to the $SALS$ system, the laser and detector are not in the same focal plane and the radiation pattern (incident and scattered) is guided through a specific mirror configuration. In the rheometer, the parallel plate geometry consists of a quartz-made bottom plate and a coated upper plate, to avoid multiple scattering issues. This set-up collects scattered radiation at fixed scattering vector $q \approx 33\ \mu m^{-1}$, *i.e.* $\theta \approx 170°$. The data acquisition principle is a modified version of the multispeckle autocorrelation theory [74], where g_2 is obtained as a result of the average of both time and thousands of speckles [77]. This modification, called time-resolved correlation (TRC) consists of a speckle comparison between multiple images taken at different times $\tilde{t}$ with respect to the one at $t_i = 0, 1, 2, ..., n$. The output, called c_I, corresponds to Eq.1.41 and graphically appears as Fig.1.27.

$$C_i(t_i, \tilde{t}) = \frac{\langle I_p(t_i) I_p(t_i + \tilde{t}) \rangle}{\langle I_p(t_i) \rangle \langle I_p(t_i + \tilde{t}) \rangle} - 1 \tag{1.41}$$

Where I_p is the intensity of the i-pixel and the brackets indicate the average of the pixels.

As shown in Fig.1.27, each trace corresponds to the c_I taken at a certain lag time. In other words, at $\tilde{t} = 10s$, I_p derives from the comparison of speckles at time $t_i = 0, 1, 2, ..., n$ and $t_i + 10$, *e.g.* if $t_i = 5s$, the corresponding image is at $15s$. The "extremes" in $\tilde{t}$, *i.e.* $\tilde{t} = 1s$ and $\tilde{t} = 10000s$, show a c_I saturation and uncorrelated intensities, respectively. With this in mind, c_I values averaged over the full range of $\tilde{t}$ at fixed analysis time, gives the autocorrelation function g_2. With the ability to access long lag times ($\tilde{t} > 10000s$), one can probe ultra-slow dynamics, characteristic of jammed and soft-solid materials, plus perform rheological measurements simultaneously.

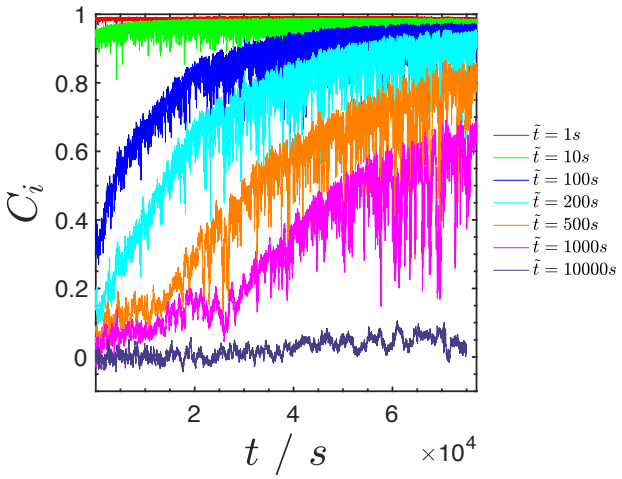

Figure 1.27: C_i plot of a physical gel. Different colors represent C_i signals at different $\tilde{t}$.

A typical rheo-speckle experiment on a soft-solid material consists of two steps of analysis. The first one, termed spontaneous dynamics, tracks the dynamics of the sample with no stress applied. This allows the determination of the dynamical arrest at the probed length scale. At this point, one can perform the simultaneous rheology *DLS* experiment, typically creep or step strain relaxation.

1.3.3 Static scattering: other radiation sources

As stated earlier, the q range depends on the scattering angle θ and wavelength λ source. Hence, the alternative use of X-ray and neutron radiation with $\lambda \approx 0.05 - 1\ nm$, allow the investigation of materials at even higher q and so, smaller L, than visible light. A summary of wavelengths, length scales and techniques is provided in Fig.1.28.
Generally speaking, at small angles, the scattering formalism is similar for light, X-rays and neutrons but the scattered intensity derives from different radiation-medium interactions [63]. Scattered X-rays come from electrons of a sample, where the scattered intensity is proportional to the number of electrons.

Scattered neutrons arise from atomic nuclei and the scattering varies non-systematically with the atomic number [61]. Moreover, different isotopes of the same atom may scatter in a different ways, due to their different scattering length densities. In this perspective, the common issue in neutron scattering is the negative scattering length density given by hydrogen's nucleus (-3.74·10^{-15} m). This can be easily bypassed however, by using deuterium (6.67·10^{-15} m). The substitution allows contrast enhancement and highlighting structural information at very short length scales[61].

For non-interacting particles and in the limit of low q, the data interpretation can be applied to *SAXS* and *SANS* experiments as well. Thus, the Guinier formalism permits the determination of the global structure of the scattered object. Again, this rule applies for $qR_g < 1$. Generally, in the limit of $qR_g >> 1$, the scattering corresponds to an asymptotic power-law regime $I(q) \propto q^{-p}$ that describes the organization of the structure. Generally: (i) $p = 4$ describes sharp interfaces, called the Porod regime; $3 \leq p < 4$, surface fractal; $p < 3$, mass fractal; $p \approx 2$, Gaussian polymer chain [63].

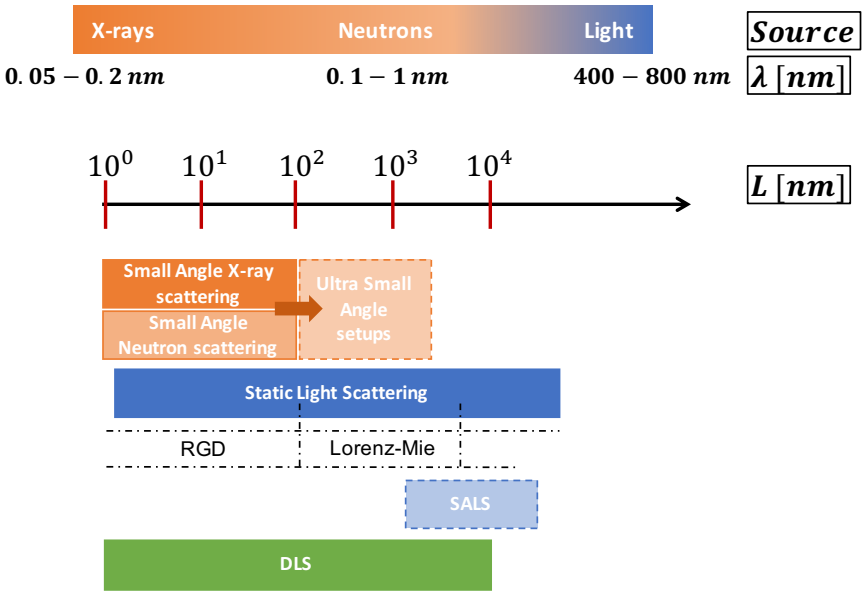

Figure 1.28: Schematic representation of probed length scales via different scattering techniques at their operational wavelength.

Chapter 2

Materials and Methods

2.1 Materials

Amidated low methoxyl pectin LMP GRINSTED® Pectin LA 210 from DANISCO-DuPont (Wilmington, Delaware, USA) was kindly donated by Mondelēz International. Specifications: (i) galacturonic acid content $\approx 91\%$, (ii) esterification degree $\approx 34\%$, (iii) amidation degree $\approx 17\%$, (iv) pH (1% solution) $\approx 4.0 - 4.8$. Sodium hexametaphosphate $Na_6P_6O_{18}$ ($SHMP$) 2 mM (Fisher Scientific, UK); Calcium chloride dehydrate $CaCl_2$ (VWR Chemicals, UK); D-(-)-fructose $C_6H_{12}O_6$ (Sigma Aldrich, UK); sorbitol syrup, solids $\approx 72\%$ (Keylink, UK); D-sorbitol $\geqslant 98\%$ (Sigma Aldrich, UK); invert sugar, *i.e.* $1\ M : 1\ M$ mixture of D-(-)-fructose and D-(+)-glucose monohydrate $C_6H_{12}O_6$; D-psicose syrup, solids $\approx 95\%$ (Tate & Lyle, USA).

2.2 Methods

2.2.1 Sample preparation

Hydrogels (W samples): LMP was dissolved in MilliQ water at temperature $T \approx 85 - 90°C$ using a hot plate stirrer (AREX, Velp Scientifica Srl, IT) and a high velocity mixer (≈ 8000 rpm) (T25 Ultra-Turrax, IKA-Werke GmbH & Co., Germany). Also, 2 mM of ($SHMP$) was added to the solution to (i) sequester any contaminant divalent ion that may form junction zones, (ii) slow down the gel

formation when the cross-linking agent is added, *i.e.* ensure the uniformity of gel formation through the entire sample., (iii) suppress LMP pectin aggregation via electrostatic screening. $CaCl_2$ was added as cross-linking agent at concentrations between 0 and 9 mM. The final concentration of LMP was fixed at 0.5 *wt.* %.

Sugar-gels: the procedure was identical to the W samples method apart from the solvent composition. In this case, the sugar was dissolved in MilliQ water to give 59.7 *wt.* % of: (i) fructose (*WF* samples); (ii) sorbitol syrup (*WS40* samples); (iii) D-sorbitol (*WS60* samples); (iv) invert sugar, *i.e.* a 1:1 molar mixture of fructose and glucose (*WIS* samples); (v) psicose syrup (*WPSI* samples).

Once prepared, hot solutions were transferred to suitable analysis cells, depending on the technique used. Otherwise stated, samples were stored at room temperature $\approx$ 20 °C.

Sample storage/analysis cells

Rheology. In order to minimize gel damage during its transfer to the rheometer, it was decided to make a disk-like gel sample with a diameter of $\approx$ 50 mm and height $<$ 1.5 mm. For this purpose, a glass Petri dish with a diameter slightly higher than 50 mm was implemented as follows. At its base, a layer of "non-stick" foil was placed and blocked with a rubber O-ring (height = 1.2 mm) whose diameter perfectly adhered to the Petri dish walls. The space, once filled with the sample, was covered with another non-stick foil layer. A bottle cap was then used as a lid, together with a PARAFILM® wrap at the edges, to prevent evaporation. This also enabled transport of samples to Montpellier (see later). In case of fluid solutions, samples were stored in sealed cylinder tubes.

Static and **dynamic light scattering**. Hot solutions were transferred to hermetically sealed glass testing tubes, diameter = 5 mm and height = 50 mm.

SALS. Quartz glass cells with optical length of 10 mm (402-OG, Hellma, DE) were filled with pectin solutions and analysed.

X-ray scattering. Quartz capillary tubes, diameter = 1.5 mm (QGCT 1.5, CTS Capillary Tube Supplies Ltd, UK) were used for these analysis. To prevent evaporation liquid spillage due experimental conditions, tubes were sealed with wax.

2.2.2 Analysis

Rheology

Tests were performed with a controlled shear stress rheometer (MCR 302, Anton Paar GmbH, DE) equipped with a Peltier temperature controller. Fluid samples such as polymeric solutions and/or sugar solutions were analysed with shear-rate dependent tests. For these measurements, a 50 mm cone-plate geometry (cone angle = 2°) was used, with a fixed gap of 0.328 mm. The $\dot{\gamma}$ range, where not specified, was between 10^{-2} and 10^{3} s^{-1}. At low $\dot{\gamma}$ values, viscosity η values were considered only when the minimum torque value of the machine was reached , *i.e.*, 0.01 μ Nm. In shear tests, time-dependent η was performed at constant $\dot{\gamma}$ at 0.1 and 10 s^{-1}. Unless stated otherwise, measurements were performed at T = 25 °C. To prevent evaporation, a custom-made solvent trap allowed the homogeneous distribution of a low viscosity (0.35 Pa s) silicone oil (47 V 350 Rhodorsil Oil, Bluestar Silicones, N) at the edge of the geometry.
Viscoelastic materials (gels) were analysed via oscillatory tests in a parallel plate geometry, diameter 50 mm. After sample loading, the gap between the plates was set by keeping track of the normal force N_F, *i.e.* force derived from the compression imposed by the upper plate. For all experiments, N_F did not exceed ≈ 1 N and, most of the tests were carried out with a plate gap = 1 mm. Pre-N_F fluctuations were tracked for $\approx$ 5 min before starting the analysis. For strain sweep tests, the evaluation of the linear viscoelastic regime LVE was performed in a γ range from 0.1 and 100 %. Detailed experiments were carried out at γ = 10^{-2} and 10^{3} %, angular frequency ω = 1 rad s^{-1} T = 25°C, unless otherwise stated.

Frequency sweep tests were carried out at constant γ = 1 and $\omega = 10^{-1}$ - 10^{2} rad s^{-1}, T = 25°C, unless stated. In temperature dependence frequency sweeps, the ω was reduced to $10^{-1} - 10^{1}$ rad s^{-1} (to make the experiment less time consuming) and the temperature was varied from T = 25 to 75°C. Time-dependent oscillatory test were carried out at γ = 1 % and $F = 10^{0}$ rad s^{-1}, for a time t = 60 min, T = 25°C. For rotational tests, (i) data were considered when the minimum torque was reached, (ii) solvent trap was used.

Capillary viscometry

An Ubbelohde glass capillary viscometer (1625/02, PSL-Rheotek, UK) was used for low-viscosity measurements. The capillary was suspended in the vertical position inside a thermally controlled water bath at $T = 25 \pm 1°C$ using laboratory clamps. After sample loading, the fluid level was adjusted to the required position (see section: 1.4.2 Capillary viscometer) and left at rest for $\approx$ 15 min. The sample temperature was tracked via a thermocouple. To track the fluid flow time, a simple chronometer was used.

Static and Dynamic light scattering

SLS and *DLS* measurements were performed using a 3D LS spectrometer (LS Instruments, Switzerland) equipped with a He-Ne laser (λ = 660.0 nm, power: 21 mW), an automated laser attenuator and two avalanche photodiode (APD) detectors. All measurements were performed with vertically polarized incident and detected light in pseudo-cross correlation mode, which removes after-pulsing effects and allows the investigation of lag times $\tilde{t}$ as low as 25 ns. All samples were transparent and we confirmed that multiple scattering did not have to be taken into account, *i.e.*, data comparison between 2D and 3D mode. Thus, all measurements were performed using the 2D mode, corresponding to the standard set-up of LS measurements. For *DLS* tests, the scattering angle θ was either kept fixed at 90° or varied from 30 to 130°, in steps of 10°. For ergodic (liquid-like) samples, data was collected over a period of $\approx$ 900 s. For gelled samples (non-ergodic regime), time and ensemble averages were collected separately. In the former, the experiment time was typically $\approx$ 3600 s, whereas ensemble averages were collected over $\approx$ 300 s by rotation of the sample. Additional DLS experiments were performed when varying the temperature from 25 to 65°C but the same the experiment/data-collection times above were followed.

For *SLS* samples, θ was from 15 to 140°, in steps of 0.5°. Ergodic media were scanned for a time of $\approx$ 20-30 s, repeated 3 times. In the case on non-ergodic media, the same test conditions were applied with the additional rotation of the sample.

Small angle light scattering

SALS experiments were performed on a custom-built set-up at University of Montpellier, France (details in section: 2.2.1 Advanced LS set-ups I: Small Angle Light Scattering). Laser wavelength λ= 532 nm, 48 probed pixel rings ($\approx 2{\cdot}10^6$ total pixels processed), corresponding to q vector range from $\approx 10^{-2}$ to $7{\cdot}10^{-1}$ μm^{-1}. Experimental parameters were as follows: (i) number of acquisitions per run 35, (ii) time maximum per runs $\approx$ 492 ms, (iii) delay time between run 5 s. The intensity distribution collected at the CCD was corrected for the optical background (solvent) and azimuthally averaged to obtain $I(q)$. The temperature was maintained at 23 $\pm$ 2°C.

Rheo-optics

Rheo-optics experiments were carried out with a controlled shear stress rheometer (MCR 302, Anton Paar GmbH, DE) with a light scattering set-up placed underneath, equipped with a green light laser λ = 534 nm. The custom-built apparatus is located at University of Montpellier, France. Gelled samples were loaded onto the bottom plate and the gap was set by checking the N_F and the image of the sample collected by the camera to check the gap was homogeneously filled. Two distinct rheology and LS experiments were performed simultaneously at 25°C. The first one, referred to as "spontaneous dynamics" was performed with no imposition of stress by the rheometer; at the same time, LS set-up recorded 1000 images per run, with a exposure time of 800 ms and a lag time between runs of 1000 s The number of runs was decided on the basis of the sample and following data analysis. Upon completion, the sample was not removed from the set-up and a step-strain relaxation test (rheology) was applied, *i.e.* strain of $\dot{\gamma}$ = 1% was applied. The resulting stress relaxation was monitored for 10^5 s. *DLS* was performed at the same time.

Recorded images were then analysed with a supplementary custom-written software. With this software and the experimental imaging recording parameters, pixel intensities between the images at assigned lag times $\tilde{t}$ were compared for each time-dataset. The final output was the so called C_i function.

X-ray scattering

X-ray scattering was performed with the synchrotron $SAXS$ set-up at Diamond Light Source (beamline I22, Didcot, UK); $\lambda = 1.4$ Å (energy $E \approx 8.9\ keV$), distance sample-detector 5 m allowing small scattering vector detection, acquisition time 10 s and $T = 25$°C, q range $\approx 2.3{\cdot}10^{-4}$ – $3.8{\cdot}10^{-1}$ Å. Both sample and solvent were scanned under the same conditions and data beam-corrections were carried out by operators at the beamline. Then, background subtractions was performed according to [78], following the steps: (i) all recorded X-ray pattern were corrected for the background scattering of the empty capillary rack, (ii) all recorded X-ray pattern were normalized by their measured transmission, (iii) the normalized capillary scattering was subtracted from both, the normalized sample plus capillary and solution plus capillary scattering, and finally (iv) the pure and normalized solution scattering was subtracted from the pure and normalized sample scattering, hereby taking into account the volume fraction of the solution in the sample.

Transmission Electron Microscopy (SEM)

Transmission electron microscopy (SEM) images were taken in both the School of Chemistry and Chemical Engineering at the University of Leeds (UK).

For SEM images performed in the School of Chemistry, small aliquots of samples were frozen in liquid nitrogen and freeze dried for 24 hours at a pressure of 0.05 mbar, temperature in collector -50°C (FreeZone 1, LABCONCO, USA). After freeze drying, the samples were coated with a 3 nm thick layer of Pd/Pt through a sputter coating. The image acquisition was performed with a FEI Nova 450 FEG-SEM (USA) instrument, operating at 3 kV. Sample preparation was performed by Dr. A. Kulak.

The images taken at in the School Chemical Engineering were performed with a cryo-SEM device. The sample was placed on a cryo shuttle using 2 freezing rivets and plunged into slushed nitrogen previously prepared (*i.e.*, liquid nitrogen under vacuum conditions). Once the sample equilibrated its temperature, it was transferred to the preparation chamber (FEI Helios G4 CX DualBeam, USA).

The latter, kept at both controlled pressure (10^{-7} mbar) and temperature (-145°C). The sample was fractured using a cooled knife, then sublimed by raising the temperature to -90°C for 3 min and then coated in Pt. Finally, the sample was transferred into the SEM system (PP3010 cryo-FIB/SEM, USA) and imaged using 1.5 kV accelerating voltage and 0.1 nA beam current. Sample preparation and test was performed by Mr. Stuart Micklethwaite.

Data processing

All data were processed and plotted with MatLab (The MathWorks, Inc., UK). All the fitting procedures were performed with both linear and non-linear least squares analysis.

Chapter 3

Polymer Characterization

This chapter aims to characterize the polymer in solution (*i.e.*, in absence of gelation) via different techniques, such as rheology, dynamic light scattering (DLS) and static light scattering (SLS and $SALS$). Experiments were mainly performed in water however, some tests were performed in the presence of fructose as a co-solutes.

3.1 Rheological characterization

The LMP characterization was performed as described in section 1.2.1. Viscosities of solutions of different pectin concentrations ($[LMP]$) in water were investigated using an Ubbelohde glass viscometer. The flow time ($t_{[LMP]}$) was used to calculate the specific (η_{sp}) and reduced viscosity (η_{red}) as follows:

$$\eta_{sp} = \frac{t_{[LMP]} - t_0}{t_0} \tag{3.1}$$

$$\eta_{red} = \frac{\eta_{sp}}{[LMP]} \tag{3.2}$$

where t_0 is the flow time at $[LMP] = 0$ *wt.* % , *i.e.*, water. Results are shown in Fig.3.1(a). In the low $[LMP]$ range between 0.1 - 0.5 g dL^{-1}, η_{red} is constant and does not vary with the polymer concentration. The intrinsic viscosity ($[\eta]$), as the η contribution of a single polymer chain, was extrapolated using Huggin's

relation [13]:

$$\eta_{red} = [\eta] + k_1[\eta]^2[LMP]. \tag{3.3}$$

Here, k_1 is a characteristic constant of the polymer-solvent system. In the η_{red} vs. $[LMP]$-independent range, $[\eta] = 4.3 \pm 0.4$. This value is in agreement with data obtained in similar studies on low methoxyl pectins [2][32][79]. Knowing $[\eta]$ allows estimation of the weight averaged molecular weight (M_w), via the Mark-Houwink-Sakurada (MHS) relation. Typical values for the exponent a and pre-factor K for citrus LMP [79] [80] were used to provide an estimate for M_w,

$$\eta = 9.55 \cdot 10^{-2} \cdot {M_w}^{0.72} \tag{3.4}$$

yielding a value of 91 kDa, which is similar to typical M_w values obtained for citrus LMP in the literature [2][79], *i.e.*, < 100 kDa. The relationship $C^* = [\eta]^{-1}$ [13] allowed the estimation of the $[LMP]$ where short range interactions between polymer chains start to occur, *i.e.*, ≈ 0.23 g dL^{-1}, indicated with the arrow in the η_{sp} vs. $[LMP]$ plot in Fig.3.1(b).

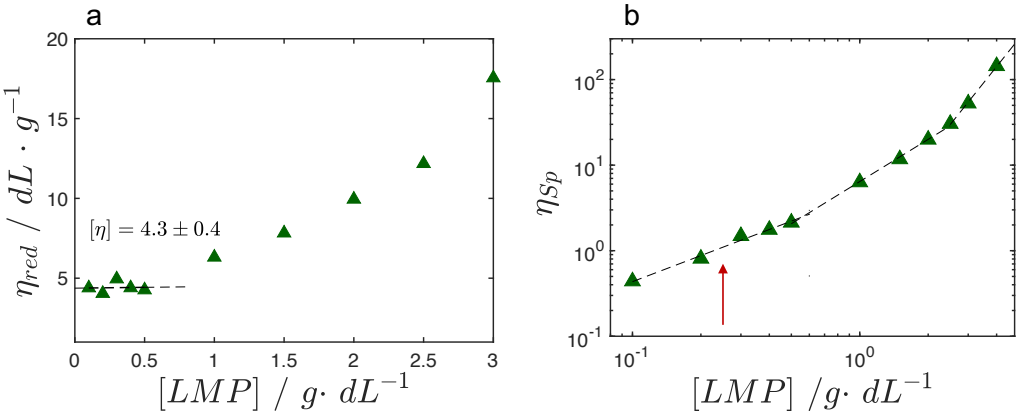

Figure 3.1: LMP dissolved in water and analysed via capillary viscometer. (a) η_{red} vs. $[LMP]$ for the determination of $[\eta]$ via Huggin's relation. (b) double-logarithm plots of η_{sp} vs. $[LMP]$ for the individuation of the overlap concentration.

Due to the increased η of LMP solutions dispersed in 60 *wt.* % of fructose,

the analysis could not be performed via capillary viscometry. Hence, a shear-controlled rheometer was used for this purpose. Results are shown in Fig.3.2. As shown in the figure, $[LMP]$ between 0 and 0.25 *wt.* %, η shows no $\dot{\gamma}$ dependence, indicating Newtonian behaviour. For this reason, the zero shear viscosity (η_0), *i.e.*, η at $\dot{\gamma}$ =0, was taken as the intercept of the linear fit of the η vs. $\dot{\gamma}$ data. For $[LMP] \geq 0.5$ *wt.* %, the flow curves show shear thinning behaviour. In this situation, the η vs. $\dot{\gamma}$ curves were fitted with a generalized Carreau model [59], as:

$$\frac{\eta(\dot{\gamma})}{\eta_0} = \frac{1}{(1 + (c_1 \cdot \dot{\gamma})^2)^p} \tag{3.5}$$

where η_0 is the zero shear viscosity; c_1 and p are the Carreau constant and exponent respectively. Fit parameters and errors are reported in the table next to Fig.3.2. η_{red} vs. $[LMP]$ plots for these data yielded a value of $[\eta] \approx 4$, similar to that obtained for the LMP-water system.

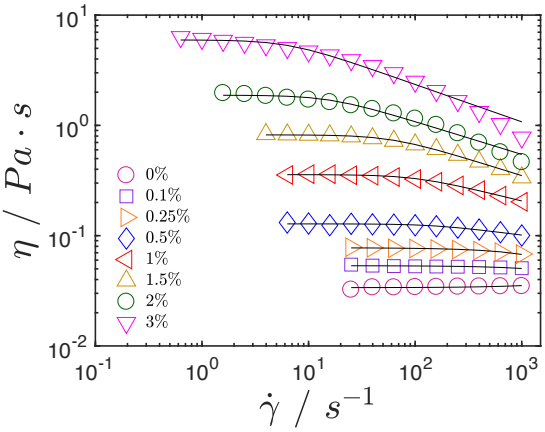

Concentration %	η_0	c_1	p
0.5	0.128 ± 0.001	0.007 ± 0.002	0.062 ± 0.011
1	0.358 ± 0.002	0.011 ± 0.001	0.120 ± 0.006
1.5	0.820 ± 0.005	0.017 ± 0.001	0.151 ± 0.007
2	1.879 ± 0.033	0.063 ± 0.012	0.149 ± 0.012
3	5.957 ± 0.121	0.155 ± 0.029	0.170 ± 0.013

Figure 3.2: Different $[LMP]$ dissolved in 60 *wt.* % fructose. (a) η vs. $\dot{\gamma}$ results obtained via rotational rheology analysis. Fit lines corresponding to interpolation via the Carreau equation are shown as well. (b) Carreau fit parameters and errors for $[LMP] \geq 0.5$ g dL^{-1}.

The $[LMP]$ suggested by Mondelēz International for the gel production, *i.e.*, 0.5 *wt.* % , is therefore around the C^*, before addition of Ca^{2+}. All subsequent

gelation experiments were carried out at this $[LMP]$.

3.2 Dynamic light scattering characterization

Dynamic light scattering (DLS) experiments allow for the characterisation of a number of physical properties, such as hydrodynamic length scales and relaxation modes. The data obtained and the analysis performed are initially shown for $[LMP] = 0.5$ *wt.* % dispersed in water.

Fig.3.3(a) shows the intensity-intensity autocorrelation function $g_{2-1}(q, \tilde{t})$ versus lag time $\tilde{t}$ for a pectin solution at $[Ca^{2+}] = 0$ mM, collected at a fixed angle ($\theta = 90°$) and therefore a fixed scattering vector, q ($\approx 18\ \mu m^{-1}$). As shown, $g_{2-1}(q, \tilde{t})$ in the probed $\tilde{t}$ range decays exponentially from 1 to 0. Firstly, the data were converted to the electric field autocorrelation function $g_1(q, \tilde{t})$ (Fig.3.3(b)), via the Siegert relation $g_2(q, \tilde{t}) = 1 + \sigma\big[g_1(q, \tilde{t})\big]^2$, where σ is the spatial coherence factor. In practical terms, σ corresponds to the intercept of $g_1(q, \tilde{t})$ at zero lag time.

$g_1(q, \tilde{t})$ vs. $\tilde{t}$ data were described with a stretched exponential function, known as the Kohlrausch-Williams-Watts (KWW) function, widely used for polymers and pre-gelled system [81].

$$g_1(q, \tilde{t}) = A \cdot exp^{(-\Gamma\tilde{t})^{\beta}} \tag{3.6}$$

where (i) A is the amplitude of the $g_1(q, \tilde{t})$ function; (ii) Γ is the decay rate and corresponds to $\Gamma = \tau^{-1}$, *i.e.*, inverse of the relaxation time τ; (iii) β is the stretching exponent, a measure of the breadth of the underlying distribution of relaxation times [82] [83] [84]. Fig.3.3(b) shows the $g_1(q, \tilde{t})$ vs. $\tilde{t}$ data fitted with the above mentioned KWW function.

As shown in Fig.3.3(b), the $g_1(q, \tilde{t})$ data at high $\tilde{t}$ has relatively high levels of noise, related to the long data collection time required to achieve better statistics, especially for these disordered systems. For this reason, the KWW fit function was applied in a $g_1(q, \tilde{t})$ range between 1 and and 0.1.

The transformation to $g_1(q, \tilde{t})$ involves the square root of $g_{2-1}(q, \tilde{t})$, a procedure that highlights the noise level of the data. Hence, it was decided to use

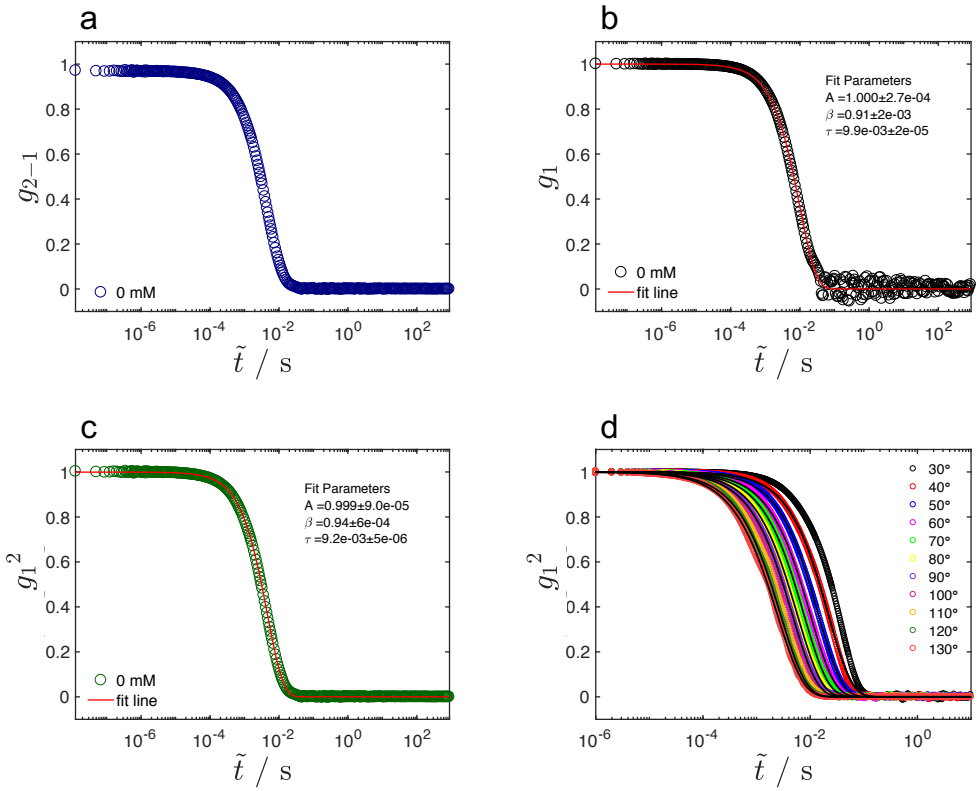

Figure 3.3: (a) Intensity-intensity autocorrelation function (g_{2-1}) vs. lag time ($\tilde{t}$) for W sample and $[Ca^{2+}] = 0$ mM. (b) Conversion to electric field autocorrelation function (g_1) vs. $\tilde{t}$ via Siegert relation of data displayed in (a); the plot show the KWW fit and relative fit parameters. (c) σ-renormalized time-intensity autocorrelation function $g_{2-1}/\sigma = {g_1}^2$ vs. $\tilde{t}$ and relative KWW fit line and parameters. (d) ${g_1}^2$ vs. $\tilde{t}$ at different angles and relative KWW fits.

$g_{2-1}(q, \tilde{t})$ renormalized by σ as $\frac{g_{2-1}}{\sigma} = {g_1}^2$, as shown in Fig.3.3(c). For the $g1^2$ function, the KWW model becomes $g1^2 = A \cdot e^{(-2\Gamma\tilde{t})^\beta}$. Fitted KWW results showed $\tau_{g_1} = 9.9 \cdot 10^{-3}$ s and $\tau_{g_1{}^2} = 9.2 \cdot 10^{-3}$ s. The stretched exponential parameter β was 0.91 and 0.94 for g_1 and ${g_1}^2$, respectively.

Fig.3.3(d) shows the angular dependence of the measurement and relative KWW fit lines, from 30 to 130°, corresponding to q values between 6 and 24 μm^{-1}. As discussed in section 1.3.1, q is a parameter that characterizes the length scale at which interference effects are probed where $L \approx q^{-1}$.

Fig.3.4(a) shows the q dependent values for β. The fit parameter decreases

from 1 to ≈ 0.9, indicating greater heterogeneity levels at smaller length scale (large q). Hence, due to the β contribution, the averaged relaxation time relation was used, *i.e.*, $< \tau >= (\tau/\beta)\tilde{\Gamma}(\beta^{-1})$, where $\tilde{\Gamma}$ is the Euler gamma function [32][65][85]. Results for both τ and $< \tau >$ as a function of q are shown in Fig.3.4(b). The double logarithm plot of Γ vs. q obtained from both τ and $< \tau >$ is shown in 3.4(c). The Γ vs. q data show a power law behaviour, with an exponent $\Lambda = 2.1 \pm 0.03$. For ideal diffusive behaviour, $\Gamma = D \cdot q^2$ (D = diffusion coefficient), *i.e.*, $\Lambda = 2$. Since the Λ value obtained from these data was close to this value, the relaxation is therefore assumed to be largely due to diffusive behaviour. To estimate the diffusion coefficient D, Γ vs. q^2 plots where utilised (Fig.3.4(d)). The linear dependence of Γ vs. q^2 was fitted with a straight line angular coefficient equal to D. Therefore, from τ and $< \tau >$, $D_\tau = 3.4 \cdot 10^{-7} \pm 8.7 \cdot 10^{-9}$ m^2 s^{-1}. As indicated in the plot, the slight difference between τ and $< \tau >$ is due to the relatively small heterogeneity (*i.e.*, $\beta \approx 1$), though the difference is larger at higher q (lower L). However, the difference is still small and further relaxation times will be given as $< \tau >$.

Fig.3.4(e) shows ${g_1}^2$ (measured at different q) versus $\tilde{t} \cdot q^2$. In the case of diffusive behaviour, the q-dependent ${g_1}^2$ should collapse onto a master curve [81]. This confirms the diffusive character for $[LMP] = 0.5$ *wt.* % dispersed in water. Knowledge of the diffusion coefficient allows the corresponding hydrodynamic radius (or length scale) to be calculated via the Stokes-Einstein relation. Here, the viscosity η of water at 25°C $= 0.894 \cdot 10^{-3}$ Pa s^{-1}. For this sample, $R_h = 0.72 \pm 0.02$ μm.

Hence, it is likely that the observed relaxation process derives from an ensemble of chains and/or interactions rather than individual molecules, given the proximity to C^*. More information can be determined using the quantity qR_h. When $qR_h < 1$, one can obtain information regarding the global dynamics and individual translational diffusion coefficients for each individual molecule [86]. On the other hand, at $qR_h > 1$ the dynamical behaviour is a combination of translational diffusion and internal relaxation modes of the material.

The Γ vs. q dependence of the relaxation modes may indicate: (i) diffusive character Λ =2; (ii) hydrodynamic interactions (Zimm mode), Λ =3; (iii) screened hydrodynamic interactions (Rouse mode), Λ =4 [81][86]. However, the

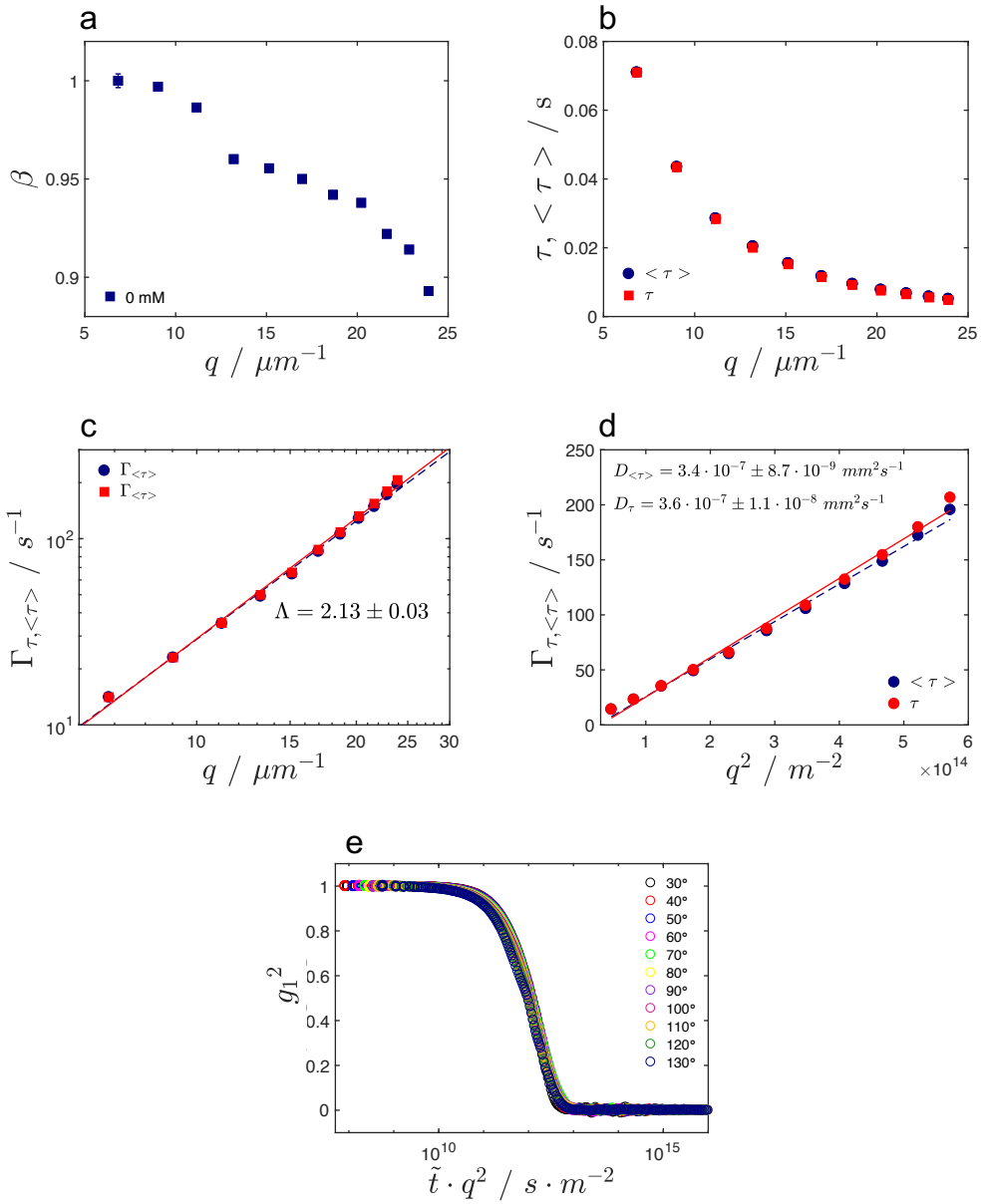

Figure 3.4: (a) β parameter from KWW fitting function for ${g_1}^2$ vs. $\tilde{t}$ collected at different q. (b) τ values from KWW fit function and $< \tau >$ from $(\tau/\beta)\tilde{\Gamma}(\beta^{-1})$ vs. q. (c) Double-logarithm plot of Γ from τ and $< \tau >$ vs. q and linear fit; the angular coefficient Λ (power law in linear plot) of the fit is shown as well. (d) Linear plot of Γ from τ and $< \tau >$ vs. q^2, with corresponding D values given. **e**. ${g_1}^2$ vs. $\tilde{t} \cdot q^2$ at collected at different q.

${g_1}^2$ versus $\tilde{t}$ data do not show a clear indication of secondary $< \tau >$ components. Nevertheless, for this sample, $qR_h > 1$ and thus it was decided to try to describe the ${g_1}^2$ traces with a double exponential function, but very similar $< \tau >$ values yielded a Λ exponent (via Γ vs. q plots) value ≈ 2. Hence, the net separation of translational diffusion from internal relaxation was not possible. Thus, since both $< \tau >_F$ and $< \tau >_S$ showed similar values, a dominance of diffusive-like behaviour was assumed.

With the aim of decoupling global dynamics from the individual translational diffusion coefficients of the polymer molecules, *i.e.*, $qR_h < 1$, it was decided to dilute samples to several lower concentrations, *i.e.*, 0.1, 0.08, 0.05 and 0.02 *wt.* %. Results are shown in Fig.3.5 as Γ vs. q^2. The straight line fits highlight the linearity between Γ and q^2 for the $[LMP] = 0.02$ *wt.* %. This is confirmed by the inset of the plot, where the double logarithm Γ vs. q plot shows $\Lambda \approx 2$. For this $[LMP]$, the R_h was calculated to be 0.55 ± 0.08 μm, in the qR_h >1 limit. By increasing the $[LMP]$ to $= 0.1$ *wt.* % , Γ vs. q^2 deviates from linearity, indicating non-diffusive behaviour. Again, this is confirmed by $\Lambda = 2.6$ for 0.1 *wt.* % $[LMP]$. The gradual increase towards q^3 behaviour may indicate possible hydrodynamic interactions. Once again, ${g_1}^2$ versus $\tilde{t}$ data did not have clear indications of more than one relaxation processes.

A common procedure used to characterize LMP via light scattering is to filter the samples, thus removing impurities and/or undissolved material [79][80][85][87]. However, this should be undertaken with caution, since it is also possible to lose part of the sample: knowledge of the length scales in the sample a priori and the selection of the correct filters pore-size according to these length scales is crucial. According to the literature [87], LMP solutions are frequently filtered through systems with a 0.2 μm cut-off before light scattering analysis. This was performed for $[LMP] \leq 0.5$ *wt.* % , and the overall scattered intensity decreased but the signal became more susceptible to dust, *i.e.*, contamination. For filtered $[LMP]$= 0.08 *wt.* % , Γ vs. q^2 plot gives $\Lambda \approx 2$, and $R_h = 0.44 \pm 0.05$ μm. This value is of the same order of magnitude as that determined for the non-filtered $[LMP] = 0.02$ *wt.* % , for which $R_h = 0.55 \pm 0.08$ μm. Finally, for filtered $[LMP] = 0.1$ *wt.* %, $\Lambda > 2$, indicating a contribution from internal relaxations. Thus, according to these results, filtration of the sample affects the dynamical

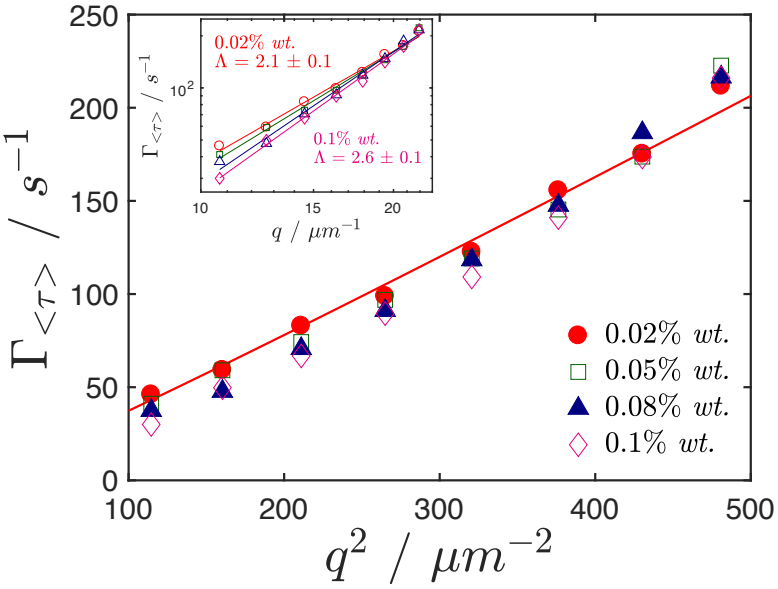

Figure 3.5: Main Figure: Γ vs. q^2 data for samples with different $[LMP]$. The red fit line indicates the linearity for $[LMP] = 0.02$ % *wt.*. Inset: Γ vs. q for the same $[LMP]$; fit lines and relative Λ values are displayed as well.

properties of the pectin solution. Therefore this was not considered a helpful or reliable procedure for future work, since the effects will obviously be highly dependent on $[LMP]$ and the filter pore-size. Furthermore, this would have meant that pectin solutions differ from commercial LMP that are normally used in real products.

As previously seen in Figs.3.4(c) and (d), unfiltered $[LMP] = 0.5$ *wt.* %, yielded a $\Lambda \approx 2$, *i.e.*, diffusive behaviour. This aspect may be contradictory to the above results on filtered pectin, as one expects a $\Lambda > 2$. On the other hand, this aspect is consistent with 0.5 *wt.* % being close to C^* determined via viscometry earlier. Chain overlapping may create an ensemble of chains that diffuse as a single object. In fact, this explains why R_h is larger than the one calculated for $[LMP] = 0.02$ *wt.* %.

Fig.3.6(a) shows ${g_1}^2$ vs. $\tilde{t}$ data for $[LMP] = 0.5\%$ *wt.* dissolved in 60% *wt.* fructose solution. As shown, ${g_1}^2$ decays at larger $\tilde{t}$ than for water solutions due to the η contribution of the medium. Additionally, the ${g_1}^2$ function shows a fast relaxation mode at $\tilde{t} \approx 10^{-5}$ s, as shown in the inset of 3.6(a). Even though this makes a new contribution to the overall decay, the small time scale contribution does not affect the overall $< \tau >$ of the sample. However, it was decided to investigate its origin. Due to the small amplitude of this fast relaxation mode ($< \tau >_F$), a double KWW fit was not easily achievable. Hence, the ${g_1}^2$ vs. $\tilde{t}$ data were divided into two sections: (a) from 10^{-8} to 10^{-4} s and (ii) from 10^{-4} to 10^2 s and each were fit using a single KWW function. Fig.3.6(b) shows a plot of ${g_1}^2$ versus $\tilde{t}$ data collected at different θ for the sample under investigation. For clarity, the fit lines describing the fast mode have been omitted.

In Fig.3.6(c), $< \tau >$ fit parameters are represented as Γ vs. q. Both fast and slow mode show a diffusive-like character, with $\Lambda \approx 2$. For the slow mode, a R_h value (an indication of a length scale) was calculated using the Stokes-Einstein relation, yielding a value of 1.03 ± 0.04 μm (for 60 *wt.* % fructose at 25°C, $\eta =$ 0.034 Pa s). On the other hand, the R_h value calculated for the fast mode yielded $R_h = 41 \pm 0.9$ Å (see next section). As reported in literature this relaxation is usually attributed to the solvent relaxation, whenever the solvent molecules are big enough [88] . The effect has been seen in HMP solutions in presence of high concentrations of sucrose [85]. This aspect will be discussed later (3.2.1 section).

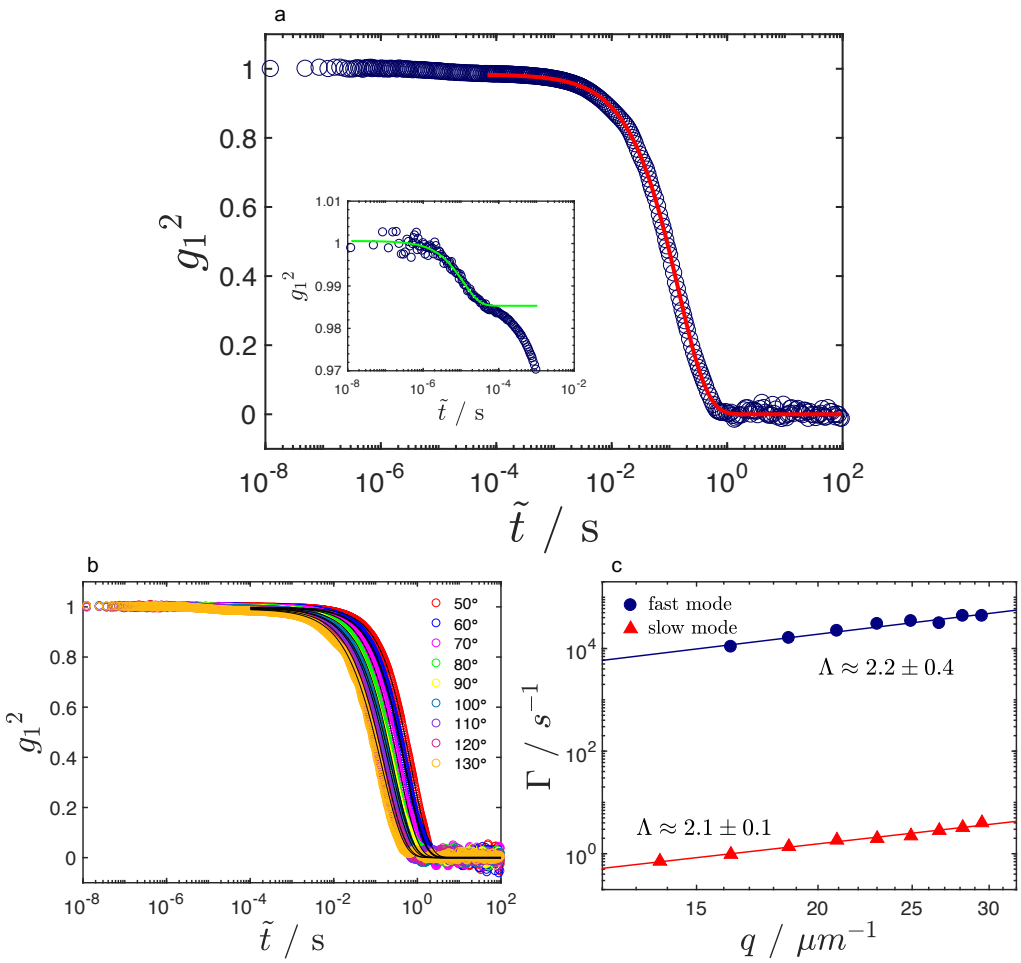

Figure 3.6: $[LMP] = 0.5$ % *wt.* dissolved in fructose solution. (a) Main. ${g_1}^2$ vs. $\tilde{t}$ at $\theta = 90°$ and relative KWW fit line for the slow mode. Inset. Same sample and fit for the fast mode. (b) q dependence of ${g_1}^2$ vs. $\tilde{t}$ and fit lines for the slow mode. (c) Γ vs. q for the both fast and slow modes, with relative Λ values.

The *DLS* results suggest relatively large hydrodynamic length scales for $[LMP]$= 0.5% *wt.*, *i.e.*, 0.72 μm in water and 1.03 μm in fructose solutions. Moreover, the $[LMP]$ in the vicinity of C^*, increases the possibility of chain-chain interactions, suggesting the formation of an entangled molecules that diffuse through the medium.

3.2.1 Solvent relaxation

At high concentrations, sugar solutions (*e.g.*, glucose, fructose, maltose, *etc.*) form a continuous hydrogen-bonded carbohydrate network [44] [89] [90].

As stated in the previous section, a low-amplitude fast relaxation mode at $\tilde{t} \approx 10^{-5}$ s for the *WF* sample at $[LMP] = 0.5$ *wt.* % showed a $\Gamma \propto q^2$ dependence, *i.e.*, diffusive character. This fast mode is related to the so-called 'solvent relaxation' [85]. With this in mind, one can ask the question: what is the behaviour of relaxation modes of the pure solvent at higher lag times? To attempt to answer this question,a q-dependent *DLS* analysis of the 60 *wt.* % fructose solution was performed. ${g_1}^2$ vs. $\tilde{t}$ data acquired from this analysis are shown in Fig.3.7.

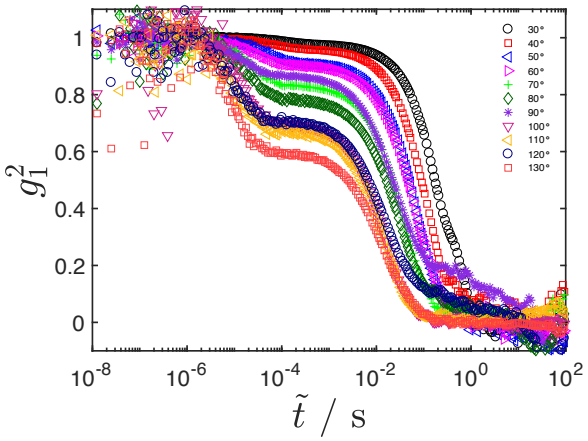

Figure 3.7: ${g_1}^2$ vs. $\tilde{t}$ for 60 *wt.* % fructose, collected at different θ.

At higher q values, the fast relaxation mode has a larger amplitude and so a clear double-relaxation process is clearer over the entire ${g_1}^2$ dataset. These results

are in accordance with DLS studies performed by Sidebottom *et. al.* [89] [44], in which the relaxation modes of sugar solutions (*i.e.*, glucose, maltose, sucrose) were investigated at different concentrations and temperatures. Although these relaxation modes show universality in the studied sugar solutions, there have been no comparable investigations concerning fructose solutions specifically.

In this section, the data obtained to try to explain the complex relaxation mechanisms involved in fructose solutions at different concentrations and temperatures will be presented, with specific focus on the behaviour of the solvent relaxation in samples with and without the addition of LMP.

Recalling Fig.3.6(b), for $[LMP] = 0.5$ *wt.* % dispersed in fructose solutions, the $< \tau >_F$ values obtained corresponded to relatively small amplitudes (*i.e.*, $\approx$ 0.06), indicating suppression of the fast mode when the polymer is added to the solution. Similarly, $< \tau >_S$ values obtained in the presence of LMP show different behaviour than those obtained from analysis of the the pure solvent using DLS. Figs.3.8 show combined Γ vs. q data for both fast and slow relaxation modes, in the presence and absence of LMP.

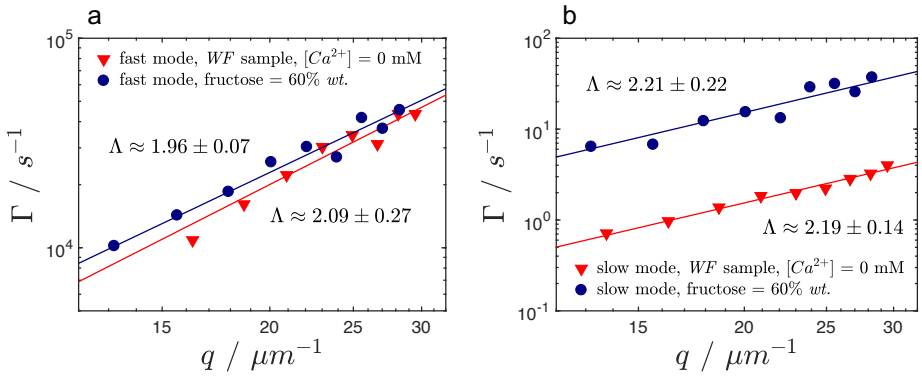

Figure 3.8: Γ vs. q plots for 60 *wt.* % fructose solutions and WF samples. (a) and (b) show fast and slow relaxation modes, respectively.

Fig.3.8(a) shows Γ versus q data for the fast mode observed in samples with and without the addition of LMP. Within the error, both sets of data show q^2 dependence (moreover, Γ has similar values, indicating similar relaxation timescales $\Gamma =< \tau >^{-1}$). In panel (b) of Fig.3.8, Γ versus q data obtained for the

observed slow mode in both systems are shown and display a q^2 dependence. As shown, the presence of LMP decreases the decay rate Γ by approximately one decade, indicating slower relaxation decay rates.

The q^2 dependence for both Γ obtained from $< \tau >_F$ and $< \tau >_S$ allowed the determination of D, via Γ vs. q^2 plots. For the fast mode, $D = 5.5{\cdot}10^{-11}$ $\pm$ $3.8{\cdot}10^{-12}$ m^2 s^{-1} and for the slow mode $D = 5.4{\cdot}10^{-14}$ $\pm$ $4.9{\cdot}10^{-15}$ m^2 s^{-1}. The D coefficient obtained from the $< \tau >_F$ is similar to values for D coefficients obtained at similar fructose concentrations via NMR studies [43]. From Stokes-Einstein relation, R_h was calculated as 45 ± 1.7 Å, much larger than an individual fructose or water molecule. This value also shows agreement with the size ranges obtained from DLS studies of glucose at similar concentrations [89], and provides additional evidences for clusters of sugar molecules, hold together presumably by hydrogen bonds [91].

On the other hand, the D coefficient corresponding to the slow mode was not physically attributed to any particular species: $R_h = 5.4 \pm 2\ \mu m$. This size is much larger than the R_h value obtained for the LMP in fructose solutions. Referring to Sidebottom *et al.* , the typically observed hydrodynamic length scale of the slow mode is around ≈ 100 nm. Such length scales were attributed to hydrodynamic interactions between sugar clusters that diffuse through the media (*i.e.*, water).

To conclude, it has been observed that: (i) the fast mode may indicate the presence of fructose clusters, whether LMP is absent or present; (ii) The slow mode observed in samples containing LMP is mostly driven the presence of the polymer. In this case, a decoupling between both the fructose and LMP relaxation contributions was not possible. It would be interesting to perform complimentary experiments by adopting (i) a different sample preparation procedure, *i.e.*, filtering different fructose solutions at different concentrations in order to obtain clear data for $< \tau >_S$; (ii) adding various $[LMP]$ to the fructose solution to observe how the relaxation changes. The cluster-cluster interactions in fructose solutions may vary when the polymer is added to the solution.

3.3 Static light scattering characterization of LMP solutions

Static light scattering was used to investigate the static properties of the polymer, such as the static length scale (for simplicity called radius of gyration R_g) and correlation lengths (ξ), as the measure of the average distance between different scattered objects [92]. All the scattered intensities obtained were renormalized for background solvent and the experimental setup and are presented as the excess Rayleigh ratio ($\Re_{ex}$) (as explained in section 1.3.1).

Fig.3.9(a) shows the $\Re_{ex}$ vs. q data obtained for LMP solutions dissolved in water and $[LMP]$ = 0.5, 0.1, 0.08, 0.05 and 0.02 *wt.* %. As shown, for all the $[LMP]$, $\Re_{ex}$ exhibits q dependence, indicating the presence of a structure. Generally, the plot can be split in two parts: (i) at low q, $\Re_{ex}$ levels off as a plateau, indicating the overall length scale of the scattered object; (ii) at large q, $\Re_{ex}$ assumes an approximate power law behaviour which can be parametrised as $\Re_{ex} = q^{-df}$ where df is the power law exponent. This parameter is related to polymer solvation and conformational state, as discussed in section 1.2.1. Finally, increased $[LMP]$ corresponds to an increase in the overall magnitude of $\Re_{ex}$, as typical for polymer solutions [93].

For $[LMP]$= 0.02 *wt.* %, the $\Re_{ex}$ data at large q (*i.e.*, between $q \approx 10$ and 25 μm^{-1}) shows $df \approx 2.6$, suggesting the presence of branched regions (typical in LMP) and/or aggregation. At smaller q, the $\Re_{ex}$ data levels off, yielding a plateau-like shape. The Guinier approximation (see section 1.3.1) was tested in this region of data to determine R_g but the results yielded not certain values due to the limit $qR_q > 1$. However, the shape of the $\Re_{ex}$ data at low q suggests that a Guinier regime at q values lower than the range of the light scattering set-up may be present. Hence, one expects bigger length scales which cannot be detected with this instrument.

$[LMP]$ = 0.05 *wt.* % resembles the previous sample (0.02 *wt.* %). In this case, df = 2.5. At higher $[LMP]$, *i.e.*, 0.08 and 0.1 *wt.* %, the magnitude of $\Re_{ex}$ increases and the q dependence is persistent across the probed q range. The extended df over the probed q range indicates the presence of a continuous structure, justified by the concentration close to C^* (the extended fit lines in

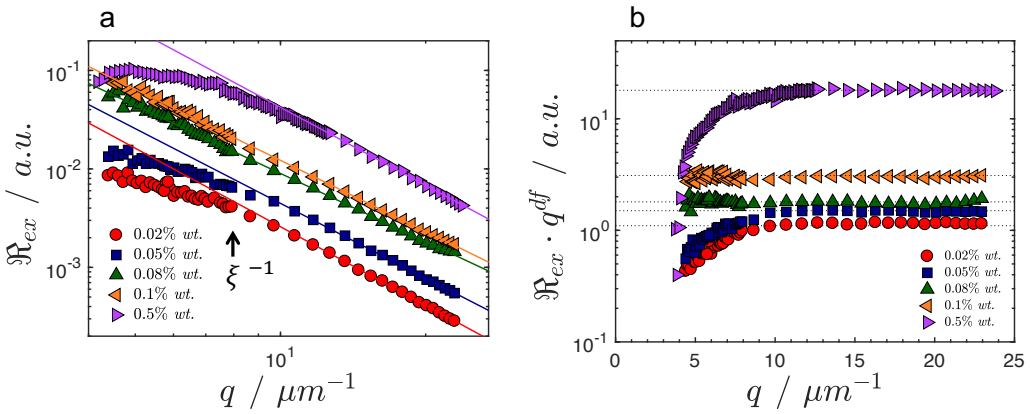

Figure 3.9: (a) $\Re_{ex}$ vs. q for different $[LMP]$ dissolved in water. Fit lines for df determination are shown as well. (b) $\Re_{ex} \cdot q^{df}$ vs. q plots for the ξ parameter extrapolation. Dashed lines as a guide for the plateaus at large q.

Fig.3.9(a), used for the determination of df, aid one to follow this trend). Finally at $[LMP] = 0.5$ *wt.* % , at large q, $df = 2.60$. However, at small q, $\Re_{ex}$ levels off as a plateau, similar to $[LMP]$= 0.02 *wt.* %. These aspects reflect the DLS studies presented in section 3.2 in fact, $[LMP]$ from 0.02 to 0.1 *wt.* %, Λ increases from $\approx$ 2 to 2.6, *i.e.*, from global molecular dynamics to enhanced hydrodynamic interactions (Fig.3.3). However, at $[LMP]$= 0.5 *wt.* % , the sample showed diffusive behaviour. Therefore, both SLS and DLS results suggest formation of an ensemble of chains, with a characteristic length scale, that diffuses through the medium.

The point where the intensity diverges from plateau to power law regime, is referred to the correlation length (ξ). To facilitate the reading of ξ, $\Re_{ex} \cdot q^{df}$ vs. q plots were utilised. The plot, is shown in Fig.3.9(b). From large to small q, $I(q)$ assumes a q dependence, where the diverging point corresponds approximately to ξ^{-1}. Hence, for (i) $[LMP] = 0.02$ and 0.05 *wt.* %, $\xi \approx 0.1$ μm; (ii) $[LMP] =$ 0.08 and 0.1 *wt.* % , no divergence was observed, *i.e.*, $\Re_{ex} \cdot q^{df} \approx 2$ and 3 *a.u.*, respectively; (iii) $[LMP] = 0.5$ *wt.* % $\xi \approx 0.08$ μm.

To conclude, the main differences for these samples are in the shape of $\Re_{ex}$ at low q. df appears constant for all the tested $[LMP]$ and ξ shows very similar values for $[LMP] = 0.02$ and 0.5 % *wt.*

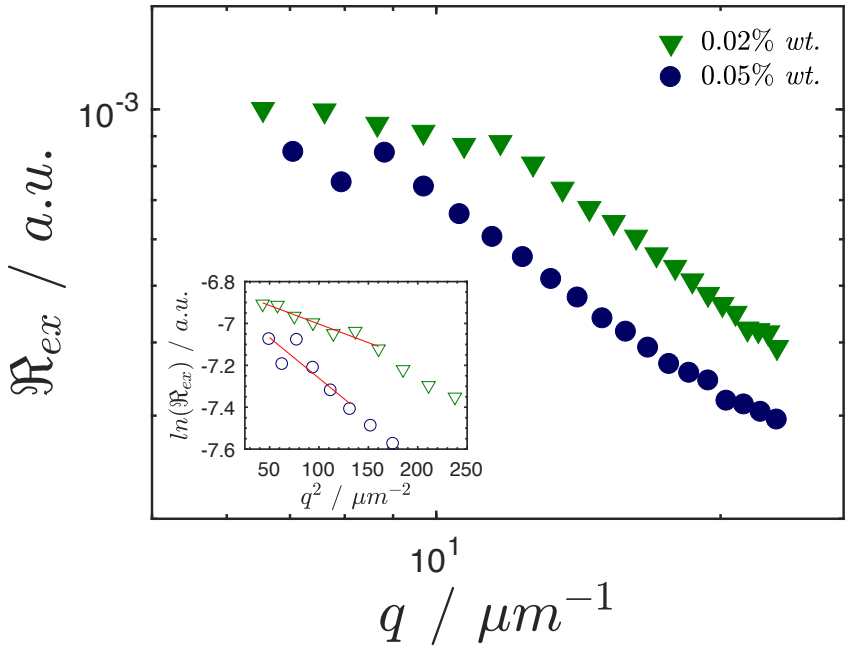

Figure 3.10: Main. $\Re_{ex}$ vs. q plots for 0.2 μm filtered $[LMP] = 0.08$ and 0.1 % *wt.* samples. Inset. Guinier plots and fit lines for the determination of R_g for the same samples.

Filtered $[LMP]$ solutions were also investigated. Once again, $[LMP] \leq 0.05$ % *wt.* samples were weakly scattered giving noisy data, that was not analysed further. Main figure Fig.3.10 shows $\Re_{ex}$ vs. q data obtained for $[LMP] = 0.08$ and 0.1 *wt.* % The overall scattered intensity appears lower than that obtained for unfiltered samples (Fig.3.9(a)), even though the q dependence of the data indicates structural behaviour of LMP in solution. In the larger q range, a $df \approx 1.2$, suggesting less aggregated structures. In this case, at low q, $\Re_{ex}$ levels off. The inset of Fig.3.10 shows Guinier plots for these two $[LMP]$ and relative fit lines. Here, $R_g = 0.07 \pm 0.01$ μm and 0.11 ± 0.03 μm for $[LMP] = 0.08$ and 0.1 *wt.* % , respectively. In both cases, $qR_g < 1$. For these types of systems, further investigations may be performed via size exclusion chromatography coupled with multi angle light scattering devices. These devices are able to separate different species in the sample and analyse them separately with the LS device.

Fig.3.11 shows LMP dispersed in fructose solutions, $[LMP] = 0.5$ *wt.* %, tested and compared with the same $[LMP]$ dispersed in water. In the presence of fructose, the overall $\Re$ is shifted towards higher q values due to refractive index of the solvent. At larger q, $df = 2.3$, whereas at lower q, $\Re$ shows a minimal curvature suggesting, again, flattening at smaller q. Inset of Fig.3.11 shows $\Re_{ex} \cdot q^{df}$ vs. q plot for both LMP samples dispersed in fructose and water. For fructose LMP solutions, $\xi \approx 0.06$ μm. The slightly smaller ξ value may be attributed to the presence of fructose, which reduces the free water in the system, "dehydrating" the pectin and promoting closer association of the LMP chains.

The SLS results suggest the presence of structures with large length scales, which cannot be probed properly with q range employed. For this reason $SALS$ was employed to investigate selected systems further.

3.4 Small angle light scattering (SALS) characterization of LMP solutions

Small angle light scattering ($SALS$) was used to investigate $[LMP] = 0.5$ *wt.* % in water and fructose solution. The $I(q)$ vs. q data obtained from these

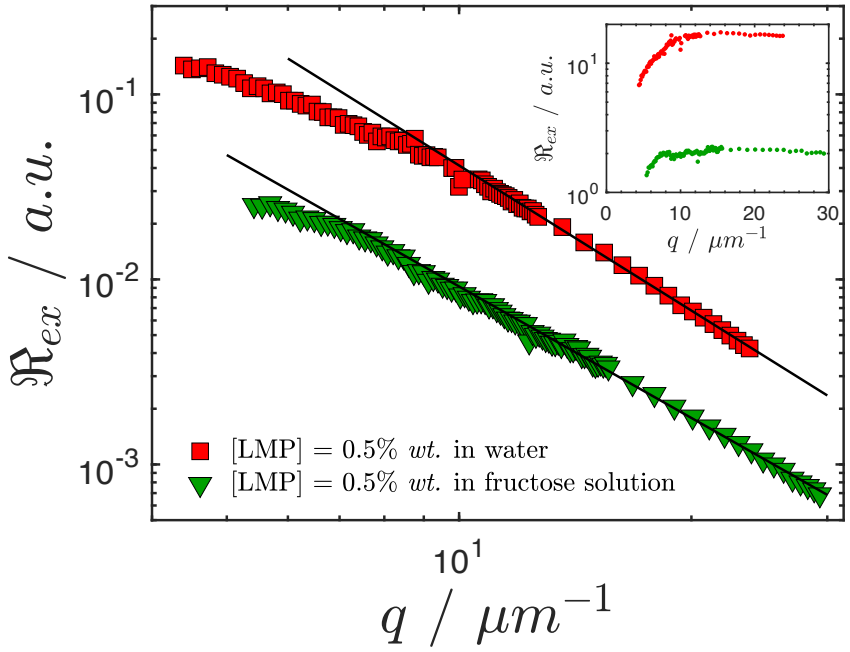

Figure 3.11: Main. $\Re_{ex}$ vs. q plots for $[LMP] = 0.5$ *wt.* % dissolved in water (red squares) and fructose solution (green triangles). Fit lines for *df* determination are displayed as well. Elongation of the fit line as a eye guide for the $\Re_{ex}$ bend at low q. Inset. Same samples plotted as $\Re_{ex} \cdot q^{df}$ vs. q for ξ determination.

experiments are shown in Fig.3.12. $I(q)$ shows typical behaviour where (i) at low q the $I(q)$ plateaus and (ii) $I(q)$ at large q decays as a power-law. As discussed in the SLS section, the presence of the levelling towards low q values represents the crossover between the distinct scattered object and the internal structure [75]. Due to the q limit of the plateau, this effect may refer to the presence of large aggregates/polymers length scales at the supramolecular level that coexist with smaller ones [75].

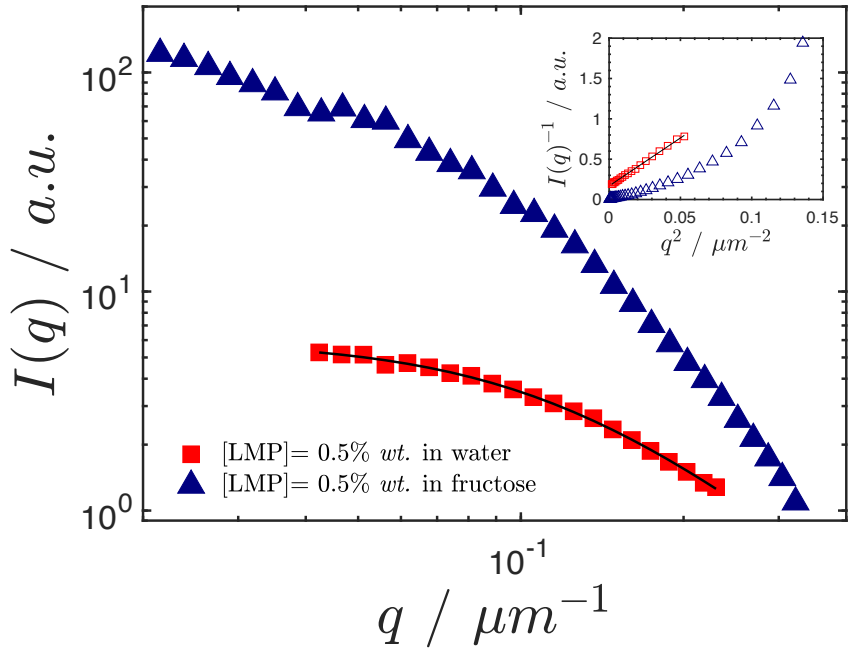

Figure 3.12: Main plot. $I(q)$ vs. q for $[LMP] = 0.5$ *wt.* % dissolved in water (red squares) and fructose solution (blue triangles). Fit line in the sample dissolved in water refers to the Ornstein-Zernicke model. Inset. Zimm plots as $I(q)^{-1}$ vs. q^2 for the same samples.

In the probed q range, length scales were estimated via the Guinier plots and yielded values of (i) 12 ± 0.07 μm for LMP in water and (ii) 27 ± 0.01 μm for LMP in 60 *wt.* % fructose. In both cases, $qR_g < 1$. The larger R_g value obtained for the fructose solution and the dramatic increase of $I_{q\to 0}$ suggests aggregation

effects at the supramolecular level, due to the reduced free water of samples of $[LMP]$ dispersed in fructose solution. As previously discussed in section 3.3, the asymptotic region assumes a power law behaviour with exponent df related to polymer solvation and conformational state [13] [75]. For the samples tested in this work (Fig. 3.12), this regime is rather short and so, it is difficult to attribute the df value to a fractal regime.

However, assuming the validity of the df value obtained from the fit of the data, one can use this parameter to estimate the compactness of the domains affected by the presence and concentration of Ca^{2+}, *i.e.*, a steeper power law corresponds to more compact domains [76]. Fig.3.13 show a hypothetical fit used for the determination of the power law fit. In other words, the fit started from the last point of $I(q)$ and continues until the $I(q)$ deviates from the linearity (red arrow in Fig.3.13). The point of deviation is taken as when the data (within the error) lies off the straight line.

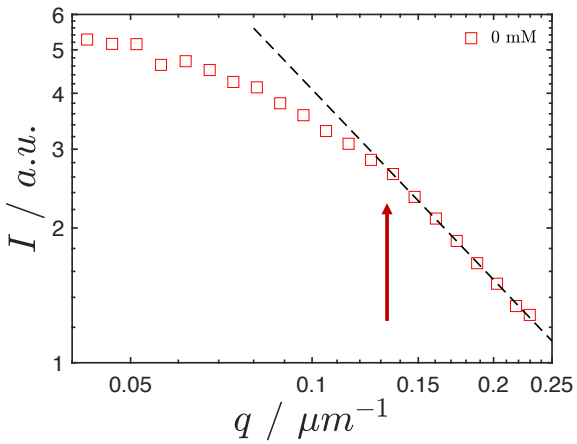

Figure 3.13: $I(q)$ vs. q for W samples with $[Ca^{2+}] = 0$ mM. The power law fit for df determination extends up to the $I(q)$ deviation from linearity, as indicated by the arrow.

Hence, $df \approx 1.4$ and ≈ 4.3 for $[LMP]$ in water and fructose solutions were obtained, respectively. The smaller df value for LMP in water, accompanied by the broader change of $I(q)$, suggests a broad distribution of structures, that coexist with smaller ones [75]. Vice-versa for LMP dispersed in fructose.

The inset of Fig.3.12 shows the Zimm plots, *i.e.*, $I(q)^{-1}$ vs. q^2, also suggesting aggregation effects for LMP in fructose solutions. Even though the $I(q)^{-1}$ data for LMP in water has a relatively narrow range, it appears as a straight line. In this condition, the correlation length was estimated with the Ornstein-Zernicke (OZ) relation,

$$I(q) = \frac{I(0)}{(1 + q^2\xi^2)} \tag{3.7}$$

where $I(0)$ is the $I(q)$ at $q = 0$. For the polymer solution in water, ξ = 8.4 $\pm$ 0.1 μm (fit lines in main and inset of the figure). In contrast, the LMP in fructose solution shows non-linear dependence, suggesting aggregate formation. In this case, ξ was estimated via the $I(q) \cdot q^{df}$ versus q plot, yielding a value of $\approx$ 3.5 μm. It should be noted that the same method of determination of ξ for LMP in water yielded a value of $\xi \approx 7.2$ μm, similar to the one obtained via the OZ relation.

Cryo-SEM imaging

To verify the R_g values obtained in $SALS$, *i.e.*, the presence of such larger structures compared to the conventionally accepted dimensions of LMP molecules ($\approx$ 160-180 nm) [85], cryo-SEM imaging was performed on the sample. Fig.3.14(a) apparently shows a linear LMP chain and relative short side chains (branched regions). According to the scale, the chain depicted is $\approx$ 4 μm long. However, as indicated by the arrows, the chain length seems to elongate underneath the ice mass. In Fig.3.14(b) one can apparently see branched regions of LMP that extend over larger scales (red arrows highlight the chains). It should be noted that the apparent thickness of the main chain, indicated by the yellow arrow, results from an artefact of the freezing and/or fracture of the sample during its preparation.

The cryo-SEM micrographs thus seem to provide additional evidence for the presence of at least some structures with the length scales suggested in the $SALS$ experiments. For this reason, cryo-TEM was also attempted in order to obtain higher resolution images of the samples. Unfortunately, for unknown reasons, the experiment was unsuccessful, *i.e.*, thick layers of ice prevented image acquisition.

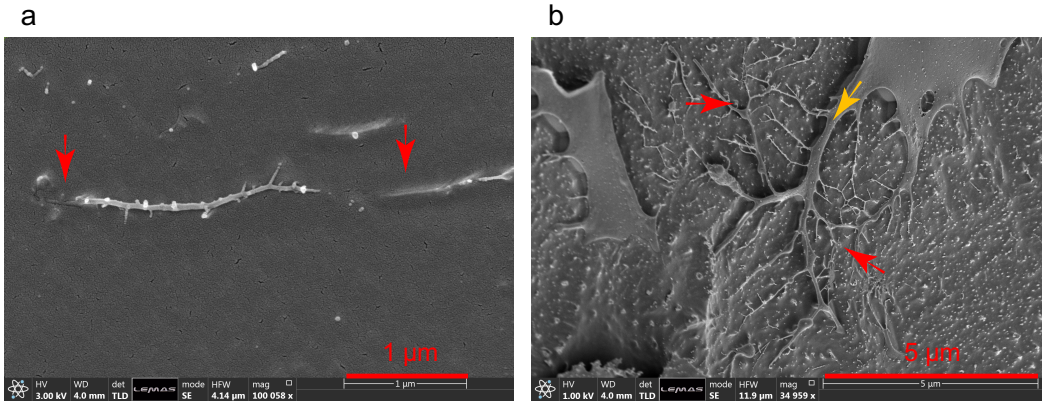

Figure 3.14: Cryo-SEM micrographs for $[LMP] = 0.5$ *wt.* % dissolved in water. 1 and 5 μm scales are showed in (a) and (b), respectively. Red arrows indicate the polymer chains and yellow arrow indicates possible artefacts during sample's fracturing.

According to the $I(q)$ data at large q obtained in $SALS$ experiments and the $\Re_{ex}$ data at lower q obtained in SLS experiments, the total intensity does not appear to scale linearly. This aspect will be explained in detail in Chapter 3. At present, one can confirm the presence of two large length scales (aggregates or polymer chains) coexisting with smaller ones. This fact complicates the LMP characterization and the interpretation of the behaviour of LMP in solution. Undoubtedly, this characteristic may also effect LMP gel formation in the presence of Ca^{2+} ions.

3.5 Conclusions

In this Chapter, detailed LMP characterization in both water and fructose solution was performed via a variety of techniques. Rheological characterization and M_w values seem to agree with typical values obtained for citrus LMP, *i.e.*, $<$ 100 kDa. Both DLS and SLS data in the q range between $\approx$ 5 to 25 μm^{-1} did not show distinct sizes for either R_h and R_g. The q dependence for both DLS and SLS indicates a clear structure of the systems in absence of cross-linking agents. This structure-like may be related to a variety of factors such as the: (i) proximity to C^*, (ii) absence of screening agents (*e.g.*, Na^+) and therefore

poor solvent conditions and (iii) absence of ultra-fine processing of LMP (*e.g.*, removal of side chains, impurities). At ultra-low q ($SALS$), the intensity data clearly indicate the presence of large structures and/or aggregates that are more pronounced when LMP is dissolved in the fructose solution. The length scales for LMP dissolved in water in the ultra-low q range seem to agree to those determined from cryo-SEM micrographs. At large q, probed in $SAXS$ analysis, reliable data were not able to be measured. The various aspects covered in this chapter will be further explored in chapter 3, where a full static study for both sol and gel material will be presented.

Chapter 4

Rheological and DLS characterization of gels with and without fructose

In this chapter gels prepared in water (W) and water+fructose (WF), with different concentrations of Ca^{2+}, will be compared. Particular emphasis will be placed on rheological and dynamic properties obtained via DLS. The first part starts with a brief rheological overview of LMP gels prepared in water (W samples), in terms of structure development *i.e.*, ageing as a function of $[Ca^{2+}]$.

4.1 Cross-link development as a dynamic event

As reported in the Chapter 1, stabilization of junction zones and consequent gel formation of LMP in water is often determined by the stoichiometric ratio between the number of Ca^{2+} and the number of non-methoxylated $GalA$ residues ($R = 2[Ca^{2+}]/[COO^{-}]$) [10][1]. This however, does not take into account many of LMP chemical characteristics, such as, amidation, distribution of pectin's side chains. In addition, complex environmental conditions *e.g.*, the presence of ion-chelators, co-solutes, *etc.* may significantly effect the R value, resulting in higher values (*i.e.* more calcium required). In fact, for $[Ca^{2+}]$ of 6 and 8 mM, the corresponding values of R, calculated from the estimated $M_w \approx 91\ kDa$, are 1.0 and 1.3, respectively. These values are slightly higher than the values obtained,

$R \approx 0.5$, assuming that all the Ca^{2+} are used to stabilize most of the junction zones. Rather than rely on the stoichiometric ratio, it was decided to track a range of $[Ca^{2+}]$ from 0 to 9 mM, to identify the critical concentration at which the sol/gel transition occurs. Moreover, this range of $[Ca^{2+}]$ was suggested by the industrial supervisor.

Fig.4.1(a) shows shear viscosity η results for $\dot{\gamma} = 10\ s^{-1}$ vs. $[Ca^{2+}]$. The values at relatively high $\dot{\gamma}$ were selected due to the experimental limits of the rheometer at low shear rates *i.e.*, this is an unsuitable geometry for such very low viscosity fluids. The panel (a) clearly shows a plateau in η for $[Ca^{2+}]$ between 0 and 4 mM, indicating that the solution behaves as a Newtonian fluid because there are insufficient Ca^{2+} to cross-link pectin molecules.

At $[Ca^{2+}] = 5$ and 6 mM, η increases in magnitude. The increase in viscosity is a consequence of junction zone stabilization mediated by Ca^{2+} addition. The inset of Fig.4.1(a) shows η vs. $\dot{\gamma}$ results for $[Ca^{2+}] = 6$ mM. The observed shear thinning corresponds to the breaking of the junction zones, initiating flow followed by a progressive breaking of local junction zones as $\dot{\gamma}$ increases.

Fig.4.1(b) shows $\bar{\tau}$ vs. $\dot{\gamma}$ plots for $[Ca^{2+}] = 5$ and 6 mM samples. As shown in the main plot, the shear stress data increase linearly with $\dot{\gamma}$ for both samples, suggesting Newtonian behaviour. The inset of panel (b) shows the same data but in a $\dot{\gamma}$ range between 0 and 0.3 s^{-1}. Here, for $[Ca^{2+}] = 6$ mM, a steep increase in slope in the range $\dot{\gamma} \approx 0.02$ - $0.1\ s^{-1}$, flattening off at $\dot{\gamma}$ is observed. The inflection point indicates where the corresponding shear stresses overcome the internal forces of the material and cause it to flow [59]. Thus, the W sample at $[Ca^{2+}] = 6\ mM$ was just about stabilized by a sufficient number of cross-links so that structure development was observed after 1 hour.

Thus, the $[Ca^{2+}]$ necessary to stabilize a reasonable density of junction zones, is believed to occur in $[Ca^{2+}]$ between 5 and 6 mM. However, time-dependent η measurements at relatively high $\dot{\gamma}$ (10 s^{-1}), displayed the effect of low $[Ca^{2+}]$ added to LMP (tests performed immediately after sample preparation). Fig.4.1(c) shows the $\eta_{\dot{\gamma}=10s^{-1}}$ vs. time (t) (0 to 60 min) for $[Ca^{2+}]$ between 0 and 6 mM. The black dashed line shows the constant η ($\approx 3{\cdot}10^{-3}$ Pa s) observed for $[Ca^{2+}]$ between 0 and 3 mM. In this plot: (i) increasing the $[Ca^{2+}]$ results in a step-like

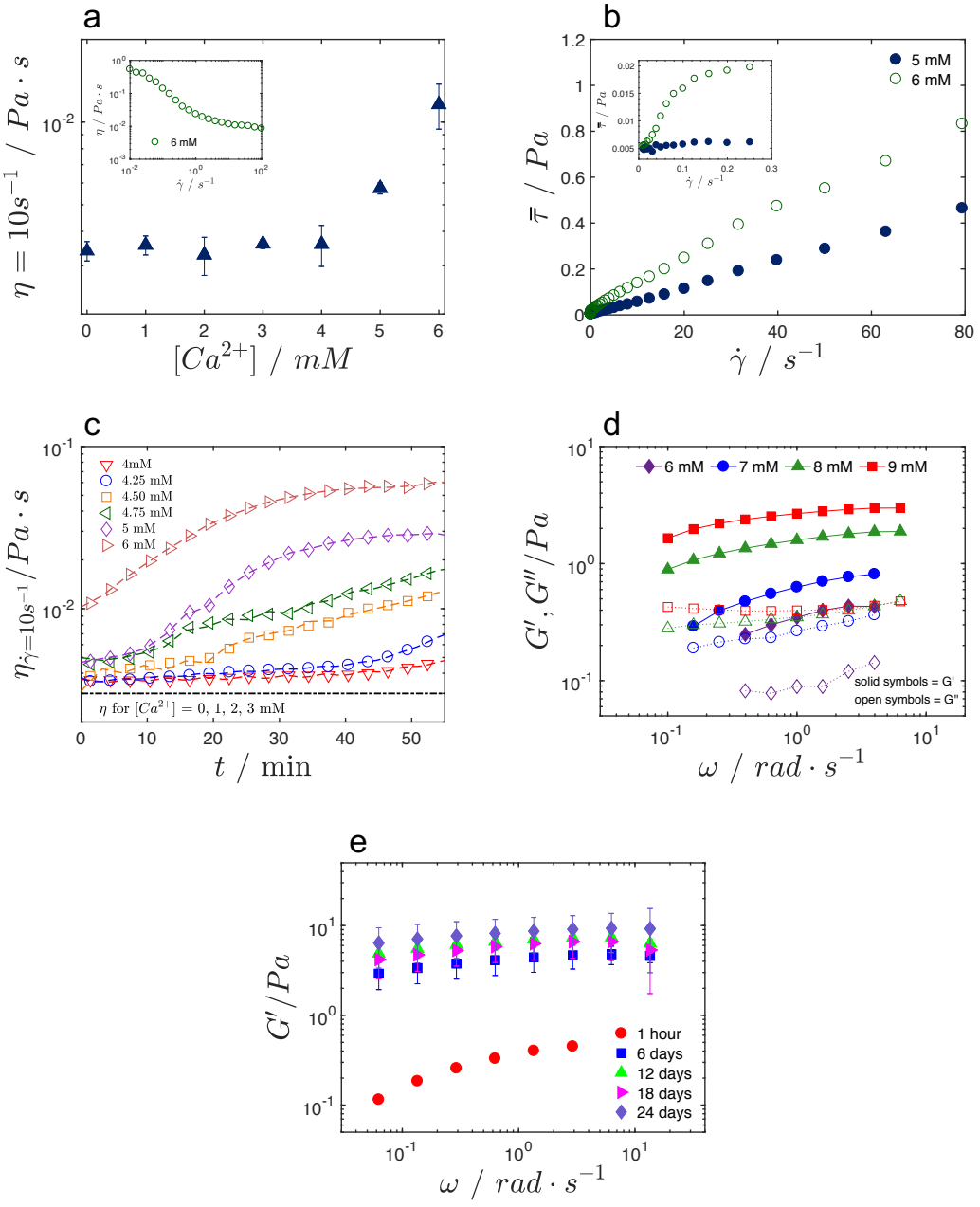

Figure 4.1: (a) η at 10 $\dot{\gamma}$ s^{-1} from shear tests of LMP in water and $[Ca^{2+}]$ from 0 to 6 mM. The inset shows the η vs. $\dot{\gamma}$ for W sample at $[Ca^{2+}] = 6$ mM. (b) $\bar{\tau}$ vs. $\dot{\gamma}$ for $[Ca^{2+}] = 5$ and 6 mM; the inset highlights the $\dot{\gamma}$ range between 0 and 0.3 s^{-1}. (c) η values at $\dot{\gamma} = 10$ s^{-1} vs. time for samples with $[Ca^{2+}]$ from 4 and 6 mM; dashed line denotes the averaged $\eta_{\dot{\gamma}=10s^{-1}}$ values in a $0 \leq [Ca^{2+}] \leq 3$ mM. (d) Frequency sweep tests, $G^{'}$ and $G^{''}$ vs. ω for $[Ca^{2+}]$ from 6 to 9 mM, taken 6 days after preparation. (e) $G^{'}$ and $G^{''}$ vs. ω for W sample at $[Ca^{2+}] = 7$ mM taken at 1 hour and 6, 12, 18 and 24 days.

η increase occurs at lower time; (ii) the increase in η at both $t = 0$ and 55 min, rises dramatically as a function of the calcium concentration.

It is important to clarify that the ageing studies here were carried out at relatively high $\dot{\gamma}$ and not under quiescent conditions. Moreover, the shear applied may facilitate Ca^{2+} diffusion throughout the sample and so, stabilize small/minor junction zones, yielding the η increase.

1 hour after preparation, higher concentrations of $[Ca^{2+}]$, *i.e.* 6, 7, 8 and 9 mM visually gave self-supporting structures. These were analysed via oscillatory rheology. Fig.4.1(d) shows the storage ($G^{'}$) and loss ($G^{''}$) moduli measured by frequency sweep tests, with the angular frequency (ω) ranging between 0.1 to 10 rad s^{-1}, at a constant strain $\gamma = 1\%$ (previously determined via strain sweep tests, data not shown). For all four $[Ca^{2+}]$: (i) $G^{'} > G^{''}$ over the tested ω range; (ii) the overall magnitude of $G^{'}$ increases systematically with $[Ca^{2+}]$; (iii) moduli were of low magnitude and showed frequency dependence, which is characteristic of weak gels [45] ; (iv) the terminal relaxation ω shifts towards lower values on increasing the $[Ca^{2+}]$, *i.e.*, the hypothetical $G^{'}$ and $G^{''}$ crossing-over point at low frequencies.

LMP gel formation is a time-dependent event and its rheological characterization has been studied [2] [17][46] in the past. In this study, however, the focus was on the impact of the initial stages of gel formation (*i.e.*, up to $\approx 10^4$ s) and long-term evolution was not analysed. For practical reasons, rather than leaving the sample between the rheometer's plates and tracking the mechanical properties over long periods of time, it was decided to prepare gels, store them at room temperature (T = 20-22 °C) and analyse them at predetermined ageing times. Therefore, the ageing process occurred under static conditions with no stress was applied.

Even though LMP gels are weak physical gels and extremely dynamic *i.e.*, a finite lifetime for reversible cross-links that break and reform continuously [13], the structure evolves to a point where the macro-mechanical variability reaches a stability. In this specific case, Fig.4.1(e) shows the $G^{'}$ responses for frequency sweep test ($\omega \approx 10^{-1} - 10$ rad s^{-1}, $\gamma = 1\%$, $T = 25$°C) of a W sample at $[Ca^{2+}]$ = 7 mM after 1 hour, 6, 12, 18 and 24 days. It seems that $G^{'}$ changed most significantly between the first hour and the sixth day after preparation. For this

reason, all following experiments were analysed after one hour and 6 days after preparation for all the techniques used in this thesis. Clearly, smaller changes occurred over longer time scales (up to at least 24 days in this case) but it was impractical to apply the full range of tests to samples stored for longer than 6 days or so.

4.2 Comparison of the effects of fructose

The previous section illustrated the general behaviour of W samples in terms of (i) $[Ca^{2+}]$ needed to cross the sol/gel transition, (ii) cross-link dependence as a function of $[Ca^{2+}]$ and (iii) the time for arrest and network development. The whole range of WF samples were analysed using same methods and selected samples of both W and WF samples were used to make a comparison between them.

4.2.1 Rheological comparison

Figs.4.2(a) and (b) show strain sweeps (γ= 10^{-2} - 20 % , $\omega = 1$ rad s^{-1}, $T = 25°C$) and frequency sweeps ($\omega \approx 10^{-1} - 10$ rad s^{-1}, $\gamma = 1\%$, T =25°C), respectively, for WF samples at different $[Ca^{2+}]$, performed 1 hour after preparation . Due to the low $G^{'}$ values for solutions with $[Ca^{2+}]$ from 0 to 2 mM, the data are not shown in either plots. Generally, both strain and frequency responses of WF samples showed (i) $G^{'} < G^{''}$ in the $[Ca^{2+}]$ range between 0 and 5 mM and (ii) $G^{'} > G^{''}$ at higher $[Ca^{2+}]$.

Strain sweeps in Fig.4.2(a) show the linear viscoelastic (LVE) regime is in the range 10^{-2} - 20 % for all the $[Ca^{2+}]$. As shown in the figure, at $[Ca^{2+}] = 9$ and 8 mM, $G^{'}$ and $G^{''}$ were no longer in the LVE at $\gamma \approx 10^{1}$ %, whilst at $[Ca^{2+}] =$ 6 and 7 mM were γ independent. The difference in LVE between 6 and 9 mM highlights the gel strengthening at higher $[Ca^{2+}]$.

The frequency dependence in Fig.4.2(b), from the lowest (2 mM) to the highest (9 mM) $[Ca^{2+}]$, show both an increase in magnitude and a decrease in ω-dependence of $G^{'}$. Moreover, $G^{'} < G^{''}$ in the $[Ca^{2+}]$ range between 2 and 5 mM, with a progressive increase of both moduli, indicating the sol/gel transition point.

In the range of $[Ca^{2+}]$ from 6 to 9 mM: (i) $G^{'} > G^{''}$; (ii) moduli are less ω-independent; (iii) $G^{'}$ $G^{''}$ separates. These effects indicate the increase in strength of the gels as a function of $[Ca^{2+}]$.

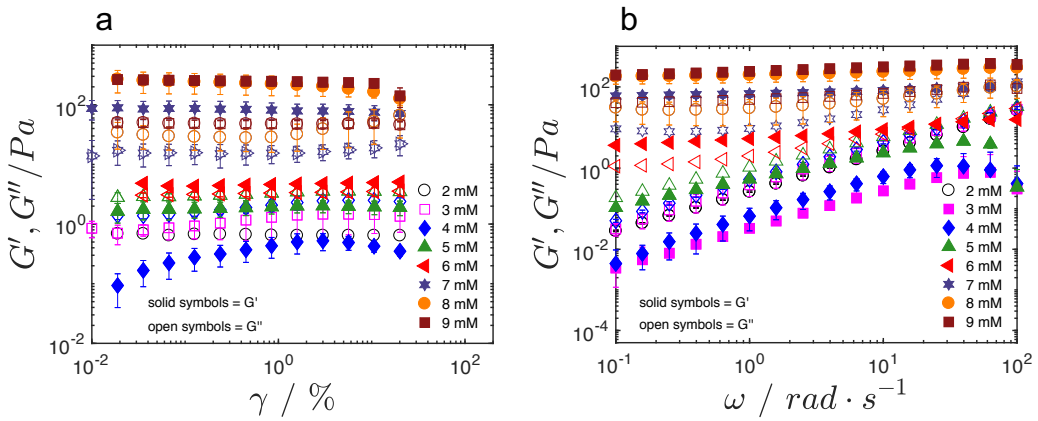

Figure 4.2: (a) Strain sweeps of $G^{'}$ and $G^{''}$ vs. γ for WF samples with $[Ca^{2+}]$ from 2 to 9 mM. (b) $G^{'}$ and $G^{''}$ vs. ω for same samples. In both plots, solid symbols denote $G^{'}$ and, open symbols denote $G^{''}$.

To make a comparison between W and WF samples, it was decided to choose a $[Ca^{2+}]$ close to the sol/gel transition and use the frequency sweep results. Figs.4.3 show the results for both systems comparing ageing times of 1 hour and 6 days after preparation. Error bars have been omitted for clarity. For all the measurements, the standard deviation for $G^{'} \approx 0.1$ Pa and ≈ 0.01 Pa for $G^{''}$.

Figs.4.3(a) and (b) shows the frequency dependence of W systems for a range of $[Ca^{2+}]$ from 6 to 9 mM, taken (a), after 1 hour and (b), after 6 days of preparation. The results show that, moduli increase in magnitude and flatten over 6 days of ageing (*i.e.*, less ω-dependent), indicating the process time-dependent [17] [46] [2].

In Fig.4.3(b), two main differences can be observed: firstly, there is a $G^{'}$ gap for $[Ca^{2+}]$ 6-7 and 8-9 mM; this identifies indicates that $[Ca^{2+}]$ required to get a significant streghtening of W samples. Furthermore, the $G^{'}$ and $G^{''}$ similarity at $[Ca^{2+}] = 8$ and 9 mM probably indicates that the majority of junction zones are stabilized by $[Ca^{2+}] = 8$ mM. Secondly, for $[Ca^{2+}] = 6$ mM, the moduli crossover at ≈ 6 rad s^{-1}. In contrast, higher $[Ca^{2+}]$ did not display this feature over the

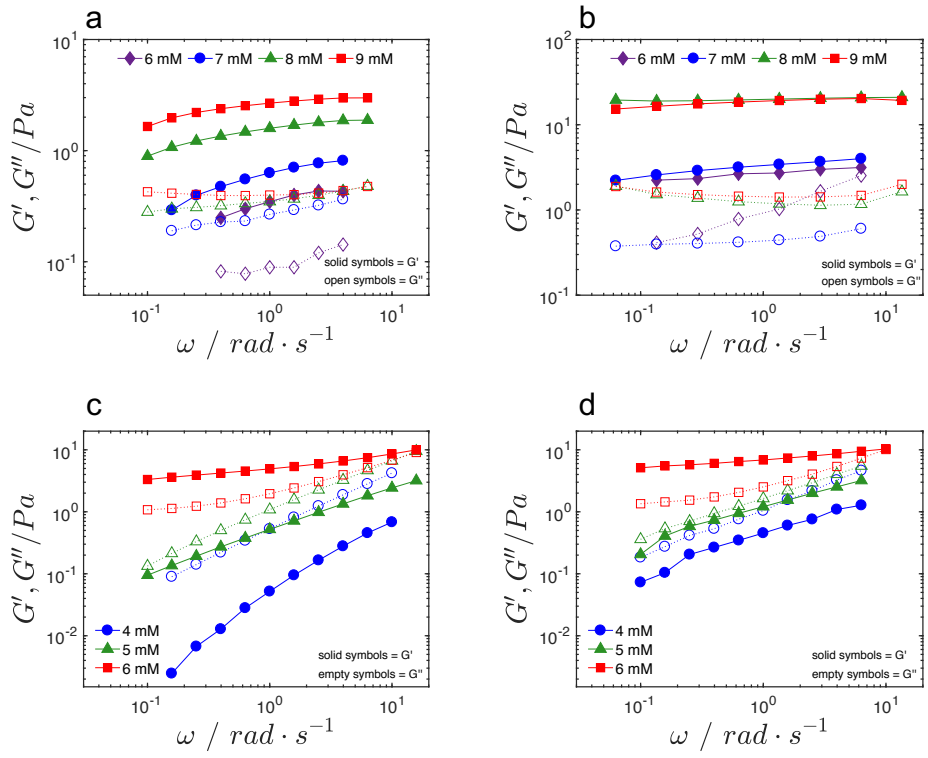

Figure 4.3: (a) and (b) $G^{'}$ and $G^{''}$ vs. ω for W samples at $[Ca^{2+}]$ = 6, 7, 8 and 9 mM measured 1 hour and 6 days after preparation, respectively. (c) and (d). Same frequency sweep test for WF samples at $[Ca^{2+}]$ = 4, 5, 6 mM.

probed ω, *i.e.*, crossing over at higher ω. This indicates the weakness of the sample prepared with $[Ca^{2+}] = 6$ mM.

Figs.4.3(c) and (d) show the frequency dependence of WF samples for $[Ca^{2+}]$ = 4, 5 and 6 mM. Although $[Ca^{2+}] = 4$ and 5 mM showed $G' < G''$ over the 6 days, both moduli show a progressive increase, indicating a possible crossing-over could occur after longer ageing times *i.e.* $G' > G''$. However, $[Ca^{2+}] = 6$ mM the moduli measured at the selected ageing times, did not show significant changes *i.e.* unchanged moduli magnitude and frequency dependence. At the same $[Ca^{2+}] = 6$ mM , W and WF samples at ageing time = 6 days, showed the following features: (i) increase in G' in the presence of fructose [10] [46] [94] with G' at 1 rad s^{-1} = 2.73 ± 0.31 Pa and 6.06 ± 1.10 Pa for W and WF samples, respectively. (ii) similar trends in G'' for both systems the in presence or absence of fructose.

To summarise, the presence of fructose (at equal $[Ca^{2+}]$) enhances the strength of the gels; increases rate of gel formation [46]; inhibits any long-term ageing of WF samples.

4.2.2 Dynamic light scattering investigation of W and WF systems

DLS can provide further insights into the dynamics of formation and internal structure of the gel state, supplementary to rheological studies described above. DLS is inherently non-destructive, whereas any rheological test applying finite external stresses or strains must affect the system.

Dynamics of ageing at fixed q

W and WF samples were prepared, stored at room temperature (T = 20-22 °C) and analysed via DLS immediately after preparation and every day, for 6 days. DLS is a non-destructive method: sample manipulation is reduced to a minimum *i.e.*, once prepared, the sample is stored in a glass tube with no further manipulations. Based on the previous rheology measurements and identification of $[Ca^{2+}]$ where systems cross the sol/gel transition, representative samples were selected and tested for ageing, initially at fixed $\theta = 90°$.

Figs.4.4 show ageing effects of W samples at different $[Ca^{2+}]$. ${g_1}^2$ vs. $\tilde{t}$ traces were taken from 1 hour to 6 days after preparation.

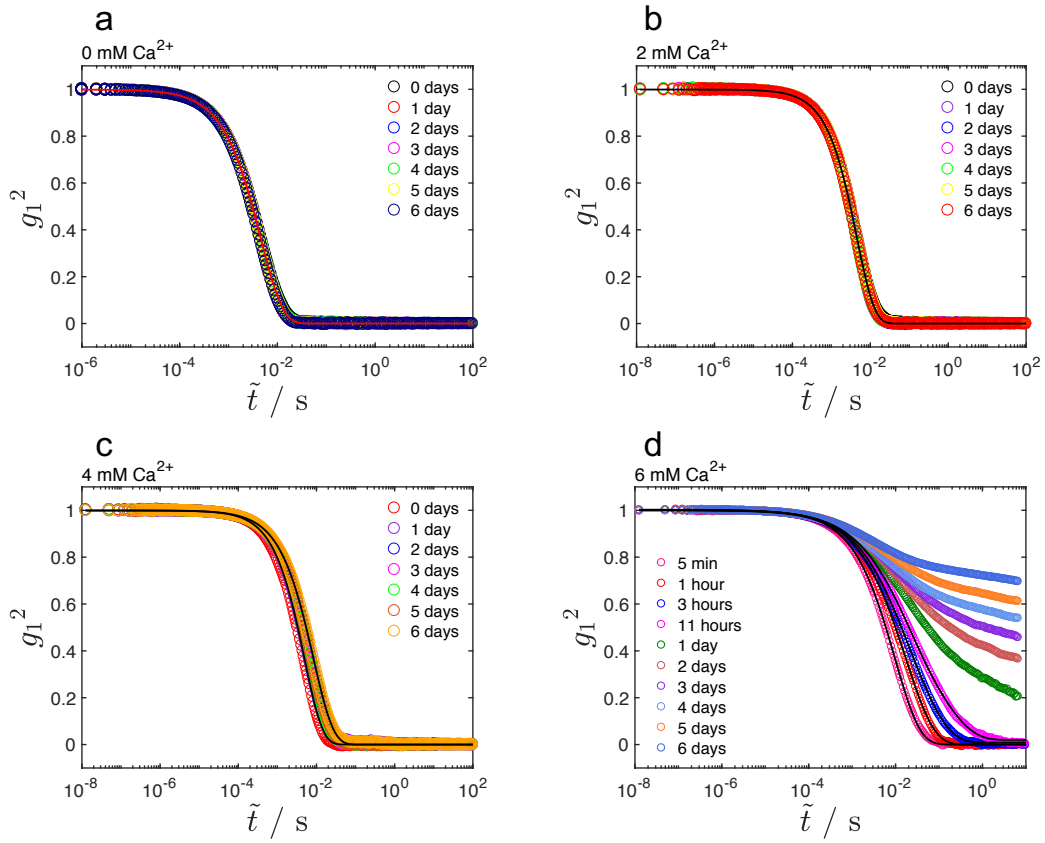

Figure 4.4: Ageing test: ${g_1}^2$ vs. $\tilde{t}$ taken at constant $\theta = 90°$ for W samples at $[Ca^{2+}]$ = (a) 0 mM, (b) 2 mM, (c) 4 mM, (d) 6 mM.

Fig.4.4(a) shows an absence of dynamic effects on ageing for $[Ca^{2+}] = 0$ mM. In this case, $< \tau > = 9 \cdot 10^{-3}$ s with no changes over 6 days. The same result was obtained for $[Ca^{2+}] = 2$ mM (Fig.4.4(b)), where the $< \tau >$ value persisted over the ageing time. At $[Ca^{2+}] = 4$ mM (Fig.4.4(c)), $< \tau >$ increased from $9 \cdot 10^{-3}$ s to $2 \cdot 10^{-2}$ s over six days. This understandable increase of $< \tau >$ indicates the growth of the scattering objects due to cross-link formation between LMP molecules.

Clearly there is a distinct effect of ageing on the dynamics for $[Ca^{2+}] = 6$ mM visible in Fig.4.4(d). Even though between 5 minutes and 11 hours after

preparation ${g_1}^2$ always shows a full relaxation, β <1 and two relaxations processes (more than one exponential decay) are observed. As reported in the literature for gel materials, the broadening of the β function *i.e.*, $\beta < 1$, describes a variety of relaxation processes, typical when polymer chains start to cross-link and form a wide range of structures. Moreover, multiple relaxation time scales indicate structuring on different levels. At 5 minutes and 1 hour, $< \tau >$ evolves from $2 \cdot 10^{-2}$ s to $5 \cdot 10^{-2}$ s , and β parameter changes from 0.76 to 0.67. The fast evolution of dynamics became markedly different between 3 and 11 hours. In these cases, ${g_1}^2$ showed two components that could be separated by fitting to double exponential function:

$$ {g_1}^2 = A_1 \cdot e^{(-2\Gamma_1 \tilde{t})^{\beta_1}} + A_2 \cdot e^{(-2\Gamma_2 \tilde{t})^{\beta_2}} \tag{4.1} $$

The β parameter for the first component was fixed to $\beta = 1$. Rather than analyse the singular components of the fit, the overall $< \tau >$ was estimated as the weighted average:

$$ < \tau >= \frac{(< \tau >_1 \cdot A_1) + (< \tau >_2 \cdot A_2)}{A_1 + A_2} \tag{4.2} $$

As a result, $< \tau >$ increased from 0.14 $\pm$ 0.08 s at 3 h to 0.43 $\pm$ 0.14 s at 11 h.

For ageing times of 1 day and above the dynamics started to be arrested and full relaxation is not seen over the probed time-scale. As noted elsewhere [67][95] for non-ergodic gel-like materials (*i.e.* time average intensity $\neq$ ensemble average intensities) three distinguishable features can be observed: (i) reduction of the intercept of g_{2-1} ; (ii) non uniform count rate vs. time plots, *i.e.* wave-like count rate; (iii) ${g_1}^2{}_{t\to\infty} \neq 0$ *i.e.*, g_{2-1} does not decay within the probed $\tilde{t}$ range, which depends on the experimental set-up.

For the present work, the non-ergodic method proposed by Pusey and van Megen [67] was utilised to obtain the field autocorrelation function (see section 1.3.2). At this stage, however, the present work was not focussed on a quantitative analysis. For this reason, it was decided to (i) re-convert g_1 to g_{2-1} and (ii) re-normalize by the σ value, to provide a direct comparison to ergodic media (*i.e.*, sol state) and a unique intercept of ${g_1}^2$.

The output shows a two-step decay: (i) a fast relaxation mode at small $\tilde{t}$ followed by (ii) a plateau whose height increases with the degree of dynamic arrest of the material. Referring back to Fig.4.4(d), in the ageing time between 1 and 6 days, the height of the plateau at high $\tilde{t}$ indeed increases systematically over time, indicating the time-dependent cross-link development (dynamic arrest).

In terms of ageing, the DLS results for LMP at $[Ca^{2+}] = 6$ mM can be directly linked to oscillatory rheology results in Figs.4.3(a) and (b). For $[Ca^{2+}] = 6$ mM 1 h after preparation (Figs.4.3(a)) $G^{'} > G^{''}$ over the probed ω. DLS analysis of the same sample (red slope in Fig.4.4(d)), shows a timescale of relaxation of $< \tau >= 5 \cdot 10^{-2}$ s (ergodic behaviour). The conversion of $< \tau >$ (s) to ω (rad s^{-1}), gives a value of ≈ 140 rad s^{-1} ($\omega = 2 \cdot \pi \cdot f$, where $f = 1/ < \tau >$). Thus, this result is consistent with the previous obtained via rheology in Figs.4.3(a), *i.e.*, $G^{''} > G^{'}$.

The same procedure was performed for WF samples. Data for $[Ca^{2+}] = 0$, 4, 5 and 6 mM are shown in Figs.4.5. As explained in chapter 3.2.1, KWW applies only to the slow mode, *i.e.*, $\tilde{t} > 10^{-4}$ s, due to the solvent relaxation effect. Generally, for samples that are fully ergodic (Figs.4.5(a), (b) and (c)), the material fully relaxes at $\tilde{t} \approx 1$ s. The decay over longer times, compared to W samples, is due to the contribution of the viscosity of the fructose solution.

Dynamics for $[Ca^{2+}] = 0$ mM showed no changes during the 6 days of ageing, with a constant value of $< \tau >= 0.44 \pm 0.01$ s (Fig.4.5(a)). Increasing $[Ca^{2+}]$ to 4 mM caused a slight increase in $< \tau >$ from ≈ 0.6 to 0.8 s, indicating the start of the junction zone stabilization process (Fig.4.5(b)). Fig.4.5(c) shows $[Ca^{2+}] =$ 5 mM; here, the dynamics started to slow down more, *i.e.*, $< \tau > \approx$ from 1.2 to 3.0 s, with a simultaneous β decrease. As shown in panel (d), by $[Ca^{2+}] = 6$ mM a significant slowing of the dynamics is observed, even at short ageing times. 1 h after preparation, ${g_1}^2$ plateau sits at ≈ 0.8. For longer ageing times the height of the plateau is essentially independent of the ageing time, as shown in the inset plot of the figure. Thus, compared to W samples at $[Ca^{2+}] = 6$ mM, (i) the presence of fructose sped up the dynamics of formation and (ii) the degree of dynamical arrest was higher *i.e.*, ${g_1}^2$ at $\tilde{t} = 10$ s was 0.60 and 0.95 in absence or presence of fructose, respectively.

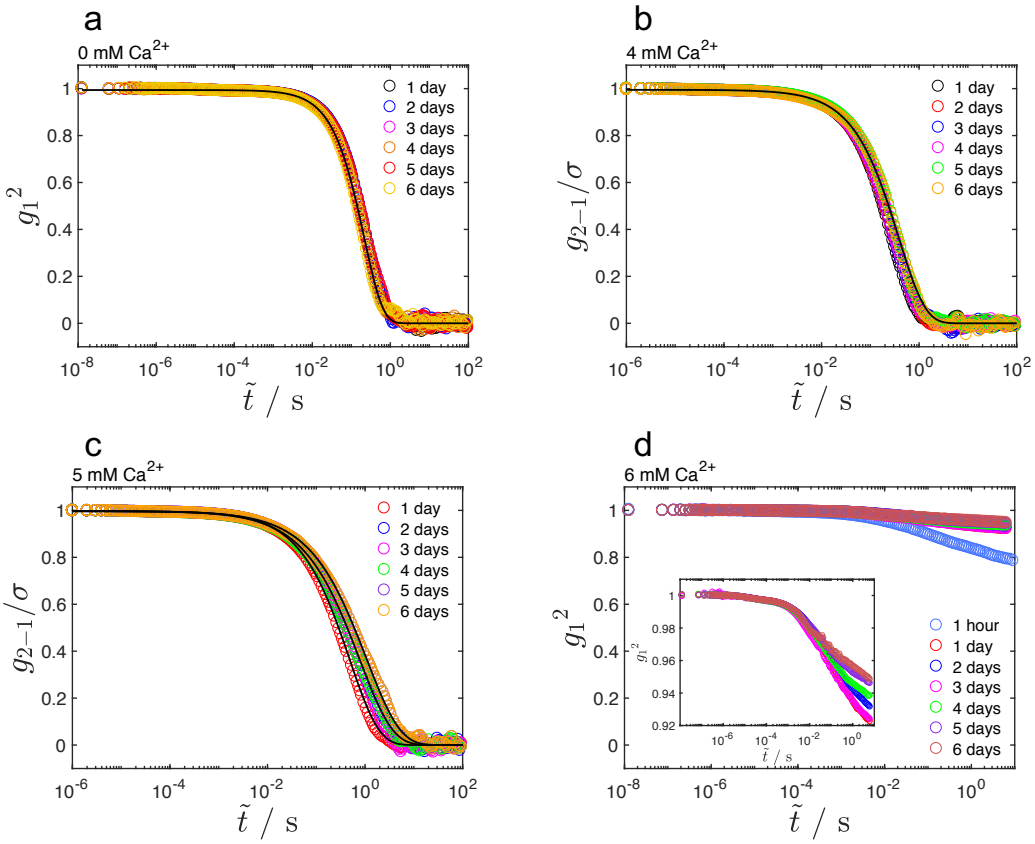

Figure 4.5: Ageing test: ${g_1}^2$ vs. $\tilde{t}$ taken at constant $\theta = 90°$ for WF samples at $[Ca^{2+}]$ = (a) 0 mM, (b) 4 mM, (c) 6 mM, (d) 6 mM; the inset of the shows the rescaling of ${g_1}^2$ from 1 to 0.92.

In conclusion, dynamics across the gel point *i.e.* $[Ca^{2+}] = 5$ and 6 mM for both systems, showed different gelling kinetics. As mentioned above, the sol/gel transition in WF samples $[Ca^{2+}] = 6$ mM occurred almost instantaneously. There seems to be no other similar DLS studies on LMP gel formation in presence of sugars. However, rheological studies on similar systems (LMP gels in presence on 30 *wt.* % fructose at different $[Ca^{2+}]$), emphasized the same trend of fructose in LMP gels *i.e.*, faster gel formation and improved mechanical properties [46], compared to W samples.

Dynamics of aged systems at fixed q

Here, ${g_1}^2$ functions for both W and WF samples at different $[Ca^{2+}]$ are reported at ageing time = 6 days. To provide a complete picture, intermediate $[Ca^{2+}]$ were also studied in addition to the $[Ca^{2+}]$ studied previously (Figs.4.6(a) and (b)).

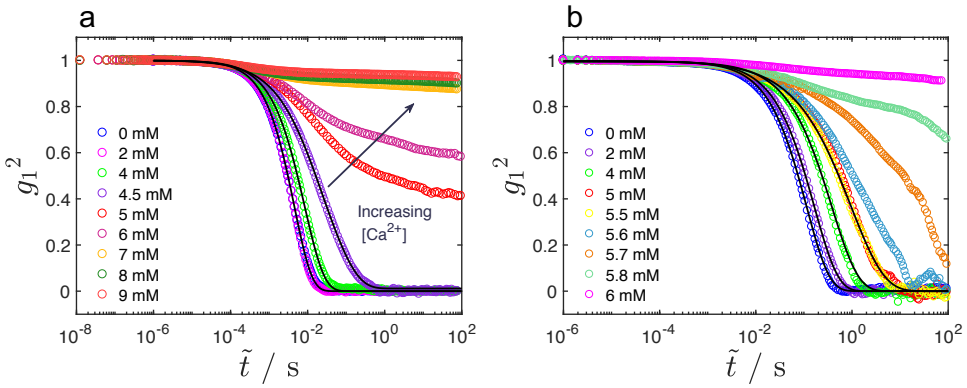

Figure 4.6: ${g_1}^2$ vs. $\tilde{t}$ (fixed q) for (a) W and (b) WF samples at different $[Ca^{2+}]$ after 6 days ageing.

Fig.4.6(a) shows the $[Ca^{2+}]$ dependence for W samples. As indicated in the figure, $[Ca^{2+}] = 0$ and 2 mM show a similar decay with $< \tau >= 10^{-2}$ s. The averaged time-scale at $[Ca^{2+}] = 4$ mM is $3 \cdot 10^{-2}$ s; this indicates the starting point of the internal structure growth. The onset of gel formation is even more clearly seen at $[Ca^{2+}] = 4.5$ mM. In this situation, ${g_1}^2$ vs. $\tilde{t}$ shows two relaxations modes, a fast (short $\tilde{t}$) and slow (long $\tilde{t}$). The estimated averaged $< \tau >$ value (two relaxation modes) for this sample was 0.160 ± 0.05 s. At $[Ca^{2+}] = 5$ mM, ${g_1}^2$ shows an initial decay at short $\tilde{t}$, followed by a plateau at long $\tilde{t}$ *i.e.*, ${g_1}^2_{\tilde{t}\to 100s} \approx 0.4$. Hence, this system shows dynamic arrest behaviour at the probed length scale. For higher $[Ca^{2+}]$, the height of the plateau increases, as observed previously.

Analogously, the dynamics in presence of fructose are shown in Fig.4.6(b). The overall shift of all ${g_1}^2$ decays to higher $\tilde{t}$ is due to the viscosity of the medium. For $[Ca^{2+}] \leq 4$ mM, the dynamics showed similar behaviour to W samples at given calcium concentrations. Unexpectedly, $[Ca^{2+}] = 5$ mM showed a fully ergodic behaviour, with no sol/gel transition with a $< \tau > = 2.8$ s and ${g_1}^2_{\tilde{t}=10s} \approx 2$. A similar effect was observed for $[Ca^{2+}] = 5.5$ mM *i.e.*, $< \tau >= 2.7$ s. The slowing

down of the dynamics increased at $[Ca^{2+}] = 5.6$ mM, with $< \tau >= 9.7$ s. It is noteworthy that the present ${g_1}^2$ function was better described by double KWW components.

As shown in Fig.4.6(b), $[Ca^{2+}] = 5.7$ mM exhibits a ${g_1}^2$ decay to 0 at $\tilde{t} >>$ 100 s, which is beyond the limit of the machine's autocorrelator. The angular dependence (see following section) showed $Y = \langle I(q) \rangle_E / \langle I(q) \rangle_T$, fluctuating from ≈ 0.98 and 1. This indicates the border between ergodic and non-ergodic regime *i.e.*, sol/gel transition. For these reasons, the data analysis of $[Ca^{2+}] = 5.7$ mM was not performed.

The system with $[Ca^{2+}] = 5.8$ mM, showed arrested dynamic behaviour. The ${g_1}^2$ function showed an initial decay up to $\tilde{t} \approx 5$ s followed by a small plateau and the beginning of another decay. Possibly, longer $\tilde{t}$ would show another relaxation process. To conclude, $[Ca^{2+}] = 6$ mM shows a clear plateau, indicating the high degree of dynamic arrest.

Comparing these two plots and what has been described for both systems, the presence of fructose and $[Ca^{2+}]$ close to the sol/gel transition, inhibits gel formation. In this regard, the $[Ca^{2+}]$ necessary to cross the sol to gel transition resides between 4.5-5 mM in W samples and 5.5-6 mM for the WF ones. On the other hand, the presence of fructose in the gel state (*i.e.*, $[Ca^{2+}] = 6$ mM) caused a higher degree of dynamical arrest *e.g.* ${g_1}^2_{\tilde{t}=10s} \approx 0.6$ and 0.94 for W and WF samples, respectively.

Fig.4.7(a) summarizes $< \tau >$ vs. $[Ca^{2+}]$ for both systems. Assuming the validity of $< \tau >^{-1} = D \cdot q^2$ and using the Stokes-Einstein relation for both systems, yields $\frac{<\tau>_{H_2O}}{<\tau>_{fruct.}} \propto \frac{\eta_{H_2O}}{\eta_{fruct.}}$. The application of this formalism to W samples is displayed in Fig.4.7(b). Accounting for the η differences in this way, supports the idea that different dynamics of formation in WF systems are not exclusively due to viscosity effects.

In terms of the β exponent (Fig.4.7(c)), an increase in $[Ca^{2+}]$ promotes its suppression, *i.e.* broadening of the ${g_1}^2$ function at higher $\tilde{t}$. As mentioned previously, β describes a range of (slow) relaxation modes that correspond to the gel initiation. For $[Ca^{2+}]_{W\text{-}gels} = 4.5$ mM, $\beta = 0.67$, indicates a broad distribution of relaxation times, since the sample is getting close to the sol/gel transition. The

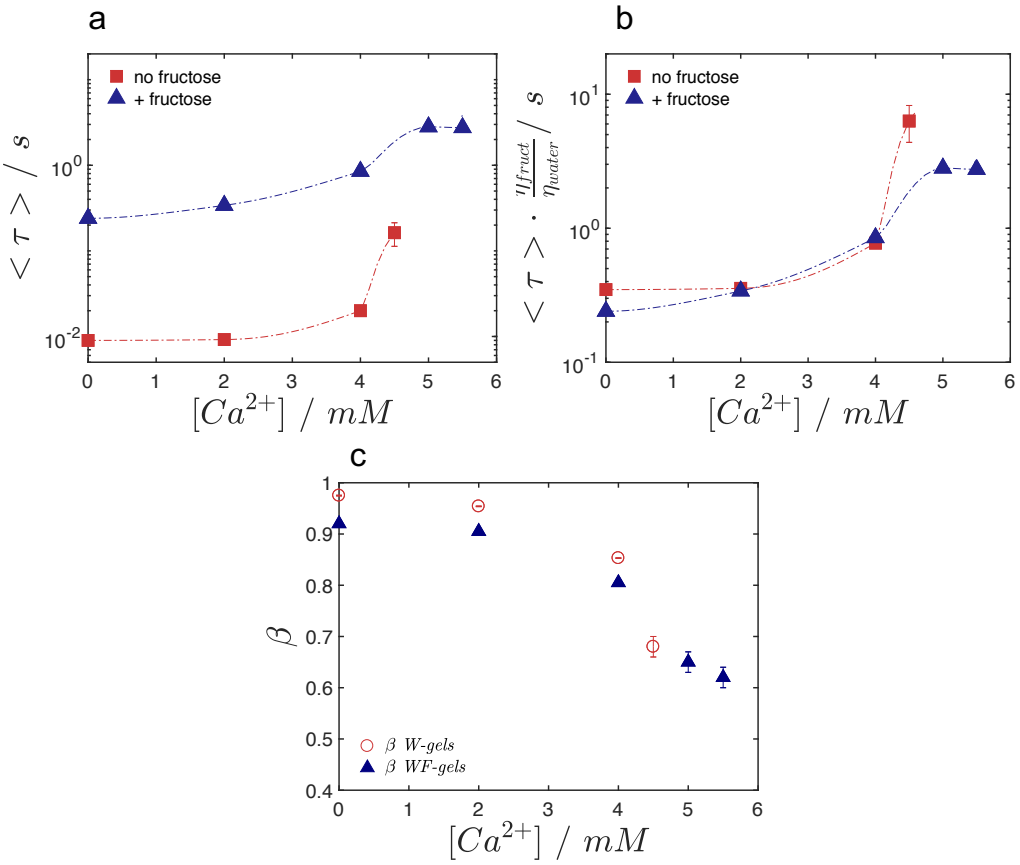

Figure 4.7: (a) KWW-estimated $< \tau >$ vs. $[Ca^{2+}]$ for W (red symbols) and WF (blue symbols) samples. (b) $< \tau > \cdot \eta_{fruct.}/\eta_{water}$ vs. $[Ca^{2+}]$; the re-compensation was applied to W samples. (c) β KWW-fit parameter for W and WF samples.

β trend of these results is in agreement with previous studies found in literature [32].

q dependence for sol and gel states

In section 3.2, the q-dependence of samples in their sol state highlight hydrodynamic interactions between LMP chains under investigation. From this perspective, the addition of cross-linking agent, *i.e.*, $[Ca^{2+}]$, may reveal a change from diffusive behaviour to a hydrodynamic interaction, since the LMP chains get closer due to cross-links. In the gel state, however, the q-dependence provides an

estimation the degree of the dynamical arrest, which is highly dependent on the probed length scale.

The aim of this section is to provide information on q-dependence of sol and gel states, on passing though the the sol/gel transition, where possible.

q dependence for sol states

Fig.4.8(a) shows $\Gamma = \tau^{-1}$ vs. q plots for samples in the sol state in the absence of fructose. $[Ca^{2+}] = 0$, 2 mM yielded a power-law $\Lambda = 2.1 \pm 0.02$, corresponding to diffusive dynamics for the averaged time-scales in the probed q-range. In practical terms, within these $[Ca^{2+}]$, the samples show no junction zone stabilization and remain in the sol state. The diffusive behaviour is confirmed in ${g_1}^2$ vs. $\tilde{t} \cdot q^2$ plots in Fig.4.8(b), as the ${g_1}^2$ functions collapse onto each other.

For $[Ca^{2+}] = 4$ mM, $\Lambda = 2.2 \pm 0.03$ with an overall downward shift of Γ vs. q (*i.e.* increase of $< \tau >$ values). One can assume this effect is due to a partial junction zone stabilization. As explained earlier, gel development may be enhanced by the presence of amide groups via -H bonding [2]. In fact, the pH of solution had fluctuating value between ≈ 4.5 and 4.8. However, identification of the two modes of cross-linking cannot be achieved in this analysis.

At $[Ca^{2+}] = 4.5$ mM (Fig.4.8(a)), Γ (from average-weighted $< \tau >$ from double exponential functions) indicated a $\Lambda = 3.6 \pm 0.02$ *i.e.*, deviation from $\approx q^2$ behaviour. This is supported in Fig.4.8(b), orange traces. The Γ vs. q-dependence for each $< \tau >_F$ and $< \tau >_S$ modes is shown in Fig.4.8(c). As reported, $\Lambda = 2.1 \pm 0.2$ for the fast mode. This aspect has been seen elsewhere for both pectin [32] and polymeric solutions / pre-gelled samples [68] [86] [82] [81] . The slow mode showed a $\Lambda = 4.1 \pm 0.1$. This effect may be attributable to the dramatic change undergone by the system *i.e.*, sol/gel transition. In this condition, the formation of a relatively large amount of LMP chain linkages hinders interpretation. The increased broadening of the ${g_1}^2$ function at higher $\tilde{t}$ ($\beta = 0.7$) suggests a variety of relaxation modes, consistent with the proximity to the gel point. This is consistent with the fact that $[Ca^{2+}] = 5$ mM (Fig.4.6(a)) shows non ergodic behaviour.

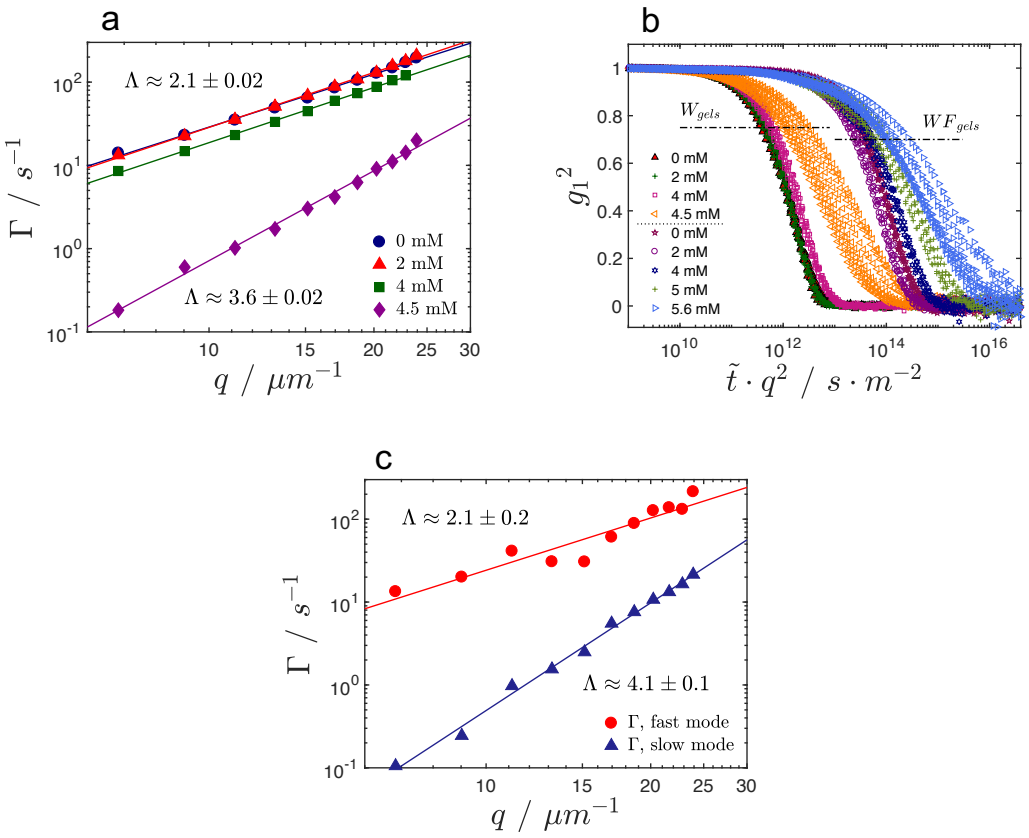

Figure 4.8: (a) Double-logarithm plot for Γ vs. q for W samples and $[Ca^{2+}]$ from 0 to 4.5 mM; fit lines and power law values are displayed as well. (b) ${g_1}^2$ vs. $\tilde{t} \cdot q^2$ plots for W and WF samples; dashed lines delimit the two family of samples. (c) Double-logarithm plot for Γ vs. q for W and $[Ca^{2+}] = 4.5$ mM, demonstrating the presence of two relaxation modes (fitted lines and values displayed).

As discussed in section 3.2.1, the presence of fructose can reveal a solvent-relaxation process. Fig.4.9(a) for $[Ca^{2+}] = 0$ mM (main and inset) illustrates the behaviour. Even though the KWW fit was mostly performed for $\tilde{t} > 10^{-4}$ s, it was decided to try to fit the fast mode ($< \tau >_F$) of WF samples in presence of Ca^{2+} ions.

The results for Γ vs. q for $< \tau >_F$ for $[Ca^{2+}] = 0$, 4 and 5 mM are displayed in Fig.4.9(b). For these materials, Λ for $< \tau >_F$ was 2.2 ± 0.2 s, 1.9 ± 0.4 s and 2.2 ± 0.4 s, with the increasing of $[Ca^{2+}]$. Moreover, the amplitude in the ${g_1}^2 = A \cdot e^{-(\Gamma\tilde{t})^{\beta}}$ function showed a constant value around ≈ 0.006, indicating

the very small contribution to the overall relaxation. Thus, the $\approx q^2$ dependence suggests a diffusive-relaxation mode for the scattering units at these time scales scales [32] that appears independent of the addition of Ca^{2+} ions added to *WF* solutions. The analysis of the fast mode for $[Ca^{2+}] = 2$ and 5.6 mM was not possible due to excess ${g_1}^2$ noise in this $\tilde{t}$ range.

Fig.4.9(c) shows the $< \tau >_S$ for $[Ca^{2+}] = 0$, 2, 4, 5 and 5.6 mM, in the $\tilde{t}$ range previously ascribed. The Λ increases monotonically with $[Ca^{2+}]$ increase. In order of $[Ca^{2+}]$ (from 0 mM): $\Lambda = 2.1 \pm 0.1$, 2.37 ± 0.1, 2.7 ± 0.2, 2.9 ± 0.3 and 3.3 ± 0.7. Compared to *W* samples, here one can see the progressive deviation from q^2 to q^3, suggesting change in dynamics.

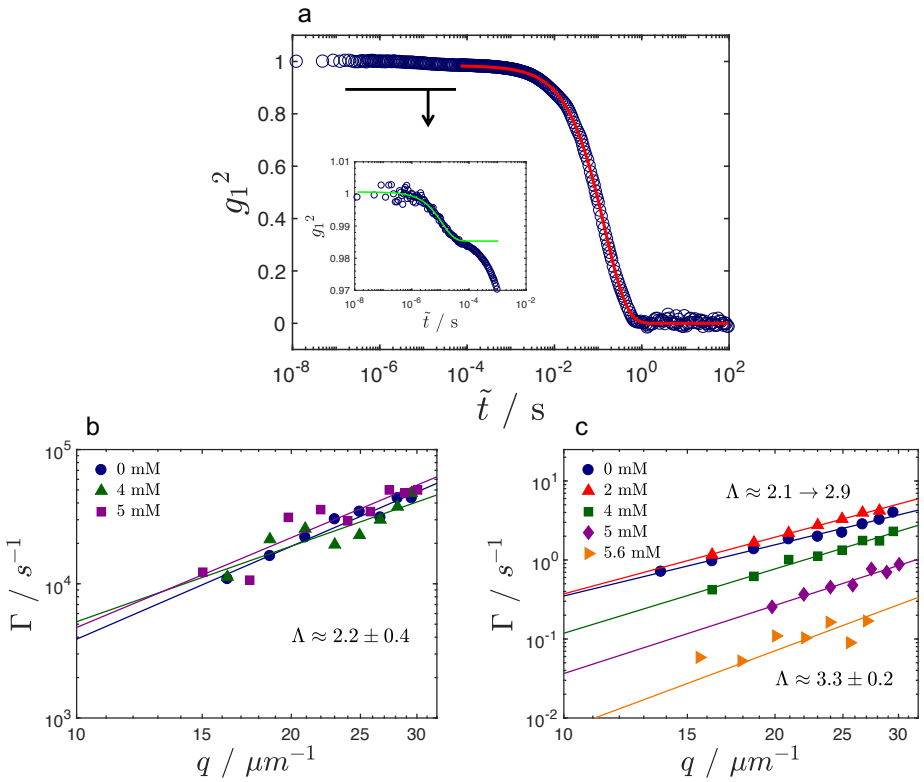

Figure 4.9: (a) ${g_1}^2$ vs. $\tilde{t}$ for *WF* sample at $[Ca^{2+}] = 0$ mM. The main plot shows the *KWW* fit for the slow mode ($< \tau >_S$) for $\tilde{t} \geq 10^{-4}$ s; the inset shows the expanded ${g_1}^2$ vs. $10^{-8} > \tilde{t} \leq 10^{-4}$ s, highlighting the fast relaxation mode ($< \tau >_F$) and relative *KWW* fit. (b) Γ values from $< \tau >_F$ vs. q and relative Λ values. **c**. Γ values from $< \tau >_S$ vs. q.

The addition of 60 *wt.* % fructose alters the dynamics of LMP gel formation and highlights some relevant physical characteristics absent in samples prepared in just water.

Several authors have attributed the main reason for these effects to the capability of sugars to bind water and thus enhance LMP chain aggregation [46] [17] [47]. The relationship between sugar and LMP gel formation was extensively studied in the past and in general this study is in agreement with the conclusion of these authors [17][46][47][96]. On the other hand, most of these previous studies did not exceed 30-40 *wt.* % of fructose (or sugars) in solution. As discussed in section 1.1.3, high concentrations of sugars promote the sugar and/or clustering formation. This condition raises the following questions: where does the LMP sit in the solution? and what are the interactions occurring between water-sugar-pectin? These difficult questions may be answered in the future by focussing attention on the solely water-fructose and water-fructose-pectin systems, with the help of auxiliary techniques.

q dependence for gel states

In an analogous manner to that used for sol state, the q-dependence of the gels was investigated. The aim of this work was to elucidate the dynamical arrest as a function of $[Ca^{2+}]$ for both W and WF samples. Fig.4.10 shows the q-dependence for $[Ca^{2+}] = 6$ mM in the absence of fructose.

As displayed in the figure, ${g_1}^2$ at different θ (or q) shows a first relaxation mode in a $\tilde{t}$ range between 10^{-4} and 10^{-1} which terminates with a plateau at higher $\tilde{t}$. Generally, with increase in q there is (i) an increase in amplitude of the fast relaxation and (ii) a decrease of height of the plateau. ${g_1}^2$ at $\theta = 130°$ appears as a very slow decay, rather than a plateau. This aspect suggests full relaxation of the material is possible at probed L and very high $\tilde{t}$ (*e.g.* $> 10^2$ s).

A common feature in dynamically arrested materials is that $< \tau >_F$ shows a q^2 dependence and so, diffusive character [71]. However, this aspect was not seen in the present system. This effect may be attributable to the intrinsic properties of the sample. In fact, most of the literature available regarding DLS on polymer-based gel systems is modelled on track for colloidal gels.

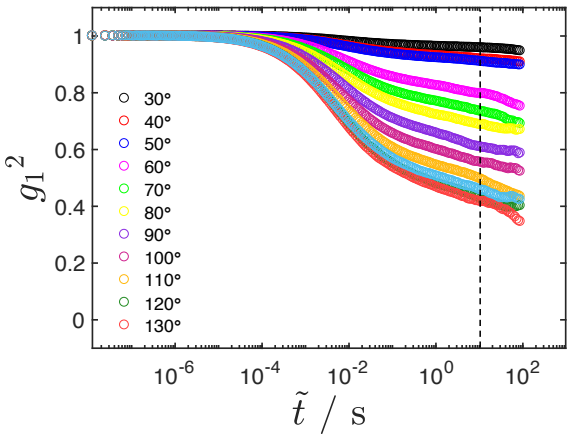

Figure 4.10: Non-ergodic averaged ${g_1}^2$ vs. $\tilde{t}$ of W system with $[Ca^{2+}] = 6$ mM collected at different θ.

At higher $\tilde{t}$, in the plateau regime, ${g_1}^2$ decreases with the increase of q. The physical meaning is related to the probed length scale (L) *i.e.* $L \approx q^{-1}$. In other words, at large L, one might probe an ensemble of cross-linked LMP chains, characterized by a high degree of dynamic arrest *e.g.*, ${{g_1}^2}_{\theta=30^\circ} \approx 0.98$. Whereas, at small L, the lower extent of dynamic arrest reflects internal motions of the gel that still occur *e.g.*, ${{g_1}^2}_{\theta=130^\circ} \approx 0.4$. This highlights the importance of the probed lengthscale in DLS analysis of gelled materials.

Rather than showing every plot, it was decided to use the ${g_1}^2$ values at a fixed $\tilde{t} = 10$ s (dashed line in Fig.4.10) and plot these vs. the scattering vector q. Fig.4.11(a) shows the ${g_1}^2$ at $\tilde{t} = 10$ s vs. q for W samples with $[Ca^{2+}] = 5$, 6 and 7 mM and WF samples with $[Ca^{2+}] = 6$ mM (red triangles). This figure clearly demonstrates the overall effect of $[Ca^{2+}]$ over the investigated L range. For example, the smallest probed L ($q \approx 24\ \mu m^{-1}$; $L = 0.26\ \mu m$) shows a ${g_1}^2 \approx 0.2$ and 0.75 for $[Ca^{2+}] = 5$ and 6 mM, respectively. This is related to the structural-compactness caused by the increased cross-link density which arrests the dynamics.

In particular, at $[Ca^{2+}] = 6$ mM in the presence of fructose there is extensive dynamic arrest, at the smallest probed L, ${g_1}^2 \approx 0.9$. Since lower $[Ca^{2+}]$ (*i.e.*

5.7 and 5.8 mM) for WF samples were in the vicinity of the sol/gel transition, non-ergodic averaging and the resulting Y ratio yielded uncertainties, with values fluctuating around 1 or slightly less. These fluctuations were more pronounced at mid-high q ranges and, for these reasons, it was decided to exclude the data in the present analysis.

With the good quality data obtained for W systems, it was decided to generalize the $[Ca^{2+}]$-dependency mechanism as a ${g_1}^2$ master-curve. Shifting factors (a) were applied in q for $[Ca^{2+}] = 6$ and 7 mM data points ($a = 0.78$ and 0.45 for $[Ca^{2+}] = 6$ and 7 mM, respectively), in order to match the 5 mM W samples. The result, shown in Fig.4.11(b), highlights the generality of cross-linking of LMP as a function of $[Ca^{2+}]$. The master-curve covers the ${g_1}^2$ range between 1 and 0.2, the lowest detectable point before the function decays to 0 which corresponds to the material fully relaxes and behaves as a liquid.

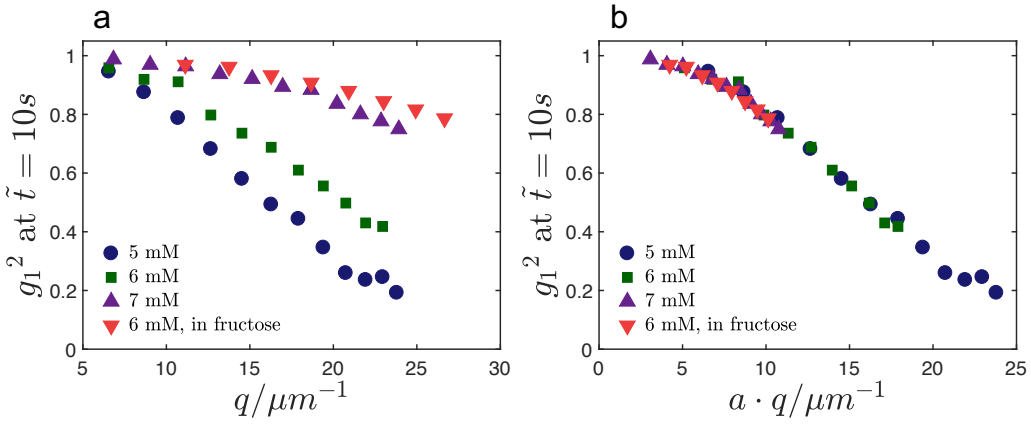

Figure 4.11: (a) ${g_1}^2{}_{\tilde{t}=10s}$ vs. q for (i) W samples and $[Ca^{2+}] = 5$, 6 and 7 mM and (ii) WF sample with $[Ca^{2+}] = 6$ mM. (b) ${g_1}^2{}_{\tilde{t}=10s}$ vs. shifted q values ($a \cdot q$) for the samples displayed in panel (a).

Additionally, data for $[Ca^{2+}] = 6$ mM in the presence of fructose was rescaled to the master-curve (red triangles in panel (b)), showing the match of the data-points at high ${g_1}^2$ values. A characteristic of the master-curve showed Gaussian-like shape. Since a Gaussian distribution of square displacements (MSD or ΔR) reflects the dynamics of the scattered objects, it was decided to fit each data (in

Fig.4.11(a)) with the function:

$$g_1{}^2{}_{\tilde{t}=10s} = e^{-\frac{2q^2}{6}\langle \Delta R^2(\tilde{t}=10s)\rangle} \tag{4.3}$$

Where $\langle \Delta R^2(\tilde{t}=10s)\rangle$ is the mean square displacements of the scatterers at $\tilde{t}=10$ s. The square root of this parameter yields the fluctuation length scale (L_F) of the frozen-in scattering objects. Fig.4.12 shows L_F vs. $[Ca^{2+}]$ for both W and WF samples; the inset of the present figure shows the MSD fit lines for the data displayed in Fig.4.11(a).

For W samples, the L_F decreases monotonically with increasing $[Ca^{2+}]$, confirming the remarkable dynamical arrest and summarizing what has already been discussed in this section. For WF samples, the L_F for $[Ca^{2+}] = 6$ mM was 0.03 $\pm$ 0.001 μm, a value slightly lower than that for the $[Ca^{2+}] = 7$ mM system in absence of fructose. As mentioned earlier, $[Ca^{2+}] < 6$ mM in the presence of fructose appears to be in the the vicinity of the sol/gel transition and the non-ergodic averages are rather noisy. However, data for $[Ca^{2+}] = 5.8$ mM in a θ range 30-90°, *i.e.* relatively low angles, showed non-ergodic behaviour. So, the mean square displacement fit was performed. The resultant L_F value shown in Fig.4.12 highlights the rapid change over these very narrow $[Ca^{2+}]$ ranges (*i.e.*, 5.8 versus 6 mM), illustrating that addition at high concentrations, *i.e.*, sharp sol to gel transition.

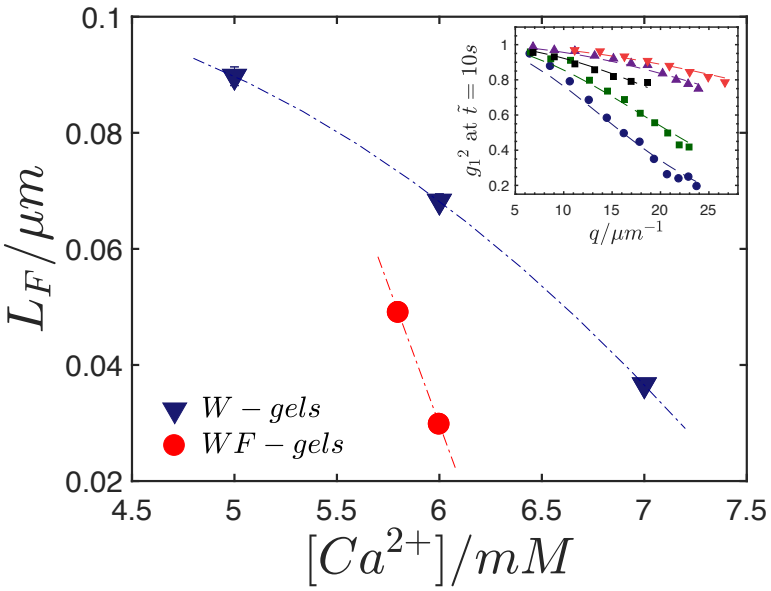

Figure 4.12: L_F values from MSD fit vs. $[Ca^{2+}]$ for both W and WF samples. The inset of the figure shows the raw data with the MSD fit lines.

4.2.3 Temperature dependence of *W* and *WF* samples

LMP gels are considered weak physical gels, with continuous breakage and reformation of junction zones between the polymer chains. An important technological feature is therefore their thermal reversibility *i.e.*, breakdown of cross-links at high temperatures and subsequent reformation at lower temperatures [2]. This allows removal of a gel's history and allows one to re-start gelation after heating then cooling. Of course, the temperature increase should not exceed the boiling point of the solution and there must be no chemical degradation of the pectin

In order to test the effects of sugars on this process, rheological and *DLS* characterization were performed in a temperature range between 25 and 70°C, for gels aged for 6 days. In particular, rheological characterization was performed via frequency sweep tests and *DLS* at fixed $\theta = 90°$.

Figs.4.13(a) and (b) show the rheological and *DLS* results for $[Ca^{2+}] = 6$ mM in absence of fructose (*W* samples). To simplify the intrepretation of the plot in panel (a), $G^{'}$ and $G^{''}$, measured at $\omega = 1$ rad s^{-1} are plotted vs. temperature (T). The inset of the figure shows the full result of the test. As shown, the T increase yields a moduli decrease, with a gel to sol ($G'' = G'$) transition at $T \approx 37$ °C. Even though the T range was between 25 and 70°C, some data points are not displayed due to low resolution of G' data at high T. This behaviour becomes markedly different for $G^{'}$ and $T > 50$ °C. Moving onto the inset of panel (a), $G^{'}$ and $G^{''}$ vs. ω in a T range between 25 and 45°C, the following features can be noted: (i) $G^{'}$ magnitude decreases, (ii) the moduli crossover at shorter ω and (iii) the moduli approach each other. At 45°C, $G^{''}$ and $G^{'}$ showed similar values in the ω range 0.2 - 0.6 rad s^{-1}. In this range, one can recall the moduli power law at the gel point *i.e.*, $G^{'} \propto G^{''} \propto \omega^{p}$ where, the p exponent may give additional information on structural properties [97]. However, the short ω range where this occurred made the analysis unfeasible. The same issue is well documented in literature for *LMP* gels [2]. For $T > 50$°C, $G^{'}$ fell to very low magnitudes and $G^{''}$ showed persistent values and ω-dependency.

The T dependence in *DLS* measurements is shown in Fig.4.13(b). For this test, ${g_1}^2$ data for a T increase from 25 to 65°C (empty circle symbols) are followed by a T decrease to 25°C (full triangle symbols), in steps of 10°C. The larger T

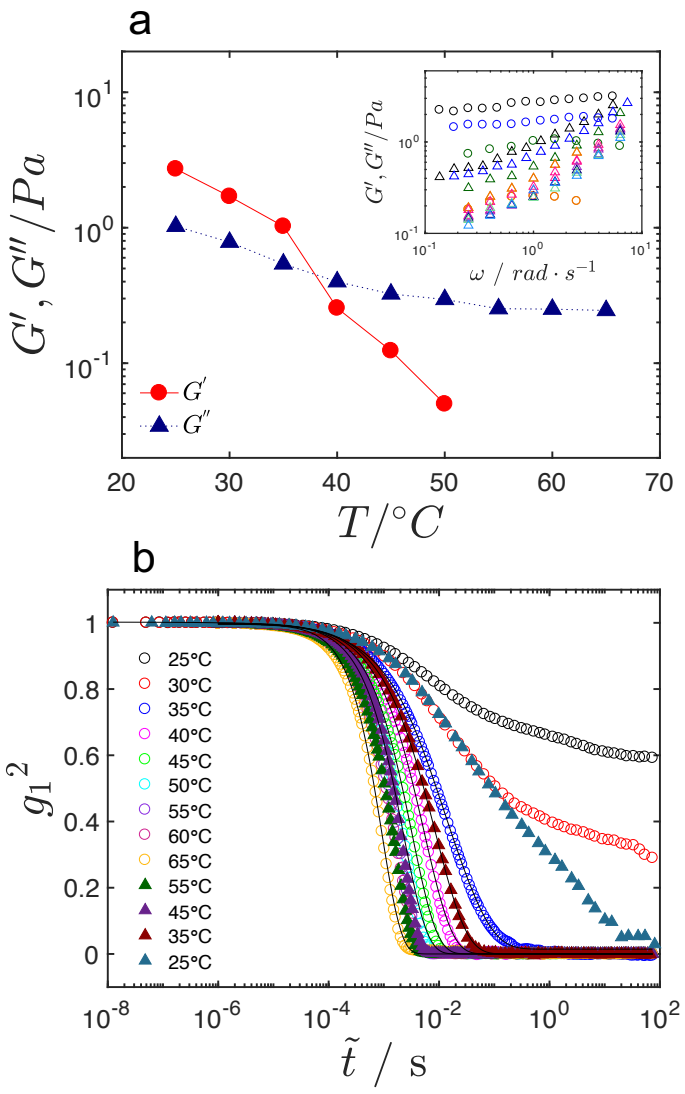

Figure 4.13: (a) Main figure: $G^{'}$ and $G^{''}$ at 1 rad·s^{-1} vs. probed T for W sample at $[Ca^{2+}] = 6$ mM; inset: $G^{'}$ and $G^{''}$ vs. ω as a function of T. (b) ${g_1}^2$ vs. $\tilde{t}$ at different T for W sample and $[Ca^{2+}] = 6$ mM.

steps on cooling were used to reduce measurement times. At $T = 25$ and 35°C (black and red, respectively), the terminal part of the ${g_1}^2$ function (*i.e.*, plateau) decreased from 0.6 to 0.3, indicating softening of the material due to junction zone destabilization and η reduction on heating.

A jump from non-ergodic to ergodic behaviour occurred between $T = 35$ and 40°C in agreement with what was seen in rheology. At $T = 40$°C, the ${g_1}^2$ function is described by a double exponential function ($< \tau > = 0.08 \pm 0.01$ s), indicating a fast and slow relaxation mode, linked to the presence of junction zones at different structural levels. The subsequent increase to 45°C (magenta symbols), showed a unique relaxation mode with $< \tau > = 7 \cdot 10^{-3}$ s. At this point, one can assume that (i) majority of junction zones are destabilized and/or (ii) the number of individual cross-links between any two LMP chains are significantly reduced.

Further T increase up to 65°C, showed a progressive reduction of the time-scale to $< \tau > = 1.5 \cdot 10^{-3}$ s at the maximum probed temperature. It should be noted that, the present fit showed a compressed exponential *i.e.*, $\beta > 1$, specifically $\beta = 1.22$. The dynamics associated with this behaviour are recognized as ballistic and have been widely studied in the past, especially at very high $\tilde{t}$. The fast motion at short $\tilde{t}$ may be attributable to the relatively high T [98] or as the onset of diffusive motion [71]. The lack of a q-dependence cannot give additional information regarding this behaviour.

Upon decreasing T to 55 and 45°C dynamics slowed down (green and purple full triangles). A marked effect was observed at $T = 35$°C (dark red full triangles), with a $< \tau > = 2 \cdot 10^{-2}$ s. Finishing, at $T = 25$°C, ${g_1}^2$ shows a decay at long times. Moreover, the upper part of the function (*i.e.*, 1 to ≈ 0.5) show similarity to $T = 35$°C during the T increase. The point at ${g_1}^2 \approx 0.5$ may be attributed to the point at which $< \tau >_S$ approaches to a non-ergodic regime. Fitted with a double exponential decay, the time-scale yielded a $< \tau > = 18.2 \pm 2.2$ s.

The above results confirms the thermal-reversibility of LMP in presence of sugars, although the relaxation processes linked to the junction zone stabilization showed different rates of cross-linking.

Moving to WF samples, rheological and DLS experiments were performed in the same way on systems with a $[Ca^{2+}] = 6$ mM. The temperature dependence yielded an unexpected result, with the loss of the thermo-reversibility in the probed T. To confirm this interesting result, the T ramp was performed twice on the same system.

The frequency sweep test in Fig.4.14(a) shows $G^{'}$ and $G^{''}$ vs. $a \cdot \omega$. The shift factor a applied in ω was used to include all the results in a single plot. As shown, in the T 25 - 45°C range, $G^{'}$ shows a remarkable frequency dependency, with a decrease of the overall magnitude. The $G^{'} > G^{''}$ condition suggested the unequivocal presence of cross-links, as demonstrated in previous results. The softening that occurs may be attributable to the reduction of the water-fructose viscosity solution as the T is increased.

Further increases in T, in the range 45 - 70°C, resulted in the progressive linear increase in $G^{'}$. One can see as well that $G^{'}$ and $G^{''}$ separation reaches its maximum point. On cooling, $G^{'}$ increasingly becomes ω-independent. Both moduli, fitted with a power law give a value of ≈ 0.06, *i.e.*, almost flat.

To facilitate the interpretation, $G^{'}$ and $G^{''}$ measured at $\omega = 1$ rad s^{-1} were plotted vs. T in Fig.4.14(b). Additionally, the plot includes the second T ramp and highlights the similar G' and G'' values obtained in the first cycle, but with lower magnitude.

To check the effective strengthening of this WF sample as a result of the temperature cycling, a strain sweep at different T was performed as well Fig.4.14(c). Here, the first sample was analysed after 6 days of ageing, with no T alterations. The result (blue triangles), shows a LVE up to 20 %, with consequent strain hardening and then moduli decrease. To test the T influence, a second sample was loaded in the rheometer and the same T cycle (*i.e.*, $25 \rightarrow 70 \rightarrow 35$°C) was performed in a γ range applied between 10^{-1} to 1 %, to leave the structure relatively undisturbed, within the LVE range. Once cooled back to 25°C, the full γ range was investigated. The upward shift of $G^{'}$ and the reduction of the LVE up to $\approx$ 0.9 %, was comparable to the T-unperturbed sample, confirming the strengthening of the gel via T cycling. Thus, for this gel thermal-reversibility was lost and the material became stronger, *i.e.*, higher density of stabilized junction zones.

Again, similar temperature sweep tests were performed as well via DLS measurements. As shown in the previous sections, the WF sample at $[Ca^{2+}] = 6$ mM shows very restricted dynamics and the T-dependence showed no clear results (omitted data). In this context, it was decided to reduce the $[Ca^{2+}]$, to aid interpretation and comparison with the tested W sample. On the first attempt,

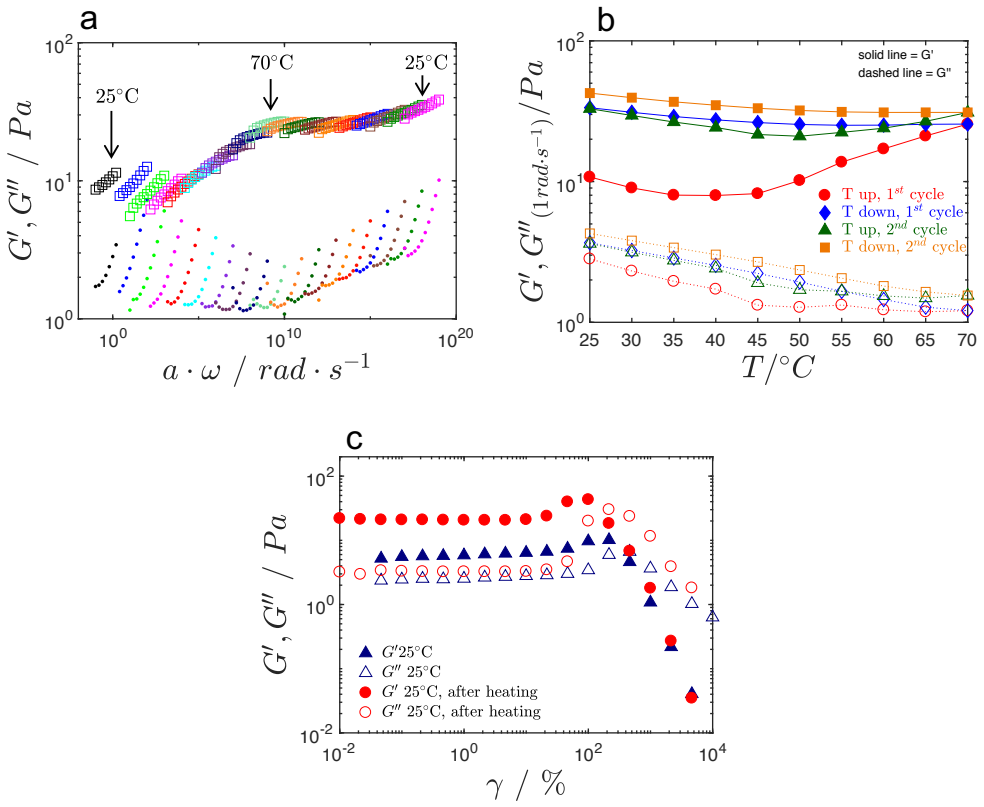

Figure 4.14: *WF* sample, $[Ca^{2+}] = 6$ mM. **a**.$G^{'}$ and $G^{''}$ vs. shifted angular frequency $a \cdot \omega$ collected from $T = 25 \rightarrow 70$°C and $70 \rightarrow 25$°C. **b**. Data representation as $G^{'}$ and $G^{''}$ at 1 rad s^{-1} vs. probed T. **c**. Strain sweep test, $G^{'}$ and $G^{''}$ vs. γ at 25°C, before and after heating to 70°C.

$[Ca^{2+}]$= 5 mM showed no relevant changes in terms of rheological characterization with $G^{''} > G^{'}$ over the whole probed temperature range.

The second attempt was performed on a $[Ca^{2+}]$= 5.5 mM gel. This $[Ca^{2+}]$ showed ergodic behaviour after 6 days of ageing (sol state). The T increase caused dramatic changes in the sample structure and dynamics. As shown in Fig.4.15(a), the $G^{''} > G^{'}$ condition persisted in a T range between 25 - 50°C. The figure clearly shows a parallel behaviour of both moduli, indicating the vicinity of the sol/gel transition [2] [45] [97]. The p exponent at $T = 25$°C was estimated as ≈ 0.6. In the aforementioned T range, p fluctuated between ≈ 0.6 - 0.7 with a slow and progressive convergence of $G^{'}$ and $G^{''}$. A detailed study performed on

LMP gel formation showed $p = 0.7$ [99], a similar value to the one determined in this study. However, this similarity has to be viewed with caution, since the sample compositions were completely different. Moreover, the scaling parameter has been debated for its non-universality [45].

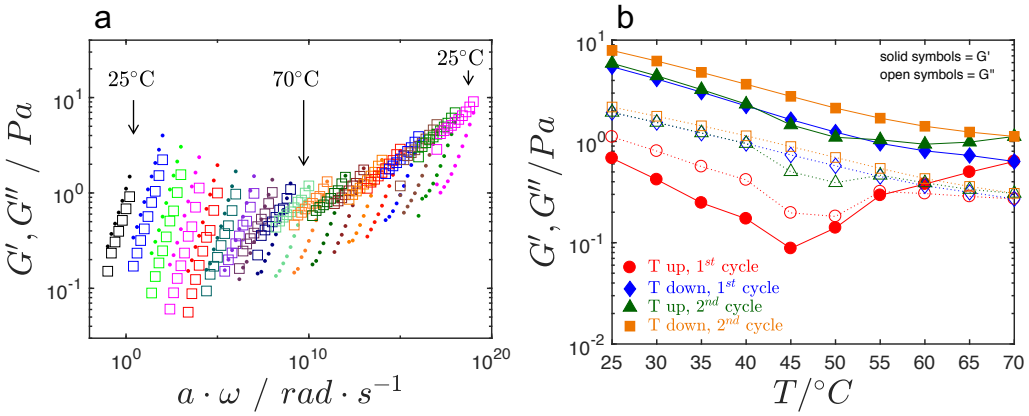

Figure 4.15: WF sample, $[Ca^{2+}] = 5.5$ mM. (a) G' and G'' vs. shifted angular frequency $a \cdot \omega$ collected from $T = 25 \rightarrow 70$°C and $70 \rightarrow 25$°C. (b) Data representation as G' and G'' at 1 rad·s^{-1} vs. probed T.

At $T = 55$ and 60°C, $G' = G''$ and diverge. From 65°C onwards, the net separation between the the moduli increases, as $G' > G''$.

During cooling, from 70 to 25°C, G' shows the following features: (i) increase in magnitude; (ii) flattening over the probed frequency, with a power-law value of ≈ 0.18. Recalling what has been seen at $[Ca^{2+}]$= 6 mM, *i.e.*, $p \approx 0.06$, it is seen that an increase of $[Ca^{2+}]$ of 0.5 mM has dramatic changes on WF samples, especially when the ΔT is applied. This is also more clear in Fig.4.15(b), where G' and G'' taken at $\omega = 1$ rad s^{-1} are plotted vs. T. The second T cycle showed a similar effect but of lower magnitude, *i.e.*, the main difference is that $G' > G''$ condition applies for the entire range.

Temperature dependent dynamic light scattering for WF samples at $[Ca^{2+}]$ = 5.5 mM is shown in Figs.4.16(a)-(d). To simplify the description of the ${g_1}^2$ functions, the plot is divided into four parts. As in the q-dependence section, the presence of $< \tau >_F$ at short $\tilde{t}$ will be described separately. Hence, the description of the slow mode has been performed from $\tilde{t} \approx 10^{-4}$ s onwards.

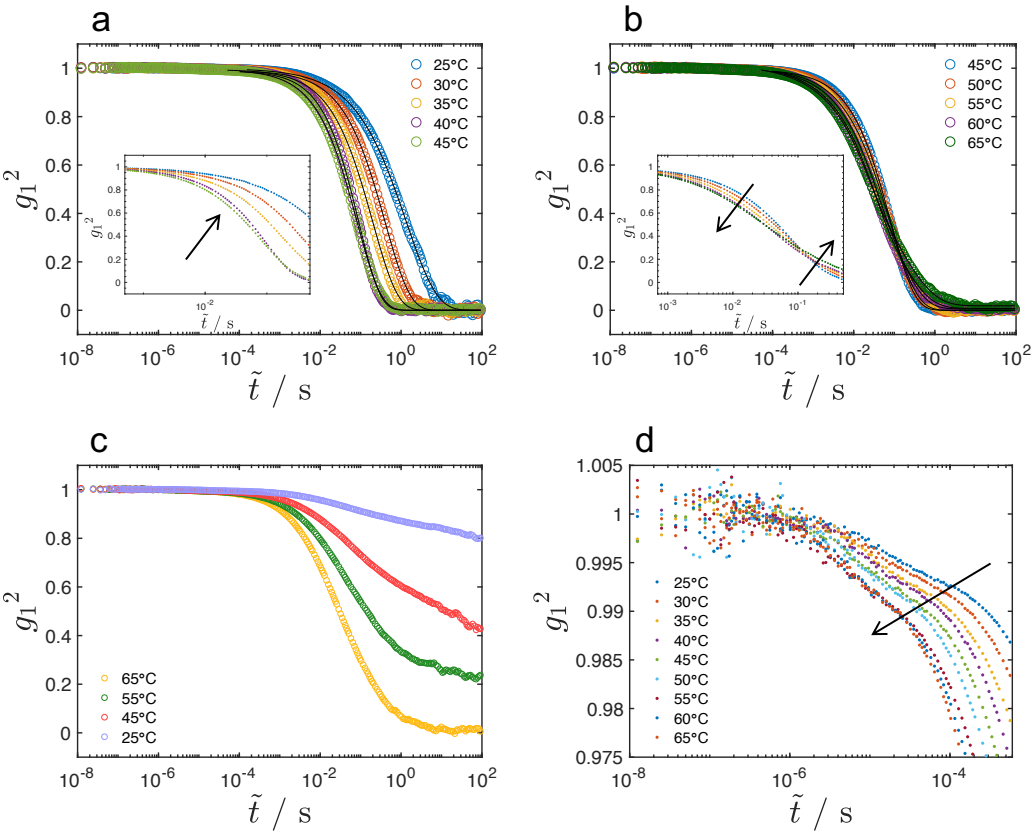

Figure 4.16: $g_1{}^2$ vs. $\tilde{t}$ for *WF* sample, $[Ca^{2+}]$ = 5.5 mM at different T. (a) T range from 25 to 45°C; the inset and arrow highlights the shoulder of $g_1{}^2$ at T = 45°C. (b) T range from 45 to 65°C; the inset figure and arrows show the change of relaxation mode as a function of T. (c) Cooling relaxation modes from 65 to 25°C. (d) Fast relaxation mode of $g_1{}^2$ in the $\tilde{t}$ range between 10^{-8} – $6{\cdot}10^{-8}$ s.

Fig.4.16(a) shows the full $g_1{}^2$ function collected in a T range from 25 to 45°C. In this case, $< \tau >_S$ decreases from 4.3 s to 0.20 s for 25 and 40°C, respectively. As in the rheological characterization, the speeding up of the dynamics is probably due to the reduction in viscosity.

At 45°C, $g_1{}^2$ shows a difference in the $\tilde{t}$ range between 10^{-4} and 10^{-1} s. The inset of panel (a) zooms-in on the results in this $\tilde{t}$ range. The arrow indicates the start-point of a $< \tau >_S$ decoupling, *i.e.*, the presence of an additional relaxation mode. However, in this condition, the $g_1{}^2$ function was described with a single *KWW* function, with a time-scale of 0.19 s.

Fig.4.16(b) shows the ${g_1}^2$ functions from 45 to 65°C. The shifting seen for $T =$ 45°C continues consistently with increasing temperature, as denoted in the inset of the figure. The arrows indicate a speeding up of dynamics at short $\tilde{t}$ and a dynamical slow down and broadening at long $\tilde{t}$.

The magnitude of this effect becomes marked for $T = 55$, 60 and 65°C, where ${g_1}^2$ was described by a double KWW function. The speed up of dynamics at short $\tilde{t}$ reflects the $< \tau >_F$ (solvent relaxation) in panel Fig.4.16(d) for $\tilde{t} < 10^{-4}$ s. Here, the dynamical speeding up caused by the T increase extends to intermediate $\tilde{t}$ *i.e.* $\approx 10^{-4}$ – 10^{-1} s, on a different time-scale. However, for $\tilde{t} > 10^{-1}$ s, the long-term interactions increase, showing a broader range of relaxation modes as $\beta = 0.46$ at $T = 65$ °C. Thus, at high T, the faster dynamics at short $\tilde{t}$ may indicate the partial disassembly of junction zones that redistribute through the sample at the probed length scale. This re-arrangement might create a situation allowing for an improved homogeneity of cross-links.

Even though multiple relaxations are present, the sample is in the full ergodic regime. The estimated $< \tau >_S$ value at 65°C is 0.37 s, corresponding to ≈ 17 rad s^{-1}. Recalling the rheological result at $T = 65$°C in Figs.4.15(a), G' and G'' crossover occurs at ≈ 9 rad s^{-1}, consistent with the DLS results.

Finally, the decrease in temperature from 65 to 25°C promotes dynamical arrest of the sample, which becomes non-ergodic (Fig.4.16(c)). The height of the plateau at high $\tilde{t}$ increases systematically with decreasing T, pending at ${g_1}^2 \approx 0.8$ at 25°C.

Thus, the DLS results confirm the loss of thermal reversibility in the probed T-range for these WF sample at this $[Ca^{2+}]$. The first T cycle creates a new sol/gel transition and strengthens the final structure. Here, one can imagine this due to a "trapping" of non-equilibrium gel states after the initial cooling. Many reasons may be attributable to this behaviour and it appears no literature shows similar phenomenon. Two possible reasons are suggested. The first one is related to the preparation and environmental conditions. When LMP is dissolved in fructose, water and sodium hexametaphosphate at $T \approx 85$°C, the $CaCl_2$ addition may not dissolve uniformly due to relatively high η of the solution. Even though the optical appearance of the solution never showed any inhomogeneities

through the solution, this may happen at a very small length scale. Once prepared, samples are cooled down to room T and this may not give enough time for homogeneous junction zone stabilization. This, in turn, is influenced by two other linked-variables: (i) an increase in the overall bulk η as T decreases, which reduces the diffusive motion of the Ca^{2+} ions through the sample; (ii) the balance between $SHMP$-Ca^{2+}. At $[Ca^{2+}] = 6$ mM, the calcium concentration may overcome the $SHMP$ effect (*i.e.*, LMP -COO^{-} saturation), reducing the chelation properties of the phosphate compound. Additionally, the reduced free water content due to the presence of fructose promotes the clustering of LMP chains. The combination of these variables strongly suppresses the internal dynamics of the sample. Possibly, when the $[Ca^{2+}]$ is reduced to 5.5 mM, the balance $SHMP$-Ca^{2+} may slow down the gel formation due to ion-chelated complexes. In this regard, the T effects previously presented for WF samples may be related to the very long-term behaviour in these samples *i.e.*, contextual utilization of temperature to speed up the kinetics of gel formatio This could be a very important point with respect to the industrial use of LMP in high sugar gels (with Ca^{2+}).

The second assumption may be related to the balance of water-fructose interactions, as explained earlier in the text. In this case, the strong fructose-fructose interaction may be destabilized when T is increased. This destabilization results in "free" fructose molecules that can bind more free water molecules to reduce the overall free water content in the whole system [96] [100] promoting the clustering of LMP chains. In Fig.4.16(d), one can see the change of the relaxation time as a function of T. This effect may be related to the breakdown of the fructose clusters. In fact, the q dependence for these data might allow the size of the clusters, found in section 3.2.1 [89]. However, due to the time-consuming nature of such tests it was not possible to carry out such measurements.

4.2.4 DLS set-up: Rheo-Speckle

As mentioned earlier, this is an innovative technique that couples rheology and DLS at fixed $\theta = 170°$ (additional details are given in the techniques chapter). The advantages of this technique for this particular study can be identified as follows. (i) Wide scattering angle means dynamics are probed at small length

scales. (ii) As seen previously in the DLS results, dynamically-arrested materials showed a plateau at high $\tilde{t}$, which means no information could be obtained for $\tilde{t} > 100$ s due to usual correlator limits. This aspect can be bypassed with the use of a CCD camera detector, extending the $\tilde{t}$ over $\approx 10^4$ s. In this $\tilde{t}$ range, g_{2-1} showing ultra-slow relaxations [71] [77]. (iii) The possibility to combine rheology and DLS tests in situ. In this case, it was decided to use a stress relaxation test to probe the long-term relaxation behaviour of the gels under study. (iv) This technique has never performed previously in pectin systems and the long term ageing behaviour of gels is of particular technological significance.

The test was split in two contiguous experiments: (i) in the first part, the spontaneous dynamics were probed, DLS with no stresses applied, probing any dynamical changes under quiescent conditions. (ii) In the second part, a stress relaxation experiment was performed with a step-strain of $\gamma = 1\%$ applied. A step-strain applied within the LVE should be followed by a time-dependent recovery (*i.e.*, relaxation) of the structure that approaches the equilibrium state, [59]. During the relaxation process, the local dynamics were additionally probed via DLS. In order to obtain more information on the thermal-irreversible WF samples, the temperature dependence was also investigated.

The spontaneous dynamics for W samples with $[Ca^{2+}] = 9$ and 6 mM are shown in the multi-panel Fig.4.17. Panels (a) and (b) show the C_i function vs. analysis time (t) for $[Ca^{2+}] = 6$ and 9 mM, respectively. The different traces corresponds to the different $\tilde{t}$. As shown, $\tilde{t} = 1$ s (red trace) C_i remains constant at ≈ 1 *i.e.*, saturation. On the other hand, at $\tilde{t} = 10000$ s, full decorrelation of the C_i function occurred, showing final value fluctuating around 0. These two values represent the upper and lower plateaus of the auto-correlation function g_{2-1}. The C_i values at intermediate $\tilde{t}$ describe the shape-decay of g_{2-1}.

Hence, values of g_{2-1} are calculated by averaging any selected t ranges and values are plotted vs. $\tilde{t}$. The output is shown in Figs.4.17(c) and (d) for $[Ca^{2+}]$ = 9 and 6 mM, respectively.

For $[Ca^{2+}] = 9$ mM, C_i (panel (a)) shows a continuous increase over t, where the plateau is reached at $\approx 7 \cdot 10^4$ s ($\approx$ 19 hours). The overall C_i functions show the low degree of noise, typical of gelled materials. Fig.4.17(c) shows the calculated g_{2-1} functions vs. $\tilde{t}$. As shown, g_{2-1} shifts at longer $\tilde{t}$ as a function of

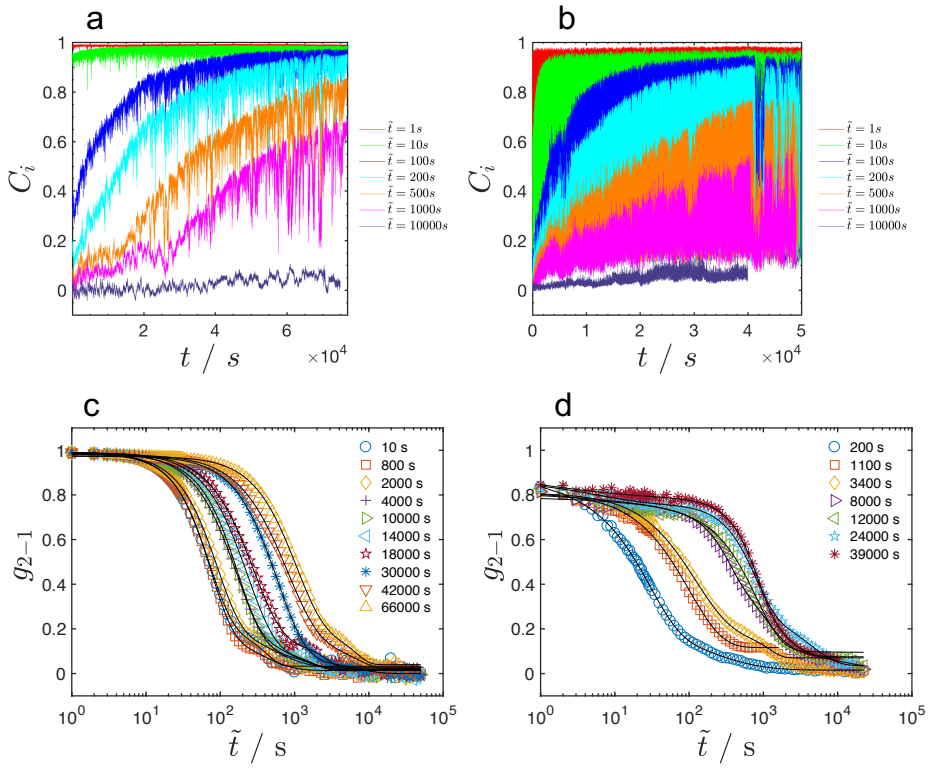

Figure 4.17: (a) and (c) C_i vs. t and relative g_{2-1} vs. $\tilde{t}$ for W sample and $[Ca^{2+}]$ = 9 mM, respectively. (b) and (d) Same as before, performed in W sample with $[Ca^{2+}] = 6$ mM.

the t. This gel curing effect could be an effect of the external stresses imposed imposed on the sample when transferred to the rheometer. In other words, this procedure may disrupt the gel structure to some extent, that is recovered during the experiment.

In the $\tilde{t}$ range between 1 and 10 s, g_{2-1} constantly fluctuates around 1. This plateau can be viewed as an extension of the one seen in conventional DLS (*e.g.*, Fig.4.6(a) for $[Ca^{2+}] = 9$ mM at $q \approx 20\ \mu m^{-1}$). However, the lack of q-dependence at these $\tilde{t}$ ranges does not allow a comparison between the height of the two plateaus given by the two different techniques. In all the cases, the full decay indicates the complete structural relaxation at the probed length scale (L) at large time-scales.

C_i vs. t for $[Ca^{2+}] = 6$ mM in Fig.4.17(b), shows a similar gel-curing be-

haviour. For this sample, C_i functions at a given $\tilde{t}$ show a slower increase, accompanied by a broader signal. These two aspects indicate the gel is even weaker. Calculated g_{2-1} signals vs. $\tilde{t}$ are shown in Fig.4.17(d). Here, few differences can be underlined: (i) at low $\tilde{t}$, the $g_{2-1\tilde{t}\to 0} \approx 0.8$, indicating less dynamical arrest at these $\tilde{t}$. In conventional DLS, the lowest plateau reached at $q \approx 24\ \mu m^{-1}$ was ≈ 0.4 (Fig.4.6(a)). The height difference between the two techniques may be attributable to experimental limits and the analysis method utilised in conventional DLS *i.e.*, smaller surface area of detection and averaged gel inhomogeneities.

At small t, g_{2-1} shows a fast exponential-relaxation that starts from $\tilde{t} = 1$ s. The gel-curing effect shifts the g_{2-1} decay to larger time-scales, indicating reassembling of the gel structure, lost due to mechanical stresses of sample preparation (similar to $[Ca^{2+}] = 9$ mM). Again, all the g_{2-1} functions shows a full decay, *i.e.*, complete relaxation, occurring at large $\tilde{t}$ (and large q). All the g_{2-1} functions were described with a multi component KWW (from 1 to 4 components), to determine the total relaxation time.

Once the spontaneous dynamics t limit was reached, a step strain was applied. The result for $[Ca^{2+}] = 6$ mM is shown in Fig.4.18(a). The G modulus response during the relaxation test approaches 2 Pa at the highest probed t. In the probed t, the modulus does not approach 0, indicating the solid viscoelasticity behaviour. However, (i) the vicinity to 0 indicates the weakness of the material and (ii) longer t may show additional decrease in G, indicating the liquid-like behaviour at even longer time-scales [59].

The inset of the figure shows the double logarithm plot of G vs. t. The overall relaxation is split into two parts: (i) fast relaxation region from $t = 0$ to $5{\cdot}10^3$ s and (ii) slow relaxation region for $t > 5{\cdot}10^3$ s. The fast relaxation may be attributable to the fast recovery of the applied stress of the main network. The slow mode may reflect to the long-term rearrangements of the structure over time. The latter suggest a continuous gel-curing behaviour, as seen elsewhere [76]. The dynamics measured via DLS and plotted as $< \tau >$ (red triangles in main plot), show a steep increase of $< \tau >$ that flattens at high t. The rheological and DLS analysis thus follow the same overall trend.

Fig.4.18(b) shows the $< \tau >$ values for the spontaneous and stress-relaxation tests. The red triangles show the curing effect that reaches a plateau at $t \approx 10^4$ s.

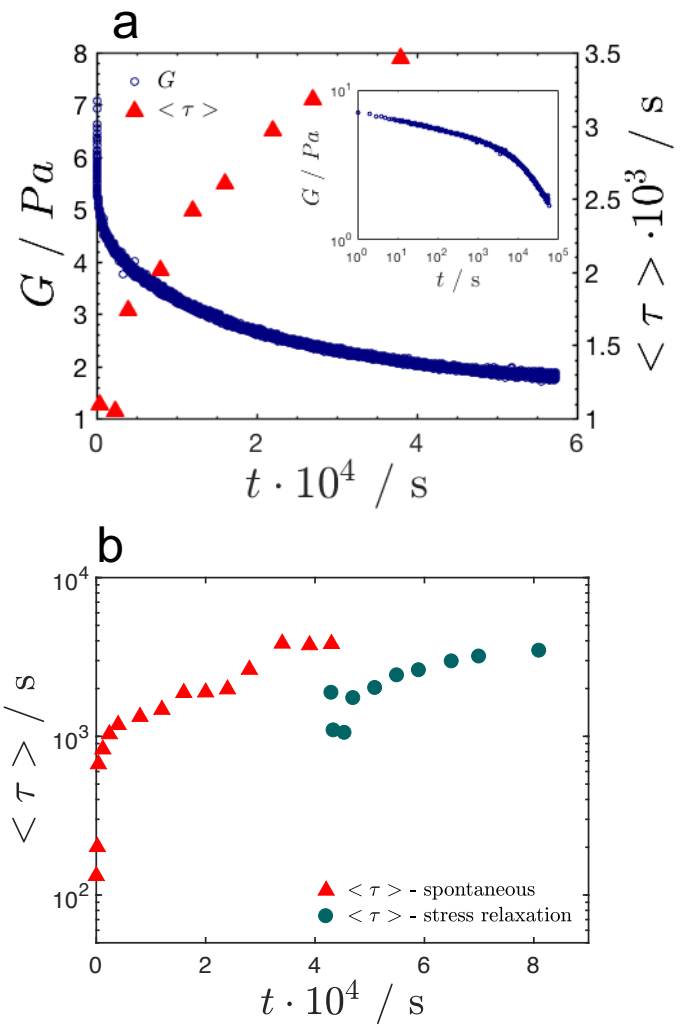

Figure 4.18: W sample at $[Ca^{2+}] = 6$ mM. (a) The main plot shows G vs. t for a stress relaxation test; the second y-axis shows $< \tau >$ vs. t from DLS, collected simultaneously to the stress relaxation test. Inset: double-logarithm plot for G vs. t. (b) $< \tau >$ values from spontaneous and stress relaxation test vs. the total analysis time t.

Immediately after the 1% step-strain, $< \tau >$ falls to $\approx 10^3$ s and starts to increase during the structure recovery/rearrangements, as described earlier in the text.

For WF samples at $[Ca^{2+}] = 5.5$ mM, spontaneous and stress relaxation tests were performed at $T = 25$, 45, 65 and 25°C, on the same sample. Figs.4.19(a) and

(b) show g_{2-1} vs. $\tilde{t}$ taken at 25°C before and after the T increase, respectively.

Before heating (Fig.4.19(a)), $g_{2-1\tilde{t}\to 0s} \approx 0.9$, indicating restricted dynamic fluctuations at this L. As shown, g_{2-1} slowly decays to 0 with a number of relaxation modes (*i.e.*, 2-3), suggesting a non-homogeneous structure. Due to the relatively high η of the media, the gel-curing effect appears rather small compared to *W-gels*.

Fig.4.19(b) shows g_{2-1} vs. $\tilde{t}$ plots of the *WF* sample after T increase to 65°C and subsequent cooling down to 25°C. From $t = 700$ s, g_{2-1} shows a progressive elongation of the plateau in the $\tilde{t}$ range 1 to 100 s. At the end of each plateau, *i.e.*, large $\tilde{t}$, g_{2-1} fully relaxes to 0, indicating full relaxation of the material.

Fig.4.19(c) summarizes the $< \tau >$ values at different t and T. As shown, the overall trend of $< \tau >$ is to decrease with the T increase *i.e.*, faster dynamics.

However, when T is restored to 25°C, the $< \tau >$ values are similar these collected before heating at the sample same temperature. Only for $t > 10^4$ s, the $< \tau >$ values are slightly higher. However, as discussed previously for panels (a) and (b), g_{2-1} change drastically the modality of decay, indicating more ordered structures mediated by the T.

Rather than reporting the raw data of the stress relaxation curve, it was decided to use a generalized Maxwell model [59] to describe the relaxation process as:

$$G(t) = \sum_i G_i \cdot e^{-\left(\frac{t}{\dot{\lambda}_i}\right)} \tag{4.4}$$

Where G_i is the G magnitude and $\dot{\lambda}_i$ is the characteristic time of relaxation for the i component. For all the systems, 5 components successfully described the entire G vs. t curve *i.e.*, $i = 5$. Estimated G_i and $\dot{\lambda}_i$ values were coinciding to the G vs. t experimental curve (data not shown). Fitted values and errors are shown in Fig.4.19(d) as G_i vs. $\dot{\lambda}_i$ for: (i) *W-gel* $[Ca^{2+}] = 6$ mM (red symbols) and (ii) *WF* sample $[Ca^{2+}] = 5.5$ mM at different T (*i.e.*, 25, 45, 65 and 25°C).

For the *W* sample, the first three $\dot{\lambda}_i$ points reflect the fast relaxation mode and the last two the slow one, as explained earlier in the text. For the *WF* sample at 25°C before heating, the characteristic time-scales are shifted towards lower t, compared to the *W* sample. Moreover, $\dot{\lambda}_i$ at high t show a shallower slow

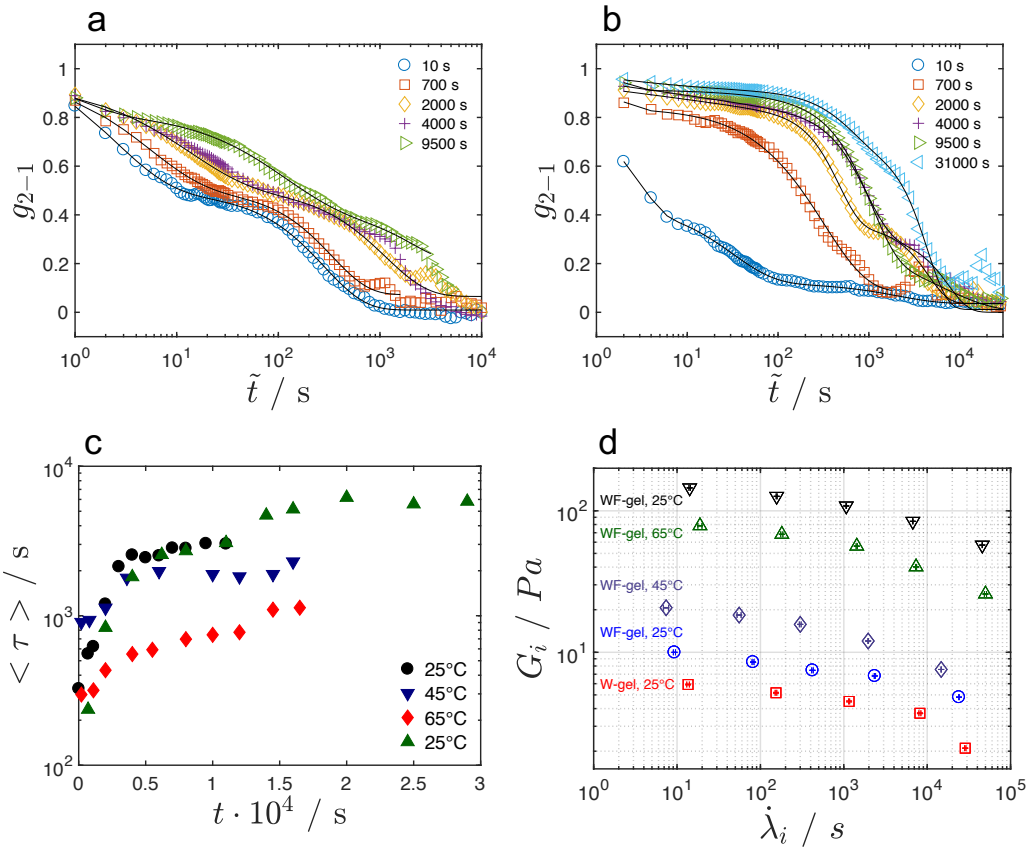

Figure 4.19: *WF* sample, $[Ca^{2+}] = 5.5$ mM. (a) and (b) g_{2-1} vs. $\tilde{t}$ at 25°C before and after heating to 65°C. (c) $< \tau >$ vs. t collected during spontaneous dynamics at different T. (d) G_i vs. $\dot{\lambda}_i$ obtained from the generalized Maxwell equation, collected at different T. Also, *W* sample and $[Ca^{2+}] = 6$ mM fitted values are plotted.

relaxation mode. This behaviour may reflect the incomplete junction zone stabilization in *LMP* chains, where viscous behaviour drives the material relaxation. In fact, the T increase to 45°C shows an additional shift of the overall $\dot{\lambda}_i$ towards lower t, due to η reduction. At the same time, G modulus increases to $G_0 \approx 20$ Pa.

Both a η reduction and G increase indicate that the initial step of network reinforcement is via junction zone stabilization, with the reduction in the viscosity enhancing the Ca^{2+} mobility through the sample. This conclusion was

also described in the section 4.2.3. At $T = 65°C$, G dramatically increases to $G_0 \approx 75$ Pa and all the $\dot{\lambda}_i$ shift to longer t. These changes highlight the dramatic strengthening of the WF samples.

At $T = 25°C$ (*i.e.*, after heating and cooling back to 25°C), in the WF sample (black symbols), G_0 dramatically increase to $\approx$ 150 Pa. In terms of $\dot{\lambda}_i$, the estimated time-scales correspond to the ones in the W sample, particularly in the $\dot{\lambda}_i \leq 10^3$ s limit. As seen in panels (a) and (b) of the same figure, the T cycle promotes a rearrangement of the structure, yielding a more homogeneous gel. Hence, being closer to the equilibrium gel state, the cross-linked LMP network shows fast relaxation characteristics, independently of the presence/absence of fructose.

The diverging time-scales at $\dot{\lambda}_i > 10^3$ s may reflect to long-term rearrangements of the structure/interactions. On the other hand, the G_0 increase solely due to the addition of 60% *wt.* fructose corresponds to $\approx$ 145 Pa.

The DSL analysis during the stress relaxation test showed a similar $< \tau >$ trend as reported in Fig.4.18(b) with the exception of $T = 45$ and 65°C. In these cases the step-strain showed no perturbation at the probed L and $< \tau >$ continued to increase over the analysis time t. In fact, the overall g_{2-1} vs. $\tilde{t}$ plots at different t collapsed onto each other.

4.3 Conclusions

This chapter highlighted the differences between LMP gels prepared without and with 60 *wt.* % fructose, mostly investigated via rheology and DLS techniques. A synoptic summary of the results is presented to aid the reader and (i) give a final overview of the work completed and (ii) to identify any additional investigation needed to clarify some aspects.

A. The junction zones stabilization via cross-links for 0.5 *wt.* % LMP in water start to occur at $[Ca^{2+}] > 4$ mM. Due to the weakness of the samples (*i.e.*, low density stabilized junction zones), oscillatory rheology characterization was only achievable for $[Ca^{2+}] \geq 6$ mM. The gel curing is a time-dependent event and it reaches stabilization only 6 days after preparation.

When prepared with 60 *wt.* % of fructose, LMP gel formation via Ca^{2+} ions showed a different behaviour. In particular, at $[Ca^{2+}] = 6$ mM, the WF sample did not show any ageing effect, with the $G^{'}$ modulus higher than the W sample at equal $[Ca^{2+}]$. Hence, the presence of 60 *wt.* % of fructose changes the final characteristics of the LMP gel.

B. Dynamics of the sol-gel transition were investigated with DLS at fixed q, 6 days after preparation. The overall results reflect the rheological characterization for both W and WF samples: (i) at low $[Ca^{2+}]$, the material undergoes full relaxation at probed L and time-scale and (ii) at high $[Ca^{2+}]$ (*i.e.*, gel state), full relaxation does not occur.

In WF samples, the sol/gel transition occurs in a very narrow $[Ca^{2+}]$, between 5.6 to 6 mM. However, the gel formation dynamics at the same q show different behaviour from W samples.

C. For W samples in the sol state with $[Ca^{2+}]$ between 0 and 4 mM, Λ shows a q^2 behaviour, characteristic diffusive character. Close to the sol/gel transition, at $[Ca^{2+}] = 4.5$ mM, ${g_1}^2$ decouples into two modes, a fast at low $\tilde{t}$ and slow at high $\tilde{t}$. In WF samples, two main relaxations processes occurred across the probed $\tilde{t}$ range. (i) A fast mode $< \tau >_F >$ at $\approx 10^{-5}$ s whose q dependence showed a q^2 behaviour, independent of the $[Ca^{2+}]$. (ii) A slow mode $< \tau >_S$ for $\tilde{t} \geq 10^{-4}$ s, whose q dependence showed a q^2 that increased up to $q^{3.3}$ with increasing $[Ca^{2+}]$.

For dynamically arrested materials, the height of the plateau in q-dependent indicates different dynamics, according to $q = L^{-1}$. Generally, increased $[Ca^{2+}]$ suppresses the dynamics in the entire range of investigated L. For W samples, data as a function of $[Ca^{2+}]$ were rescaled onto master-curve, describing the generality of the dynamic arrest in LMP gels. In the presence of fructose (*i.e.*, WF sample) the dynamic arrest is faster/greater than W at equal of $[Ca^{2+}]$. The data, described with a mean square displacement, allowed the estimation of the length scale of fluctuation of the scattered objects.

D. LMP gels are physical gels and they normally are thermally reversible. Rheological and DLS investigation on W samples at $[Ca^{2+}] = 6$ mM, confirmed this behaviour. Generally, the junction zone re-stabilization, after heating and cooling the sample, showed longer time for reformation. In WF samples, thermal-reversibility is lost. At $[Ca^{2+}] = 5.5$ mM, close to the sol/gel transition, the T

increase/decrease accelerated the kinetics of formation, with an improved strength of the final gel ($T = 25°C$). The DLS analysis at fixed q and different T highlighted the presence of a variety of relaxation processes, indicating the complexity of the system. The heating/cooling cycle may resolve the non-equilibrium trapped state in the WF samples. As elevated T is commonly used to speed up (anneal) formation, the non-equilibrium state may be resolved at very long ageing times.

E. The rheo-speckle tests performed on W samples and a WF sample at $[Ca^{2+}] = 5.5$ mM, gave further information on the gels. The spontaneous dynamics in W samples showed very long-time rearrangements of the scattering objects at $q = 31\ \mu m^{-1}$. In the WF sample, the time-scales before and after heating to 65°C and cooling back to 25°C, showed similar values. However, the change of the g_{2-1} function shape suggests a different relaxation mode of the material after heating and cooling. The stress-relaxation tests at different T showed different time-scales and amplitudes of the main G decay over time. Of particular interest was the relaxation time-scales of the WF sample after the T cycle. In this case, the fast relaxation mode in $t \leq 10^3$ showed time-scales comparable to the W sample. Hence, the fast relaxation mode shows similarity, whether the fructose is present or absent. In contrast, the slow relaxation mode $t > 10^3$ showed different behaviour in W and WF samples. This may reflect the long-term rearrangements, which are slowed down when fructose is present.

The overall complexity of gel formation in the presence of fructose needs further investigation. As explained earlier in the text, a concentrated fructose solution ($i.e \geq 60\ wt.\ \%$) shows intrinsic chemical-physical characteristics which alter the molecular organization of both water and fructose, hydration of the sugar. This may lead to the formation of water and/or sugar pockets in the solution *i.e.*, a water confinement effect, aspects of which are still under debate [40]. The addition of LMP to the system, further complicates the sample characteristics. In the first Chapter 3.4, the presence of a bigger L at a supramolecular level was suggested by $SALS$, which may heavily affect gel formation in LMP. Hence, it was decided to explore further the static properties, at an extended range of L, via different techniques and additional scanning electron microscopy work.

4. RHEOLOGICAL AND DLS CHARACTERIZATION OF GELS WITH AND WITHOUT FRUCTOSE

Chapter 5

SALS, SLS and SAXS characterization of gels

The aim of this chapter is to highlight the static properties of both sol and gel states via static scattering techniques. The present static scattering investigation aims to yield information at different q ranges via small angle light scattering ($SALS$), static light scattering (SLS) and small angle X-ray scattering ($SAXS$) for both W and WF samples at different $[Ca^{2+}]$. Furthermore, in the large q range investigated through $SAXS$ at variable temperatures, measurements were performed in order to understand the absence of thermal-reversibility observed in WF samples.

Static scattering characterization of both polymeric solutions and gels is rather complex [63][93]. Intrinsic chemical characteristics of the polymer molecule, polymer concentration and solvent conditions may drastically affect the data. As a consequence, analysis of data with specific models may yield different results, leading to different physical interpretations. Typically, for biopolymers, length scales characterizations are performed on finely tuned polymer molecules, *e.g.*, removal of side chains, impurities, *etc.* In this study, as already stated, the LMP utilised was not chemically modified or purified. Moreover, the LMP water dispersion did not contain electrostatic screening agents. The literature on LMP in both sol and gel states is scarce and most examples involve investigation via $SAXS$ experiments.

The following sections will describe the experimental results from the smallest to the largest q range probed.

5.1 Small angle light scattering

Small angle light scattering ($SALS$) is a useful technique to probe relatively large length scales, on the order of a few μm. The experimental details of this technique are presented in section 1.2.1. W and WF samples were compared in (i) their aged state and (ii) during ageing, when applicable.

The first investigation was performed on W samples with $[Ca^{2+}]$ = 0, 2, 4, 5, 6 and 9 mM in their aged state *i.e.* 6 days following their preparation. Results for these experiments are shown in Fig.5.1(a). For $[Ca^{2+}]$ between 0 and 5 mM, the scattered intensity $I(q)$ vs. q shows typical behaviour in which at low q, $I(q)$ plateaus (with $I_{q\to 0} \approx 4$ expressed in arbitrary units (a.u.)) and at large q the scattering assumes a power-law behaviour. As discussed in the polymer characterization chapter (section 3.4), the presence of a plateau towards low q values may be attributed to the crossover of the scattering from the distinct whole object and its internal structure [75]. The low value of q at which the $I(q)$ levels off, indicate a large supramolecular length scale (L) at the level is being probed [75]. In the $[Ca^{2+}]$ range investigated, Guinier plots yielded R_g values of $\approx 12 \pm 0.07\ \mu m$, within the $qR_g < 1$ limit. According to previous previous investigations, these larger L co-exist with smaller ones, that can be detected via SLS.

At large q, the plateau bends down asymptotically with a power law behaviour. The df exponent was determined with all the precautions described in section 3.4. In the $[Ca^{2+}]$ range from 0 to 5 mM, df increases from $\approx$ 1.4 to 2.0, suggesting more compact domains as the junction zone density increases. Knowledge of df was also used to determine the point where the $I(q)$ converges from a plateau to asymptotic regime. This point coincides with the correlation length ξ, corresponding to the average distance between interchain points and/or the length scale at which the system is considered uniform [92] as is indicated in Fig.5.1(a).

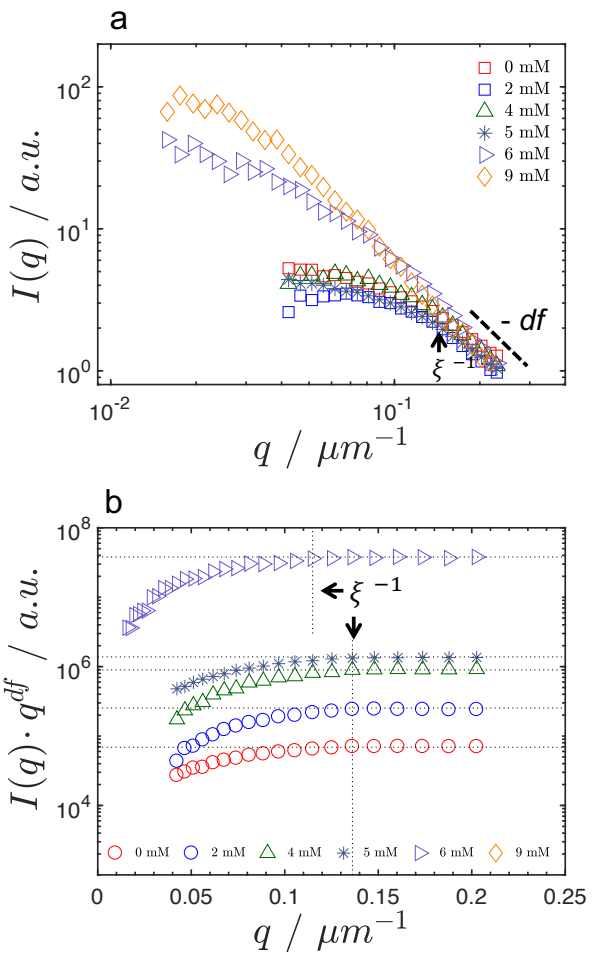

Figure 5.1: (a) $I(q)$ vs. q for W samples in a $[Ca^{2+}]$ between 0 and 9 mM; df and ξ^{-1} paramaters are reported as well. (b) $I(q) \cdot q^{df}$ vs. q plots for the graphical individuation of ξ.

As discussed in section 3.4, ξ can be estimated using the Ornstein-Zernike (OZ) function; for $[Ca^{2+}] = 0$ mM, $\xi = 8.40 \pm 0.11$ μm. For $[Ca^{2+}] > 0$ mM, the OZ relation was no longer applicable due to the presence of large structures, *i.e.*, deviation from linearity in Zimm plots. Therefore, the determination of ξ was performed using $I(q) \cdot q^{df}$ vs. q plots, shown in Fig.5.1(b). In these plots, the ξ value corresponds where $I(q) \cdot q^{df}$ diverge from being horizontal. As shown in Fig.5.1(b), the q value at which the shape of the $I(q)^{-1}$ changes remains constant in the $[Ca^{2+}]$ range between 0 and 5 mM. The corresponding ξ value of 7.3 μm was similar to that obtained using the OZ relation for the polymeric solution without Ca^{2+}.

At $[Ca^{2+}] = 6$ and 9 mM, the $I(q)$ vs. q data (panel (a)) show two common features which differ from lower $[Ca^{2+}]$: (i) increased magnitude of $I_{q\to 0}$ and (ii) $I(q)$ shows a high value of df at low q. However, there are two key differences between the signals obtained from these two samples. The sample at $[Ca^{2+}] =$ 6 mM shows a broader $I(q)$ signal over the q range which reflects the shape of the data obtained for lower $[Ca^{2+}]$. Moreover, $df \approx 2.2$, suggests more compact domains. From Fig.5.1(b)), the estimated ξ value for this sample was 8.7 μm, which is similar to the ξ values obtained at lower $[Ca^{2+}]$. In contrast, the $[Ca^{2+}]$ = 9 mM data show a sharp increase of the magnitude of $I(q)$ and the overall shape differs from other samples in this series. It is not possible to make a complete interpretation of this effect but one can speculate that large $[Ca^{2+}]$ may cause cross-links to form very quickly between LMP chains, with the formation of significant structural inhomogeneities in the samples. Also, the fast gel formation may interfere with the sample degassing operation prior to the $SALS$ test. At these q ranges, scattering from air bubbles might significantly affect the data.

The scattering results were compared with results from SEM investigations of W samples. Generally, the pectin molecules, associated with amorphous water, are shown as the white regions, whilst the black regions represent the cavities previously occupied by the sublimated water [16]. For these images, aged samples at $[Ca^{2+}] = 0$, 4, 6 and 9 mM were freeze-dried and then, analysed. As shown in Fig.5.2, in the $[Ca^{2+}]$ range between 0 and 6 mM ((a), (c) and (e) in Fig.5.2), the typical distance between the domains is similar to the estimated ξ values obtained from the $SALS$ analysis *i.e.*, $\approx$ 7-8 μm. Similarly, larger magnification images

of the same samples ((b), (d) and (f) in Fig.5.2) show the increased compactness of the domains as the $[Ca^{2+}]$ increases, reflecting the *df* values obtained. The difficult interpretation of the $SALS$ results at $[Ca^{2+}] = 9$ mM is exemplified by the SEM micrographs ((g) and (h) in Fig.5.2)). In this case, the structure appears very compact and almost collapsed.

To investigate the SAS properties during ageing, $[Ca^{2+}] = 5$ and 6 mM samples were scanned at different ageing times (t_a). Fig.5.3(a) shows the $SALS$ during ageing time for $[Ca^{2+}] = 5$ mM. Generally, the magnitude of $I_{q\to 0}$ systematically decreases with ageing and a clear plateau emerges at low q. At shorter values of t_a *i.e.*, 15 and 100 min, $df \approx 2.9$. At intermediate q, the $I(q)$ assumes a power law over which is indicated with the black star symbol in the plot. In the t_a range between 190 min to 2 days (for $t_a \geq 2$ days, the system reaches equilibrium), (i) $I_{q\to 0}$ decreases from ≈ 200 to 4 a.u. and (ii) *df* decreases from ≈ 2.6 to 2.0. As previously discussed, ξ was determined (inset in Fig.5.3(a)) and a value of ≈ 6 μm was obtained for all samples. Whilst ξ remains approximately constant, the more compact domains (increased *df* value) suggest structural rearrangements, as a function of t_a. Making this assumption, the explanation of this event may be related to the one ascribed to the cross-links induced by Ca^{2+}. On the other hand, there is no full explanation of the $I(q)$ behaviour at the early stages of ageing; possibly, this effect may be attributed to the high degree of L disorder and/or fluctuations due to water-induced LMP transport.

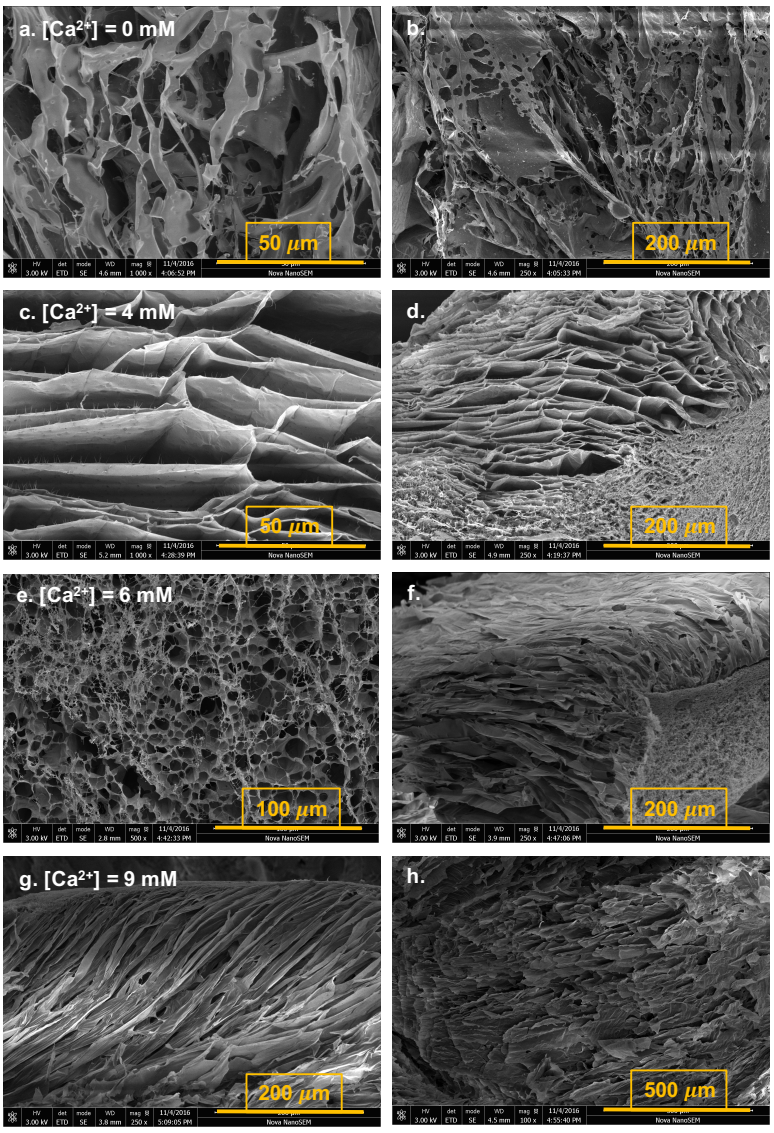

Figure 5.2: SEM micrographs for freeze-dried W samples at different magnification for: (a-b) = 0 mM, (c-d) = 4 mM, (e-f) = 6 mM and (g-h) = 9 mM.

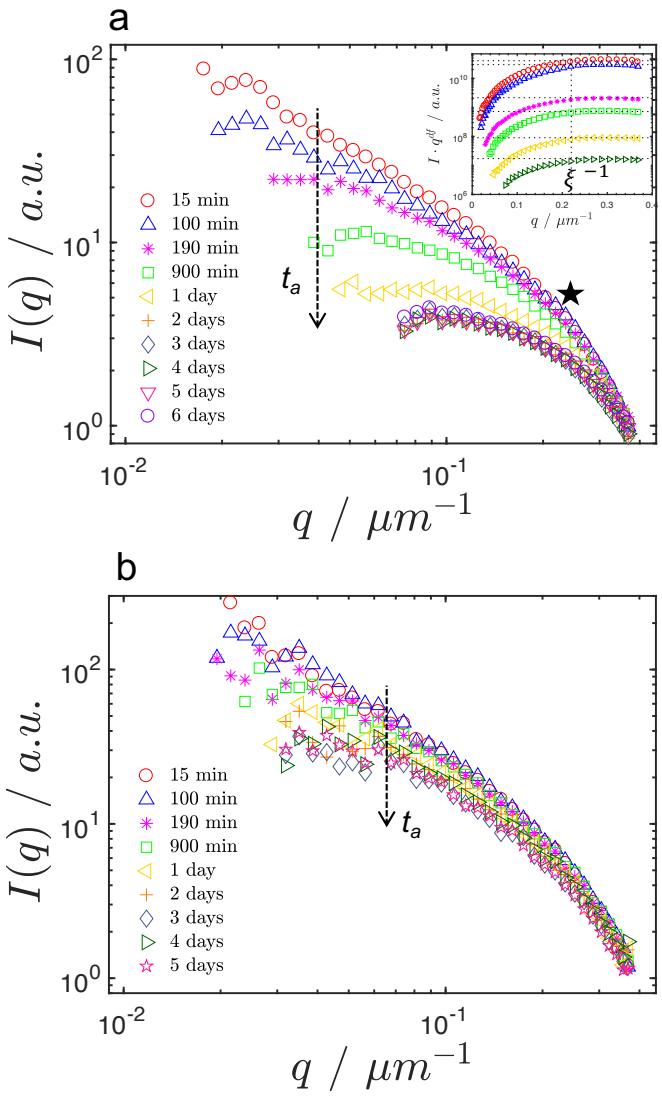

Figure 5.3: $I(q)$ vs. q plots for W samples during ageing. (a) $[Ca^{2+}] = 5$ mM, t_a and arrow show the ageing $I(q)$ pattern and the black star indicates the ξ^{-1} point. Inset: $I(q) \cdot q^{df}$ vs. q for the graphical extrapolation of ξ. (b) $[Ca^{2+}] = 6$ mM.

Fig.5.3(b) shows $SALS$ results for $[Ca^{2+}] = 6$ mM, where weak ageing effects were seen in the investigated q range. Similarly, the system appears to reach structural stability at $t_a \approx 2$ days. In this case, $R_g = 42 \pm 0.1\ \mu m$, as estimated using the Guinier approximation (at $t_a = 5$ days).

$SALS$ results for WF samples with $[Ca^{2+}] = 0$, 2, 4 and 6 mM are shown in Fig.5.4(a). The first feature of note is that the presence of 60 *wt.* % fructose yields dramatic changes in the behaviour of the $I(q)$ vs. q data. The $I_{q\to 0}$ values in the $[Ca^{2+}]$ range between 0 and 4 mM range have constant values at around $\approx$ 100 a.u. For $[Ca^{2+}] = 0$ mM, the $I(q)$ behaviour indicates bigger length scales, different to that obtained for the W samples. In the short range of the asymptotic behaviour, a df value of ≈ 4.3 suggests significant aggregation effects. In fact, $df \approx 4$ is typical of sharp interfaces that usually occur between the scattered object and the solvent. $I(q) \cdot q^{df}$ vs. q plots in the inset of the figure allow for the determination of $\xi \approx 3.5\ \mu m$. The smaller value of ξ, compared to the one estimated for the W samples at the same $[Ca^{2+}]$ ($\xi \approx 7.3\ \mu m$) may be attributed to the increased proximity of LMP chains due to the reduction of free water in the system. In fact, the Zimm plot ($I(q)^{-1}$ vs. q^2) for this sample did not show linearity, indicating the presence of structure. Together with the df value, this suggests either aggregation and/or formation of larger structures. In the low q regime, *i.e.*, the point at which $I(q)$ plateaus, the R_g estimated via the Guinier approximation, is $\approx 27\ \mu m$, approximately twice of that obtained in the W samples. At $[Ca^{2+}] = 2$ and 4 mM, the overall shape of the $I(q)$ data changes significantly at q values between 0.02 and 0.2 μm^{-1} whereas df is almost unvaried (*i.e.*, ≈ 3.5). The enhanced rolling off effect at higher $[Ca^{2+}]$ might be attributed to the reorganization of the LMP chains through the influence of Ca^{2+} ions. The formation of limited amounts of cross-links may stabilize the distances between the polymer chains, yielding more rigidity between the junction zones (or nodes); in fact, ξ was determined to be 3.9 and 4.3 μm for $[Ca^{2+}] = 4$ and 2 mM, respectively. However, this conclusion is purely speculative, since SEM analysis was not possible to perform on the WF samples.

At $[Ca^{2+}] = 6$ mM, df values at larger q shows similarity to $[Ca^{2+}] = 2$ and 4 mM however, for $q < 0.25\ \mu m^{-1}$, $I(q)$ continues to increase with no plateau. This suggests larger L, which cannot be determined in this q range. R_g obtained

via the Guinier approximation and ξ values for both W and WF samples as a function of $[Ca^{2+}]$ are summarized in Fig.5.4(b).

5.2 Static light scattering

Static light scattering (SLS) measurements were performed to probe the q range between 5 – 25 μm^{-1}. As previously discussed in section 3.3, R_g determination for $[LMP] = 0.5$ *wt.* % yielded not good approximations since the limit $qR_g > 1$ was exceeded. However, the flattening of $\Re_{q\to 0}$ suggests the presence of a plateau at lower q. The small plateau width was also observed as well by different authors [85][87][101].

Fig.5.5 shows $\Re$ vs. q data obtained at concentrations of $[Ca^{2+}] = 0$ and 6 mM for both W and WF samples. As shown, the data for W samples in both sol and gel states overlap for most of the probed q range. In particular, $\Re$ data in the q range between ≈ 10 and 24 μm^{-1} range shows a df value of 2.6. The df value cannot be directly related to the asymptotic regime obtained in $SALS$. In fact, as previously reported, the low asymptotic q ranges do not allow a direct comparison between the two techniques. The extension of the fit line highlights the broad downturn of $\Re$ in the lower q range. For the sample in the gel state (*i.e.*, $[Ca^{2+}] = 6$ mM), the $\Re_{q\to 0}$ clearly flattens off , suggesting the formation of a defined length scale. R_g estimated via the Guinier approximation yielded $\approx$ 0.2 μm but, again, $qR_g > 1$. Even though the $qR_g > 1$ condition is reached, the value is within the range of those obtained by Bulone *et al.* [85]. The estimated ξ for both $[Ca^{2+}]$ (*i.e.*, 0 and 6 mM) these samples were obtained via $\Re \cdot q^{df}$ vs. q plots and a value of ≈ 0.08 μm ($= 80$ nm) were obtained.

The results were compared to previous studies performed in cross-linked polyacrylamide gels. Generally, the greater the cross-link density, the larger the (i) the overall magnitude of $I(q)$ and (ii) q dependence [68] [93]. These two effects are due to the excess scattering contribution from large heterogeneities caused by the cross-links *i.e.*, spatial fluctuations of polymer concentration larger than a polymer solution at the same concentration. In this view, the so called "fluctuating part" ($< I_F(q) >_T$) was estimated as $< I_F(q) >_T = < I(q) >_E \cdot [1 - g_1(q, \infty)]$ where, $< I(q) >_E$ is the ensemble average of scattered objects (*i.e.*, renormalized

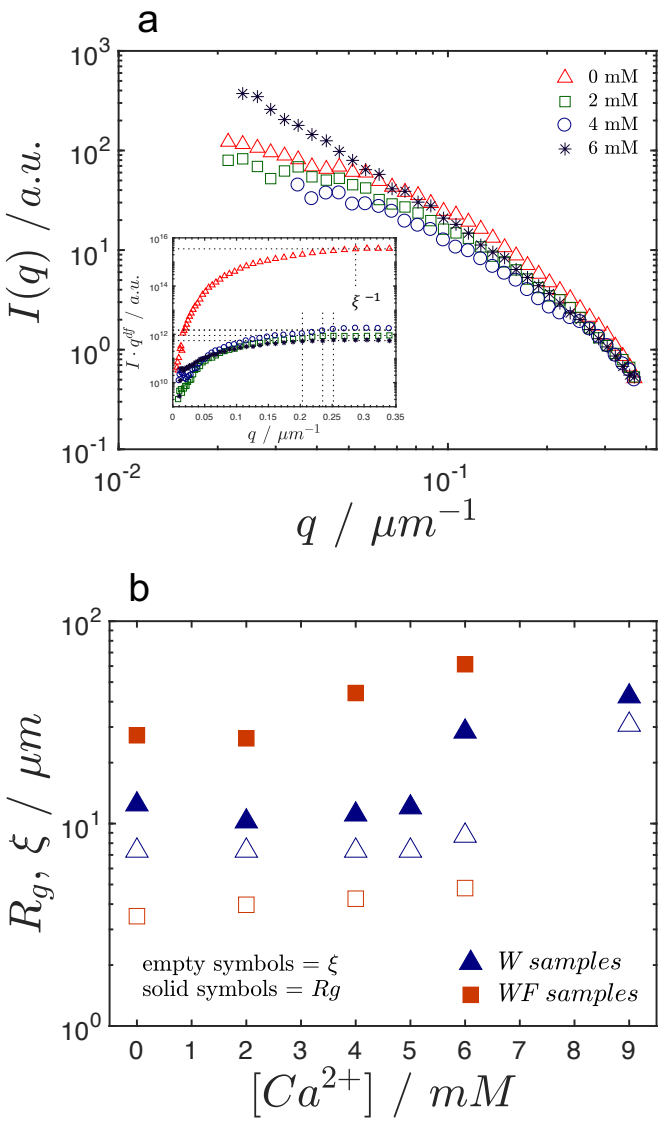

Figure 5.4: (a) $I(q)$ vs. q for WF samples at different $[Ca^{2+}]$, from 0 to 6 mM. The inset of the figure shows the $I(q) \cdot q^{df}$ vs. q plots for the graphical determination of ξ. (b) Summary of R_g and ξ values vs. $[Ca^{2+}]$ for both W and WF samples.

$I(q)$ collected during sample rotation, as described in the previous chapter) and $g_1(q,\infty)$ is the DLS g_1 value at $\tilde{t} \to \infty$ at given q. As a result, the $< I_F(q) >_T$ data obtained from the non-ergodic samples should collapse onto the data of the non cross-linked sample (*i.e.*, the polymer in solution with no cross links) [68]. In similar fashion, it was decided to use this model for W samples at $[Ca^{2+}] = 0$ and 6 mM. The fluctuating part was calculated from the renormalized intensity data, *i.e.*, $\Re$, and yielded constant values fluctuating around $< I_F(q) >_T \approx 3{\cdot}10^{-3}$ a.u. over the full q range. Thus, the difference in the amplitude of $\Re$ between the fluctuating part and the experimental $\Re$ at $[Ca^{2+}] = 6$ mM may represent an excess scattering contribution given by inhomogeneities. However, the fluctuating part cannot be directly compared with the $[Ca^{2+}] = 0$ mM sample, since the full decay to 0 in DLS yields $< I_F(q) >_T = < I(q) >_E$. Therefore, the $\Re$ vs. q remains unvaried, *i.e.*, $\Re$ for the polymer solution shows the same q dependence of the gel state.

Additionally, for $[Ca^{2+}] = 7$ mM, the $\Re$ data shows similar values to the $[Ca^{2+}] = 0$ and 6 mM data but $< I_F(q) >_T$ decreases to $\approx 9{\cdot}10^{-5}$ a.u. The results obtained are contradictory if the $< I_F(q) >_T$ data for gel and sol states are compared. In fact, one should expect the fluctuating part similar to the $I(q)$ obtained from the polymer in solution, *i.e.*, scattering profile with no q dependence. Nonetheless, both sets of data show a decrease of $< I_F(q) >_T$ with increasing $[Ca^{2+}]$.

With regards to the scattering profile of the polymer solution (*i.e.*, $[Ca^{2+}] = 0$ mM), one may expect that LMP in absence of cross-linking agent may form a structure, driven by hydrogen bonding between amide groups. Moreover, being the $[LMP]$ close to the C^*, the polymer chains interact strongly than a dilute regime. These potential explanations would require further investigations in order to confirm them, such as measurement of the scattering profile of low $[LMP]$ samples in presence and absence of screening agents (*e.g.*, $NaCl$).

For WF samples with $[Ca^{2+}] = 0$ and 6 mM, *i.e.*, sol and gel state, $\Re$ shows similar behaviours to the W systems. Here, $\Re_{q\to 0}$ shows less evident levelling off, suggesting larger structures. For both samples, $\xi \approx 0.06$ (63 nm). Similarly, the fluctuation part showed the same trend as W samples. Generally, the data obtained from SLS experiments on both W and WF samples provided limited

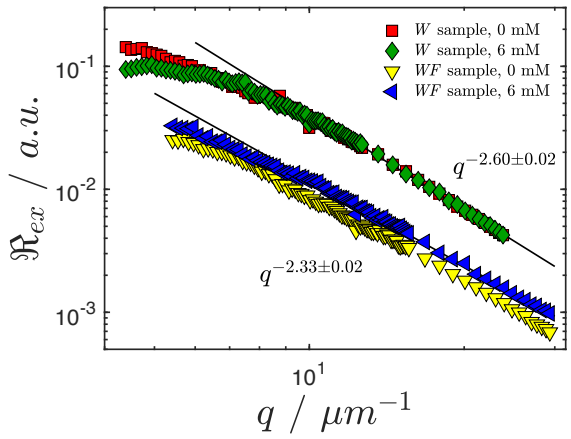

Figure 5.5: Excess Rayleigh ratio $\Re_{ex}$ vs. q for both W and WF samples at $[Ca^{2+}] = 0$ and 6 mM. Power laws at large q and relative values are reported as well.

information, as the R_g could not be estimated. The short and unclear levelling at $\Re_{q\to 0}$ means that the determination of a lenght scale is not possible. Both the Guinier approximation and other other models found in literature [75][85] were unsuccessful in describing the data *i.e*, the qR_q limit was always greater than 1. The determined ξ values may refer to a secondary correlation length at smaller length scales, coexisting with the larger length scale as determined through $SALS$ measurements.

The importance of the SLS results is their link with the hydrodynamic length scale obtained in DLS. Considering $R_h = 0.72\ \mu m$ and $\xi = 0.08\ \mu m$, this means that the DLS measurements probed an ensemble of ξ. The obtained df values seem to agree with previous experimental studies [102] in which the interpretation of the data suggested three-dimensional reaction-limited aggregation. However, this needs more investigation which is beyond the scope of this study. Finally, intermediate $[Ca^{2+}]$ were neglected from the last figure due to the similarity of the magnitude of $\Re$ and the lack of signal at small q ranges ($\theta < 30°$).

5.2.1 Superposition of SALS and SLS data

The asymptotic region at large q in the $SALS$ data and the possible emergence of a plateau at low q in the SLS data raises the question: what is the behaviour of $I(q)$ in the intermediate q range? Whilst the static properties gathered in $SALS$ and SLS analysis for both W and WF samples in sol and gel states were discussed separately in the previous sections, this section will focus on this intermediate q range. The aim of this part is try to make a *I(q)* master curve to understand the low and middle q ranges.

To facilitate rescaling between the intensities of the scattering results obtained by the two light scattering setups, a solution of melamine particles , [C] = $2.86{\cdot}10^{-5}$ *w/w* (batch MF-R-S1706, Micro Particles Gmbh, DE) with a diameter of 2.05 μm, polydispersity 0.04 % was measured using both $SALS$ and SLS. A theoretical curve calculated via Mie theory (MiePlot, http://www.philiplaven.com/mieplot.htm) using the the characteristic properties of the melamine particle suspension (radius = 1.025 μm, $\lambda = 0.635$ μm; $n_{solvent} = 1.33$; $n_{particle} = 1.68$; polydispersibility = 2% Gaussian, provided good interpolation of the $SALS$ data. The Mie curve and $SALS$ data were rescaled by a factor of 4 onto the $\Re$ data obtained in SLS experiments.

The result of this rescaling are shown in Fig.5.6(a) for W samples and (b) for WF samples, using data obtained for $[Ca^{2+}] = 0$ and 6 mM. Also, in panel (a), the theoretical Mie-curve and the SLS data obtained for melamine particles are shown. In Fig.5.6(a), the rescaled $I(q)$ vs. q data obtained for the W samples do not show continuity as a straight line with a characteristic df. The behaviour of the $I(q)$ data at the terminally/initially probed q collected with $SALS$ and SLS suggests that there could be a plateau of $I(q)$ in the intermediate q range. The data for the WF samples in Fig.5.6(b) show a similar behaviour. Unfortunately, previous literature studies for these particular systems in the intermediate q range are scarce and the data obtained do not appear to follow the same behaviour.

Similar studies, in guar gums and rubber fillers, show $I(q)$ values which span several decades in q with a constant fractal dimension df [75] [103]. To quantify the observed behaviour in this study an additional LS technique, covering the intermediate q range, is needed. As pointed out in the last paragraph of the SLS

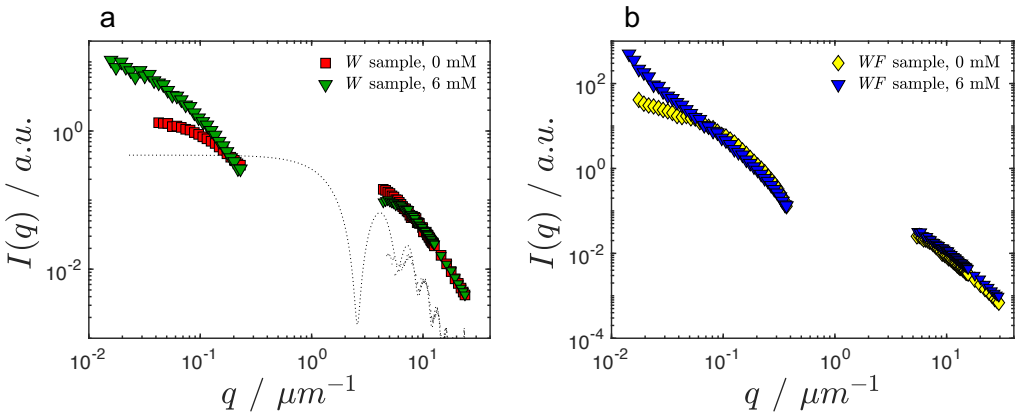

Figure 5.6: (a) Combined $SALS$ and SLS data for W samples with $[Ca^{2+}] = 0$ and 6 mM. Theoretical Mie curve and SLS data for melamine particles are shown as well. (b) Same as before, for WF samples with $[Ca^{2+}] = 0$ and 6 mM.

section, $qL > 1$. In the very small q range, this limit exceeds 1 by a few decimals (*i.e.*, 1.120 onwards), yielding $L \approx 0.2\ \mu m$ via the Guinier approximation. Hence, the possible presence of the plateau in the missing q range may indicate a proper Guinier regime, for which $qL < 1$. In fact, as reported in [85], the typical L value calculated, but for HMP, fluctuates around 0.16 – 0.19 μm.

5.3 Small angle X-ray scattering

To investigate larger q and the local structures of both the sol and gel states, small angle X-ray scattering ($SAXS$) was utilized. The results shown in this section were collected at the Diamond Light Source synchrotron facility (beamline I22), since the X-ray equipment available at the University of Leeds did not have sufficient power to investigate the systems studied. The first part of the results show a comparison between aged ($t_a = 6$ days) W and WF samples at 25°C. The second part will highlight the features of the data obtained for both W and WF samples at different temperatures T, relevant the thermal reversibility/irreversibility features described in section 4.2.3. Relatively simple data representation and models will be used to describe this data.

5.3.1 SAXS measurements of aged *W* and *WF* samples

Fig.5.7(a) shows the $SAXS$ profiles for W samples at $[Ca^{2+}]$ = 0, 4, 5, 6 and 8 mM. As shown, $I(q)$ increases as a function of $[Ca^{2+}]$. For both $[Ca^{2+}]$ = 0 and 4 mM, $I(q)$ shows compact structures [104] in the q range between $6{\cdot}10^{-3}$ and $1.7{\cdot}10^{-2}$ Å^{-1}, with a $q^{-3.3}$ and $q^{-3.0}$, respectively. The transition between the df regime at low q and the change of the q-dependence at intermediate/low q lies at $q^* \approx 0.02$ Å^{-1} for both $[Ca^{2+}]$ = 0 and 2 mM. q^* denotes the $q-$limit at which the scattering arises from local structures [15]. For $[Ca^{2+}]$ = 0 and 4 mM at $q > q^*$, the correlation length was estimated using the OZ relation, combined with a power-law. This, allowed to take account of all the $I(q)$ contributions of the sample (Fig.5.8(a))

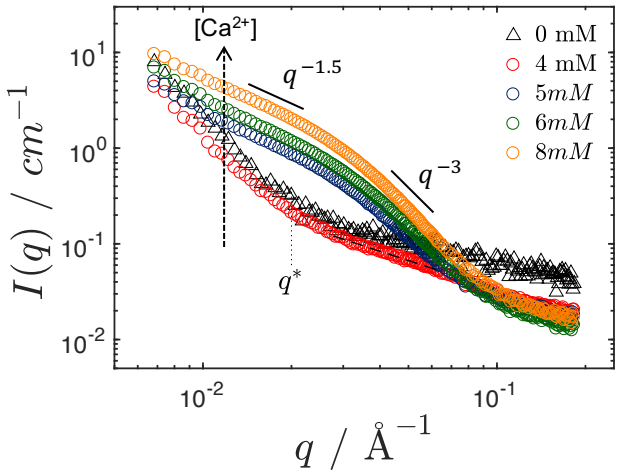

Figure 5.7: $I(q)$ vs. q plots for $SAXS$ results for W samples at different $[Ca^{2+}]$.

As shown in Fig.5.8(a), the composite fit successfully described the data. ξ values obtained from the OZ relation were 13.7 ± 0.5 Å and 16.9 ± 0.2 Å for $[Ca^{2+}]$ = 0 and 4 mM respectively. At low q, a power law of ≈ 3 was obtained. Similar ξ values for LMP have previously been obtained in the literature, for example Ref. [92], *i.e.*, ≈ 18 Å. The ξ value corresponds to the distance between neighbouring chains (Fig.5.8(b)). Where aggregation effects are present, ξ may be overestimated due to polymer-rich regions that increase the overall ξ distances,

as drawn in panel Fig.5.8(c). Even though ξ for $[Ca^{2+}] = 0$ mM may be overestimated, the increased distance obtained for $[Ca^{2+}] = 4$ mM may be attributed to the enhanced reorganization of the LMP chains due to Ca^{2+} ions. This promotes an increase of the electron density at the level of the junction zones, enhancing the scattered signal.

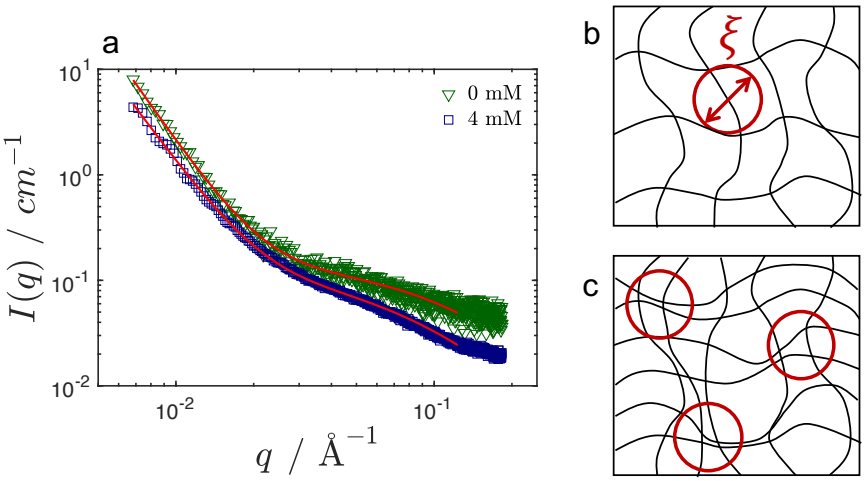

Figure 5.8: (a) $I(q)$ vs. q for W samples at $[Ca^{2+}] = 0$ and 4 mM. Fit line from composite fit, *i.e.*, power law and Ornstein-Zernike relation for the respective samples. (b) Graphical representation of ξ, typical of semi-dilute polymers solutions. (c) Inhomogeneities effects on semi-dilute polymer solutions and/or cross-links between polymer chains.

The $I(q)$ behaviour for the gel states *i.e.*, $[Ca^{2+}] = 5$, 6 and 8 mM in Fig.5.7, generally show a concave downward shape (with respect to the q axis) with $I(0)$ values that increase as a function of the $[Ca^{2+}]$. The present results are in agreement with $SAXS$ data obtained in Ref. [105] for LMP. The power law exponent changes from $\approx q^{-1.5}$ at low q to $\approx q^{-3}$ at large q (indicated in the figure), corresponding to rough surface fractals.

A graphical $SAXS$ representation typically used for biopolymers is the so-called Kratky plot. The transformed $I(q)$ in Kratky plots, *i.e.*, $I(q) \cdot q^2$ vs. q, highlight the degree of flexibility of the scattering object [106]. Kratky plot for W gels are shown in Fig.5.9. Generally, $I(q) \cdot q^2$ has a parabolic-like peak at low q, followed by an elevated baseline at large q. The height of the baseline

at large q indicates the degree of flexibility of the scattered object. Thus, when the parabolic peak terminates to the baseline (at large q), the object has low flexibility (*i.e.*, more rigid structure). In contrast, the further elevation of the hyperbolic peak at large q (*i.e.*, higher $I(q) \cdot q^2$ values than the peak), is typical of random coils or Gaussian chains [106] [107] [62].

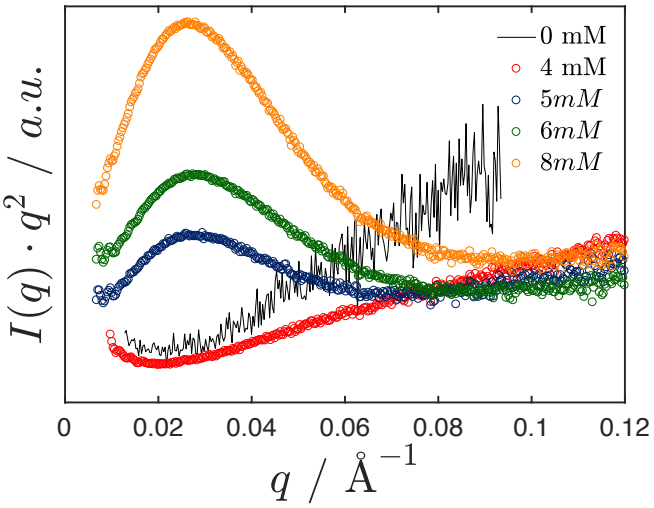

Figure 5.9: Kratky plots as $I(q) \cdot q^2$ vs. q for W samples at different $[Ca^{2+}]$.

Combined experimental and molecular simulations studies performed by Schuster *et. al.* [92] related the degree of the overall flexibility linked to the number of cross-linked chains in LMP samples. Theoretical curves for our study were not calculated, but the experimental results seem to agree with the data presented by Schuster *et al.*, *i.e.*, a narrow parabolic peak suggesting an ensemble of large bundles of rod-like LMP chains of limited flexibility and therefore increased persistence lengths.

The data obtained for W samples as a function of $[Ca^{2+}]$ were compared to data obtained for WF samples. The $SAXS$ data for both are displayed in Figs.5.10(a) and (b). $[Ca^{2+}] = 0$ mM shows a $q^{-2.5}$ behaviour in the q range between $\approx 6{\cdot}10^{-3}$ and $2{\cdot}10^{-2}$ Å^{-1}, which flattens with no significant q dependence at intermediate and large q. This effect may be related to the low electron density

contrast, as previously described for W samples. The $[Ca^{2+}]$ increase to 4 mM showed similar behaviour to the W sample at same $[Ca^{2+}]$. In this case, at low q, $q^{-3.5}$ (vs. q^{-3} in the W sample) and $q^{-0.95}$ at large q (vs. $q^{-1.0}$ in W sample). The q^* parameter shifts to ≈ 0.026 Å^{-1}, corresponding to a L_p value of ≈ 73 Å (vs. $L_p \approx 95$ Å obtained for the W sample). The ξ value calculated via the OZ equation was 14.1 ± 0.3 Å, similar to that obtained for the W sample at the same salt concentration. At $[Ca^{2+}] = 5$ mM, the $I(q)$ vs. q data shows a similar shape to the W sample (Fig. 5.7) with increasing $I(0)$. Compared to the W sample at the same $[Ca^{2+}]$, the curve appears broader, with $q^{-2.3}$ behaviour at large q (vs. q^{-3} behaviour for the W sample). At $[Ca^{2+}] = 5.5$ mM, the $I(q)$ data show unexpected behaviour, with a trend similar to polymeric solutions and with an $I(0)$ value lower than $[Ca^{2+}] = 4$ mM. As discussed in the previous chapter, at this $[Ca^{2+}]$ and around the onset of gelation, one may expect trapping of a non-equilibrium structures. The excess Ca^{2+} may be not compensated with $SHMP$ and therefore, localized gelation may occur. This effect is clearly demonstrated for the $[Ca^{2+}] = 6$ mM sample. Lastly, at $[Ca^{2+}] = 8$ mM, a $q^{-3.5}$ dependence at low q (aggregation effects) is followed by the typical concave shape at intermediate/large q.

The Kratky representation of the data in Fig.1.15(b) shows consistency between $[Ca^{2+}] = 4$ mM in the sol state and $[Ca^{2+}] = 5$ mM in the gel state. For the gel state, the centre of the hyperbolic-like curve lies at ≈ 0.05 Å^{-1} ($1/q \approx 20$ Å), higher than ≈ 0.03 Å^{-1} ($1/q \approx 34$ Å) obtained in W samples in gel state. The lower size in WF samples may indicate more packed domains, due to the presence of fructose. For $[Ca^{2+}] = 8$ mM, the peak is poorly defined due to greater aggregation effects at low q (*i.e.*, upturn of $I(q)$).

Non-homogeneous gel formation for $[Ca^{2+}] > 5$ mM suggests the presence of rich junction zones areas (lumps), coexisting with smaller ones. These possible lumps may lead to phase separation, *i.e.*, large condensed lumps that lead to local syneresis. As seen in the previous chapter, this non-equilibrium condition in WF samples is temperature dependent.

According to the literature, the total scattered intensity $I(q)$ for polymeric gels contains an additive contribution of the polymer ($I(q)_L$, Lorentz function)

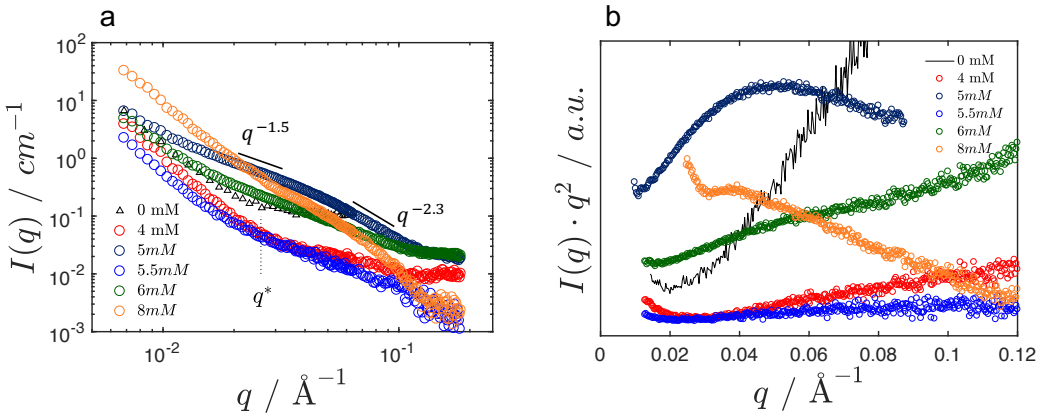

Figure 5.10: (a) $I(q)$ vs. q for WF samples at different $[Ca^{2+}]$. (b) Kratky plots for the same samples.

and the excess scattering from inhomogeneities ($I(q)_G$, exponential function) [62] [107] [93] [108]. The Lorentz-Gauss Gel (GL) model for gel structures was applied:

$$I(q) = I(0)_G \cdot exp^{\left(-\frac{q^2\Xi^2}{2}\right)} + \frac{I(0)_L}{(1+q^2\xi^2)} \tag{5.1}$$

where $I(0)_G$ and $I(0)_L$ are the $I(q)$ at $q = 0$ for the gel and sol contributions respectively. Ξ is the static correlation length, attributed to the average size of long-lived cross-links [108]; ξ is the (dynamic) correlation length (*i.e.*, corresponding to the OZ relation), which refers to length scale fluctuations between cross-links. The results for both W and WF samples are displayed in Fig.5.11.

For the W samples, the GL model described the scattered curves up to $[Ca^{2+}]$ = 5 mM, where both sol and gel contributions were identified. For higher $[Ca^{2+}]$, the total $I(q)$ magnitude is due to the excess scattering of the inhomogeneities (junction zones). Therefore, ξ was no longer estimated. On the other hand, Ξ values show constant values for $[Ca^{2+}] \geq 5$ mM, suggesting the typical size ($\approx$ 60 Å) of the junction zones between LMP chains. For WF samples with $[Ca^{2+}]$ = 4 and 5 mM, ξ shows a similar trend to the W samples. However, no further information were yielded for higher $[Ca^{2+}]$.

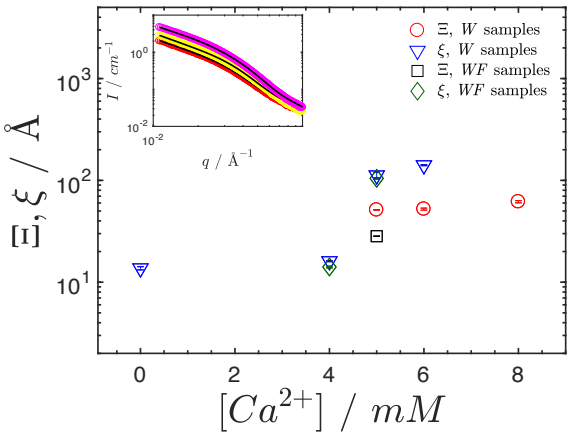

Figure 5.11: Ξ and ξ vs. $[Ca^{2+}]$ for both W and WF samples. The inset of the figure shows the GL fitted lines for W samples.

5.3.2 Temperature dependence of *W* and *WF* samples

Temperature-dependent measurements for W samples, $[Ca^{2+}] = 6$ mM, and WF samples, with $[Ca^{2+}] = 5$, 5.5 and 6 mM, were performed at (i) $T = 25 \rightarrow 65°$ and (ii) $T = 65 \rightarrow 25°$. The results are shown in Fig.5.12. The top row of the figure shows data obtained with increasing T (T_{UP}), whereas the bottom row shows the data obtained with decreasing T (T_{DOWN}). The inset of each figure shows the equivalent Kratky plots.

Generally, the data for W samples (panels (a) and (a')) shows no significant features in terms of $I(q)$ vs. q. However, the Kratky plots highlight some flexibility changes as T is increased. In fact, the peak height decreases systematically from 25 to 45°C but increases from 55°C. This increase stops at $T = 65$°C, where the peak height corresponds to the one obtained at 25°C. However, the sharper shape and the complete decay at larger q, suggests more compact domains (*i.e.*, less LMP flexibility due to cross-links). As discussed earlier, increasing T accelerates gel-curing kinetics, decreasing the degree of cross-link rearrangements at very long ageing times. The data obtained upon decreasing T to 25°C (panel (a')) show no significant temperature effects.

T effects become more notable in the presence of fructose. Generally, by in-

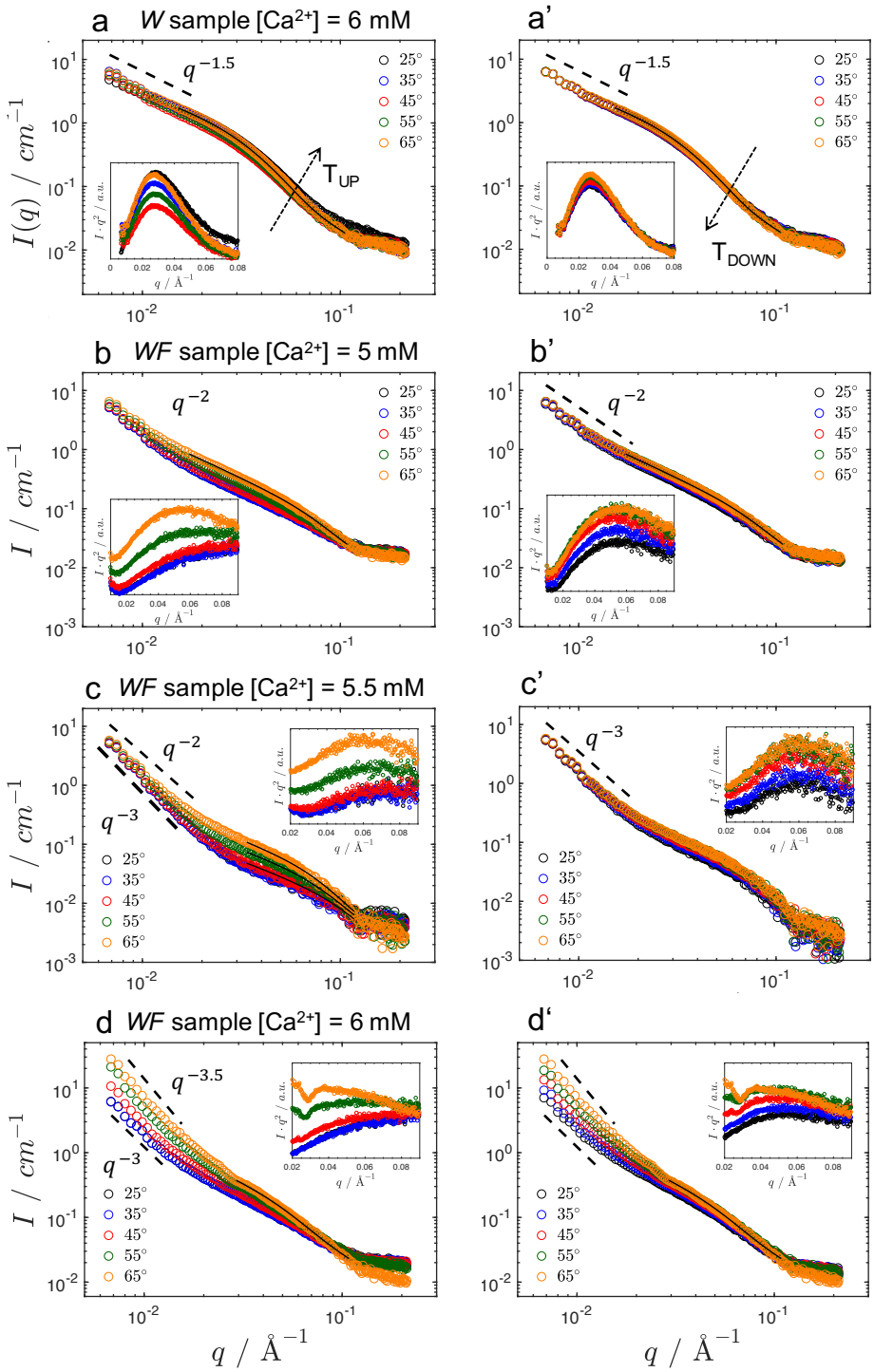

Figure 5.12: First row: $I(q)$ vs. q plots for T increase from 25 to 65∘C. The inset of each figure shows the Kratky representation. Second row: same as before, in a T range from 65 to 25∘C. (a), (a') W sample with $[Ca^{2+}] = 6$ mM; (b), (b') WF sample and $[Ca^{2+}] = 5$ mM; (c), (c') WF sample and $[Ca^{2+}] = 5.5$ mM; (d), (d') WF sample and $[Ca^{2+}] = 6$ mM.

creasing the $[Ca^{2+}]$ from 5 to 5.5 mM (panels (b) and (c)), one can see two main changes: (i) lengthening of $I(q)$ at low q, accompanied by a gradient change (indicated in the figures); (ii) the typical hump of the gel state in $I(q)$ is shifted towards larger q (*i.e.*, $\approx 2.5 \cdot 10^{-2}$ and $2.5 \cdot 10^{-2}$ Å^{-1} for $[Ca^{2+}] = 5$ and 5.5 mM, respectively) and its shape changes drastically with increasing T. The Kratky plots highlight the T effects, suggesting the formation of more equilibrated gels *i.e.*, more compact domains. The data obtained upon decreasing T to 25°C in $[Ca^{2+}] = 5$ mM (panel (b')) shows a broad hyperbolic peak with an elevated baseline at larger q *i.e.*, indicating enhanced flexibility. Similarly, the data obtained for decreasing T for the $[Ca^{2+}] = 5.5$ mM sample (panel (c')) shows a consistent $I \cdot q^2$ change. For this sample, however, the elevation at large q cannot be identified due to the significant signal noise.

At $[Ca^{2+}] = 6$ mM (panel (d)), $I(q)$ data shows a power-law scaling at low q, due to aggregates. At larger q, the gel shoulder shifts to $5 \cdot 10^{-2}$ Å^{-1}, a value much larger than obtained for lower $[Ca^{2+}]$. Here, changing T strongly effects the $I(0)$ value and the q dependence (*i.e.*, slope). Again, the Kratky plots in the figures inset, highlight the formation of more compact domains driven by the T modulation.

A quantitative description of the data was performed by using (i) the Lorentzian part of Eq.5.1 for samples in sol state and (ii) the GL function for samples in the gel state (fit lines shown in Figs.5.12). Due to the excess $I(q)$ noise at large q, the determination of ξ was unreliable for some samples. This is particularly accentuated in the data obtained for the WF sample with $[Ca^{2+}] = 5.5$ mM. Figs.5.13(a) and (b) show ξ and Ξ vs. T, for both W and WF samples at given $[Ca^{2+}]$.

The dynamic length scale ξ for the W sample with $[Ca^{2+}] = 6$ mM obtained at different T is constant, fluctuating around 200 Å (Fig.5.13(a)). The initial ξ increase at $T_{UP} = 25$ to 45°C may be attributed to a reorganization of the mesh size throughout the sample. The respective inhomogeneity size Ξ for this sample was estimated around 50 Å, with no changes observed in the probed T range (Fig.5.13(b)). In the presence of fructose and $[Ca^{2+}] = 5$ mM, ξ values increases from 35.9 ± 0.9 to 126.7 ± 5.9 Å in the T range from 25 to 65°C. Upon decreasing T, ξ remains unvaried at ≈ 130 Å (panel (a)). For this sample, Ξ (panel (b))

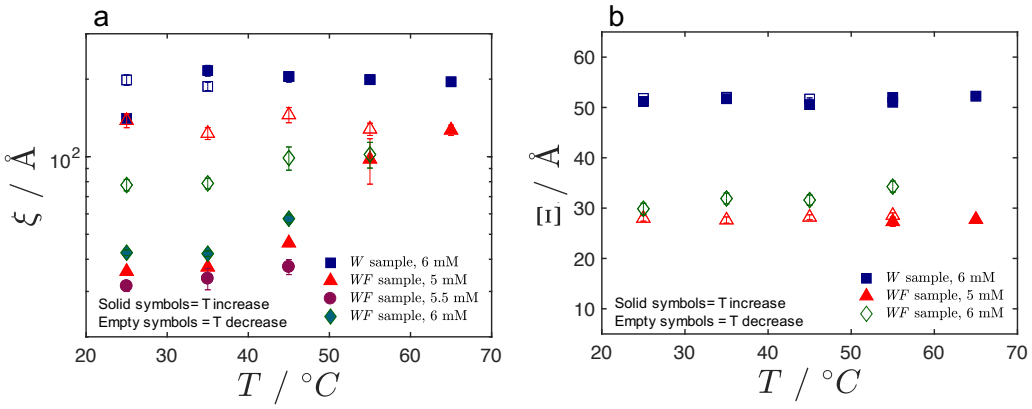

Figure 5.13: (a) ξ values vs. T for both W and WF samples. (b) Inhomogeneities length scales as Ξ vs. T for the same samples.

decreases to $\approx$ 30 Å. Hence, the presence of fructose indicates a narrower mesh size and smaller junction zones than for the W sample. The ξ reduction may be attributed to the reduced free water in the system, which promotes an increase in the proximity of LMP chains, as proposed elsewhere [2]. At the same time, smaller junction zones may be due to the sugar molecules that can interfere with the cross-link formation [96]. Similar ξ and Ξ vs. T trends are observed for the WF sample with $[Ca^{2+}] = 6$ mM as well. However, the dynamic length scale is further reduced when the system is cooled down to 25°C *i.e.*, $\xi \approx 80$ Å. This could be due to a higher tendency towards aggregation at lower q, that affects $I(q)$ at large q

Thus, it appears that the $SAXS$ technique also detects the non-equilibrium gel state in the presence of fructose. The reorganization of distances between junction zones of the LMP chains affect larger length scales structures, changing both the mechanical and dynamic properties of WF gels.

5.4 Conclusions

In this section the aim is to summarize all the characteristic length scales obtained by the different SAS techniques used. The cartoon in Fig.5.14 describes the possible gel structural configurations at different length scales, in the presence or

absence of fructose at $[Ca^{2+}] = 6$ mM. The specific length scales reported for the *WF* sample are those extracted from the scattering data after the *T* cycle.

As illustrated, the different techniques show that, the presence of fructose appears to decrease the overall mesh sizes (ξ) of the system, probably due to the reduced free water in the system, bound by the fructose molecules. Narrow meshes with smaller junction zones may be responsible for the enhanced mechanical properties and slow dynamics as reported in rheological and DLS characterization. According to Flory's network cross-link density (ρ_x) [108], one can relate ρ_x to the mesh size ξ. Ideally, the empty volume associated with each cross-link is a sphere, centered at the cross-link, with a diameter equal to ξ [108]. Thus:

$$\xi = \sqrt[3]{6/(\pi \rho_x N_A)} \tag{5.2}$$

According to Fig. 2.15, ρ_x for *WF* sample at $[Ca^{2+}] = 6$ mM ≈ 0.013. The relative ξ calculated via Eq. 5.2, yields 65 nm, which is approximately the same calculated from *SLS* data ($\xi \approx 60$ nm). Hence, the relaxation modes detected with *DLS* experiments (Fig. *2.17*) appear to refer to an ensemble of cross-links with size Ξ (3 nm) and a spacing of 15 nm. Similar values were yielded for the *W* samples as well.

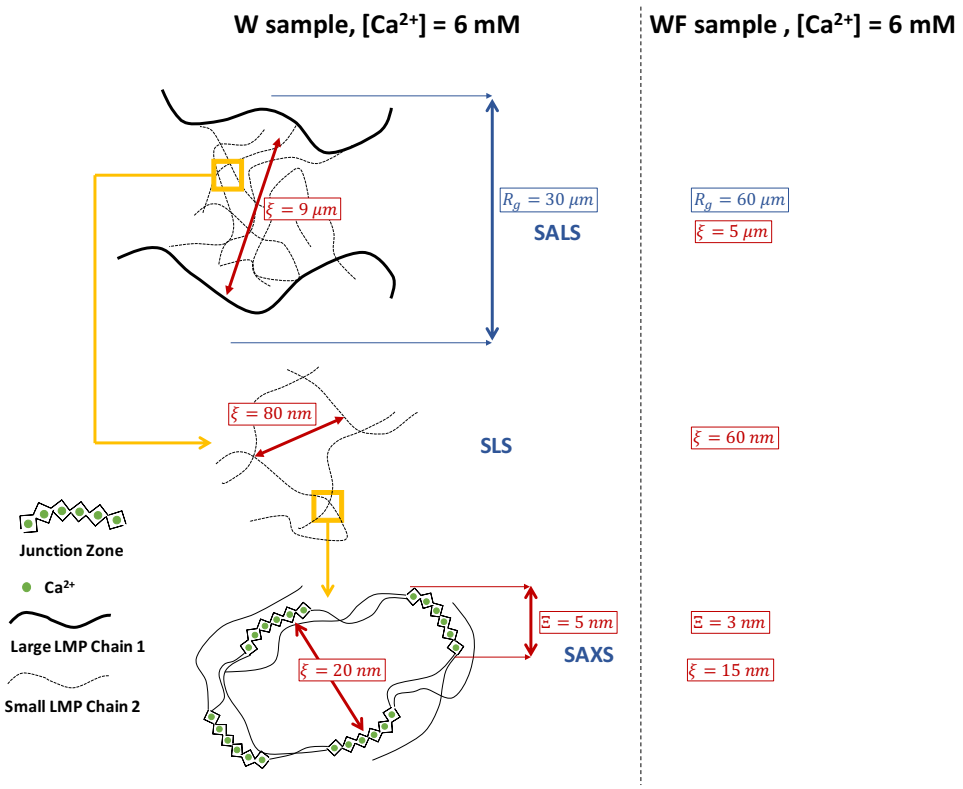

Figure 5.14: Summary of characteristic sizes as R_g, ξ and Ξ obtained from different SAS techniques. The values are compared between W and WF samples at $[Ca^{2+}] = 6$ mM.

Chapter 6

LMP gel formation with different sugars

In this chapter, the same formalism and analysis was used to characterize LMP gels prepared with different sugars/polyols. The present characterization was performed via rheological and DLS techniques.

6.1 Rheological Characterization for LMP samples with different sugars

As pointed out in the results in chapter 4, the addition of 60 *wt.* % fructose alters the LMP gel-formation kinetics and absolute rigidity values of the gels. This effect is mostly attributable to the aqueous sugar solvent characteristics, such as molecular stereochemistry of the sugar and ability to coordinate water molecules throughout the sample [46][47][96][100]. Moreover, for concentrated sugar solutions, *i.e.*, $\geq$ 50 *wt.* %, sugar-water mixtures demonstrate a clustering effect of sugar molecules [89] [44], also observed in some of the results in section 3.2.1.

According to [2][47][17], the presence of different sugars may either strengthen, weaken or impede gel formation (at given $[Ca^{2+}]$). In this case, it was decided to compare LMP samples prepared in 60 *wt.* % sorbitol (WS), D-psicose ($WPSI$), invert sugar (WIS) and 40 *wt.* % sorbitol ($WS40$). Rheological results for aged

systems are shown in Figs.6.1. The figure shows the results of the samples at ageing time (t_a) = 6 days.

Fig.6.1(a) shows η vs. $\dot{\gamma}$ results for *WPSI* samples at $[Ca^{2+}]$ = 0, 4, 6 and 8 mM. The viscosity magnitude increases as a function of $[Ca^{2+}]$ but no sol/gel transition is observed. In fact, in the $[Ca^{2+}]$ range between 0 and 6 mM, the material behaves as a Newtonian liquid. At the highest $[Ca^{2+}]$, 8 mM, viscosity increases significantly and shear thinning is observed, suggesting the onset of the junction zone formation. This is confirmed by the ageing observed for this $[Ca^{2+}]$, as shown in the inset of panel (a). D-psicose is a monosaccharide obtained from the epimerization of fructose at C3 through enzymatic activity [109]. The sugar ring β-D-psicopyranose has one -OH group in the equatorial position. Therefore one might expect a lower water affinity than with fructose. In solution, it forms 5 different tautomers, present in approximatively similar percentages at room temperature [109]. The lack of gel formation for *WPSI* samples is difficult to attribute to a specific mechanism, due to the scarce literature available for this molecule in solution and/or interactions.

Fig.6.1(b), η vs. $\dot{\gamma}$ shows the results for *WS60* samples at $[Ca^{2+}]$ = 0, 4, 6, 8 and 10 mM. Generally, η vs. $\dot{\gamma}$ plots show an increase in magnitude as a function of $[Ca^{2+}]$. In the $[Ca^{2+}]$ range between 5 and 10 mM, the shear thinning behaviour suggests an increased density of junction zones with an increased $\dot{\gamma}$ breaking a low fraction of junction zones in the sample.

According to Ref. [110] [111], sorbitol shows affinity for Ca^{2+} ions, leading to complex formation. This effect may create a competition between LMP and sorbitol for the Ca^{2+}, as seen elsewhere for LMP gels [26]. A key difference to other sugars such as fructose and glucose, *i.e.*, sugar rings, is that sorbitol cannot adopt ring structures in acqueous solutions. The lack of a ring structure removes the equatorial -OH groups which are compatible with the water organization. This, in turn, results in the inability of sorbitol to immobilize free water [2]. Moreover, studies of HMP in the presence of sorbitol [112], pointed out the possibility of polymer-sorbitol interactions which can effectively perturb the pectin chain-chain interactions/associations. Altogether, these features reflect the ability of sorbitol to frustrate cross-linking of LMP via Ca^{2+} ions.

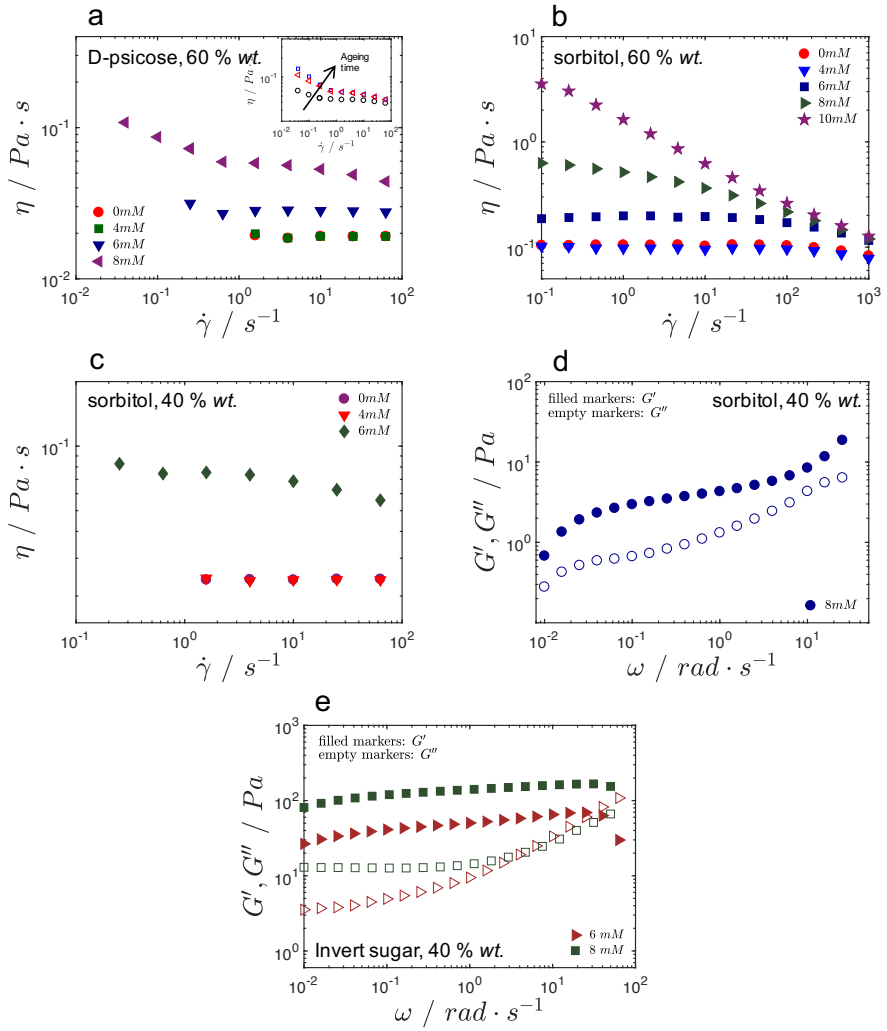

Figure 6.1: (a). Rotational rheology results (η vs. $\dot{\gamma}$) for 60% *wt.* D-psicose samples (*WPSI*) with $[Ca^{2+}]$ = 0, 4, 6 and 8 mM. The inset of the figure shows the ageing behaviour for $[Ca^{2+}]$ = 8 mM sample. (b) η vs. $\dot{\gamma}$ plots for 60% *wt.* sorbitol samples (*WS60*) in a $[Ca^{2+}]$ between 0 and 10 mM. (c) η vs. $\dot{\gamma}$ results for 40 *wt.* % sorbitol samples (*WS40*) and $[Ca^{2+}]$ = 0, 4 and 6 mM. (d) Oscillatory rheology results as $G^{'}$ and $G^{''}$ vs. ω for *WS40* sample with $[Ca^{2+}]$ = 8 mM. (e) $G^{'}$ and $G^{''}$ vs. ω for *WIS* samples (60 *wt.*% invert sugar) at $[Ca^{2+}]$ = 6 and 8 mM. All measurements were performed at 25°C.

For these reasons, it was decided to reduce the amount of sorbitol to 40 *wt.* %, for comparison with studies elsewhere [45] [47]. The results are shown in Figs.6.1(c) and (d). In panel (c), η vs. $\dot{\gamma}$ for $[Ca^{2+}]$ = 0, 4, 6 mM. Here, the overall viscosity decreases due to lower dissolved sugar content. For $[Ca^{2+}]$ = 0 and 4 mM, Newtonian behaviour is observed, meaning no structural changes. However, for $[Ca^{2+}]$ = 6 mM, η increases significantly suggesting cross-linking in this sample. Increase of $[Ca^{2+}]$ to 8 mM showed a macroscopic gel structure, that was analysed with oscillatory rheology, to give $G^{'}$ and $G^{''}$ vs. ω in Fig.6.1(d). In the figure, one can see a low $G^{'}$ magnitude and the decrease of both moduli at low ω, indicating a liquid-like behaviour at long relaxation times. Hence, the reduced amount of sorbitol has less impact on the LMP gel formation, reducing the magnitude of effects at 60 *wt.* % described in the previous paragraph.

Finally, $G^{'}$ and $G^{''}$ vs. ω for *WIS* samples with $[Ca^{2+}]$ = 6 and 8 mM are shown in Fig.6.1(e). The results are reminiscent of what has been observed for WF samples, in that the LMP gels strengthen. The invert sugar used was a 1:1 M mixture of glucose and fructose. The availability of large amount of equatorial -OH groups (3 per molecule of fructose and 4 per molecule of glucose), reduces the free water in the system, enhancing LMP chain-chain interactions as described earlier.

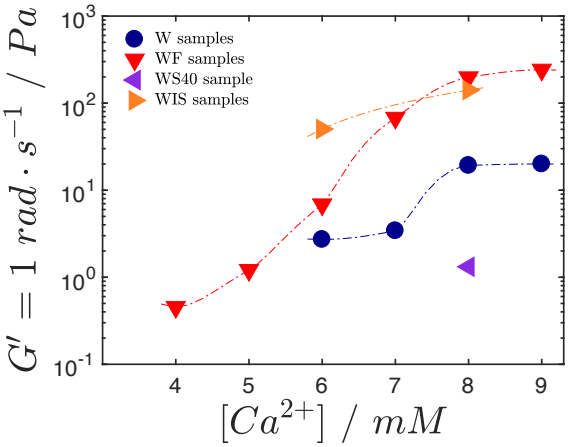

Figure 6.2: $G^{'}$ values taken at 1 rad s^{-1} from previous frequency sweep tests for *W*, *WF*, *WIS* and *WS40* samples.

Fig.6.2 shows the summary of the gel samples, *i.e.*, samples tested via oscillatory rheology, plotted as $G^{'}$ measured at 1 rad s^{-1} vs. $[Ca^{2+}]$, for all the samples tested in this work. As shown, *WIS* with $[Ca^{2+}] = 8$ mM have similar $G^{'}$ magnitude to *WF* samples with equal $[Ca^{2+}]$, indicating a certain degree of cross-linking saturation when ring sugars are present, *i.e.*, independent of the free water content. On the other hand, *WIS* with $[Ca^{2+}] = 6$ mM, shows higher values than *WF*, suggesting a tighter network of cross-linked *LMP*, related, again, to the free water content. As described in chapter 2, the temperature dependence of *LMP* gels in presence of fructose changes the mechanical properties. Therefore, one may expect a similar behaviour for these samples, which will be discussed later. The single point for *WS40* sample sits under the the *W* sample at the same $[Ca^{2+}]$ (*i.e.*, 8 mM). This highlights the extreme weakening effect of sorbitol in *LMP* gel formation, similar to that seen in previous studies [2] [46] [26] .

6.2 DLS Characterization for LMP samples with different sugars

In this section, *DLS* was utilised to probe dynamics during ageing and in the aged state ($t_a = 6$ days), in a similar manner to section 4.2.2. All the *DLS* were analysed and described according to section 3.2. Due to the solvent relaxation process described previously for *WF* samples, the fit range of ${g_1}^2$ was from $\tilde{t} > 10^{-4}$ s. Fig.6.3, first column ((a) – (d) figures), shows $< \tau >$ vs. t_a for *LMP* prepared with different co-solutes (sugars). The second column in Fig.6.3 ((a') – (d') figures) shows the ${g_1}^2$ vs. $\tilde{t}$ plots for the aged systems, together with the *KWW* fit lines.

In panel (a), *WPSI* samples show no $< \tau >$ increase during t_a, for any $[Ca^{2+}]$, so no ageing effects. Adding $[Ca^{2+}] = 8$ mM, slows down the overall dynamics to $< \tau > \approx 9{\cdot}10^{-1}$ s, suggesting the formation of a low density of junction zones, as similarly suggested by the rotational rheology results (Fig.6.1(a)). This can be more clearly seen in panel (a'), where ${g_1}^2$ vs. $\tilde{t}$ plots highlight a shift towards long lag times.

Fig.6.3(b) *WS60* samples show similar-magnitude $< \tau >$ in the range of $[Ca^{2+}]$ between 0 and 6 mM, with no ageing effects. This reflects the dynamic behaviour for $[Ca^{2+}] \leq 4$ mM seen in *W* and *WF* samples as well, *i.e.*, the $[Ca^{2+}]$ is not enough to stabilize junction zones. For $[Ca^{2+}] = 8$ mM, $< \tau >$ increases to ≈ 0.9 s, indicating cross-link formation. The unchanged $< \tau >$ values with t_a suggest the limited amount of Ca^{2+} ions available to *LMP*, are complexed by sorbitol [26][46]. For $[Ca^{2+}] = 10$ mM, $< \tau >$ increases its magnitude and shows ageing effects. In this situation, the sorbitol may saturate its capability to complex Ca^{2+} [113] [57], leaving the residual ions able to stabilize junction zones in *LMP*. In panel (b'), one can see the slowed dynamics for $[Ca^{2+}] = 6$ and 8 mM, as ${g_1}^2$ vs. $\tilde{t}$ plots. The overall shift towards longer $\tilde{t}$ is mostly due to the increased η viscosity of the medium.

The explanation of the behaviour in *WS60* samples seems to be with what when the concentration of sorbitol is reduced to 40 *wt.* %, as shown in Fig.6.3(c). Up to $[Ca^{2+}] = 6$ mM, the $< \tau >$ trend is similar to *WS40*, again suggesting the possibility of Ca^{2+}-sorbitol complexes. However, at $[Ca^{2+}] = 8$ mM and $t_a \geq 72$ hours, ${g_1}^2$ vs. $\tilde{t}$ no longer decay as a single exponential. Here, a double *KWW* describes the data. The double-component ${g_1}^2$ and longer time-scales ($< \tau >$ at 72 and 144 hours was 5.3 $\pm$ 0.6 s and 7.8 $\pm$ 0.6 s, respectively), suggesting the proximity to the sol/gel transition at the respective length scale.

The reduction of the amount of sorbitol limits the capability to complex Ca^{2+}, leaving in solution larger quantity free ions. In turn, the free ions can take part in cross-linking. In fact, the slower dynamics achieved at $[Ca^{2+}] = 8$ mM are considerably different compared to *WS* samples at $[Ca^{2+}] = 10$ mM. As shown in panel (c'), ${g_1}^2$ vs. $\tilde{t}$ at $[Ca^{2+}] = 8$ mM clearly shows the double relaxation, identifying the border line between the sol and gel states.

Finally, Fig.6.3(d) show the results for *WIS* samples. Here, the dynamics of ageing are similar to the ones obtained previously for *WF* samples. $< \tau >$ vs. t_a for $[Ca^{2+}] = 0$ mM does not show any changes as expected. For $[Ca^{2+}] = 4$ mM, the time scale shows an ageing effect between 1 and 72 hours then, it remains stable. Higher $[Ca^{2+}]$ results in fully non-ergodic samples, with a high degree of dynamic arrest, as shown in Fig.6.3(d'). These results were expected due to the high water binding of both fructose and glucose, as explained previously.

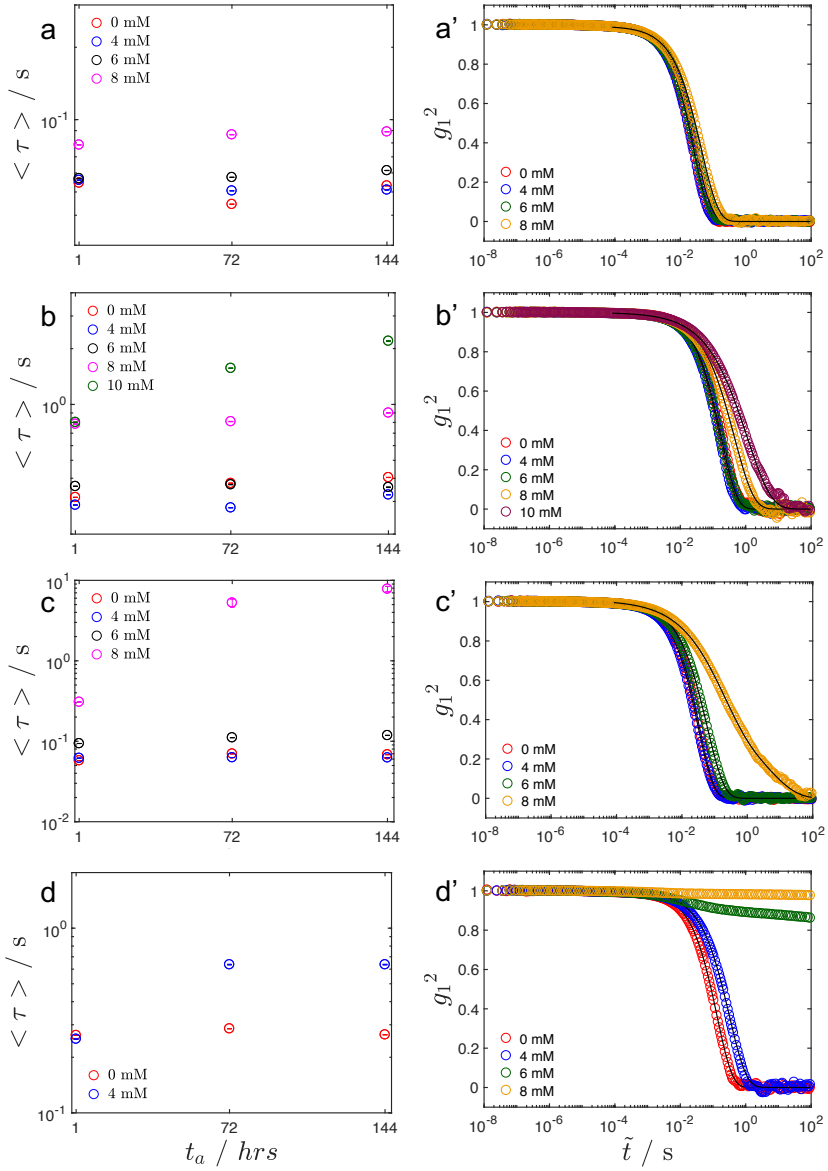

Figure 6.3: First column, from (a) to (d) $< \tau >$ values collected at $\theta = 90°$ at different ageing times: 1, 72 and 144 hours for *WPSI*, *WS60*, *WS40* and *WIS* samples ((a) – (d), respectively). The second column shows ${g_1}^2$ vs. $\tilde{t}$ plots for the respective samples as ageing time = 144 hours (6 days), as a function of $[Ca^{2+}]$. Fitted lines from *KWW* fitting-functions are included.

Undoubtedly, the most interesting points of these results reside in the D-psicose and sorbitol. Unfortunately, the lack of literature on D-psicose cannot easily address a possible cause of the lack of a sol/gel transition. According to stereochemical studies, calcium-sugar complexes usually occur in open sugar chains (*e.g.*, xylitol, sorbitol, *etc.*). In this case, of the five tautomers in solution, only 0.2 % of D-psicose is present in the chain-form [109]. Therefore, it is unlikely that such low percentage can form complexes with the majority of Ca^{2+} ions. No additional information appears to be available of the physical properties of D-psicose in solution. Speculating, one can expect three effects: (i) partial Ca^{2+} complexes, (ii) dilution effects and (ii) cluster formations via water-structuring effects. Even though the missed gel formation of LMP in the presence of sorbitol was attributed to calcium-sorbitol complexes, additional chemical-physical characteristics may accompany this behaviour, *e.g.*, water structuring.

6.2.1 *q*-dependence of LMP samples with different sugars

The q-dependence of DLS for both sol and gel states was performed as described in section 3.2 . Fitted $< \tau >$ results are displayed as decay rate Γ vs. q in Fig.6.4. For all the samples, the power-law (Λ) fit from the Γ vs. q plots is shown in Fig.6.5. To compare the whole range of co-solvents, Λ values for W and WF samples are also shown (red circles and blue triangles, respectively).

Generally, for all the co-solutes, the overall $< \tau >$ magnitude increases proportionally with the $[Ca^{2+}]$ increase (vice-versa for Γ). As previously discussed, longer relaxation times can be attributed to LMP chain-chain interactions via cross-link stabilization. In the same way, the q-dependence identifies the possible nature of the interactions, such as diffusive and hydrodynamic.

For all the ${g_1}^2$ vs. $\tilde{t}$ at different q, a single KWW function was utilized for $\approx \tilde{t} \geq 10^{-4}$, leaving apart the solvent relaxation decay at low lag-times. Fig.6.4(a), shows $WPSI$ samples with $[Ca^{2+}] = 0$, 4 6 and 8 mM. The q-dependence for $[Ca^{2+}] = 0$ mM showed a $\Lambda \approx 2.0$, stabilizing at the highest $[Ca^{2+}]$ at a slighter higher value ≈ 2.5 (Fig.6.5, green diamonds symbols). Therefore, $WPSI$ samples did not showing Λ changes consistent with a sol/gel transition, even at relatively high $[Ca^{2+}]$, in agreement with the earlier observations.

Panel (b) shows *WS60* samples in a $[Ca^{2+}]$ range from 0 to 10 mM. The overall Γ magnitude is low due to the high viscosity contribution of the medium ($\eta = 0.035\ Pa\ s$). The $[Ca^{2+}]$ increase from 0 to 10 mM promotes slower dynamics and stronger q dependence. In fact, as shown in Fig.6.5 (magenta triangles), for $[Ca^{2+}]$ between 0 and 4 mM, $\Lambda \approx 2.3$. From $[Ca^{2+}] = 6$ to 10 mM, the q dependence progressively increases up to $\Lambda = 4.3$ (at 10 mM). Interestingly, the highest $[Ca^{2+}]$ utilised, did not show more than one slow relaxation mode, as reported in Fig.6.4(b).

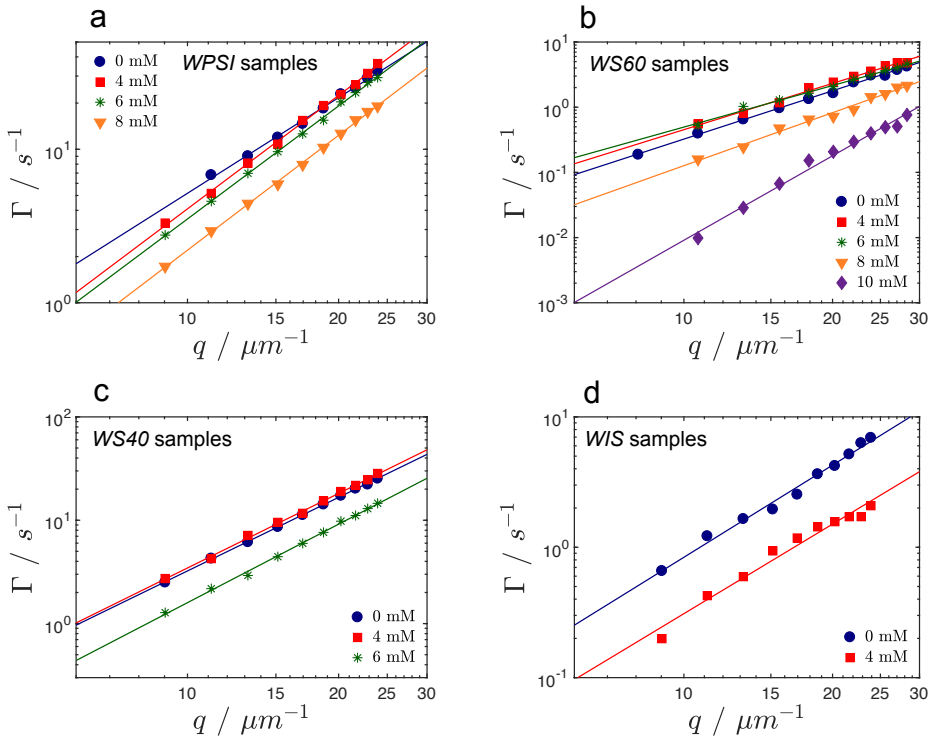

Figure 6.4: Γ (from KWW-fitted ${g_1}^2$ vs. $\tilde{t}$ plots at different q) vs. q plots with relative power-law fit lines for:(a) *WPSI*, (b) *WS60*, (c) *WS40* and (d) *WIS* samples.

Fig.6.4(c) shows the Γ vs. q plots for *WS40* samples. In this case, *LMP* is dissolved in a more dilute (40 *wt.* %) sorbitol solution, with a lower $\eta = 0.0062$ Pa s, explaining the higher Γ magnitudes. From Fig.6.5 (orange triangles), one can easily see the similarity of the Λ values determined for both *WS40* and

WS60 samples. Regardless of the sorbitol concentration, the added Ca^{2+} up to 6 mM has a similar effect on the q-dependence. This behaviour agrees with the explanation of ion complexation driven by the sorbitol, which leaves the LMP junction zones unchanged. Interestingly, for both *WS40* and *WS60* samples at $[Ca^{2+}] = 0$ mM, $\Lambda \approx 2.4$, higher than the Λ for LMP dissolved in water, fructose and D-psicose solutions at same $[Ca^{2+}]$. The shift of Λ to higher values could be accounted for simply by indirect effect of sorbitol-LMP interactions. On the other hand, neutron scattering and MD simulations for sorbitol-water solutions have highlighted the presence of inhomogeneities on the nanometre scale, *i.e.*, water clusters [114]. This effect may interfere with the dynamics of *WS40* samples without the Ca^{2+} addition. With respect to this feature, no literature can be found on sorbitol-water-pectin interactions. For $[Ca^{2+}] = 8$ mM, *WS40* samples showed the presence of two modes in the ${g_1}^2$ function, indicating the proximity of the sol/gel transition.

Finally, *WIS* samples at $[Ca^{2+}] = 0$ and 4 mM are shown in Fig.6.4(d). The magnitude of the decrease in Γ at $[Ca^{2+}] = 4$ mM was enhanced, suggesting junction zone stabilization. The relatively poor data quality in the Γ vs. q plots may be attributable to the solvent characteristics and its relaxation processes. As shown in Fig.6.5 (black squares), $\Lambda \approx 2.3$.

Higher $[Ca^{2+}]$ showed full non-ergodic behaviour, indicating a gel state at the probed q.

For non-ergodic samples, data acquisition and interpretation were undertaken as described in section 4.2.2 [67]. Once again, the data are shown together with *W* and *WF* samples, for comparison. As shown in Fig.6.3, non-ergodic behaviour was seen only for *WIS* samples with $[Ca^{2+}] = 6$ and 8 mM. From the q dependent data, ${g_1}^2$ at $\tilde{t} = 10$ s were plotted vs. q and fitted with the mean square displacement equation (inset of Fig.6.6). The fitted length scale of fluctuations (L_F) vs. $[Ca^{2+}]$ is shown in Fig.6.6.

L_F for *WIS* samples are shown in the figure as the green star symbols. At $[Ca^{2+}] = 6$ mM, L_F shows a similar value to the one obtained for *WF* sample at same $[Ca^{2+}]$. This may suggest a similarity in the dynamics for the two samples at the specific ageing time. At $[Ca^{2+}] = 8$ mM, L_F decreased to $0.015 \pm 0.002\ \mu m$, indicating more highly suppressed dynamics, as expected. The similar values of

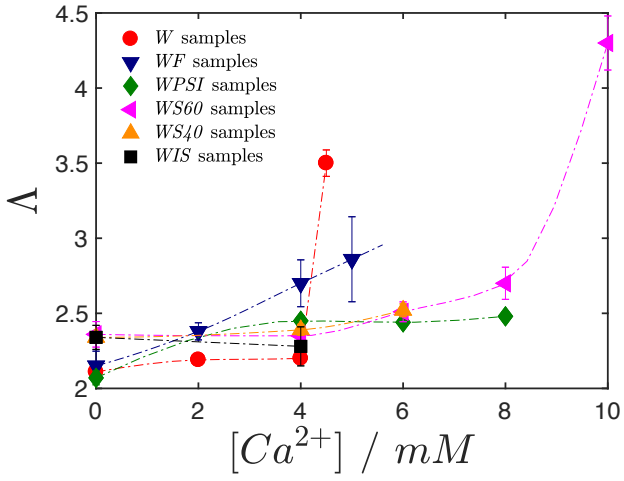

Figure 6.5: Power-law exponents Λ vs. $[Ca^{2+}]$, taken from q dependent DLS analysis for *W*, *WF*, *WPSI*, *WS60*, *WS40* and *WIS* samples.

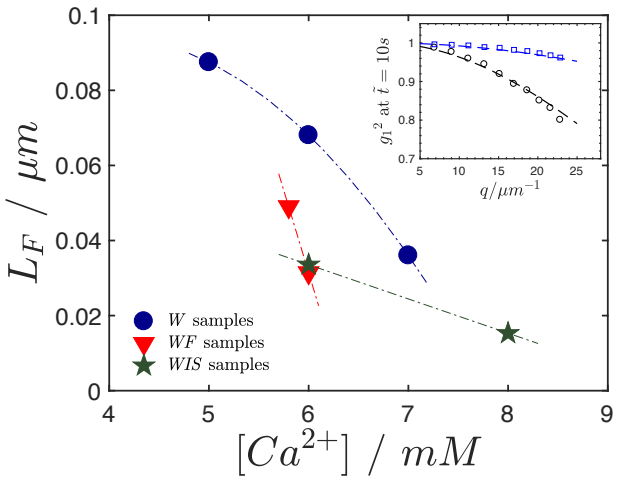

Figure 6.6: L_F (parameter from mean square displacement fit) vs. $[Ca^{2+}]$ for *W*, *WF*, *WIS* and *WS40* samples.

L_F for both *WIS* and *WF* samples with $[Ca^{2+}] = 6$ mM suggest similar dynamics for the samples, whichever sugar is added. Being a mixture of 1:1 M of glucose and fructose, the total amount of the equatorial OH groups in *WIS* solutions responsible to the water-binding is slightly increased compared to *WF* solutions. However, one also has to consider sugar-clustering effects, that may change the dynamics of cross-link formation, as discussed previously.

6.3 Temperature dependence of *WS40* and *WIS* samples

In the previous section, the formation of gel structures for *WS40* samples with $[Ca^{2+}] = 8$ mM and *WIS* samples with $[Ca^{2+}] = 6$ and 8 mM was revealed. The aim of this section is to investigate whether the three systems show similar thermal-reversibility (or lack of thermal-reversibility) as seen for the *WF* samples in section 4.2.3.

Rheological temperature T-dependent results for *WS40* at $[Ca^{2+}] = 8$ mM are shown in Figs.6.7, as: (a) G'' and G' vs. shifted angular frequency $(a \cdot \omega)$ and (b) G'' and G' measured at $\omega = 1$ rad s^{-1} vs. T. Figs.6.7(a) and (b) show the results in the T range 25 to 35°C, G'' and G'. Results can be summarized as follow: (i) increased the ω dependency (ii) decreased their magnitude and (iii) showed crossing-over of G' and G'' ($G'' > G'$). The results indicate the junction zones disassemble on increase in T. This condition persists up to $T = 50$°C. Here, G'' starts to reverse its behaviour and increase until the maximum probed T is reached (Fig.6.7(b)). The increase of the storage modulus G' is accompanied by a reduction in the ω-dependence (*i.e.*, flattening of the moduli) and the recovery of the $G' > G''$ condition, as clearly seen in Fig.6.7(a). During the controlled T cooling from 70 to 25°C, $G' > G''$ and G' progressively increased in magnitude. The second T cycle, 25 to 70°C then 70 to 25°C, did not give any significant changes in the mechanical properties of the gel.

Hence, for the *WS40* sample, one can see a weak initial junction-zone disassembly, followed by a non reversible, trend behaviour as same for the *WF* samples

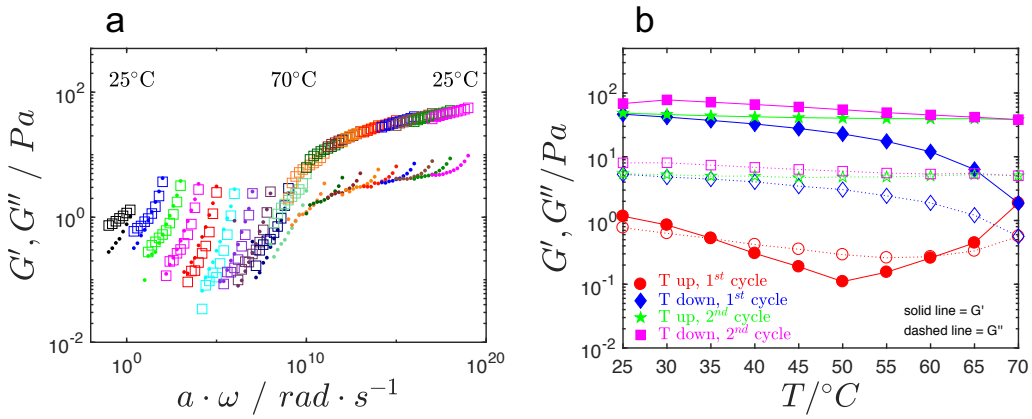

Figure 6.7: (a) G' and G'' vs. shifted angular frequency ($a \cdot \omega$) for *WS40* sample with $[Ca^{2+}]$ = 8 mM, taken at T from 25 to 70°C (heating) and 70 to 25°C (cooling). (b) G' and G'' at 1 rad s^{-1} vs. T plots for a double T ramp.

in section 4.2.3. From the perspective of T as an annealing agent, one might therefore expect long-time gel-curing effects. The final value of the G' at 1 ω = 1 rad s^{-1} corresponds to ≈ 80 Pa, double the G' obtained for the *WF* sample with $[Ca^{2+}]$ = 6 mM (*i.e.*, ≈ 40 Pa). This is evidence of the long-term junction zone stabilization that reaches a saturation, such that the majority of the Ca^{2+} ions are now used as cross-linking agent. Once again, it is believed that sugar-water interactions may lead to a non-equilibrium trapped gel state, that might disappear on very long gel-curing times or application of such a temperature annealing process.

To confirm this, the same test was performed on *WIS* samples with two $[Ca^{2+}]$, *i.e.*, 6 and 8 mM. As seen in Figs.6.8(a) and (b), ($[Ca^{2+}]$ = 6 mM), $G' > G''$ persists for the entire test. Once again, the T increase from 25 to 70°C promoted an initial softening of the material, followed by a strengthening. Recalling the *WF* sample with the same $[Ca^{2+}]$ (see Fig. 2.15(a)), this showed a similar trend in the first T cycle. The final G' at 1 ω = 1 rad s^{-1} (after two T cycles) ≈ 100 Pa. The higher value obtained than with the *WF* sample (*i.e.*, ≈ 40 Pa) may be attributable to the junction-zone reinforcement given by the invert sugar, which has higher propensity to bind free water in the system.

To conclude, the *WIS* sample with $[Ca^{2+}]$ = 8 mM showed a similar effect to

samples with $[Ca^{2+}] = 6$ mM, but with greater $G^{'}$ values. In this case, the change from the non-equilibrium trapped gel state (sample aged 6 days at room temperature) and the double-T cycle, increased $G^{'}$ from $\approx$ 100 to 300 Pa. This range of values is similar to the ones obtained in the frequency sweep tests for *WF* samples with $[Ca^{2+}] = 8$ mM at the ageing time = 6 days (see Fig.*2.1*(b)). The result suggests a non-equilibrium trapped gel state when the sol/gel transition is at its boundary. When the $[Ca^{2+}]$ exceeds this limit, the gel formation/stabilization occurs quickly. This may be attributed to the excess Ca^{2+} ions that are not counterbalanced by the $SHMP$ (that slows down the junction zone stabilization), together with the co-solute contributions.

Thus, the lack of thermal reversibility appears to be the case in both *WF* and *WIS* samples, in which sugars have similar chemical characteristics, comprising ring structures with eOH groups, whilst effects are weaker for open chain sorbitol, binding Ca^{2+} ions, as explained earlier.

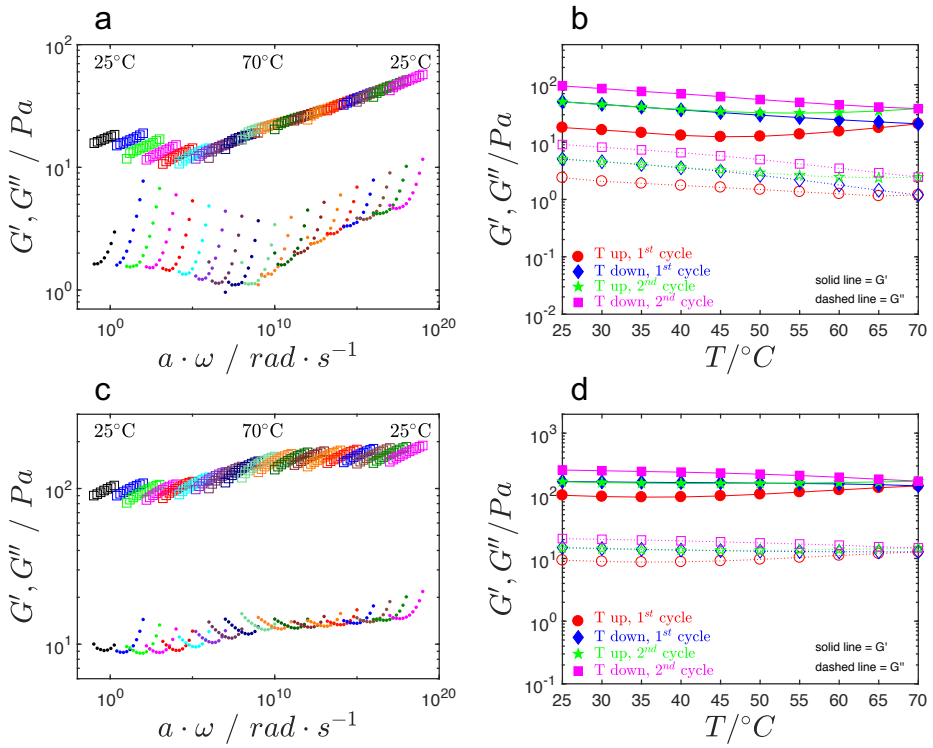

Figure 6.8: (a) G' and G'' vs. shifted angular frequency ($a \cdot \omega$) for *WIS* sample with $[Ca^{2+}] = 6$ mM, taken at T from 25 to 70°C (heating) and 70 to 25°C (cooling). (b) G' and G'' at 1 rad s^{-1} vs. T plots for a double T ramp. (c) and (d) panels show the same analysis for *WIS* samples with $[Ca^{2+}] = 8$ mM.

6.4 Additional investigation for *WS40* samples

The interesting contrast provided by the 40% *wt.* sorbitol (*WS40*) systems was further investigated with *SALS* (section 1.2.1) and rheo-speckle (section 1.2.1). In terms of static properties of the polymer solutions/gels, the *SALS* techniques highlighted structural differences. *SLS* gave only poor quality data for some reasons and data are not shown. Unfortunately, there was no time to investigate shorter length scales via *SAXS*.

For the rheo-speckle technique, T-dependence was measured as a test of the spontaneous dynamics. The stress-relaxation test was discarded due to poor adherence between the sample and the plates, *i.e.*, causing slip during application of the step-strain.

6.4.1 SALS analysis of *WS40* samples

Aged *WS40* samples with $[Ca^{2+}]$ = 0, 4, 6 and 9 mM are displayed in Fig.6.9. The data description and interpretation are the same as described in sections 3.4 and 5.1. As shown, for $[Ca^{2+}]$ = 0 and 4 mM, $I(q)$ vs. q plots show an extended power-law like behaviour in the low q range. This effect demonstrate the presence of larger aggregates in the sample, where the $I(q)$ may reach the plateau at lower q values. In fact, for these samples, a Guinier approximation yielded values of $qR_g > 1$, confirming the presence of large aggregates.

The ability of sorbitol to sequester Ca^{2+} ions may be the cause of this effect, where a lack of stabilized junction zones of *LMP* persists in the highly-disordered state. *df* values for $[Ca^{2+}]$ = 0 and 4 mM were 1.8 and 3.1, respectively. These values, allowed ξ to be determined via the $I(q) \cdot q^{df}$ vs. q plots, as $\xi \approx 6\ \mu m$ and 4 μm at 0 and 4 mM, respectively. The ξ for $[Ca^{2+}]$ = 0 mM is similar to the same parameter obtained for *W* samples in section 5.1. However, for $[Ca^{2+}]$ = 4 mM, the values are more similar the ones obtained for *WF* at same $[Ca^{2+}]$. Both ξ and *df* values highlight the presence of compact domains when $[Ca^{2+}] \geq 4$ mM is added to the *LMP* solution.

At $[Ca^{2+}]$ = 6 mM, $I(q)$ starts to level off at low q, indicating a characteristic length scale (Fig.6.9). At larger q, a *df* value of $\approx$ 2.4 was obtained. For this sample, $\xi \approx 4\ \mu m$. Lastly, *WS40* with $[Ca^{2+}]$ = 9 mM showed increased $I(q)$

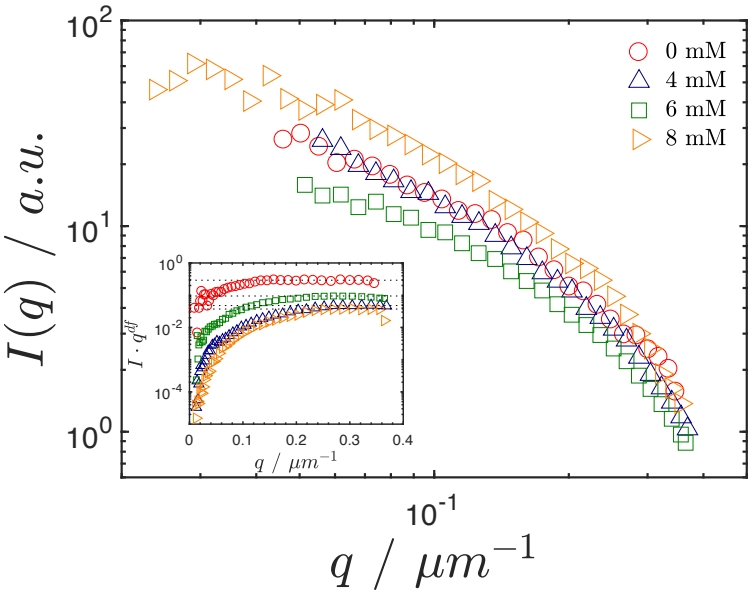

Figure 6.9: SALS results as $I(q)$ vs. q plots for *WS40* samples at different $[Ca^{2+}]$. The inset of the figure shows the $I(q) \cdot q^{df}$ vs. q plots for the graphical determination of ξ.

approaching a plateau towards low q. The increase in df to 3.5 indicates more compact domains, whereas ξ shows a constant value of 4 μm. In this case, $R_g = 36 \pm 0.05$ μm in the $qR_g < 1$ limit. According to Fig. 1.4(b), the value is comparable to WF samples in the $[Ca^{2+}]$ range 2 and 4 mM.

Comparing the $SALS$ results with those for W and WF samples, the supramolecular length scales in the presence of 40 *wt.* % sorbitol appear similar to those in the WF samples, indicating large aggregates that are not fully dispersed in solvents different than water. Moreover, the $[Ca^{2+}]$ required to stabilize junction zones is higher for *WS40* samples, due to the Ca^{2+} complexation by sorbitol.

6.4.2 Rheo-Speckle analysis of *WS40* samples

For these experiments, the $[Ca^{2+}] = 9$ mM was chosen to ensure a sufficient density of cross-links. Analysis of the spontaneous dynamics was performed at different temperatures, *i.e.*, 25, 45, 65 and cooled down back to 25°C. Both rheological and dynamic data acquisition during the stress relaxation tests were unsuccessful due to slip between the plate and the sample. Therefore, these data are not shown.

As in section 4.2.4, g_{2-1} vs. $\tilde{t}$ plots obtained at 25°C before and after heating to 65°C are shown in Fig.6.10. At the beginning of the analysis (panel (a) of Fig.6.10), the dynamics show stability after $\approx$ 4500 s, as g_{2-1} converge for high analysis times. Here, one can see a clear relaxation mode at $\tilde{t} \approx 100$ s, followed by a secondary one at higher $\tilde{t}$. The latter may reflect long-term rearrangements of the components of the system.

The T increase to 45°C results in a significant change of g_{2-1} in the short $\tilde{t}$ regimes (indicated as an arrow in panel (a)). In this case, the autocorrelation function decayed at shorter $\tilde{t}$, indicating an increase in dynamics due to the increase in T. The former, was followed with the same slower relaxation mode seen at 25°C. Further increase to 65°C, showed a change on the dynamics, where both modes assumed a unique relaxation behaviour.

Finally, cooling back to 25°C (Fig.6.10(b)), g_{2-1} vs. $\tilde{t}$ plots showed a single-mode relaxation with the following characteristics: (i) suppressed amplitude to $\approx$ 0.8, indicating arrested dynamics; (ii) elongation of the plateau at short $\tilde{t}$, with

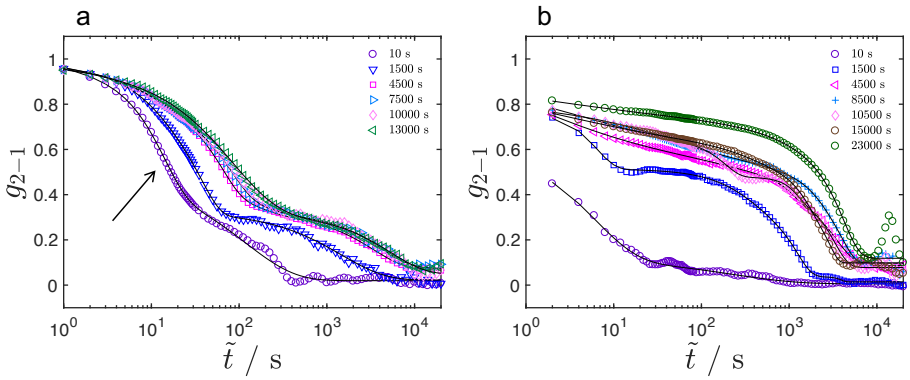

Figure 6.10: g_{2-1} vs. $\tilde{t}$ plots from spontaneous dynamics tests. The plots show the *WS40* sample with $[Ca^{2+}] = 10$ mM: (a) 25°C before heating; (b) 25°C after heating to 65°C and cooling down. Fit lines from KWW function are included as well.

a (ii) decay occurring at high $\tilde{t}$. These features highlight the dynamic change of the structures, where the sample passes from a unstable gel to a stable one.

The average relaxation times for all the investigated T, are summarized in Fig.6.11. As shown in this figure, $< \tau >$ values decrease with increasing T, indicating faster dynamics. Then, cooling to 25°C shows $< \tau >$ values approximatively the same as the before heating the sample. Similar to the *WF* sample, the relaxation modes rather than the total relaxation time highlights the change of the dynamics related to the structural rearrangements in the sample. It is difficult to interpret these data fully, since only one scattering vector was investigated. In a better scenario, it would be useful to use a similar DLS set-up to gather information at a range of q. One could then obtain detailed information on diffusivity and interactions.

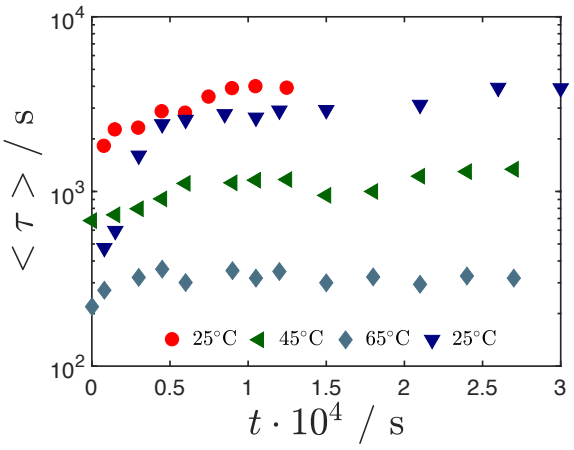

Figure 6.11: $< \tau >$ vs. analysis time (t) for *WS40* sample with $[Ca^{2+}] = 10$ mM at 25, 45, 65 and 25°C. $< \tau >$ values obtained by *KWW* fits of g_{2-1} vs. $\tilde{t}$ plots at different analysis time and temperatures.

6.5 Conclusions

In this section an attempt is made to compare *LMP* samples with different co-solutes and the previous *W* and *WF* samples.

The *LMP* gel formation changes accordingly to the type of co-solute and its concentration. The presence of D-psicose, resulted in no gel formation over a broad $[Ca^{2+}]$. The lack of literature on this type of sugar makes this behaviour hard explain completely. Speculating, the effect may be attributable to strong Ca^{2+} ion chelation, making them unavailable for the polymer to stabilize junction zones.

The effect of the *LMP* gel formation in presence of invert sugar (*i.e.*, *WIS* samples) was similar but slightly stronger than with fructose only (*WF* samples), as might be expected. The simultaneous presence of glucose and fructose can bind more water, making the latter unavailable for the polymer and Ca^{2+} ions. As a direct consequence, the dynamics are highly suppressed and the gel formation occurs more rapidly [17][47][96]. The application of the temperature to *WIS* samples show less changes than *WF* samples, indicating less freedom of *LMP* to

rearrange in a to a more stable structure. In terms of sugar clustering, there was no clear evidence of the interaction between the glucose and fructose.

Finally, the presence of sorbitol in LMP solutions shows reduced gel formation. This is dependent on the co-solute concentration, which probably reflects the ability of sorbitol to complex Ca^{2+} ions, making them unavailable for the junction zone stabilization. Although this effect was previously seen in similar systems, it is believed that the sorbitol interaction plays an indirect effect role in this phenomenon. In fact, as seen in the DLS analysis of this study, the typical fast mode seen in water-sugar solutions appears all the time, indicating clustering effects. Evidence in the literature highlights the possibility of sorbitol to form clusters in water solutions [114] [115] [116] . This raises the same unanswered question as to where the LMP sits in the system? Static properties of *WS40* seem to identify to two important points: (i) the difficulty of forming junction zones due to the reduced free availability of Ca^{2+} and (ii) solubility/aggregation of LMP in the sorbitol solution at large length scales. Finally, rheo-speckle results show non-thermal reversibility, similarly to WF and WIS samples, with a $[Ca^{2+}]$ that allows the gel formation.

Chapter 7

Overall Conclusions

In this work, commercial LMP gels prepared with high concentrations of sugars were investigated. To understand the possible mechanisms of gelation, LMP solutions with and without Ca^{2+} were investigated.

In chapter 3, rheological characterization of the LMP dispersed in water with no Ca^{2+} showed similar properties to those commonly found in literature for this type of pectin, in terms of intrinsic viscosity and the inferred molecular weight. As suggested by the industrial co-sponsor, Mondelez International, the concentration used for the LMP gel preparation (0.5 *wt.* %) resides around the overlap concentration C*, *i.e.*, across the dilute and semi-dilute regimes. This reflects the results obtained in DLS, where the limit $qRh > 1$ indicates translational diffusion combined with internal relaxation modes of the material dominate. Dilute solutions in water up to 0.02 *wt.* % LMP seemed not to change the $qRh > 1$ condition. These effects were also in agreement with SLS studies performed on the same systems. $SALS$ investigation of the LMP solutions suggested the presence of large length scale structures, *i.e.*, at the supramolecular level that may coexist with smaller ones. This indicates aggregation of LMP molecules even in dilute solution in the absence of added salts or sugars. The presence of co-solutes seemed to enhance aggregation.

In chapter 4, rheological and DLS investigation of LMP with added with Ca^{2+} identified two key factors: (i) the $[Ca^{2+}]$ needed to induce the sol to gel transition is $\approx$ 6 mM; (ii) gel formation is time-dependent and it takes $\approx$ 6 days to reach both mechanical and dynamical stability. In the presence of 60 *wt.* %

fructose: (i) faster gel formation was observed plus stronger mechanical properties after 6 days; (ii) for $[Ca^{2+}] \geq 6$ mM, the systems showed no appreciable ageing effects, *i.e.*, quasi-instantaneous gel formation with no changes 1 hour after preparation; (iii) DLS results showed a narrower $[Ca^{2+}]$ where the system crossed from sol to gel, compared to systems prepared in water. The latter was made particularly clear when angular dependent DLS experiments were performed for both sol and gel states. Being a physical and thermo-reversible gel, LMP prepared in water with $[Ca^{2+}] = 6$ mM behaves as expected. However, the presence of 60 *wt.* % fructose alters this characteristic. In fact, rather than melting, increasing the temperature gave an increase in the storage shear modulus $G^{'}$. Moreover, although the system at $[Ca^{2+}] = 5.5$ mM 6 days after preparation remained in the sol state, the T increase promoted a sol to gel transition. The DLS results clearly show the change of the relaxation modes during this transition. The observations were confirmed using rheo-speckle set-up. At small length scales, the DLS results show similar relaxation times at 25°C before and after temperature cycles. However, the number of the relaxation modes between the two methods show consistent changes, *i.e.*, from ≈ 3 relaxation modes to ≈ 1. This change indicates the formation of a more ordered structure, *i.e.*, increasingly uniform density of junction zones throughout the sample. From these features, we deducted that the gels prepared in fructose reside in a non-equilibrium trapped state, that can be resolved by application of high temperatures or very long ageing times.

Chapter 5 describes static scattering characterization on gels with and without fructose was investigated at extended observational length scales using $SALS$, SLS and $SAXS$. Major differences between the two systems could be detected at both very large and very small L. The intermediate static properties investigated via SLS did not show any interesting behaviour. In particular, $SAXS$ investigation of LMP gels in fructose as a function of $[Ca^{2+}]$ suggested junction zone stabilization up to $[Ca^{2+}] = 5$ mM. Higher concentrations (*i.e.*, $[Ca^{2+}] = 5$ and 6 mM) showed unexpected scattering profiles. Again, temperature cycling on these samples suggested changes in the structural properties of the samples that enhanced the cross-linking of the LMP chains via junction zone stabilization. The results seemed to be in agreement with the characteristic length scales calculated via a simple model widely used for gelled materials. The main conclusion

of chapter 5, considering the combination of estimated length scales obtained via the various models utilized, is that there are clear differences in the structure of LMP gels prepared in water and fructose. In particular, the presence of fructose decreases the amount of the free water of the system, promoting the closer association of the LMP chains.

In Chapter 6 it was shown that LMP gels prepared in the presence of 60 *wt.* % invert sugar behaved similarly to those prepared with 60 *wt.* % fructose. In particular, the invert sugar gels were even stronger than fructose gels. This is related to the ability of the equatorial -OH groups of the sugar molecules to bind water, making them less available to the pectin. On the other hand, 40-60 *wt.* % sorbitol and 60 *wt.* % D-psicose showed inhibition of gelation. For sorbitol, the effect is related to its ability to compete with $[Ca^{2+}]$ ions, making them less available for LMP junction zone stabilization, since it is an open chain polyol with less tendency to bind water due to the absence of equatorial -OH groups. For D-psicose there is very little information available elsewhere, but the strong inhibition of gelation probably have the same origin as with sorbitol. In conclusion, LMP gel formation in presence of high concentrations of sugars depends on the chemical characteristics of the sugar used, *i.e.*, straight chain or ring structures and the number of equatorial -OH groups in the case of the latter, plus possible effects of chelation of Ca^{2+} ions. Further investigation is needed to understand completely the behaviour of the polymer in these environmental conditions, such as the hydration properties of both the sugars and LMP molecules, the dynamics at small L, plus sugar clustering due to strong sugar-sugar interactions.

The results obtained in this thesis might have impact in both industrial applications and pure scientific field. The utilisation of a commercial LMP with high concentrations of sugars strongly impact the gel formation and the ageing over long times. These effect may significantly alter the quality of the product, yielding unwanted texture effects on the food matrix. The final target could be achieved using specific combinations of both $[Ca^{2+}]$ and sugars. Additionally, the final food product contains a variety of other ingredients, such as proteins, flavours, *etc.* that might additionally alter the interactions between LMP and sugars. In the scientific aspect, the work shows the complexity of a physical characterization of the solution and/or gel. Often, physical characterisation is

performed on monodisperse and tailored biopolymers. As shown in this thesis, a commercial LMP makes this characterization difficult, making the complete understanding difficult.

References

[1] S. Taylor and R. H. Walter, *The Chemistry and Technology of Pectin*. Academic Press, 2012. 1, 3, 4, 6, 9, 81

[2] J. L. Da Silva and M. Rao, "11 pectins: Structure, functionality, and uses," *Food polysaccharides and Their Applications*, vol. 160, p. 353, 2016. 1, 3, 4, 7, 8, 9, 10, 58, 84, 86, 96, 104, 108, 145, 149, 150, 153

[3] B. L. Ridley, M. A. O'Neill, and D. Mohnen, "Pectins: structure, biosynthesis, and oligogalacturonide-related signaling," *Phytochemistry*, vol. 57, no. 6, pp. 929–967, 2001. xv, 2

[4] S. Christiaens, S. Van Buggenhout, K. Houben, Z. Jamsazzadeh Kermani, K. R. Moelants, E. D. Ngouemazong, A. Van Loey, and M. E. Hendrickx, "Process–structure–function relations of pectin in food," *Critical Reviews in Food Science and Nutrition*, vol. 56, no. 6, pp. 1021–1042, 2016. 2, 3

[5] W. G. Willats, J. P. Knox, and J. D. Mikkelsen, "Pectin: new insights into an old polymer are starting to gel," *Trends in Food Science & Technology*, vol. 17, no. 3, pp. 97–104, 2006. 2

[6] P. L. Rockwell, M. A. Kiechel, J. S. Atchison, L. J. Toth, and C. L. Schauer, "Various-sourced pectin and polyethylene oxide electrospun fibers," *Carbohydrate Polymers*, vol. 107, pp. 110–118, 2014. 3

[7] B. R. Thakur, R. K. Singh, A. K. Handa, and M. Rao, "Chemistry and uses of pectina review," *Critical Reviews in Food Science & Nutrition*, vol. 37, no. 1, pp. 47–73, 1997. 3, 8

[8] S. H. Christensen, "Pectins," *Food Hydrocolloids*, vol. 3, pp. 205–230, 1986. 3

[9] V. Evageliou, R. Richardson, and E. Morris, "Effect of ph, sugar type and thermal annealing on high-methoxy pectin gels," *Carbohydrate Polymers*, vol. 42, no. 3, pp. 245–259, 2000. 3

[10] I. Fraeye, T. Duvetter, E. Doungla, A. Van Loey, and M. Hendrickx, "Fine-tuning the properties of pectin–calcium gels by control of pectin fine structure, gel composition and environmental conditions," *Trends in Food Science & Technology*, vol. 21, no. 5, pp. 219–228, 2010. 4, 6, 8, 9, 81, 88

[11] J. D. Ferry, *Viscoelastic properties of polymers*. John Wiley & Sons, 1980. 4, 27

[12] Y. Lan, M. Corradini, a. G. Weiss, S. Raghavan, and M. Rogers, "To gel or not to gel: correlating molecular gelation with solvent parameters," *Chemical Society Reviews*, vol. 44, no. 17, pp. 6035–6058, 2015. 4

[13] M. Rubinstein and R. Colby, *Polymers physics*, vol. 767. Oxford Oxford, UK, 2003. 4, 5, 58, 77, 84

[14] R. A. Jones, *Soft condensed matter*, vol. 6. Oxford University Press, 2002. 5

[15] A. Assifaoui, A. Lerbret, H. T. Uyen, F. Neiers, O. Chambin, C. Loupiac, and F. Cousin, "Structural behaviour differences in low methoxy pectin solutions in the presence of divalent cations (ca 2+ and zn 2+): a process driven by the binding mechanism of the cation with the galacturonate unit," *Soft Matter*, vol. 11, no. 3, pp. 551–560, 2015. 5, 137

[16] C. Kyomugasho, S. Christiaens, D. Van de Walle, A. M. Van Loey, K. Dewettinck, and M. E. Hendrickx, "Evaluation of cation-facilitated pectin-gel properties: Cryo-sem visualisation and rheological properties," *Food Hydrocolloids*, vol. 61, pp. 172–182, 2016. 5, 126

[17] H. Kastner, U. Einhorn-Stoll, and B. Senge, "Structure formation in sugar containing pectin gels–influence of ca2+ on the gelation of low-methoxylated pectin at acidic ph," *Food Hydrocolloids*, vol. 27, no. 1, pp. 42–49, 2012. 6, 7, 12, 84, 86, 99, 149, 168

[18] I. Braccini and S. Pérez, "Molecular basis of ca2+-induced gelation in alginates and pectins: the egg-box model revisited," *Biomacromolecules*, vol. 2, no. 4, pp. 1089–1096, 2001. xv, 6

[19] G. T. Grant, E. R. Morris, D. A. Rees, P. J. Smith, and D. Thom, "Biological interactions between polysaccharides and divalent cations: the egg-box model," *FEBS Letters*, vol. 32, no. 1, pp. 195–198, 1973. 6

[20] W. Mackie, S. Perez, R. Rizzo, F. Taravel, and M. Vignon, "Aspects of the conformation of polyguluronate in the solid state and in solution," *International Journal of Biological Macromolecules*, vol. 5, no. 6, pp. 329–341, 1983. 6

[21] I. Braccini, R. P. Grasso, and S. Pérez, "Conformational and configurational features of acidic polysaccharides and their interactions with calcium ions: a molecular modeling investigation," *Carbohydrate Research*, vol. 317, no. 1-4, pp. 119–130, 1999. 6

[22] Y. Fang, S. Al-Assaf, G. O. Phillips, K. Nishinari, T. Funami, and P. A. Williams, "Binding behavior of calcium to polyuronates: comparison of pectin with alginate," *Carbohydrate Polymers*, vol. 72, no. 2, pp. 334–341, 2008. 6

[23] C. K. Siew, P. A. Williams, and N. W. Young, "New insights into the mechanism of gelation of alginate and pectin: charge annihilation and reversal mechanism," *Biomacromolecules*, vol. 6, no. 2, pp. 963–969, 2005. 6

[24] S. M. Cardoso, M. A. Coimbra, and J. L. Da Silva, "Temperature dependence of the formation and melting of pectin–ca2+ networks: a rheological study," *Food Hydrocolloids*, vol. 17, no. 6, pp. 801–807, 2003. 6

[25] C. Garnier, M. A. Axelos, and J.-F. Thibault, "Selectivity and cooperativity in the binding of calcium ions by pectins," *Carbohydrate Research*, vol. 256, no. 1, pp. 71–81, 1994. 6, 10

[26] C. Grosso, P. Bobbio, and C. Airoldi, "Effect of sugar and sorbitol on the formation of low methoxyl pectin gels," *Carbohydrate Polymers*, vol. 41, no. 4, pp. 421–424, 2000. 7, 13, 150, 153, 154

[27] F. Capel, T. Nicolai, D. Durand, P. Boulenguer, and V. Langendorff, "Calcium and acid induced gelation of (amidated) low methoxyl pectin," *Food Hydrocolloids*, vol. 20, no. 6, pp. 901–907, 2006. 7

[28] R. Lutz, A. Aserin, L. Wicker, and N. Garti, "Structure and physical properties of pectins with block-wise distribution of carboxylic acid groups," *Food Hydrocolloids*, vol. 23, no. 3, pp. 786–794, 2009. 8

[29] I. Fraeye, A. De Roeck, T. Duvetter, I. Verlent, M. Hendrickx, and A. Van Loey, "Influence of pectin properties and processing conditions on thermal pectin degradation," *Food Chemistry*, vol. 105, no. 2, pp. 555–563, 2007. 8

[30] E. R. Morris, A. Cutler, S. Ross-Murphy, D. Rees, and J. Price, "Concentration and shear rate dependence of viscosity in random coil polysaccharide solutions," *Carbohydrate polymers*, vol. 1, no. 1, pp. 5–21, 1981. 9

[31] M. Rinaudo and M. Milas, "Interaction of monovalent and divalent counterions with some carboxylic polysaccharides," *Journal of Polymer Science: Polymer Chemistry Edition*, vol. 12, no. 9, pp. 2073–2081, 1974. 9

[32] J. Narayanan, V. W. Deotare, R. Bandyopadhyay, and A. Sood, "Gelation of aqueous pectin solutions: A dynamic light scattering study," *Journal of Colloid and Interface Science*, vol. 245, no. 2, pp. 267–273, 2002. 10, 58, 62, 95, 96, 98

[33] A. Ström, E. Schuster, and S. M. Goh, "Rheological characterization of acid pectin samples in the absence and presence of monovalent ions," *Carbohydrate Polymers*, vol. 113, pp. 336–343, 2014. 10

[34] T. E. Furia, *CRC handbook of food additives*, vol. 1. CRC press, 1973. 10

[35] P. Harris, *Food gels*. Springer Science & Business Media, 2012. 10

[36] E. De Kort, M. Minor, T. Snoeren, T. Van Hooijdonk, and E. Van Der Linden, "Calcium-binding capacity of organic and inorganic ortho-and polyphosphates," *Dairy Science and Technology*, vol. 89, no. 3-4, pp. 283–299, 2009. 10

[37] R. C. Prince, D. E. Gunson, J. S. Leigh, and G. G. McDonald, "The predominant form of fructose is a pyranose, not a furanose ring," *Trends in Biochemical Sciences*, vol. 7, no. 7, pp. 239–240, 1982. 11

[38] M. Tait, A. Suggett, F. Franks, S. Ablett, and P. Quickenden, "Hydration of monosaccharides: A study by dielectric and nuclear magnetic relaxation," *Journal of Solution Chemistry*, vol. 1, no. 2, pp. 131–151, 1972. 11

[39] L. Tavel, E. Guichard, and C. Moreau, "Contribution of nmr spectroscopy to flavour release and perception," *Annual reports on NMR spectroscopy*, vol. 64, pp. 173–188, 2008. 12, 13

[40] S. Cerveny, F. Mallamace, J. Swenson, M. Vogel, and L. Xu, "Confined water as model of supercooled water," *Chemical Reviews*, vol. 116, no. 13, pp. 7608–7625, 2016. 12, 121

[41] S. Cerveny, I. Combarro-Palacios, and J. Swenson, "Evidence of coupling between the motions of water and peptides," *The Journal of Physical Chemistry Letters*, vol. 7, no. 20, pp. 4093–4098, 2016. 12

[42] M. Feeney, C. Brown, A. Tsai, D. Neumann, and P. G. Debenedetti, "Incoherent quasi-elastic neutron scattering from fructose- water solutions," *The Journal of Physical Chemistry B*, vol. 105, no. 32, pp. 7799–7804, 2001. 12

[43] M. Rampp, C. Buttersack, and H.-D. Lüdemann, "c, t-dependence of the viscosity and the self-diffusion coefficients in some aqueous carbohydrate solutions," *Carbohydrate Research*, vol. 328, no. 4, pp. 561–572, 2000. 12, 13, 70

[44] D. Sidebottom and T. D. Tran, "Universal patterns of equilibrium cluster growth in aqueous sugars observed by dynamic light scattering," *Physical Review E*, vol. 82, no. 5, p. 051904, 2010. 12, 68, 69, 149

[45] A. Rao, *Rheology of fluid, semisolid, and solid foods: principles and applications*. Springer Science & Business Media, 2013. 12, 15, 28, 84, 108, 109, 152

[46] C. Grosso and M. Rao, "Dynamic rheology of structure development in low-methoxyl pectin+ ca 2++ sugar gels," *Food Hydrocolloids*, vol. 12, no. 3, pp. 357–363, 1998. 12, 13, 84, 86, 88, 92, 99, 149, 153, 154

[47] J.-T. Fu and M. Rao, "The influence of sucrose and sorbitol on gel–sol transition of low-methoxyl pectin+ ca 2+ gels," *Food Hydrocolloids*, vol. 13, no. 5, pp. 371–380, 1999. 12, 13, 99, 149, 152, 168

[48] R. F. Stuewer, "The hydration and physicochemical properties of pectin and its derivatives," *The Journal of Physical Chemistry*, vol. 42, no. 3, pp. 305–315, 1938. 12

[49] H. Jansson, R. Bergman, and J. Swenson, "Dynamics of sugar solutions as studied by dielectric spectroscopy," *Journal of Non-Crystalline Solids*, vol. 351, no. 33-36, pp. 2858–2863, 2005. 12

[50] K. Ngai, S. Capaccioli, S. Ancherbak, and N. Shinyashiki, "Resolving the ambiguity of the dynamics of water and clarifying its role in hydrated proteins," *Philosophical Magazine*, vol. 91, no. 13-15, pp. 1809–1835, 2011. 12

[51] A. Panagopoulou, A. Kyritsis, N. Shinyashiki, and P. Pissis, "Protein and water dynamics in bovine serum albumin–water mixtures over wide ranges of composition," *The Journal of Physical Chemistry B*, vol. 116, no. 15, pp. 4593–4602, 2012. 12

[52] J. M. Harvey and M. C. Symons, "The hydration of monosaccharidesan nmr study," *Journal of Solution Chemistry*, vol. 7, no. 8, pp. 571–586, 1978. 13

[53] P. T. Callaghan, *Principles of nuclear magnetic resonance microscopy*. Oxford University Press on Demand, 1993. 13

[54] S. J. Angyal, "Complexes of carbohydrates with metal cations. i. determination of the extent of complexing by nmr spectroscopy," *Australian Journal of Chemistry*, vol. 25, no. 9, pp. 1957–1966, 1972. 13

[55] J. K. Beattie and M. T. Kelso, "Equilibrium and dynamics of the binding of calcium ion to sorbitol (d-glucitol)," *Australian Journal of Chemistry*, vol. 34, no. 12, pp. 2563–2568, 1981. 13

[56] J. Briggs, P. Finch, M. C. Matulewicz, and H. Weigel, "Complexes of copper (ii), calcium, and other metal ions with carbohydrates: thin-layer ligand-exchange chromatography and determination of relative stabilities of complexes," *Carbohydrate Research*, vol. 97, no. 2, pp. 181–188, 1981. 13

[57] K. K. Mäkinen and E. Söderling, "Solubility of calcium salts, enamel, and hydroxyapatite in aqueous solutions of simple carbohydrates," *Calcified Tissue International*, vol. 36, no. 1, pp. 64–71, 1984. 13, 154

[58] H. A. Barnes, J. F. Hutton, and K. Walters, *An introduction to rheology*, vol. 3. Elsevier, 1989. 14, 15, 16

[59] T. G. Mezger, *The rheology handbook: for users of rotational and oscillatory rheometers*. Vincentz Network GmbH & Co KG, 2006. 18, 20, 21, 27, 28, 30, 31, 59, 82, 113, 115, 117

[60] B. J. Berne and R. Pecora, *Dynamic light scattering: with applications to chemistry, biology, and physics*. Courier Corporation, 2000. 32, 34

[61] T. Zemb and P. Lindner, *Neutrons, X-rays and light: scattering methods applied to soft condensed matter*. North-Holland, 2002. 34, 37, 46

[62] P. R. Lang and Y. Liu, "Soft matter at aqueous interfaces," 2015. 35, 36, 37, 139, 141

[63] R. Borsali and R. Pecora, *Soft-Matter Characterization*. Springer Science & Business Media, 2008. 35, 37, 46, 123

[64] B. Nystroem, K. Thuresson, and B. Lindman, "Rheological and dynamic light-scattering studies on aqueous solutions of a hydrophobically modified nonionic cellulose ether and its unmodified analog," *Langmuir*, vol. 11, no. 6, pp. 1994–2002, 1995. 41

[65] R. Bergman, "General susceptibility functions for relaxations in disordered systems," *Journal of Applied Physics*, vol. 88, no. 3, pp. 1356–1365, 2000. 41, 62

[66] J. G. Joosten, E. T. Geladé, and P. N. Pusey, "Dynamic light scattering by nonergodic media: Brownian particles trapped in polyacrylamide gels," *Physical Review A*, vol. 42, no. 4, p. 2161, 1990. 41

[67] P. Pusey and W. Van Megen, "Dynamic light scattering by non-ergodic media," *Physica A: Statistical Mechanics and its Applications*, vol. 157, no. 2, pp. 705–741, 1989. 41, 90, 158

[68] J. G. Joosten, J. L. McCarthy, and P. N. Pusey, "Dynamic and static light scattering by aqueous polyacrylamide gels," *Macromolecules*, vol. 24, no. 25, pp. 6690–6699, 1991. 41, 96, 131, 133

[69] A. B. Rodd, D. E. Dunstan, D. V. Boger, J. Schmidt, and W. Burchard, "Heterodyne and nonergodic approach to dynamic light scattering of polymer gels: aqueous xanthan in the presence of metal ions (aluminum (iii))," *Macromolecules*, vol. 34, no. 10, pp. 3339–3352, 2001. 41

[70] M. Shibayama, "Spatial inhomogeneity and dynamic fluctuations of polymer gels," *Macromolecular Chemistry and Physics*, vol. 199, no. 1, pp. 1–30, 1998. 41

[71] L. Cipelletti, L. Ramos, S. Manley, E. Pitard, D. A. Weitz, E. E. Pashkovski, and M. Johansson, "Universal non-diffusive slow dynamics in aging soft matter," *Faraday Discussions*, vol. 123, pp. 237–251, 2003. 42, 99, 106, 113

[72] A. Krall and D. Weitz, "Internal dynamics and elasticity of fractal colloidal gels," *Physical Review Letters*, vol. 80, no. 4, p. 778, 1998. 42

[73] F. Ferri, "Use of a charge coupled device camera for low-angle elastic light scattering," *Review of Scientific Instruments*, vol. 68, no. 6, pp. 2265–2274, 1997. 42, 43

[74] L. Cipelletti and D. Weitz, "Ultralow-angle dynamic light scattering with a charge coupled device camera based multispeckle, multitau correlator," *Review of Scientific Instruments*, vol. 70, no. 8, pp. 3214–3221, 1999. 42, 44

[75] M. Gittings, L. Cipelletti, V. Trappe, D. Weitz, M. In, and C. Marques, "Structure of guar in solutions of h2o and d2o: An ultra-small-angle light-scattering study," *The Journal of Physical Chemistry B*, vol. 104, no. 18, pp. 4381–4386, 2000. 43, 44, 76, 77, 124, 134, 135

[76] A.-M. Philippe, L. Cipelletti, and D. Larobina, "Mucus as an arrested phase separation gel," *Macromolecules*, vol. 50, no. 20, pp. 8221–8230, 2017. 44, 77, 115

[77] L. Cipelletti, H. Bissig, V. Trappe, P. Ballesta, and S. Mazoyer, "Time-resolved correlation: a new tool for studying temporally heterogeneous dynamics," *Journal of Physics: Condensed Matter*, vol. 15, no. 1, p. S257, 2002. 44, 113

[78] B. R. Pauw, A. J. Smith, T. Snow, N. J. Terrill, and A. F. Thünemann, "The modular saxs data correction sequence for solids and dispersions," *arXiv preprint arXiv:1706.06769*, 2017. 54

[79] M. A. Masuelli, "Viscometric study of pectin. effect of temperature on the hydrodynamic properties," *International journal of biological macromolecules*, vol. 48, no. 2, pp. 286–291, 2011. 58, 64

[80] H. Anger and G. Berth, "Gel permeation chromatography and the mark-houwink relation for pectins with different degrees of esterification," *Carbohydrate Polymers*, vol. 6, no. 3, pp. 193–202, 1986. 58, 64

[81] B. Nystrom, H. Walderhaug, and F. K. Hansen, "Dynamic crossover effects observed in solutions of a hydrophobically associating water-soluble polymer," *The Journal of Physical Chemistry*, vol. 97, no. 29, pp. 7743–7752, 1993. 60, 62, 96

[82] B. Nyström, J. Roots, A. Carlsson, and B. Lindman, "Light scattering studies of the gelation process in an aqueous system of a non-ionic polymer and a cationic surfactant," *Polymer*, vol. 33, no. 14, pp. 2875–2882, 1992. 60, 96

[83] J. F. Douglas and J. B. Hubbard, "Semiempirical theory of relaxation: Concentrated polymer solution dynamics," *Macromolecules*, vol. 24, no. 11, pp. 3163–3177, 1991. 60

[84] G. Medjahdi, D. Sarazin, and J. Francois, "Theoretical approach to enhanced low-angle scattering from moderately concentrated polymer solutions," *Macromolecules*, vol. 24, no. 14, pp. 4138–4141, 1991. 60

[85] D. Bulone, V. Martorana, C. Xiao, and P. L. San Biagio, "Role of sucrose in pectin gelation: static and dynamic light scattering experiments," *Macromolecules*, vol. 35, no. 21, pp. 8147–8151, 2002. 62, 64, 66, 68, 78, 131, 134, 136

[86] O. Marstokk, B. Nyström, and J. Roots, "Effect of denaturant and polymer concentration on the structural and dynamical properties of aqueous solutions of poly (n-acetamido acrylamide)," *Macromolecules*, vol. 31, no. 13, pp. 4205–4212, 1998. 62, 96

[87] G. Berth, H. Dautzenberg, and J. Hartmann, "Static light scattering technique applied to pectin in dilute solution. 3. the tendency for association," *Carbohydrate Polymers*, vol. 25, no. 3, pp. 197–202, 1994. 64, 131

[88] W. Brown, *Light scattering: principles and development*, vol. 53. Oxford University Press, 1996. 66

[89] D. L. Sidebottom, "Ultraslow relaxation of hydrogen-bonded dynamic clusters in glass-forming aqueous glucose solutions: A light scattering study," *Physical Review E*, vol. 76, no. 1, p. 011505, 2007. 68, 69, 70, 112, 149

[90] A. Lerbret, P. Bordat, F. Affouard, M. Descamps, and F. Migliardo, "How homogeneous are the trehalose, maltose, and sucrose water solutions? an insight from molecular dynamics simulations," *The Journal of Physical Chemistry B*, vol. 109, no. 21, pp. 11046–11057, 2005. 68

[91] C. Roberts and P. G. Debenedetti, "Structure and dynamics in concentrated, amorphous carbohydrate- water systems by molecular dynamics simulation," *The Journal of Physical Chemistry B*, vol. 103, no. 34, pp. 7308–7318, 1999. 70

[92] E. Schuster, A. Cucheval, L. Lundin, and M. A. Williams, "Using saxs to reveal the degree of bundling in the polysaccharide junction zones of microrheologically distinct pectin gels," *Biomacromolecules*, vol. 12, no. 7, pp. 2583–2590, 2011. 71, 124, 137, 139

[93] J. C. Addad, *Physical properties of polymeric gels*. Wiley Chichester, 1996. 71, 123, 131, 141

[94] T. A. Vilgis, "Gels: model systems for soft matter food physics," *Current Opinion in Food Science*, vol. 3, pp. 71–84, 2015. 88

[95] M. Shibayama and T. Norisuye, "Gel formation analyses by dynamic light scattering," *Bulletin of the Chemical Society of Japan*, vol. 75, no. 4, pp. 641–659, 2002. 90

[96] G. Sworn and S. Kasapis, "Effect of conformation and molecular weight of co-solute on the mechanical properties of gellan gum gels," *Food Hydrocolloids*, vol. 12, no. 3, pp. 283–290, 1998. 99, 112, 145, 149, 168

[97] H. H. Winter and M. Mours, "Rheology of polymers near liquid-solid transitions," in *Neutron spin echo spectroscopy viscoelasticity rheology*, pp. 165–234, Springer, 1997. 104, 108

[98] T. Morishita, "Compressed exponential relaxation in liquid silicon: Universal feature of the crossover from ballistic to diffusive behavior in single-particle dynamics," *The Journal of Chemical Physics*, vol. 137, no. 2, p. 024510, 2012. 106

[99] M. Axelos and M. Kolb, "Crosslinked biopolymers: Experimental evidence for scalar percolation theory," *Physical Review Letters*, vol. 64, no. 12, p. 1457, 1990. 109

[100] T. Afrin, N. N. Mafy, M. M. Rahman, M. Y. A. Mollah, and M. Susan, "Temperature perturbed water structure modification by d (-)-fructose at different concentrations," *RSC Advances*, vol. 4, no. 92, pp. 50906–50913, 2014. 112, 149

[101] M. Ousalem, J. Busnel, and T. Nicolai, "A static and dynamic light scattering study of sharp pectin fractions in aqueous solution," *International journal of biological macromolecules*, vol. 15, no. 4, pp. 209–213, 1993. 131

[102] R. Basak and R. Bandyopadhyay, "Formation and rupture of ca 2+ induced pectin biopolymer gels," *Soft Matter*, vol. 10, no. 37, pp. 7225–7233, 2014. 134

[103] M. Takenaka, "Analysis of structures of rubber-filler systems with combined scattering methods," *Polymer Journal*, vol. 45, no. 1, p. 10, 2013. 135

[104] J. T. Koberstein, C. Picot, and H. Benoit, "Light and neutron scattering studies of excess low-angle scattering in moderately concentrated polystyrene solutions," *Polymer*, vol. 26, no. 5, pp. 673–681, 1985. 137

[105] B. W. Mansel and M. A. Williams, "Internal stress drives slow glassy dynamics and quake-like behaviour in ionotropic pectin gels," *Soft Matter*, vol. 11, no. 35, pp. 7016–7023, 2015. 138

[106] R. P. Rambo and J. A. Tainer, "Characterizing flexible and intrinsically unstructured biological macromolecules by sas using the porod-debye law," *Biopolymers*, vol. 95, no. 8, pp. 559–571, 2011. 138, 139

[107] M. Shibayama, F. Ikkai, and S. Nomura, "Complexation of poly (vinyl alcohol)-congo red aqueous solutions. 2. sans and saxs studies on sol-gel transition," *Macromolecules*, vol. 27, no. 22, pp. 6383–6388, 1994. 139, 141

[108] C. A. Maestri, M. Abrami, S. Hazan, E. Chistè, Y. Golan, J. Rohrer, A. Bernkop-Schnürch, M. Grassi, M. Scarpa, and P. Bettotti, "Role of sonication pre-treatment and cation valence in the sol-gel transition of nanocellulose suspensions," *Scientific Reports*, vol. 7, no. 1, p. 11129, 2017. 141, 146

[109] K. Fukada, T. Ishii, K. Tanaka, M. Yamaji, Y. Yamaoka, K.-i. Kobashi, and K. Izumori, "Crystal structure, solubility, and mutarotation of the rare monosaccharide d-psicose," *Bulletin of the Chemical Society of Japan*, vol. 83, no. 10, pp. 1193–1197, 2010. 150, 156

[110] S. Anoyal, "Complexing of polyols with cations," *Tetrahedron*, vol. 30, no. 12, pp. 1695–1702, 1974. 150

[111] A. Kieboom, A. Sinnema, J. Van Der Toorn, and H. Van Bekkum, "13c nmr study of the complex formation of sorbitol (glucitol) with multivalent cations in aqueous solution using lanthanide (iii) nitrates as shift reagents," *Recueil des Travaux Chimiques des Pays-Bas*, vol. 96, no. 2, pp. 35–37, 1977. 150

[112] A. Tsoga, R. Richardson, and E. Morris, "Role of cosolutes in gelation of high-methoxy pectin. part 1. comparison of sugars and polyols," *Food Hydrocolloids*, vol. 18, no. 6, pp. 907–919, 2004. 150

[113] P. Rongère, N. Morel-Desrosiers, and J.-P. Morel, "Interactions between cations and sugars. part 8.gibbs energies, enthalpies and entropies of association of divalent and trivalent metal cations with xylitol and glucitol in water at 298.15 k," *Journal of the Chemical Society, Faraday Transactions*, vol. 91, no. 17, pp. 2771–2777, 1995. 154

[114] S. G. Chou, A. K. Soper, S. Khodadadi, J. E. Curtis, S. Krueger, M. T. Cicerone, A. N. Fitch, and E. Y. Shalaev, "Pronounced microheterogeneity

in a sorbitol–water mixture observed through variable temperature neutron scattering," *The Journal of Physical Chemistry B*, vol. 116, no. 15, pp. 4439–4447, 2012. 158, 169

[115] A. Lerbret, P. Mason, R. Venable, A. Cesàro, M.-L. Saboungi, R. Pastor, and J. Brady, "Molecular dynamics studies of the conformation of sorbitol," *Carbohydrate Research*, vol. 344, no. 16, pp. 2229–2235, 2009. 169

[116] R. Politi, L. Sapir, and D. Harries, "The impact of polyols on water structure in solution: a computational study," *The Journal of Physical Chemistry A*, vol. 113, no. 26, pp. 7548–7555, 2009. 169